

**EXPERIMENTAL ANALYSIS OF POSITIVE DISPLACEMENT  
COMPRESSORS FOR DOMESTIC REFRIGERATOR FREEZER AND  
AIR CONDITIONING APPLICATION**

by

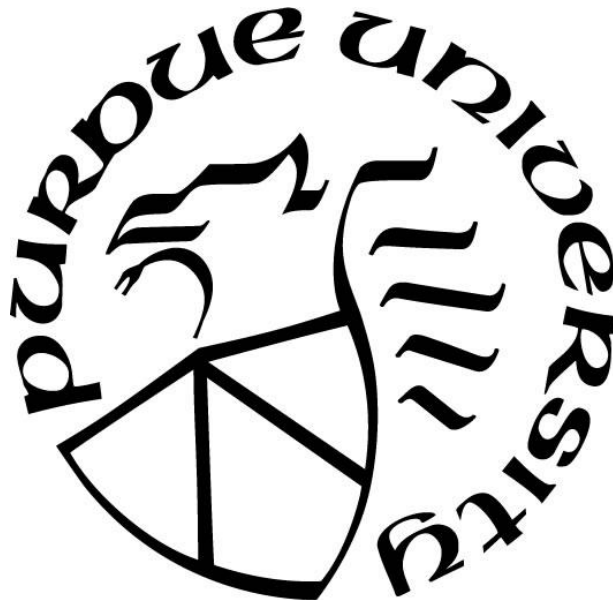
**Cai Stephen Rohleder**

**A Thesis**

*Submitted to the Faculty of Purdue University*

*In Partial Fulfillment of the Requirements for the degree of*

**Master of Science in Mechanical Engineering**



School of Mechanical Engineering

West Lafayette, Indiana

May 2019

**THE PURDUE UNIVERSITY GRADUATE SCHOOL  
STATEMENT OF COMMITTEE APPROVAL**

Dr. Eckhard A. Groll, Chair  
School of Mechanical Engineering

Dr. James E. Braun  
School of Mechanical Engineering

Dr. William T. Horton  
School of Civil Engineering

**Approved by:**

Dr. Jay P. Gore  
Head of the Graduate Program

*To my parents and brother*

## ACKNOWLEDGMENTS

I would like to start by thanking Professor Groll, Professor Braun, and Professor Horton for being on my defense committee, and deeming my work worthy of a master's degree. Additional gratitude to Dr. Groll for being an outstanding advisor that has always looked out for mine and my lab-mates' best interests while also driving us to do the best we can. Dr. Groll's intellect and experience, as well as genuine interest in his students' wellbeing, is greatly appreciated. Thank you also to Dr. Davide Ziviani and Dr. Orkan Kurtulus for providing additional guidance and spotting room for improvement in my work.

Another key figure in my success has been Frank Lee. I have done my best to thank Frank for every fitting installation, vacuum pull, leak fix, piping rewire, electrical hookup, and compressor shakedown, but I do not think it was enough. Without Frank's practical knowledge on compressor testing, or his humorous personality, I would still be miserably trying to figure out where the suction and discharge ports of a compressor are.

To my friends at the Herrick Labs; Li, Leon, Nick, Xinye, Haotian, Vatsal, Parveen, Alejandro, Akash, and Xueyang, thank you all for keeping the lab a fun place to be, and providing help when I needed it. Special thank you to Riley Barta for his example of what it means to work hard to achieve long term goals, being available at any time to debate an idea, and for keeping me alive by taking me to the store every Sunday.

Thank you also to the sponsors of my various projects; Air Squared Inc., Regal Beloit Corporation, Hi-Bar Blowers Inc., and Solvay S.A.

Lastly, I would like to thank my family for their support and certainty that I would make it through.

## TABLE OF CONTENTS

LIST OF TABLES .....	8
LIST OF FIGURES .....	10
NOMENCLATURE .....	15
ABSTRACT.....	17
1. INTRODUCTION .....	18
1.1 Motivation.....	18
1.2 Compressor Applications.....	19
1.2.1 Refrigerator Freezer Application.....	19
1.2.2 Air Conditioning Application .....	20
1.3 Investigated Compressor Types.....	20
1.3.1 Reciprocating Compressor.....	20
1.3.2 Scroll Compressor .....	22
1.3.3 Rotary Compressor .....	23
1.4 Performance Comparison of Compressors .....	25
1.4.1 Standards for Compressor Testing.....	25
1.4.2 Steady-State Qualifiers .....	27
1.4.3 General Black-Box Performance Analysis .....	28
1.4.4 Additional Analysis Capability in the Compressor Calorimeter .....	30
1.4.5 Pressure Fluctuation in Positive Displacement Compressors.....	31
1.4.6 Uncertainty .....	34
1.4.7 Available Compressor Performance Maps .....	35
1.5 Objectives .....	38
1.6 Explanation of Thesis Layout .....	38
2. DOMESTIC REFRIGERATOR FREEZER .....	40
2.1 Experimental Setup.....	40
2.1.1 Hot-Gas Bypass Vapor-Compression Cycle .....	40
2.1.2 Hot-Gas Bypass Test Stand .....	43
2.1.3 Hot-Gas Bypass Test Stand Instrumentation.....	45
2.1.4 Modifications.....	49

2.1.5	Operation .....	53
2.2	Data Acquisition and Software .....	55
2.3	Tests Performed and Results.....	56
2.3.1	Air Squared Scroll Prototype.....	56
2.3.2	Embraco Reciprocating Compressor .....	61
2.3.3	Comparison.....	67
3.	RESIDENTIAL AIR CONDITIONING .....	74
3.1	Experimental Setup.....	74
3.1.1	Tescor Calorimeter .....	74
3.1.2	Tescor Calorimeter Instrumentation .....	78
3.1.3	Modifications .....	81
3.1.4	Operation .....	86
3.1.5	Tescor Calorimeter and Compressor Limits.....	89
3.2	Data Acquisition and Software .....	90
3.2.1	Calorimeter Data Acquisition Software “Main VI” .....	90
3.2.2	High Frequency Pressure Transducer VI.....	94
3.2.3	EXV Control VI.....	96
3.3	Tests Performed and Results.....	97
3.3.1	Copeland Scroll Compressor .....	97
3.3.2	Highly Dual Rotary Compressor .....	104
3.3.3	Map Comparison .....	112
4.	CONCLUSION AND RECOMMENDATIONS .....	125
	REFERENCES .....	127
	APPENDIX A: OIL-FREE SCROLL COMPRESSOR DATA .....	130
	APPENDIX B: RECIPROCATING COMPRESSOR DATA .....	132
	APPENDIX C: COPELAND SCROLL COMPRESSOR DATA.....	136
	APPENDIX D: ROTARY COMPRESSOR DATA.....	141
	APPENDIX E: OIL-FREE SCROLL COMPRESSOR EES ANALYSIS SCRIPT .....	149
	APPENDIX F: RECIPROCATING COMPRESSOR EES ANALYSIS SCRIPT .....	152
	APPENDIX G: COPELAND SCROLL COMPRESSOR EES ANALYSIS SCRIPT .....	157
	APPENDIX H: ROTARY COMPRESSOR EES ANALYSIS SCRIPT .....	160

APPENDIX I: MATLAB FFT SCRIPT .....	163
APPENDIX J: AHRI 10-COEFFICIENT CORRELATION MATLAB SCRIPT .....	165
APPENDIX K: 10-COEFFICIENT MATLAB LEAST SQUARES SOLVERS.....	169
APPENDIX L: LI CORRELATION MATLAB SCRIPT .....	172
APPENDIX M: LI CORRELATION LEAST SQUARE SOLVER .....	176
APPENDIX N: MENDOZA-MIRANDA CORRELATION MATLAB SCRIPT.....	178
APPENDIX O: MENDOZA-MIRANDA CORRELATION LEAST SQUARES SOLVERS..	182

## LIST OF TABLES

Table 1.1: Table of accuracy requirements as described in ASHRAE 23.1 .....	25
Table 1.2: Values collected in the testing described in this paper. Units in parenthesis are alternative units that were used in data collected in this paper.....	26
Table 1.3: Maximum deviations permitted from average value in data set for each property. ....	27
Table 2.1: Original Valves for Small Hot-Gas Bypass Test Stand. All valves were manufactured by Swagelok.....	44
Table 2.2: Pressure Transducer Calibration Curves. ....	46
Table 2.3: Location and accuracy of thermocouples and pressure transducers in Small Hot-Gas Bypass Test Stand. ....	46
Table 2.4: Valve replacements for the Small Hot-Gas Bypass Test Stand.....	51
Table 2.5: List of coefficients for the reciprocating compressor with the original composition. .	69
Table 3.1: Pressure transducer calibration curves with formant $p = a1 * U + a0$ . $U$ is in volts and $P$ is in psia. The LabVIEW VI for data acquisition later converts this unit to kPa. ....	79
Table 3.2: Descriptions for each data label on the steady-state evaluation page of the Main calorimeter VI. ....	93
Table 3.3: AHRI 10 Coefficient performance predictions with a training set that covers the entire operating range.....	113
Table 3.4: Li Correlation performance predictions with a training set that covers the entire operating range.....	114
Table 3.5: Mendoza (et al.) Correlation performance predictions with a training set that covers the entire operating range.....	114
Table 3.6: AHRI 10 Coefficient performance predictions with an extrapolation focused training set. ....	119
Table 3.7: Li Correlation performance predictions with an extrapolation focused training set. ....	120
Table 3.8: Mendoza (et al.) performance predictions with an extrapolation focused training set. ....	120
Table 6.1: Measurement Data for the Scroll Compressor on the Hot-Gas Bypass Test Stand... ..	130
Table 6.2: Calculated Performance Data for the Scroll Compressor on the Hot-Gas Bypass Test Stand. ....	131
Table 6.3: Measurement Data for the Reciprocating Compressor on the Hot-Gas Bypass Test Stand. ....	132

Table 6.4: Calculated Performance Data for the Reciprocating Compressor on the Hot-Gas Bypass Test Stand. ....	134
Table 6.5: Measurement Data for the Scroll Compressor on the Tesco Calorimeter.....	136
Table 6.6: Calculated Performance Data for the Scroll Compressor on the Tesco Calorimeter. ....	139
Table 6.7: Measurement Data for the Rotary Compressor on the Tesco Calorimeter. ....	141
Table 6.8: Calculated Performance Data for the Rotary Compressor on the Tesco Calorimeter. ....	146

## LIST OF FIGURES

Figure 1.1: Compression process in a reciprocating compressor that utilizes a piston cylinder. Note the suction valve (left line) and the discharge valve (right line).....	21
Figure 1.2: Compression process for a scroll compressor as illustrated by Bell (2011). .....	22
Figure 1.3: Compression process for a Rotary Compressor. $s$ denotes the suction pocket and $d$ denotes the discharge pocket. The suction port is left and the discharge port is right (with the valve).....	24
Figure 1.4: Under-compression (left) and Over-compression (right) in the compression process as illustrated by Huang (2012). .....	32
Figure 2.1 Hot-Gas Bypass test stand circuitry .....	41
Figure 2.2: Pressure enthalpy diagram of the Hot-Gas Bypass cycle. The figure describes the three pressure levels of the cycle. ....	42
Figure 2.3: Pressure enthalpy diagrams of the Hot-Gas Bypass cycle. The figure details energy flow across the cycle. ....	43
Figure 2.4: Original Small Hot-Gas Bypass Test Stand configuration. Motor control and power supply detail described for prototype oil-free scroll compressor.....	44
Figure 2.5: Pressure Transducer Calibration Test Stand. The PCL-1B Pressure Transducer was used as the reference value for calibrating other pressure transducers. ....	45
Figure 2.6: Schematic of the Mass Flow Meter Calibration Test Stand.....	47
Figure 2.7: Original Small Hot-Gas Bypass Test Stand (Top Shelf). Pressure, temperature, and mass flow measurements can be seen. ....	48
Figure 2.8: Location of prototype scroll compressor on second shelf. ....	49
Figure 2.9: Modified Small Hot-Gas Bypass Test Stand. Oil separation was added, as well as an 8 <sup>th</sup> thermocouple closer to the discharge of the compressor and before the oil separator. ....	50
Figure 2.10: Updated Small Hot-Gas Bypass Test Stand. Note that some discharge piping (traced in red arrows) is routed above other piping. ....	53
Figure 2.11: Front panel to the VI used for testing on the Small Hot-Gas Bypass Test Stand. ...	56
Figure 2.12: Data collection into formatted text document for the Small Hot-Gas Bypass Test Stand. ....	56
Figure 2.13: Magnetic coupling between compressor shaft and motor shaft on the scroll compressor. ....	57
Figure 2.14: Operating conditions performed on the prototype scroll compressor. ....	58

Figure 2.15: Mass flow rate (left axis) and power draw (right axis) across pressure ratio of the prototype scroll compressor. ....	59
Figure 2.16: Overall compressor efficiency of the prototype scroll compressor. ....	59
Figure 2.17: Volumetric efficiency of the prototype scroll compressor. ....	60
Figure 2.18: Potential evaporating capacity (left axis) and COP (right axis) of the prototype scroll compressor. ....	60
Figure 2.19: Embraco Reciprocating Compressor. (left) original compressor shell, (center) semi-hermetic compressor undergoing a leak test by being placed underwater while pressurized internally, (right) semi-hermetic shell opened to allow for access to compressor internals. ....	62
Figure 2.20: Original composition of the piston cylinder head and the paper gasket sealing between the cylinder head (right) and the discharge valve plate (left). ....	63
Figure 2.21: Polymer replacement components for the piston cylinder head of the Embraco reciprocating compressor. (left) Buna N gasket overlaid onto discharge valve plate, (right) polymer piston cylinder head. ....	63
Figure 2.22: Operating conditions for the reciprocating compressor. All tests were performed after the compressor was modified to be semi-hermetic. ....	64
Figure 2.23: Mass flow rate over pressure ratio of both compositions of the reciprocating compressor. ....	65
Figure 2.24: Power draw over pressure ratio of both compositions of the reciprocating compressor. ....	65
Figure 2.25: Overall compressor efficiency for both compositions of the reciprocating compressor. ....	66
Figure 2.26: Volumetric efficiency of both compositions of the reciprocating compressor. ....	66
Figure 2.27: Potential evaporating capacity of both compositions of the reciprocating compressor. ....	67
Figure 2.28: Potential COP of both compositions of the reciprocating compressor. ....	67
Figure 2.29: Suction superheat comparison between the scroll compressor and the reciprocating compressor. Note that superheat control is a function of the test stand and not the compressor. ....	68
Figure 2.30: Mass flow rate comparison between the superheat corrected polymer data and the original composition map. ....	70
Figure 2.31: Power draw comparison between the superheat corrected polymer data and the original composition map. ....	70
Figure 2.32: Overall compressor efficiency comparison between the superheat corrected polymer data and the original composition map. ....	71
Figure 2.33: Volumetric efficiency comparison between the superheat corrected polymer data and the original composition map. ....	71

Figure 2.34: Potential evaporating capacity comparison between the superheat corrected polymer data and the original composition map. ....	72
Figure 2.35: Potential COP comparison between the superheat corrected polymer data and the original composition map. ....	72
Figure 3.1: General layout of the Tescor Compressor Calorimeter. ....	74
Figure 3.2: Process water circulation loop on the cooling side of the condenser. ....	75
Figure 3.3: Suction pressure control via pneumatic expansion valve (PXV). ....	76
Figure 3.4: Suction temperature control via evaporator in secondary refrigerant tank with heating elements with varying capacity. ....	77
Figure 3.5: Compressor chamber for ambient air temperature control around the compressor. ..	78
Figure 3.6: Compressor three-phase power measurement for the power supply. Originally illustrated by Mösch (2015). ....	80
Figure 3.7: Tescor Calorimeter with instrumentation. ....	81
Figure 3.8: Location of pressure transducer in both the scroll (left) and dual rotary (right) compressors in the calorimeter. ....	82
Figure 3.9: High frequency pressure transducer wiring configuration. ....	83
Figure 3.10: Control wiring diagram for the EXV in the calorimeter. ....	84
Figure 3.11: Left side of the calorimeter control panel where the EKA 164A display for the EXV is boxed in red. ....	85
Figure 3.12: Tescor Calorimeter with modifications. Note the replacement of a PXV with an EXV, and the addition of P8 (High Frequency Pressure Transducer from Kulite). ....	85
Figure 3.13: Control Panel for the Tescor Compressor Calorimeter. ....	86
Figure 3.14: Process water control and bypass valves for the calorimeter. ....	87
Figure 3.15: Piping and Instrumentation tab on the Main calorimeter VI. ....	90
Figure 3.16: Graphs tab of the Main calorimeter VI. ....	91
Figure 3.17: Steady State Evaluation tab of the Main calorimeter VI. ....	92
Figure 3.18: Data output from the Main VI on the calorimeter. ....	94
Figure 3.19: High Frequency Pressure Transducer VI. Note the Y-axis “Amplitude” is pressure in psia. ....	95
Figure 3.20: High Frequency Pressure Transducer VI data output. ....	96
Figure 3.21: EXV Control VI for the calorimeter EXV. ....	97
Figure 3.22: Operating points tested on the Copeland scroll compressor. Red lines indicate the operating boundaries of the compressor when installed in the calorimeter (Mösch, 2015). ....	98

Figure 3.23: Mass flow rate with varying pressure ratio of the Copeland scroll compressor. ....	98
Figure 3.24: Mass flow corroboration between primary and secondary calculation methods for the Copeland scroll compressor. ....	99
Figure 3.25: Power draw with varying pressure ratio of the Copeland scroll compressor. ....	99
Figure 3.26: Evaporating capacity with varying pressure ratio of the Copeland scroll compressor. ....	100
Figure 3.27: Overall isentropic compressor efficiency with varying pressure ratio of the Copeland scroll compressor. ....	100
Figure 3.28: Volumetric efficiency with varying pressure ratio of the Copeland scroll compressor. ....	101
Figure 3.29: Coefficient of performance with varying pressure ratio of the Copeland scroll compressor. ....	101
Figure 3.30: Time (left) and frequency (right) domain of the scroll compressor discharge at an evaporating temperature of -13.3 C and condensing temperature of 54.7 C (pressure ratio of 7.7). This is a case of under-compression. ....	102
Figure 3.31: Time (left) and frequency (right) domain of the scroll compressor discharge at an evaporating temperature of -8.1 C and condensing temperature of 36.1 C (pressure ratio of 4.1). This case operates near the ideal pressure ratio of the compressor. ....	102
Figure 3.32: Time (left) and frequency (right) domain of the scroll compressor discharge at an evaporating temperature of 4.3 C and condensing temperature of 37.9 C (pressure ratio of 2.7). This is a case of over-compression. ....	103
Figure 3.33: Pressure fluctuation with varying pressure ratio of the Copeland scroll compressor. ....	104
Figure 3.34: Operating points tested on the dual rotary compressor. ....	105
Figure 3.35: Mass flow rate with varying pressure ratio of the dual rotary compressor. ....	105
Figure 3.36: Mass flow rate deviation between the primary mass flow measurement and the secondary mass flow calculation. ....	106
Figure 3.37: Power draw with varying pressure ratio of the dual rotary compressor. ....	106
Figure 3.38: Evaporating capacity with varying pressure ratio of the dual rotary compressor. ..	107
Figure 3.39: Overall isentropic efficiency with varying pressure ratio of the dual rotary compressor. ....	107
Figure 3.40: Volumetric efficiency with varying pressure ratio of the dual rotary compressor. ....	108
Figure 3.41: Coefficient of performance with varying pressure ratio of the dual rotary compressor. ....	108

Figure 3.42: Time (left) and frequency (right) domain of the dual rotary compressor discharge at an evaporating temperature of -21.8 C and condensing temperature of 53.6 C (pressure ratio of 8.9). This is a condition of under compression.....	109
Figure 3.43: Time (left) and frequency (right) domain of the dual rotary compressor discharge at an evaporating temperature of -1.1 C and condensing temperature of 44.8 C (pressure ratio of 3.5). This condition operates near the ideal pressure ratio of the compressor.....	109
Figure 3.44: Time (left) and frequency (right) domain of the dual rotary compressor discharge at an evaporating temperature of -1.2 C and condensing temperature of 28.4 C (pressure ratio of 2.6). This is a condition of over compression.....	110
Figure 3.45: Pressure fluctuation with varying pressure ratio of the dual rotary compressor. ....	111
Figure 3.46: Pressure fluctuation with varying evaporating temperature of the dual rotary compressor. ....	111
Figure 3.47: Copeland scroll data used in comparing the three different maps. Note that operating points that are not used in training the maps are used for comparing map predictions.....	112
Figure 3.48: Dual rotary data used in comparing the three different maps. Note that operating points that are not used in training the maps are used for comparing map predictions.....	113
Figure 3.49: Mass flow rate comparison between the 3 maps using training data that spans the entire operating range of the respective compressors.....	115
Figure 3.50: Power draw comparison between the 3 maps using training data that spans the entire operating range of the respective compressors.....	116
Figure 3.51: Overall isentropic efficiency comparison between the 3 maps using training data that spans the entire operating range of the respective compressors.....	116
Figure 3.52: Volumetric efficiency comparison between the 3 maps using training data that spans the entire operating range of the respective compressors.....	117
Figure 3.53: Copeland scroll data used in comparing the three different maps for extrapolation predictions. Note that operating points that are not used in training the maps are used for comparing map predictions.....	118
Figure 3.54: Dual rotary data used in comparing the three different maps for extrapolation predictions. Note that operating points that are not used in training the maps are used for comparing map predictions.....	119
Figure 3.55: Mass flow rate comparison between the 3 maps using extrapolation training data.....	121
Figure 3.56: Power draw comparison between the 3 maps using extrapolation training data....	122
Figure 3.57: Overall isentropic efficiency comparison between the 3 maps using extrapolation training data.....	122
Figure 3.58: Volumetric efficiency comparison between the 3 maps using extrapolation training data.....	123

## NOMENCLATURE

<b>Symbols</b>		<b>Subscripts</b>	
$AU$	Heat leakage coefficient	$amb$	Ambient air
$C$	Current or Coefficient	$Comp$	Compressor
$COP$	Coefficient of Performance	$Cond$	Condenser
$C_v$ or $C_v$	Valve coefficient	$Dis$	Discharge
$G$	Specific gravity	$Disp$	Displacement
$h$	Specific enthalpy	$Evap$	Evaporater
$k$	Refrigerant isentropic coefficient	$exp$	Experimental
$\dot{m}$	mass flowrate	$f$	Liquid
$M$	Molecular weight	$g$	Gas
MAE	Mean Average Error	$hg$	Hot-gas
$\dot{N}$	Occurrence rate (Frequency)	$I$	Inlet
$p$ or $P$	Pressure	$is$	Isentropic
$\dot{Q}$	Power yielded from heat (heat capacity)	$is, O$	Overall isentropic
$q$	Volumetric flowrate	$liq$	Liquid line
RSME	Root Mean Square Error	$map$	Yielded from a performance map
$s$	Specific entropy	$new$	New
$T$	Temperature	$O$	Outlet
$U$	Voltage	$pred$	Predicted
$u_c$	Absolute uncertainty	$r$	Refrigerant
$V$	Volume	$refer$	Reference
$v$	Specific volume	$Rat$	Ratio
$\dot{W}$	Power yielded from work	$Rot$	Rotation

<i>Sat</i>	Saturation	<i>y</i> or <i>Y</i>	Dependent variable
<i>SC</i>	Subcooling		
<i>SH</i>	Superheat		
<i>sec</i>	Secondary		
<i>Suc</i>	Suction		
<i>V</i>	Volumetric		

### Greek and Mathematical Symbols

<i>a</i>	Constant coefficient	
<i>b</i>	Constant coefficient	
$\Delta$	Difference between 2 quantities	
<i>dp</i>	Constant coefficient	
$\eta$	Efficiency	
$\frac{\partial f}{\partial x}$	Partial derivative	
<i>f(x)</i>	Function	
<i>i</i>	Index of a vector	
<i>j</i>	Index of a vector	
<i>k</i>	Index of a vector	
<i>n</i>	Length of a vector	
$\sum x$	Summation	
$\theta$	Angle	
$W_n$	Shortened form of Euler's Formula	
<i>x</i> or <i>X</i>	Independent variable	
$\bar{x}$	Average	

## ABSTRACT

Author: Rohleder, Cai, S. MSME

Institution: Purdue University

Degree Received: May 2019

Title: Experimental Analysis of Positive Displacement Compressors for Domestic Refrigerator Freezer and Air Conditioning Application

Committee Chair: Eckhard Groll

Vapor compression cycles are the most common method used to provide cooling to environments. In the residential area, refrigerator/freezers as well as air conditioners/heat pumps almost exclusively use vapor compression cycles. The driving force behind a vapor compression cycle is the compressor, where a variety of compressor types are used in the same application. While reciprocating compressors are found in the majority of refrigerator/freezers, scroll compressors are predominantly used in residential air conditioners. Yet other compressors have emerged as replacements due to increased efficiency. A R134a oil-free prototype scroll compressor and a R134a reciprocating compressor are operated in a hot-gas bypass test stand under refrigerator/freezer conditions to compare performance. Additionally, a R407C scroll compressor and a R410A rotary compressor are operated in a compressor calorimeter under air conditioning/heat pump conditions to compare performance. Experimental results show that the reciprocating compressor far outperforms the prototype scroll compressor in the refrigerator/freezer application, while the performance between the scroll and rotary compressors are almost equal in the air conditioning application.

Pressure fluctuation at compressor discharge is also measured in the compressor calorimeter to determine feasibility of applying a novel muffling design to air conditioning compressors, although it was found that traditional muffling methods currently used are effective to a degree such that this new method is unwarranted. Data from the compressor calorimeter is also used to investigate the accuracy of the AHRI 540 10-Coefficient Correlation compressor map in predicting performance both inside and outside the tested operating conditions. The AHRI 10-Coefficient Correlation achieves high accuracy inside tested operating conditions but is inept in extrapolating performance, where other map correlations are more accurate.

# 1. INTRODUCTION

Since the 19<sup>th</sup> century, vapor-compression cycles have been used to cool spaces and objects to temperatures lower than the environment temperature (Groll, 2017). The vapor-compression cycle sustains a temperature difference between two heat exchangers, where one heat exchanger known as the evaporator absorbs heat from one medium (air, water, etc.) at a temperature below the medium temperature, and the other heat exchanger known as the condenser rejects heat to another medium at a temperature above that medium temperature. The ability to create this temperature difference is due to the coupled nature of pressure and temperature of fluids in a two-phase state, where the evaporator operates at a low-pressure level and the condenser at a high-pressure level. The driving force behind this pressure difference is the compressor, which intakes low-pressure working fluids (refrigerants) after the evaporator and compresses them to high pressures before the condenser. The compressor is the most active and complex component in a vapor-compression cycle, where most of the cycle's energy usage takes place in powering the compressor motor. In most non-industrial HVAC&R applications, a positive displacement compressor is used. Various styles of compressors are used to achieve the same compression principle in the cycle, each with their own benefits and downfalls.

## 1.1 Motivation

When attempting to improve traditional compressor design it is important to be able to maintain comparable performance parameters of the compressor in a publishable manner. Improvements to a specific compressor type typically involves a reduction in energy usage, material composition change, or reduction in noise levels, among other things. It is traditional to perform black-box testing of compressors to evaluate these improvements and remain comparable to compressors of the same or different types. In a black-box analysis, refrigerant property measurements are taken at the inlet and outlet of the compressor and no measurements inside the compressor are taken. In addition, external measurements of mass flow rate and power consumptions are taken. Manufacturers publish the black-box data when marketing their compressors and this data is used by consumers to identify the best choice for their application.

The Ray W. Herrick Laboratories have facilitated testing of prototype compressors in applications for refrigerator/freezers, and heat pump/air conditioners. Comparisons of these prototypes to the general compressor of the same style in their application are made to prove equivalency, superiority, or inferiority in performance. This thesis investigates compressor performance of scroll, reciprocating, and rotary type compressors in different projects that aimed to improve certain aspects of compressor design.

A prototype scroll compressor was designed for use in a refrigerator/freezer. The design incorporated a magnetic coupling between the compressor and motor shafts and operated without lubricating oil. A commercially available reciprocating compressor also intended for use in refrigerator/freezers was modified by replacing the metal piston cylinder head with a polymer piston cylinder head. The material switch from metal to polymer has the possibility to reduce manufacturing cost.

A commercially available scroll and rotary compressor for use in residential heat pump/air conditioners were tested to determine their dampening effectiveness in reducing pressure fluctuation at the compressor discharge. Depending on current dampening results, a novel dampening method was to be investigated. Using data from the scroll and rotary tests, evaluation of the current compressor mapping technique is also made, and alternatives proposed in the literature is investigated.

## **1.2 Compressor Applications**

### **1.2.1 Refrigerator Freezer Application**

Refrigerator/freezers are used for the cold storage of food and are one of the most common domestic appliances in the world. Most commercially available domestic refrigerator/freezers utilize the vapor-compression cycle to produce the cold air that keeps the food cold (Bansal, Vineyard, & Abdelaziz, 2011). The compressor used to drive most refrigerator/freezer vapor compression cycles is a single-speed reciprocating compressor, which cycles on and off to meet the varying load of the refrigerator (Bansal, Vineyard, & Abdelaziz, 2011). Freezer air temperatures are traditionally set to be between -15 °C and -25 °C (Choi, Han, Cho, & Lee, 2018), with condenser environment temperatures between 16 °C and 25 °C (Geppert

& Stamminger, 2013). Refrigerator freezer compressors must be able to operate in this temperature zone with a cooling capacity range of 200 to 230 W (Ghadiri & Rasti, 2014).

### **1.2.2 Air Conditioning Application**

Positive displacement compressors are also commonly used to provide cooling or heating to spaces inside residential homes. The most common compressor used in the residential AC/HP market is the scroll compressor, although rotary compressors are becoming popular due to their high efficiencies during variable-speed operation (Lin & Avelar, 2017). In residential cooling and heating applications, air conditioner/heat pumps must be able to operate in environmental temperature ranges from -30 to 10 °C in heating mode (Bertsch & Groll, 2008) and 25 to 55 °C in cooling mode (Payne & Domanski, 2002). Cooling capacity depends on the size of the home, but typically units are sold in 8.79 kW, 14.07 kW, and 17.58 kW capacities.

## **1.3 Investigated Compressor Types**

### **1.3.1 Reciprocating Compressor**

The most common compressor in refrigeration cycles is a reciprocating compressor, where the simplest design employs a single piston operating at a constant speed. Reciprocating compressors are fixed volume ratio compressors that intake a low-pressure refrigerant gas into a compression chamber (cylinder) and utilizes a piston to reduce the volume of the compression chamber. This volume reduction compresses the refrigerant into a higher pressure. Figure 1.1 shows the various stages of compression in a reciprocating compressor.

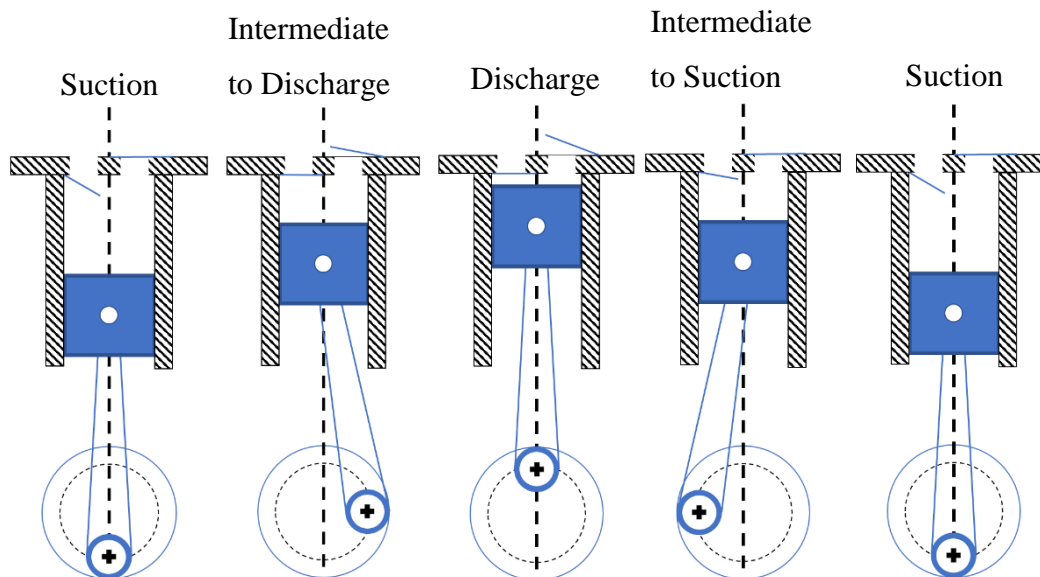


Figure 1.1: Compression process in a reciprocating compressor that utilizes a piston cylinder. Note the suction valve (left line) and the discharge valve (right line).

Piston motion is enforced by rotation of an electric motor shaft, where a piston shaft is coupled to instigate linear motion, moving the piston up and down in one complete revolution of the motor shaft. In the end of the suction stage, the cylinder is located at bottom dead center, with the compression chamber volume maximized and filled with low-pressure gas. After bottom dead center the piston moves to reduce the volume of the compression chamber, the suction valve closes and the pressure inside the chamber increases. The chamber pressure increases as the volume decreases until the pressure achieves a pressure threshold which is determined by the discharge valve. Once the piston reaches top dead center, the refrigerant in the chamber is rejected into the discharge chamber. At this point, the piston begins to move in the opposite direction, causing the discharge valve to close and the suction valve to open. The volume inside the compression chamber increases and fills with new low-pressure refrigerant. The piston continues to move until bottom dead center where the chamber volume is maximum, and the cycle repeats. Reciprocating compressors used in refrigerator/freezer applications typically operate with overall isentropic compressor efficiencies between 50 and 65% (Kim & Bullard, 2002) and with a volumetric efficiency range of 40 to 70% (Rigola, Pe´rez-Segarra, & Oliva, 2005).

### 1.3.2 Scroll Compressor

While not traditionally used for refrigerator/freezer application, scroll compressors are being considered for a wide variety of applications due to their low noise and high volumetric and energy efficiencies. Like a reciprocating compressor, scroll compressors are also positive displacement compressors with a fixed volume ratio. Two identical scroll wraps are used to achieve compression. One scroll remains stationary while the other orbits around the stationary scroll, creating pockets of refrigerant along the wraps, decreasing the volume of these pockets as the pocket approaches the center of the scrolls. A motor is used to rotate a shaft that is coupled to the orbiting scroll. Figure 1.2 displays the compression process of a scroll compressor in one compression cycle which relates to one full rotation of the motor shaft.

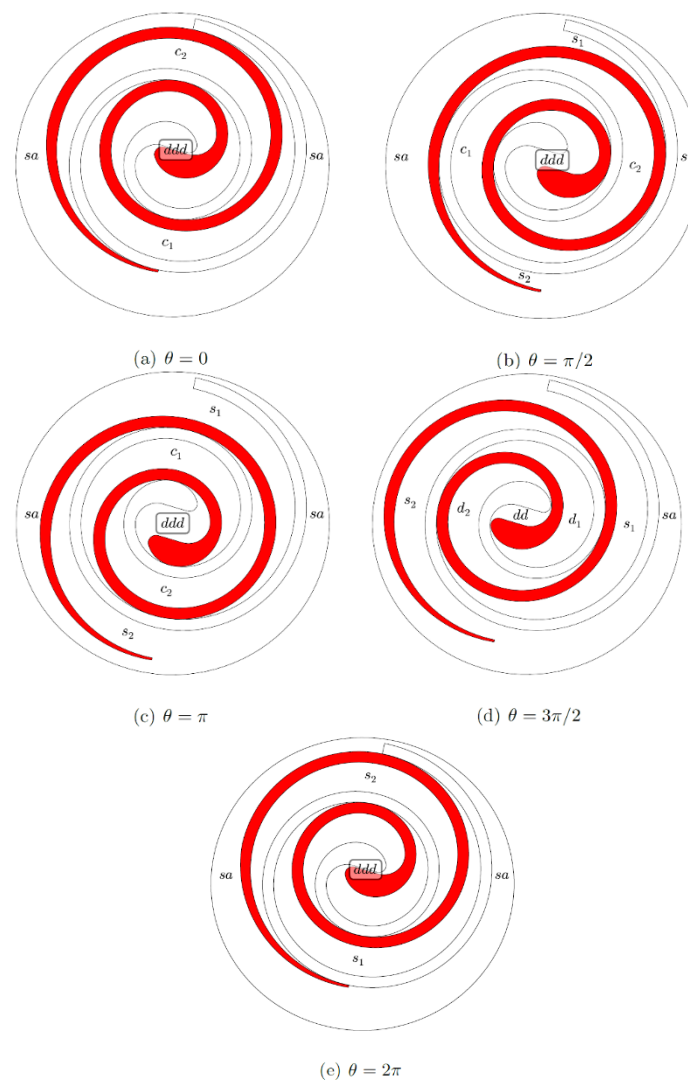


Figure 1.2: Compression process for a scroll compressor as illustrated by Bell (2011).

Following the convention that the red scroll in Figure 1.2 is orbiting around the white scroll, new refrigerant is brought in at two points in the outermost sides at the suction pockets  $s_1$  and  $s_2$ . During one full rotation, suction pockets  $s_1$  and  $s_2$  increase in volume at first and then are closed off from the suction line at the end of the first rotation ( $0$  to  $2\pi$ ). In the next rotation, suction pockets  $s_1$  and  $s_2$  and become compression pockets  $c_1$  and  $c_2$ . In this compression pocket phase the volume of each pocket decreases during half of a rotation ( $2\pi$  to  $3\pi$ ), where the pressure of the refrigerant in these pockets increases. In the next half rotation ( $3\pi$  to  $4\pi$ ) the compression pockets become discharge pockets  $d_1$  and  $d_2$  and the refrigerant is further compressed. Discharge pockets  $d_1$  and  $d_2$  combine at the center of the scroll to become discharge pocket  $ddd$  during the first half of the 3<sup>rd</sup> and final rotation ( $4\pi$  to  $5\pi$ ), and in the second half rotation ( $5\pi$  to  $6\pi$ ) pocket  $ddd$  becomes pocket  $dd$  where this pocket is exposed to the condensing line and is ejected out the center of the scroll wraps. While it takes three full rotations of the motor shaft for pockets of refrigerant to enter and leave the scroll wraps, the scroll compressor still discharges at the same rate as the rotational frequency of the motor shaft, as the scroll wraps contain three distinct pockets of refrigerant at any time, each being discharged one full rotation after the other. While larger capacity scroll compressors can achieve overall isentropic efficiencies between 50 and 70% (Mösch, 2015) (Winandy, Saavedra, & Lebrun, 2002), less common small capacity scroll compressors can experience lower efficiencies between 45 and 60% (Wang, Zhao, Li, Bu, & Shu, 2007). Volumetric efficiency also varies by capacity where more traditional larger capacity scroll compressors can achieve volumetric efficiencies between 80 and 95%, with smaller capacity scroll compressors achieving efficiencies between 60 and 80%.

### 1.3.3 Rotary Compressor

Rotary compressors (also known as rolling piston compressors) are another positive displacement type compressor that have seen an increase in usage due to their low manufacturing cost and decent efficiencies. A compression chamber with a circular cross section is divided into two sections or pockets of refrigerant, one for suction and the other for discharge. The suction pocket is continually exposed to the suction port while the discharge pocket is continually exposed to the discharge port. A cylinder rolls along the walls of the compression chamber with a reciprocating vane providing a seal between the two pockets of refrigerant. As one pocket

reduces in size, the other pocket increases in size, causing pressure differences that either pull refrigerant into the chamber, or compress and reject refrigerant out of the chamber. A discharge valve is used to force the pressure level of the discharge pocket to increase until a certain threshold is met, at which point the valve is pushed open by the high-pressure refrigerant and the refrigerant is discharged out of the compression chamber. Figure 1.3 shows the principle movement of a rotary compressor.

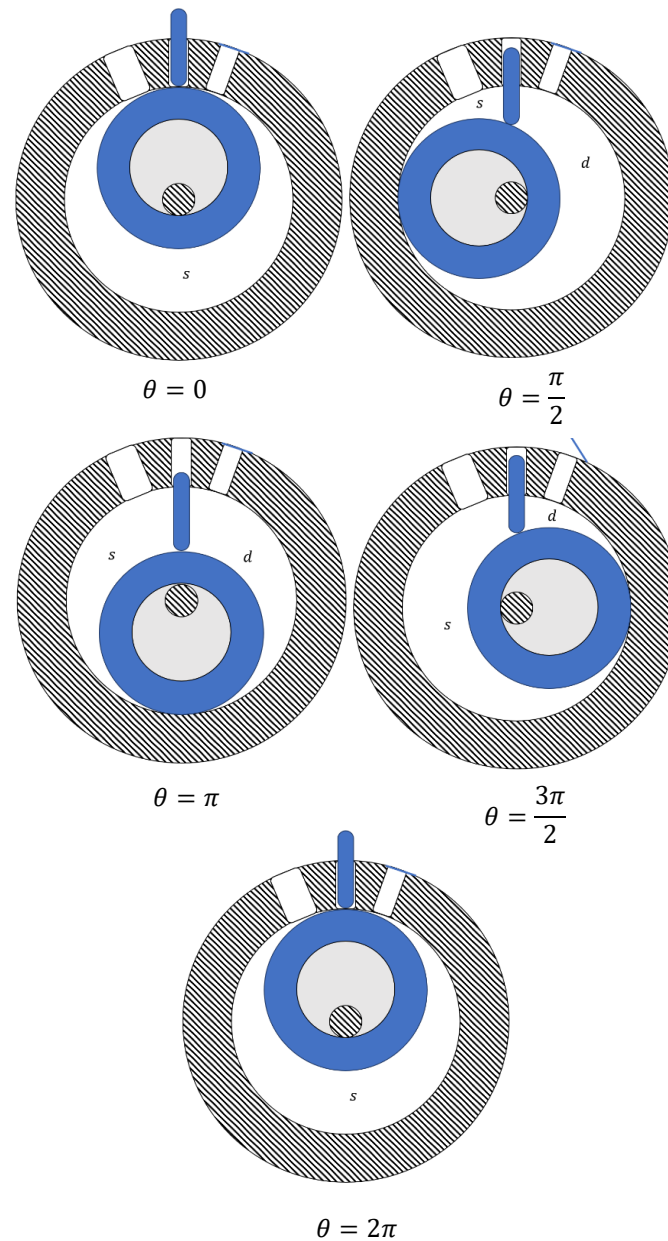


Figure 1.3: Compression process for a Rotary Compressor. *s* denotes the suction pocket and *d* denotes the discharge pocket. The suction port is left and the discharge port is right (with the valve).

The compression process begins between motor angle of  $0$  ( $2\pi$ ) and  $\pi$ , where the discharge pocket decreases in volume and the suction pocket increases in volume. In the first half rotation the discharge pocket has proportionally more volume in the compression chamber than the suction pocket. At  $\pi$ , the two pockets are identical in volume, and the pressure level of the discharge pocket has risen. As the cylinder rolls from  $\pi$  to  $2\pi$ , the discharge pocket continues to decrease in volume and the suction pocket increases in volume. At some point between  $\pi$  and  $2\pi$  the pressure of the refrigerant inside the discharge pocket will rise above the threshold set by the discharge valve and the discharge valve will open, rejecting the refrigerant into the condensing line. The discharge pocket will continue to decrease in volume until  $2\pi$ , where it will disappear entirely, with the suction pocket occupying the entire compression chamber. After rolling past  $2\pi$  the suction pocket (created before rolling past  $2\pi$ ) will become the next discharge pocket, a new suction pocket will be created, and the cycle will repeat. Rotary compressors have overall isentropic efficiencies between 50% (Sakaino, Muramatsu, Shida, & Ohinata, 1984) and 74% (Mtsuzaka & Nagatomo, 1982), with volumetric efficiencies between 70 and 95%.

## 1.4 Performance Comparison of Compressors

### 1.4.1 Standards for Compressor Testing

When testing performance of positive displacement compressors, information on the limits placed on measurement equipment, procedures, and steady-state evaluation is provided by standards from ASHRAE and AHRI. The most relevant standards are ASHRAE 23.1 (2010), and AHRI 540 (2015). Instrument accuracy is defined in ASHRAE 23.1 and is summarized in Table 1.1.

Table 1.1: Table of accuracy requirements as described in ASHRAE 23.1

Property	Accuracy Requirement
Pressure	$\pm 1$ %
Temperature	$\pm 0.3$ K ( $\pm 0.5$ °R)
Mass flow rate	$\pm 1$ %
Electrical power input	$\pm 1$ %
Coolant liquid flow rate	$\pm 1$ %

The ASHRAE 23.1 standard also lists values that must be determined at test conditions. The collected values as described by ASHRAE 23.1 and adhered to in this paper are summarized in Table 1.2.

Table 1.2: Values collected in the testing described in this paper. Units in parenthesis are alternative units that were used in data collected in this paper.

<b>Value Descriptor</b>	<b>Unit</b>
Mass flow rate	kg/s (g/s or kg/hr)
Power input	W
Compressor efficiency	W/W
Suction superheat	K
Liquid subcooling	K
Ambient air temperature	°C (°F)
Volumetric efficiency	% (-)
Compressor shaft rotational speed	Hz (RPM)

When determining certain values, other properties must be collected. Compressor efficiency, suction superheat, liquid subcooling, and volumetric efficiency are dependent on both temperature and pressure. To determine these values, temperature and pressure measurements at the inlet and outlet of the compressor must be measured.

Suction superheat is defined as the difference in the temperature of the refrigerant entering the compressor to the saturation temperature of the refrigerant at the inlet pressure. Equation (1.1) details this difference.

$$\Delta T_{SH} = T_{Suc} - T_{Sat}(P_{Suc}) \quad (1.1)$$

Liquid subcooling is defined as the difference in temperature of the refrigerant exiting the condenser to the saturation temperature of the refrigerant at the condensing pressure. When assuming no pressure loss across tubing in the cycle, the discharge pressure of the compressor can be used as a substitute for condensing pressure. Equation (1.2) details subcooling when making this assumption.

$$\Delta T_{SC} = T_{Sat}(P_{Dis}) - T_{Cond,o} \quad (1.2)$$

When pressure at the outlet of the condenser is measured, then saturation temperature of this pressure should be used instead of the compressor discharge.

### 1.4.2 Steady-State Qualifiers

When determining steady-state performance of the compressor, cycle properties may not deviate from an average of a data set. Data collected inside this set make up the average, and no one sample of data can deviate outside of certain limits as described in AHSREAE 23.1 and summarized in Table 1.3.

Table 1.3: Maximum deviations permitted from average value in data set for each property.

<b>Property</b>	<b>Deviation Maximum</b>
Electrical power input	$\pm 1 \%$
Shaft rotational speed	$\pm 1 \%$
Compressor ambient temperature	$\pm 4 \text{ K}$
Compressor suction pressure	$\pm 1 \%$
Compressor suction temperature	$\pm 1 \text{ K}$
Compressor discharge pressure	$\pm 1 \%$
Mass flowrate	$\pm 2 \%$

Steady-state duration is determined by the operator but must remain constant throughout the test plan and evaluation of the compressor. In this paper, steady-state duration was established to be 10 minutes (600 data points collected) for each operating condition. The data inside these 10 minutes could not exceed the variation listed in Table 1.3. The 600 data points were averaged, and these averaged values were used in the performance evaluation of the compressor.

For hot-gas bypass testing, ambient air temperature was not controlled by the operator, as the test stand was exposed to the ambient air inside the laboratory and not in a separate chamber. Temperature could not be pre-set to a specific temperature and thus, testing on separate days would lead to slight variation of the ambient air temperature. The laboratory air temperature is controlled via the HVAC system of the building, which produced a constant air temperature around the test stand within the limits described in Table 1.3.

Both compressors tested on the Small Hot-Gas Bypass Test Stand were prototypes or modified. This led to occasionally odd behavior seen in the cycle, particularly with the suction superheat temperature and mass flow rate. While all other properties met the requirements in Table 1.3, on occasion the superheat temperature or mass flow rate was not maintained inside the limit to be considered steady-state by the AHSRAE 23.1 Standard. Certain state points at sub-

standard steady-state conditions were still taken, because they exhibited different “steady-state” behavior such as oscillating values in a constant pattern.

### 1.4.3 General Black-Box Performance Analysis

There were no sensors placed internally to the compressors, and most geometric information about the compressors were unknown, indicating that a black-box approach for compressor performance evaluation was necessary. The general performance of each compressor tested was evaluated based on the ASHRAE 23.1 Standard.

Overall Isentropic Compressor Efficiency is the primary indicator of compressor performance. It compares the isentropic work of compression to the total work input to the compressor, as outlined in Equation (1.3).

$$\eta_{is,O} = \frac{\dot{m}_r * (h(p_{Dis}, s_{Suc}) - h(p_{Suc}, T_{Suc}))}{\dot{W}_{Comp}} \quad (1.3)$$

Where  $\eta_{Comp}$  is a dimensionless value from 0 to 1 (can be converted to a percentage by multiplying by 100),  $\dot{m}$  is in kg/s,  $h$  is in kJ/kg,  $p$  is in kPa,  $s$  is in kJ/kg-K,  $T$  is in °C, and  $\dot{W}_{Comp}$  (input electrical power to the compressor) is in kW.

Volumetric efficiency compares the actual mass flow rate to the maximum possible mass flow rate based on the displacement of the compressor and the density of the refrigerant at the compressor suction state, shown in Equation (1.4).

$$\eta_V = \frac{\dot{m}_r * v_{Suc}}{\dot{N}_{Rot} * V_{Disp}} \quad (1.4)$$

Where  $\eta_V$  is a dimensionless value from 0 to 1 (can be converted to a percentage by multiplying by 100),  $\dot{m}$  is in kg/s,  $v$  is in  $m^3/kg$ ,  $\dot{N}_{Rot}$  is the compressor chamber displacement rate in Hz, and  $V_{Disp}$  is the volumetric displacement of the compressor chamber in  $m^3$ .

While there is no evaporator in a hot-gas bypass test stand, the potential cooling capacity can be calculating by simulating a complete vapor-compression cycle based on refrigerant suction and discharge properties, along with a few assumptions. These assumptions are as follows:

1. The entire mass flow rate at the discharge of the compressor is condensed at the compressor discharge pressure to a liquid with a subcooling of 5 °C.
2. After being condensed into a liquid state, the entire mass flow rate undergoes isenthalpic expansion to the compressor suction pressure.

3. After isenthalpic expansion, the entire mass flow rate is evaporated to a superheated vapor state at the compressor suction conditions of the refrigerant.

This simulation leads to the following Equation (1.5).

$$\dot{Q}_{Evap} = \dot{m}_r * (h_{Suc} - h_{Evap,I}) \quad (1.5)$$

Where  $\dot{Q}$  is in kW,  $\dot{m}$  is in kg/s, and  $h$  is in kJ/kg.

Note that in the calorimeter there is an evaporator which is instrumented such that an adapted version of Equation (1.5) is utilized in performance analysis (to be further discussed in Section 1.4.4).

With a potential cooling capacity established, the Coefficient of Performance (COP) can also be calculated. The COP is the ratio of cooling capacity to total (electrical) work input to the compressor, as described in Equation (1.6).

$$COP = \frac{\dot{Q}_{Evap}}{\dot{W}_{Comp}} \quad (1.6)$$

Where COP is a dimensionless number,  $\dot{Q}$  is in kW, and  $\dot{W}$  is in kW.

The pressure ratio across the compressor was used in evaluating compressor performance as well. This is simply the ratio of the discharge pressure to the suction pressure, shown in Equation (1.7).

$$p_{Rat} = \frac{p_{Dis}}{p_{Suc}} \quad (1.7)$$

Where  $p_{Rat}$  is a dimensionless number, and  $p$  is in kPa.

A script in EES was written to process the collected data from compressor testing. Properties of the cycle were determined, such as state point specific enthalpy and specific entropy, and compressor performance was evaluated for each steady-state operating condition achieved.

Occasionally it is desired to predict compressor performance at suction superheat temperatures other than the suction superheat temperature achieved or used to create a compressor performance map. Dabiri and Rice proposed a correction that can be used to predict mass flow rate and power consumption still based on the original data, but with a different superheat (1981). The new mass flow rate is corrected through the density difference of the refrigerant at different temperatures, shown in Equation (1.8). Note that the term *map* is used to

denote original data or map predicted data, and the term *new* is the data determined at the new superheat.

$$\frac{\dot{m}_{new}}{\dot{m}_{map}} = 1 + F \left( \frac{\rho_{new}}{\rho_{map}} - 1 \right) \quad (1.8)$$

Where F is a correction factor recommended to be 0.75.  $\dot{m}_{new}$  is the output of this equation, where  $\rho_{new}$  is determined via refrigerant properties.  $\dot{m}$  is in kg/s and  $\rho$  is in kg/m<sup>3</sup>.

Power consumption is based on the new mass flow rate to map mass flow rate ratio, as well as the enthalpy difference ratio between new and map, shown in Equation (1.9).

$$\frac{\dot{W}_{new}}{\dot{W}_{map}} = \frac{\dot{m}_{new}}{\dot{m}_{map}} \left( \frac{\Delta h_{is,new}}{\Delta h_{is,map}} \right) \quad (1.9)$$

Where  $\Delta h_{isen}$  is the isentropic compression enthalpy difference.  $\dot{W}_{new}$  is the output of this equation.  $\dot{m}$  is in kg/s,  $\dot{W}$  is in kW, and  $\Delta h$  is in kJ/kg.

This paper will use the superheat corrections to improve the comparison of performance between the same compressor with different component compositions.

#### 1.4.4 Additional Analysis Capability in the Compressor Calorimeter

One of the test stands used in this study is a compressor calorimeter. The calorimeter has additional testing standards that must be followed. As it is outfitted currently, the Tesco Compressor Calorimeter at the Ray W. Herrick Laboratories permits black-box analysis of the compressors tested. Following the ASHRAE standards 41.9 (2011) and 23.1, the performance of the compressor can be determined. The same analysis described in Section 1.4.3 is used in the calorimeter. In addition to parameters previously discussed, the mass flow rate of the refrigerant must be confirmed with a secondary method in addition to the primary method of measurements using the Coriolis-effect mass flow meter. This secondary method is based on the evaporator heat capacity. To determine the evaporating capacity, the heat input or output to/from the secondary refrigerant tank is measured, and a heat leakage test is performed to determine the amount of heat input to the evaporator from the environment. The heat leakage test was performed on the calorimeter by Möscher (2015). The heat leakage coefficient ( $AU_{amb}$ ) is determined via a one hour steady-state test of the secondary refrigerant tank when there is no refrigerant circulating through the calorimeter and a constant temperature difference between the secondary refrigerant and the ambient is maintained via heat input into the tank from the electric

heaters. With a known heat input and a known temperature difference, the heat leakage coefficient can be determined using Equation (1.10).

$$AU_{amb} = \frac{\dot{Q}_{heater}}{(T_{sec,r} - T_{amb})} \quad (1.10)$$

With the  $AU$  in kW/K,  $\dot{Q}$  is in kW, and  $T$  is in C (where the difference is in K). Through this test, the heat leakage coefficient was determined to be  $0.004508 \pm 0.000324$  kW.

Once the heat leakage coefficient is determined, the heat leakage out of the compressor at any given time can be calculated with Equation (1.11).

$$\dot{Q}_{amb} = AU_{amb} * (T_{amb} - T_{sec,r}) \quad (1.11)$$

Where  $\dot{Q}$  is in kW,  $AU$  is in kW/K, and  $T$  is in C (where the difference is in K).

After the heat leakage due to exposure to ambient conditions is determined, an energy balance across the secondary tank can be performed, where all refrigerant properties are measured as well as heat input and output. This energy balance is described in Equation (1.12).

$$\dot{Q}_{heater} + \dot{Q}_{amb} + \dot{m}_r(h_{Evap,I} - h_{Evap,O}) = 0 \quad (1.12)$$

Where  $\dot{Q}$  is in kW,  $\dot{m}$  is in kg/s, and  $h$  is in kJ/kg.

From this energy balance, the mass flow rate can be determined. This secondary mass flow rate calculation is necessary to reinforce the mass flow rate measurement accuracy, as well as further prove the steady-state operation of the calorimeter. It is intended that the secondary mass flow rate be within 3% of the measured mass flow rate.

#### 1.4.5 Pressure Fluctuation in Positive Displacement Compressors

The reciprocating, scroll, and rotary compressors investigated in this study are positive displacement compressors with a fixed internal volume ratio. The compressor can only intake one volume of refrigerant vapor and compress it to another smaller volume of refrigerant vapor, where these inlet and outlet volumes are constant. A constant volume ratio yields a constant internal (ideal) pressure ratio, where the discharge pressure of the refrigerant is a fixed magnitude larger than the suction pressure of the refrigerant. When a compressor is working in a system the pressure ratio between the condenser and the evaporator can be different from the internal pressure ratio of the compressor due to varying condensing and evaporating temperature. In these cases, the compressor is not operating in ideal conditions, and will experience over-compression when the system pressure ratio is less than the internal pressure ratio, and under-

compression when the system pressure ratio is higher than the internal pressure ratio of the compressor. Non-ideal compression ratios can influence the efficiency of the compressor negatively, as over-compression or under-compression causes work to be wasted in the system. In under-compression cases, refrigerant already at high-pressure in the condensing line must expand to equalize with the incoming discharged refrigerant from the compressor. In over-compression cases, refrigerant discharged from the compressor must expand with refrigerant from the condensing line to equalize. This expansion of refrigerant to equalize pressure in either case is lost work. Figure 1.4 shows over-compression and under-compression in a pressure-volume diagram.

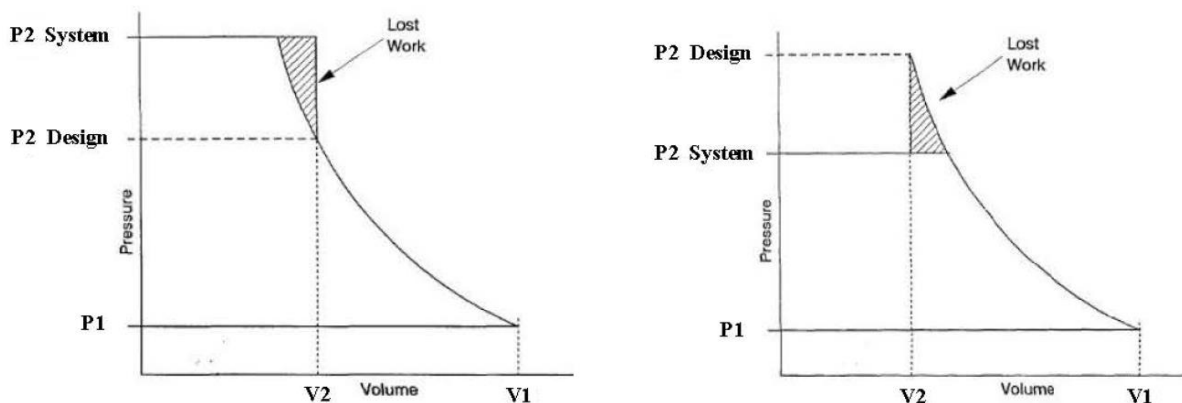


Figure 1.4: Under-compression (left) and Over-compression (right) in the compression process as illustrated by Huang (2012).

As a by-product of non-ideal pressure ratios, pressure fluctuation created by pressure equalization between the compressor and the condensing line is generated. To equalize pressure between the compression chamber and the condensing line, refrigerant must flow from the high-pressure side to the low-pressure side. This refrigerant flows in the form of a pressure wave and is the cause of pressure fluctuation. In either case of over or under-compression, pressure fluctuation in the condensing line will occur at the same rate as the compression frequency. The magnitude of pressure fluctuation can be an indicator of the reduced efficiency and can be a great source of noise in the system (Soedel, 2007).

Compressor manufacturers attempt to reduce these pressure fluctuations by implementing serial mufflers, dead volumes or discharge plenums, and valves. In particular, the addition of discharge valves affects the process of exposing the compression chamber to the condensing line. When a discharge valve is implemented, the outside of the valve will be exposed to the

condensing line pressure, and the inside of the valve will be exposed to the compression chamber pressure. The valve will not open until the pressure inside the compression chamber exceeds the sum of the pressure in the condensing line and the pressure needed to overcome the stiffness of the valve itself. In this situation, the ability for the compressor to undergo a process of under-compression is removed. Over-compression is still possible depending on the stiffness of the discharge valve. Additionally, when a discharge valve is implemented, the efficiency curve of the motor becomes more influential in determining the ideal pressure ratio of the compressor. These methods of serial muffling with valves, dead volumes, and discharge plenums do not eliminate pressure fluctuation entirely however. Modelling these pressure waves using flash tube theory (2012), Huang et al. developed a parallel muffling technique called a Shunt Pulsation Trap (SPT) that reduces the pressure fluctuation at the discharge of a Roots blower (2014). In addition to general performance analysis, pressure fluctuation at the discharge of compressors tested in the compressor calorimeter is investigated to determine feasibility of implementing this SPT in air conditioning applications. Use of a new muffling design (like the SPT) may lead to increased efficiencies in non-ideal pressure ratios, as well as reduce the overall noise of the system.

The pressure fluctuation at the discharge of the compressor is investigated via the high frequency pressure transducer at the compressor outlet. While it is possible to visualize pressure fluctuation in the time domain, it is best to quantify pressure fluctuation in the frequency domain, so that the amplitude of pressure fluctuation can be isolated by frequency. When the intended motor shaft rotational frequency of a compressor is known, it is possible to correlate pressure peaks with compressor discharge based on this frequency. MATLAB (Mathworks, 2018) is used to perform Discrete Fourier Transform (DFT) (Mathworks, 2018) using a Fast Fourier Transform algorithm (Frigo & Johnson, 2018) on the time domain pressure signal to reduce the data from a single signal to a summation of sine waves of different amplitudes and frequency. MATLAB is able to plot the reduction so that each sine wave is identified by frequency and amplitude.

Discrete fourier transform is mathematically represented using summation of sine and cosine waves written as exponentials from Euler's Formula (Weisstein, 2019). MATLAB represents the result of a DFT transformation of a vector (like the pressure signal) in Equation (1.13).

$$Y(k) = \sum_{j=1}^n X(j)W_n^{(j-1)(k-1)} \quad (1.13)$$

Where  $W_n = e^{-\frac{2\pi i}{n}}$  (Euler's Formula for representation of sine and cosine waves),  $X$  is a vector of datapoints (in the applied case: pressure), and  $n$  is the number of data points in the discrete signal. The result is a vector  $Y$  of length  $k$ ,  $Y$  is the amplitude of each signal in scaled units based on the number of data points where  $k$  is the same amount as  $n$ . The maximum frequency of sine waves discernable by a specific sampling rate is half that sampling rate. For example, a 1000 Hz sampling rate leads to a maximum discernable frequency of 500 Hz. Signals in a sine pattern with frequencies greater than 500 Hz are not accounted for. The way the FFT algorithm outputs the vector  $Y$ , the frequency spectrum outputs from 0 to the sampling frequency (1000 Hz), and the data from 0 to half the sampling frequency (500 Hz) is reflected across the y-axis at half the sampling frequency (500 Hz) from 500 Hz to 1000 Hz. This in effect duplicates the data such that all data from 500 Hz to 1000 Hz should be removed. After data is removed the amplitude vector  $Y$  can be scaled to the correct units. To scale  $Y$  to the correct units (kPa), the vector must be divided by half the length of  $n$ . Once units are scaled and duplicate frequency data is removed, the amplitude of each sine wave can be isolated to frequency, where the sine waves sum to the time domain pressure.

#### 1.4.6 Uncertainty

Post-processing of data to determine performance of the compressors tested was performed using Engineering Equation Solver (EES) (F-Chart Software, 2018). EES is also capable of propagating uncertainty of calculations when given relative or absolute uncertainties of the independent variables that comprise of the measured data. EES propagates uncertainty based on the methods outlined in the NIST Technical Note 1297 (Taylor & Kuyatt, 1994). If independent variables are represented as  $x$  and a dependent variable based on multiple  $x$  independent variables is represented as  $y$ ,  $y$  can be described as a function of those multiple independent variables  $x$ .

$$y = f(x_1, x_2, \dots, x_N) \quad (1.14)$$

The uncertainty of  $y$  is thusly dependent on the uncertainty of each independent variable uncertainty as well as the impact that each independent variable has on  $y$  in the function. This

impact is determined through partial derivatives. The equation for uncertainty of  $y$  is detailed in Equation (1.15).

$$u_c^2(y) = \sum_{i=1}^N \left( \left( \frac{\partial f}{\partial x_i} \right)^2 u^2(x_i) \right) + 2 * \sum_{i=1}^{N-1} \sum_{j=i+1}^N \left( \frac{\partial f}{\partial x_i} \left( \frac{\partial f}{\partial x_j} \right) u(x_i, x_j) \right) \quad (1.15)$$

Where  $u_c^2(y)$  is the square of the uncertainty of  $y$ ,  $u(x_i)$  is the uncertainty of each independent variable, and  $\frac{\partial f}{\partial x_i}$  is the partial derivative of the function with respect to each independent variable. Uncertainty calculated in this manner is absolute uncertainty.

#### 1.4.7 Available Compressor Performance Maps

When compressor manufacturers publish their compressor performance in technical data sheets, they must adhere to certain standards, mainly the ASHRAE standard 23.1 (2010) and the AHRI standard 540 (2015). AHRI standard 540 outlines a 10-coefficient steady-state empirical model that is used to predict compressor performance at any point inside the operating envelope of the compressor. According to standard, each compressor must be tested at specific evaporating and condensing temperatures, 95 °F (35 °C) ambient air temperature, no crossing airflow, and at nameplate voltage. The compressor must also have a constant suction temperature or a constant suction superheat temperature, and the condenser must also achieve the constant subcooling temperature depending on the tests performed. When these conditions are met the 10-coefficient performance map can be used to predict compressor performance at operating conditions not tested explicitly by the manufacturer. The map is used to predict power input, refrigerant mass flow rate, and refrigerating (evaporating) capacity, and is a regression utilizing the least squares method to calculate the 10 coefficients. Equation (1.16) details the 10 Coefficient Correlation map.

$$x = C_1 + C_2 * (T_{Evap}) + C_3 * (T_{Cond}) + C_4 * (T_{Evap}^2) + C_5 * (T_{Evap} * T_{Cond}) + C_6 * (T_{Cond}^2) + C_7 * (T_{Evap}^3) + C_8 * (T_{Cond} * T_{Evap}^2) + C_9 * (T_{Evap} * T_{Cond}^2) + C_{10} * (T_{Cond}^3) \quad (1.16)$$

Where  $x$  is either; power draw, refrigerant mass flow rate, or evaporating capacity, and the coefficients change for each dependent variable (3 polynomials for 3 parameters). Note that the 10-coefficient map is based solely on the evaporating and condensing temperatures, which is why the map has many testing constraints before it can be applied.

Other studies have shown that the AHRI 10-Coefficient Correlation compressor map used in publishing compressor performance is not capable of predicting compressor performance outside of the testing range of the test points used to create this compressor map (Jähnig, Reindl, & Klein, 2000). In other words, compressor performance cannot be extrapolated by using the 10-Coefficient Correlation.

Li modified a simplified physical model for scroll and reciprocating compressors that can be used to extrapolate compressor performance (2012), which is based on the model created by Jähnig et al. (2000). Li adjusted the original model to increase the number of constants to be determined via solving a least squares problem. The model is semi-empirical, taking some geometric inputs from the compressor and experimental compressor data, and fitting this data to non-linear curves. The curves are used to predict volumetric efficiency, overall isentropic efficiency, electric power, and discharge temperature. Volumetric efficiency is fit to the curve in Equation (1.17).

$$\eta_V = b_1 + b_2 \left( \left( \frac{p_{Cond}}{p_{Evap}(1-dp)} \right)^{\frac{1}{k}} \right) \quad (1.17)$$

Where  $b_1$ ,  $b_2$ , and  $dp$  are constant coefficients determined by experimental data, and  $k$  is the refrigerant isentropic coefficient.

Overall compressor isentropic efficiency is fit to the curve in Equation (1.18).

$$\frac{1}{\eta_{is,O}} = a_1 + \frac{a_2}{P_{Evap}} + \frac{a_3}{P_{Cond}} \quad (1.18)$$

Where  $a_1$ ,  $a_2$ , and  $a_3$  are constant coefficients determined from experimental data.

Compressor power draw is fit to the curve in Equation (1.19).

$$\dot{W} = P_{Evap} * \dot{V}_{Suc} \left( \frac{k}{k-1} \right) \left[ \left( \frac{P_{Cond}}{P_{Evap}} \right)^{\frac{k-1}{k}} - 1 \right] \eta_{is,O} + \dot{W}_{loss} \quad (1.19)$$

Where  $\dot{W}_{loss}$  is a constant determined from experimental data and  $k$  is the refrigerant isentropic coefficient.

Mendoza-Miranda et al. also developed black-box compressor models based on experimental data and minimal geometrical inputs (2016). The Buckingham-Pi method was used to identify non-dimensional groups that had an impact on compressor performance, and then a parametric study was done to determine the influence of each non-dimensional group on each

performance parameter. The resulting equations are used to predict the volumetric efficiency and overall isentropic efficiency.

$$\eta_V = \left(\frac{p_{Cond}}{p_{Evap}}\right)^{b_1} * \left(\frac{\dot{N}_{refer}}{\dot{N}}\right)^{b_2} * \left(\frac{M_{refer}}{M}\right)^{b_3} \quad (1.20)$$

Where  $b_1$ ,  $b_2$ , and  $b_3$  are constant coefficients determined from the training data set.

$$\eta_{is,O} = \left(\frac{p_{Cond}}{p_{Evap}}\right)^{a_1} * \left(\frac{\dot{N}_{refer}}{\dot{N}}\right)^{a_2} * \left(\frac{1}{\left(\frac{T_{Suc} + T_{Dis,is}}{2}\right) - T_{Comp,amb}}\right)^{a_3} * \left(\frac{M_{refer}}{M}\right)^{a_4} \quad (1.21)$$

Where  $a_1$ ,  $a_2$ ,  $a_3$ , and  $a_4$  are constant coefficients determined from the training data set. The Mendoza correlation requires some calculation to determine isentropic conditions at discharge, as well as molar mass values, which are both dependent on the refrigerant used in the compressor, setting itself apart from the other two compressor performance maps discussed. The Mendoza correlation also has variable speed prediction capability, but that will not be utilized in this analysis.

The coefficients in each of these non-linear curves are determined from experimental data and the Levenberg Marquardt method to solve the least squares problem. Each compressor mapping method is applied to experimental data of a scroll and rotary compressor to predict compressor performance inside and outside of the testing range. A subset of data for each investigation is selected to train the map, and then each map is implemented to predict all points outside of this data subset. These predictions are then compared amongst each other and the actual performance data measured.

When determining the accuracy of the different compressor mapping correlations, both the Mean Average Error (MAE) and the Root Mean Square Error (RSME) is used. The lower the average error, the more accurate the correlation to actual measured performance. Equation (1.22) details MAE when converted to a percentage.

$$MAE = \frac{100}{n} * \sum_{i=1}^n \left| \frac{x_{pred,i} - x_{exp,i}}{x_{exp,i}} \right| \quad (1.22)$$

Equation (1.23) shows the calculation for determining the RSME of predicted values.

$$RSME = \frac{100}{\bar{x}_{exp}} * \sqrt{\left(\frac{\sum_{i=1}^n (x_{pred,i} - x_{exp,i})^2}{n}\right)} \quad (1.23)$$

## 1.5 Objectives

This thesis intends to identify the benefits of using one compressor style over another in a specific application. Both the refrigerator/freezer and air conditioning/heat pumping applications will be investigated separately. For the refrigerator/freezer application, two prototype compressors will be considered; an oil-free scroll compressor and a modified commercial reciprocating compressor. For the air conditioning/heat pumping application, two commercial compressors will be considered; a scroll compressor and a rotary compressor. The superior compressor style is identified via higher overall isentropic efficiency and volumetric efficiency curves.

In the air conditioning/heat pumping application, the discharge pressure will be monitored to identify the magnitude of pressure fluctuation across testing conditions. The magnitude will determine the feasibility of implementing a new muffling design (SPT). Also, in the air conditioning/heat pumping application, a comparison of different compressor correlation maps will be made to identify the most accurate map to be used to predict compressor performance. Three maps will be considered, the AHRI 10-Coefficient Correlation, the Li Correlation, and the Mendoza Correlation (all described previously). These maps will be evaluated for predicting performance inside the tested operating range, as well as outside the tested operating range.

## 1.6 Explanation of Thesis Layout

Two compressor applications are investigated, with each application given its own section. In Section 2, the scroll and reciprocating compressors for use in refrigerator freezer application will be investigated. The section will begin with detail on the Hot-Gas Bypass Test Stand used to evaluate the compressors, followed by the operating conditions achieved on the compressor and the performance results of each compressor. In the last portion, comparisons are made between compressors.

In Section 3, scroll and rotary compressors for use in air conditioning/heat pumping application are investigated. The section will begin with a description of the Tesco Compressor Calorimeter Test Stand used to evaluate the compressors. Next, operating conditions, performance results, and pressure fluctuation results are covered, and comparisons between

compressors are made. At the end of the section, three compressor performance correlations are compared to one another.

In Section 4, conclusions are made about the results found in Sections 2 and 3, and recommendations are made.

## 2. DOMESTIC REFRIGERATOR FREEZER

### 2.1 Experimental Setup

#### 2.1.1 Hot-Gas Bypass Vapor-Compression Cycle

Compressors utilized in the vapor-compression cycle experience a variety of operating conditions in the field. The most common uncontrollable changes in operating conditions are the evaporating and condensing temperatures, which affect the pressure ratio across the compressor. To evaluate compressor performance at various possible evaporating and condensing temperatures, a test stand is needed where control over both the evaporating and condensing temperature is possible. In refrigerator/freezer applications, the evaporating temperature must be many degrees below the freezing temperature of water, and when evaluating compressor performance in a testing bench this evaporating temperature must be variable and achievable in relatively short durations between set temperatures. It is difficult to create these conditions at low cost in a testing bench however and thus, an alternative method to the traditional two heat exchanger vapor-compression cycle is used. The Hot-Gas Bypass method is a lower cost alternative, which removes the evaporator from the cycle while creating variable operating conditions experienced by the compressor.

In a Hot-Gas Bypass Test Stand, three sets of valves are used to manipulate the pressure ratio across the compressor, as well as the mass flow rate of the refrigerant. There are a set of discharge valves placed after the discharge of the compressor, and two sets of valves placed in parallel before the suction of the compressor. These valves maintain three different pressure levels in the Hot-Gas Bypass cycle; discharge pressure, intermediate (condensing) pressure, and suction pressure. The compressor experiences the discharge and the suction pressures while the intermediate pressure is held relatively fixed by a constant temperature condenser. As work is input into the refrigerant by the compressor, the condenser must be utilized to complete the cycle. After the condenser, the refrigerant is in a sub cooled state, and is expanded to the suction pressure of the compressor. Not all the refrigerant passes through this condenser however. Because there is no evaporator in the cycle, some hot-gas from the compressor discharge must be siphoned off, expanded to suction pressure, and mixed with the condensed refrigerant, creating

an appropriately superheated refrigerant that enters the compressor. This siphoned refrigerant line is the hot-gas bypass. Figure 2.1 shows the basic circuitry of a hot-gas bypass test stand.

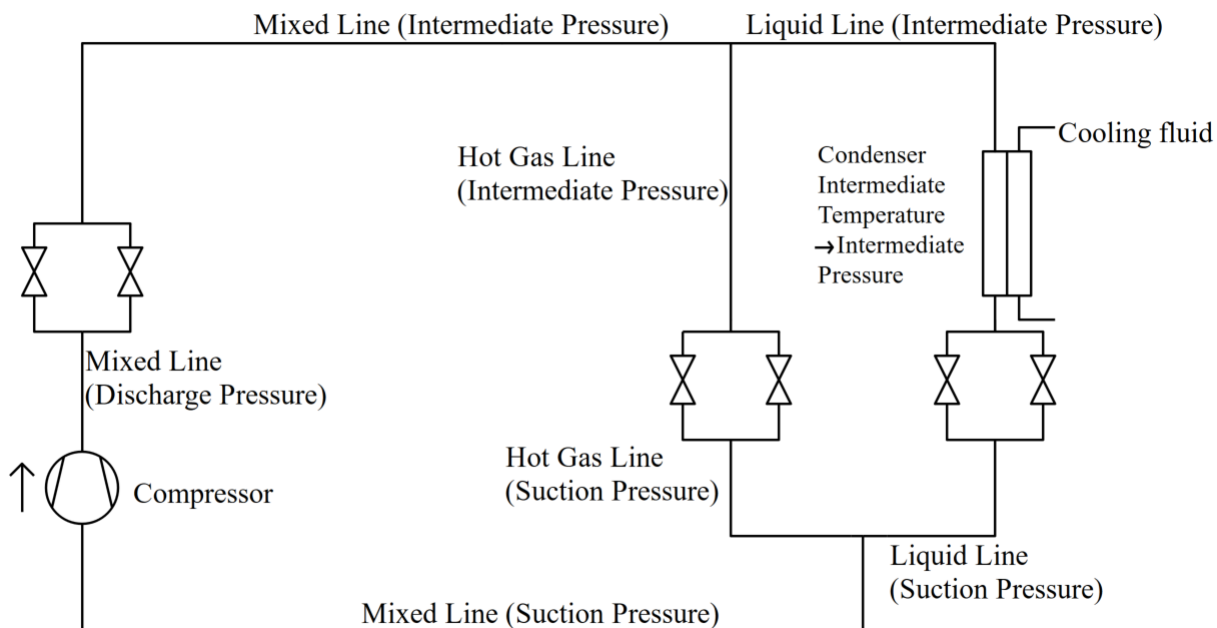


Figure 2.1 Hot-Gas Bypass test stand circuitry

As seen in Figure 2.1, the traditional condenser after the compressor and evaporator before the compressor is replaced by the three sets of valves, and the single constant temperature condenser. By removing the evaporator and fixing a condenser to be at a constant temperature, there is no longer a need to adjust the temperature of two heat exchangers to achieve different operating conditions across the compressor. Compressor testing is simplified and can be performed at an increased rate.

This configuration allows the compressor discharge and suction pressure to be controlled by the suction and discharge valves. To match the operating conditions of a condensing temperature and evaporating temperature, the discharge and suction valves merely need to be adjusted. Reducing the opening percentage of the discharge valves increases the discharge pressure of the compressor, where reducing the opening percentage of the suction (gas bypass and liquid line) valves decreases the suction pressure of the compressor. These discharge and suction pressures have a corresponding saturation temperature, where the saturation temperature of the suction pressure is the evaporating temperature, and the saturation temperature of the

discharge pressure is the condensing temperature. Figure 2.2 shows the Hot-Gas Bypass cycle in a pressure-enthalpy diagram.

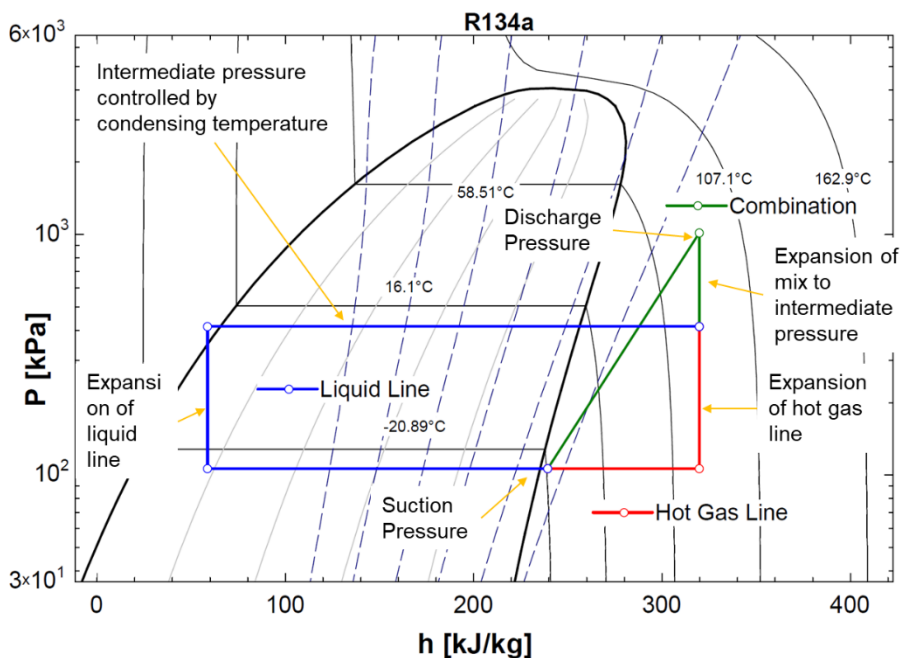


Figure 2.2: Pressure enthalpy diagram of the Hot-Gas Bypass cycle. The figure describes the three pressure levels of the cycle.

In theory, all expansion across the valves are isenthalpic, and there is no pressure loss through the piping of the test stand. The two sets of suction valves play another role in the Hot-Gas Bypass Test Stand. As with all valves, adjusting the opening percentage of the valve will change the pressure difference across the valve, as well as the mass flowrate through the valve. This mass flow control is utilized to achieve the appropriate superheat at the inlet of the compressor. The work input by the compressor increases the temperature of the refrigerant. If the refrigerant were to be expanded back to the inlet pressure of the compressor, the refrigerant would be hotter than previously (given that there is no heat rejection out of the cycle). To account for this increased heat in the refrigerant, and to achieve the appropriate superheated refrigerant temperature to be input into the compressor, the ratio of mass flow of the refrigerant through the condensing line and through the hot-gas bypass line is adjusted by actuating the respective valves. More refrigerant through the bypass line will increase the refrigerant temperature into the compressor, where more refrigerant through the liquid line will decrease the inlet temperature. The two mass flows of different enthalpies will determine the outcome of the

refrigerant enthalpy at the compressor inlet, as illustrated in Equation (2.1). This inlet (suction) enthalpy determines the inlet temperature of the refrigerant given that the pressure of each refrigerant flow is constant.

$$\dot{m}_{liq} * h_{liq} + \dot{m}_{hg} * h_{hg} = \dot{m}_{suc} * h_{suc} \quad (2.1)$$

Figure 2.3 illustrates the mixing of the two refrigerant lines in a pressure enthalpy diagram.

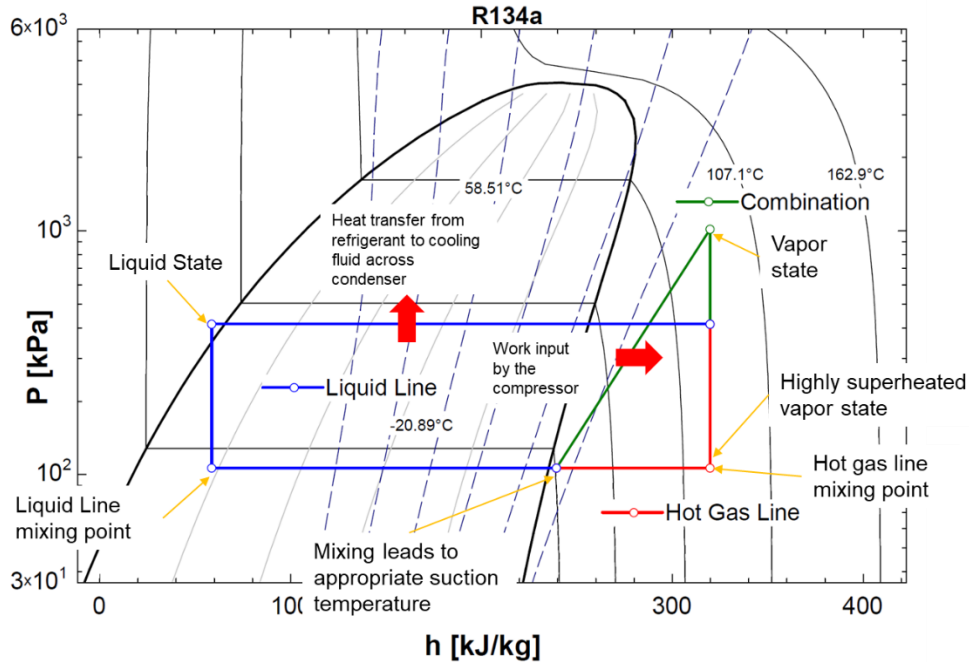


Figure 2.3: Pressure enthalpy diagrams of the Hot-Gas Bypass cycle. The figure details energy flow across the cycle.

### 2.1.2 Hot-Gas Bypass Test Stand

The Small Hot-Gas Bypass Test Stand used for evaluating refrigerator freezer compressors was originally designed for use in oil free miniature compressor applications like electronics cooling (Bradshaw, 2012). Figure 2.4 displays a schematic of the Small Hot-Gas Bypass Test Stand.

Control over the test stand is performed by actuating the 3 dual sets of valves; 1 set at the compressor discharge, and 2 sets in parallel at the compressor suction. Each set of valves has a coarse valve for targeting the pressure desired to within approximately 70 kPa, and a fine valve for tuning to this desired pressure more exactly. Table 2.1 details the valves used in the original Small Hot-Gas Bypass Test Stand.

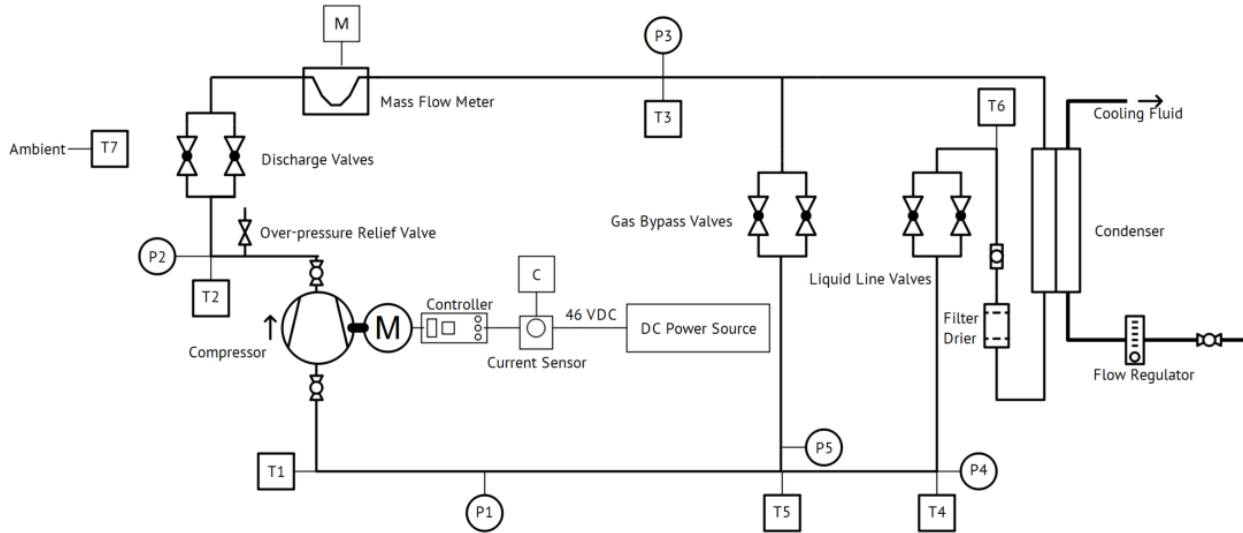


Figure 2.4: Original Small Hot-Gas Bypass Test Stand configuration. Motor control and power supply detail described for prototype oil-free scroll compressor.

Table 2.1: Original Valves for Small Hot-Gas Bypass Test Stand. All valves were manufactured by Swagelok.

Location	Identifier	Model Number	Series	Max Cv
Discharge	Coarse	B-1KM4	1	0.37
Discharge	Fine	B-4L2	L	0.16
Hot Gas	Coarse	B-4L2	L	0.16
Hot Gas	Fine	B-4MG2	M	0.03
Liquid	Coarse	B-4L2	L	0.16
Liquid	Fine	SS-SS4-VH	S	0.004

While the valve flow coefficient ( $C_v$  value) is not intended for specification when expanding two-phase fluids, it can be used as a guide to determine the resolution received when actuating the valve. Each valve can be turned a total of 10 turns from closed to the maximum  $C_v$  listed by the manufacturer. Each valve also has a curve associating the amount of turns from closed to a corresponding  $C_v$  value between 0 and the maximum  $C_v$ . The smaller the maximum  $C_v$  value, the more “fine” the valve is when actuated as the opening difference between 2 turns is smaller.

Additional control over the test stand is enabled via the flow regulator on the cooling fluid in the coaxial tube in tube condenser. For testing with the prototype scroll compressor, a water glycol mixture maintained at  $-16^\circ\text{C}$  by a separate chiller was utilized. This low

temperature was used to lower the condensing pressure of the system, increasing the pressure difference across the discharge valves, and decreasing the pressure difference across the suction valves. As there was some difficulty in achieving a subcooled liquid state in the liquid line, a maximum amount of cooling fluid flow was enabled through the regulator to increase the condenser to its maximum cooling capacity.

### 2.1.3 Hot-Gas Bypass Test Stand Instrumentation

As seen in Figure 2.4, 7 T-type thermocouples and 5 OMEGA model PX176 pressure transducers were used to determine refrigerant properties at various points in the original hot-gas bypass test stand. The pressure transducers were excited by an 18 VDC power supply and sent a 1-6 VDC signal to the data acquisition device. The pressure transducers were calibrated using a separate pressure transducer calibration test stand with nitrogen as a working fluid, where pressure was referenced from an OMEGA PCL-1B which measures from 0-1000 psig with an accuracy of  $\pm 0.25$  psig. Figure 2.5 displays the schematic of the pressure transducer calibration test stand.

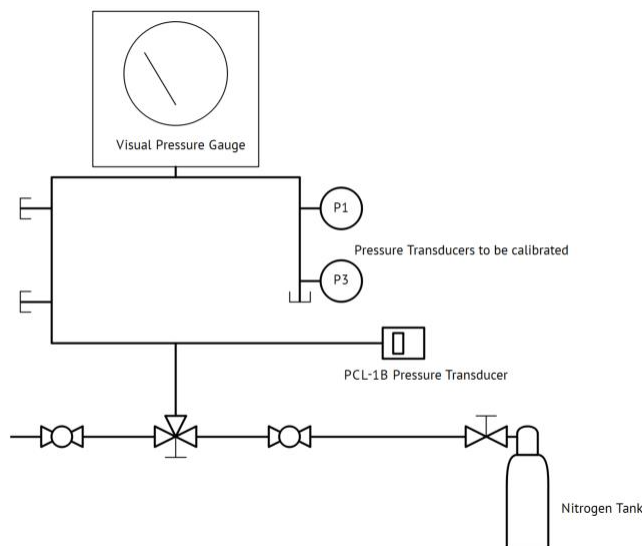


Figure 2.5: Pressure Transducer Calibration Test Stand. The PCL-1B Pressure Transducer was used as the reference value for calibrating other pressure transducers.

The pressure transducers were exposed to the nitrogen at multiple pressures, and a linear regression was fit to each pressure transducer to match an output voltage to a corresponding pressure value in psig with Equation (2.2) displaying the correlation in variable format.

$$p(U) = a_1 * U + a_0 \quad (2.2)$$

Where  $U$  is in volts and  $p$  is in psig (later converted to absolute pressure in kPa).

Table 2.2 displays the linear curves for each pressure transducer used.

Table 2.2: Pressure Transducer Calibration Curves.

<b>Transducer</b>	<b>Location</b>	<b>Slope <math>a_1</math></b>	<b>Offset <math>a_0</math></b>
P1	Compressor Suction	40.07	-39.41
P2	Compressor Discharge	100.8	-98.645
P3	Intermediate State	40.339	-81.733
P4	Liquid Line	40.48	-39.328
P5	Hot-Gas Bypass Line	40.069	-29.331

The thermocouples were Copper-Constantan (T) type thermocouples. National Instrument's LabVIEW has an internal curve fit for T type thermocouples that was used to identify temperature from the voltage difference across the thermocouples. Table 2.3 displays the points where temperature or pressure is sampled in the refrigerant line.

Table 2.3: Location and accuracy of thermocouples and pressure transducers in Small Hot-Gas Bypass Test Stand.

<b>State point</b>	<b>Location</b>	<b>Thermocouple Accuracy</b>	<b>Pressure Transducer Range</b>	<b>Pressure Transducer Accuracy</b>
<b>[-]</b>	<b>[-]</b>	<b>[C]</b>	<b>[psig]</b>	<b>[psig]</b>
1	Compressor Suction	$\pm 1$	200	$\pm 1$
2	Compressor Discharge	$\pm 1$	500	$\pm 2.5$
3	Intermediate State	$\pm 1$	200	$\pm 1$
4	Liquid Line	$\pm 1$	200	$\pm 1$
5	Hot-Gas Bypass Line	$\pm 1$	200	$\pm 1$
6	Liquid Line Condenser Discharge	$\pm 1$		
7	Ambient Air	$\pm 1$		

A model CMF010M Coriolis-effect mass flow meter by MicroMotion is used at the intermediate section of the test stand to determine the mass flow rate of the working fluid in its gas phase. This mass flow meter has a variable uncertainty of  $\pm 0.10\%$  of mass flow rate, and a maximum flow rate of 30 [g/s]. The output signal is converted from a 4 to 20 mA signal to a 2 to

10 V signal by shorting the output terminals with a 500  $\Omega$  resistor, and using the Pro-Link 3 software, the mass flow meter output range is limited from 30 [g/s] to 5 [g/s]. The mass flow meter was calibrated from a reference mass flow meter used for calibrating all mass flow meters at the Herrick Laboratories. The two mass flow meters are mounted on a separate mass flow meter calibration stand and connected in series. Figure 2.6 displays a schematic of the separate mass flow meter calibration test stand.

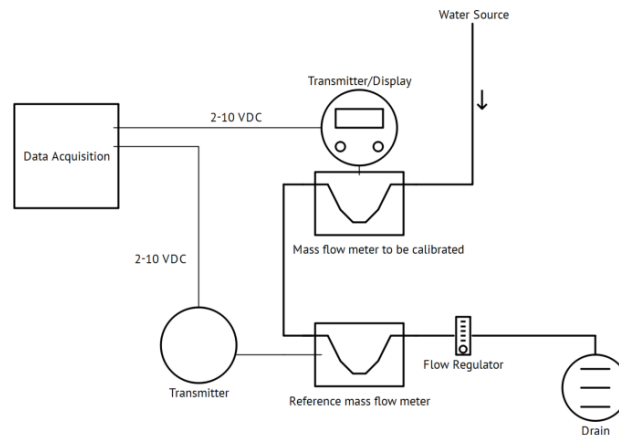


Figure 2.6: Schematic of the Mass Flow Meter Calibration Test Stand

Processed water from the building is used as the working fluid in calibration. The Flow Regulator is used to limit the mass flowrate of water flowing through the circuit, although the regulator indicator is inaccurate to the actual flow rate. To account for this, the display on the to-be-calibrated mass flow meter is used as a gauge to determine the flow rate of water during calibration (note that this was not the value used in actual calibration). The reference mass flow meter and the mass flow meter to-be-calibrated each send a voltage signal to the data acquisition device, the reference mass flow meter signal is converted to a corresponding mass flow rate in [g/s], and a linear regression is used to fit the to-be-calibrated mass flow meter voltage to the mass flow rate. In testing of the prototype scroll compressor, the mass flow meter regression is shown in Equation (2.3).

$$\dot{m} = 0.674946 * U - 1.249999 \quad (2.3)$$

Where  $\dot{m}$  is in g/s and  $U$  is in volts.

A Sorensen DCS 60-18 power supply was used in powering the prototype scroll compressor. The power supply has a range of 0-60 V and 0-18 A, with accuracy of  $\pm 0.35$  V and  $\pm 0.14$  A, and a stability of  $\pm 15$  mV and  $\pm 4.5$  mA.

A Hawkeye 923 Open Loop Hall Effect current transducer by Veris Industries was used to measure the current draw of the compressor placed into the test stand. The transducer has an accuracy of  $\pm 0.6$  A over a range of 30 A, with an output signal of 0-10 VDC. The transducer was calibrated using current draw data listed on the power supply display, where a linear regression was fit to convert the voltage signal to a corresponding current. The linear regression for the current transducer is listed in Equation (2.4).

$$C = 4.3442 * U + 0.6033 \quad (2.4)$$

Where  $C$  is in amps and  $U$  is in volts.

Figure 2.7 displays the top shelf of the original Small Hot-Gas Bypass Test Stand.

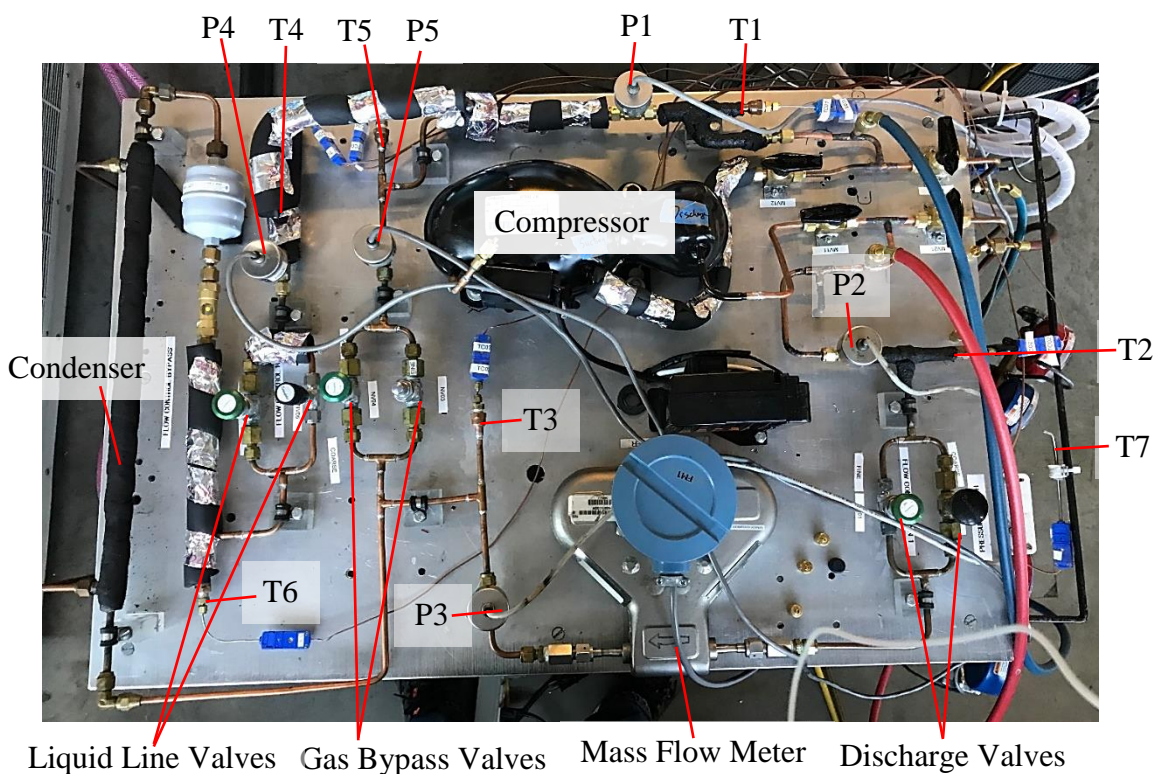


Figure 2.7: Original Small Hot-Gas Bypass Test Stand (Top Shelf). Pressure, temperature, and mass flow measurements can be seen.

Note that power source/monitoring and the prototype Air Squared scroll compressor are out of view on the lower shelf of the test stand. Figure 2.8 displays the prototype Air Squared scroll compressor on the lower shelf.

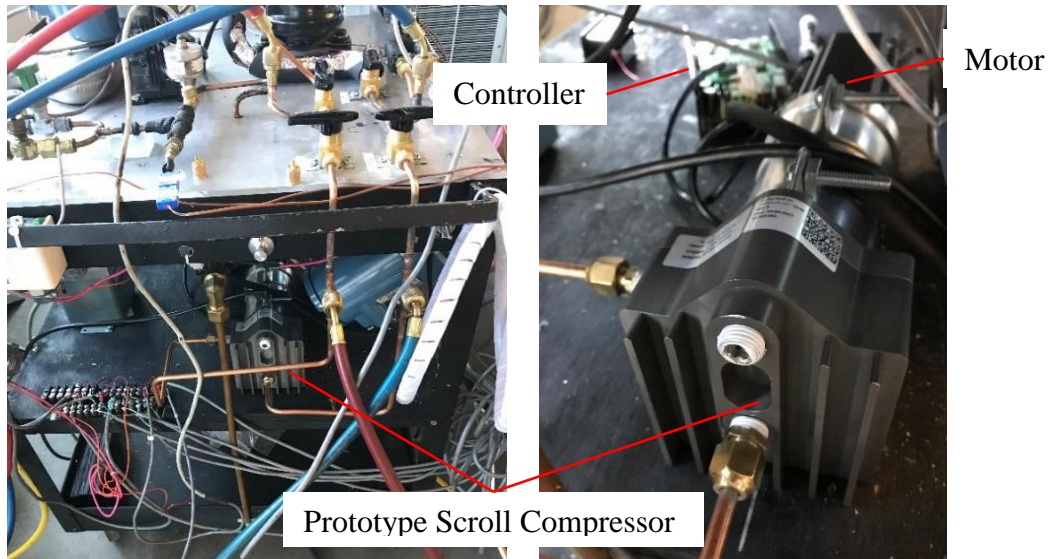


Figure 2.8: Location of prototype scroll compressor on second shelf.

#### 2.1.4 Modifications

Due to various issues with the original composition of the Small Hot-Gas Bypass Test Stand, some modifications were made to increase control over testing, and add capability for testing of oil lubricated compressors. Primary modifications were the addition of an oil separator and oil return line from the oil separator to the compressor suction, and the replacement of metering valves to better fit the small compressor size. Figure 2.9 displays a schematic of the updated hot-gas bypass test stand.

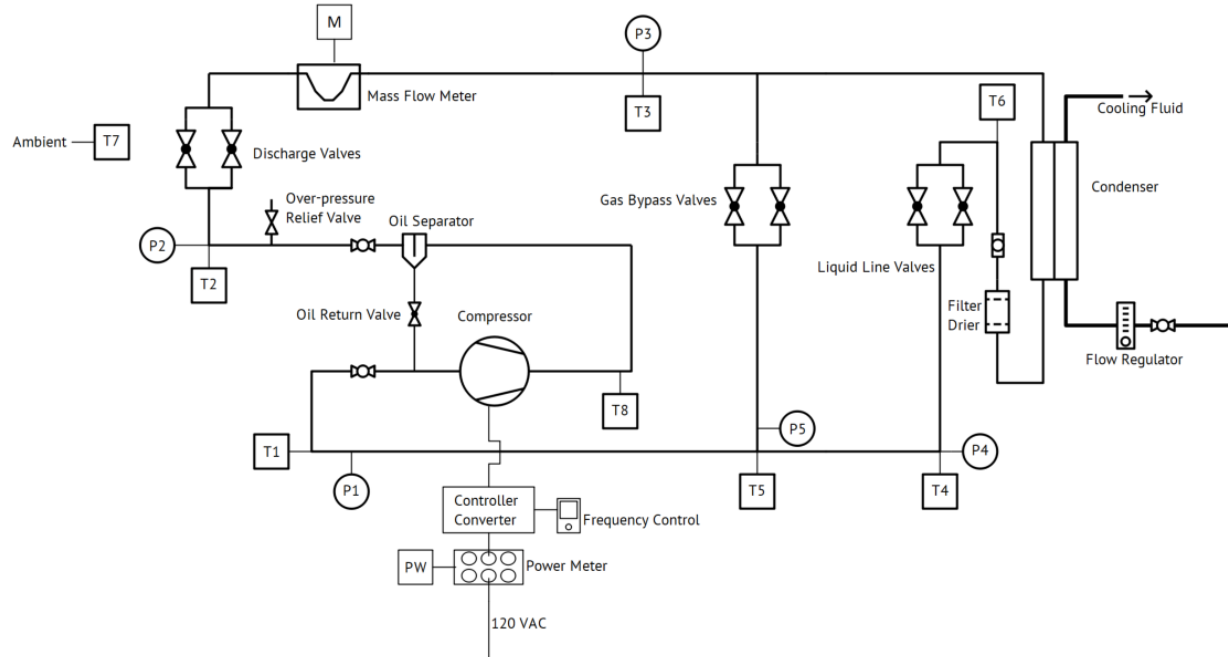


Figure 2.9: Modified Small Hot-Gas Bypass Test Stand. Oil separation was added, as well as an 8<sup>th</sup> thermocouple closer to the discharge of the compressor and before the oil separator.

Unseen in Figure 2.9 are the replacement of valves for better control. The valves were replaced due to negative experiences with minimal control over the test stand, and the realization that the valves are too large for the compressors being tested on the stand. Sizing of the new valves is based on the semi-applicable valve coefficients that valve manufacturers list with their product. A valve sizing guide published by the valve manufacturer Swagelok was used to identify the appropriate valve sizes for the new test stand (2007). Three equations relating the  $C_v$  value of a valve to the density and pressures of the working fluid and flow rate through the valve were utilized. Equations (2.5) and (2.6) apply to valve specification when gas flow is expected through the valve. Equation (2.5) is to be used when the outlet pressure is more than half of the inlet pressure, and Equation (2.6) is used for when the outlet pressure is less than half of the inlet pressure.

$$q = N_2 C_v p_1 \left( 1 - 2 * \frac{p_1 - p_2}{3 * p_1} \right) * \sqrt{\frac{p_1 - p_2}{p_1 * G_g * T_1}} \quad (2.5)$$

$$q = 0.471 * N_2 * C_v * p_1 * \sqrt{\frac{1}{G_g * T_1}} \quad (2.6)$$

Equation (2.7) is utilized when liquid flows through the valves.

$$q = N_1 * C_v * \sqrt{\frac{p_1 - p_2}{G_f}} \quad (2.7)$$

Where  $N_1$  and  $N_2$  are dependent on the units selected; when using std L/min for flowrate ( $q$ ), bar for pressure ( $p$ ), and K for temperature ( $T$ ),  $N_1$  is 14.42 and  $N_2$  is 6950. A basic Engineering Equation Solver (EES) script was written to simulate the Hot-Gas Bypass Test Stand to estimate the valve sizes needed. The equations above were added to the script, where it is assumed that only gas would flow through the discharge and hot-gas bypass valves and liquid would flow through the liquid line valves. The assumption that only liquid would flow through the liquid line valves is incorrect, as pressure drop causes the liquid to flash into a two-phase mixture, so a full gas calculation across the liquid line valves was also made and a Cv value estimate between the two outcomes was selected. Mass flow, pressures, and refrigerant properties are all determined by the hot-gas bypass simulation, so volumetric flowrate ( $q$ ), specific gravity ( $G$ ), pressures ( $p_{\#}$ ), and temperatures ( $T_{\#}$ ) are all predetermined before the valve sizing equations are utilized. This allows for the Cv value for each valve to be calculated, approximately indicating the correct valve needed. Due to the relatively small flowrate of refrigerant in the test stand and the relatively even pressure difference between the discharge pressure and the intermediate pressure, and the intermediate pressure and the discharge pressure, the valves were greatly reduced in size and each set of valves necessary was determined to be the same for the discharge, hot-gas, and liquid line valve sets. Table 2.4 indicates the new valves on the Small Hot-Gas Bypass Test Stand.

Table 2.4: Valve replacements for the Small Hot-Gas Bypass Test Stand.

New Valves for R134a HGB Test Stand				
Location	Identifier	Model Number	Series	Max CV
Discharge	Coarse	SS-4MG-MH	M	0.03
Discharge	Fine	SS-SS4-VH	S	0.004
Hot Gas	Coarse	B-4MG2	M	0.03
Hot Gas	Fine	SS-SS4-VH	S	0.004
Liquid	Coarse	SS-4MG-MH	M	0.03
Liquid	Fine	SS-SS4-VH	S	0.004
Oil Return Valve for R134a HGB Test Stand				
Location	Identifier	Model Number	Series	Max CV
Oil Return	Coarse	B-1KM4	1	0.37

With the new valves, control of the flow through the test stand as well as the three pressure levels of the cycle is increased. To maintain more even pressure distributions across the cycle, the condensing cooling fluid was replaced with chilled process water at 20 °C, raising the intermediate pressure of the cycle.

Another necessary replacement was made to the mass flow meter, as the processor of the flow meter was damaged irreparably. Replacing the processor necessitated a new linear regression, which is listed in Equation (2.8). Please note that the limit on flow was changed from 0 to 5 [g/s] to 0 to 10 [g/s], as well.

$$\dot{m} = 1.3743 * U - 2.712 \quad (2.8)$$

Where  $\dot{m}$  is in g/s and  $U$  is in volts.

To monitor power on a different compressor, a Columbus Scientific model XL5C5-A2-8 power meter was used. The power monitor has an accuracy of  $\pm 0.2\%$  of the reading, with a 4-20 mA output. This output was manipulated to be a 2-10 VDC output via a resistor short across the output terminals.

Figure 2.10 shows the top shelf of the updated Hot-Gas Bypass Test Stand.

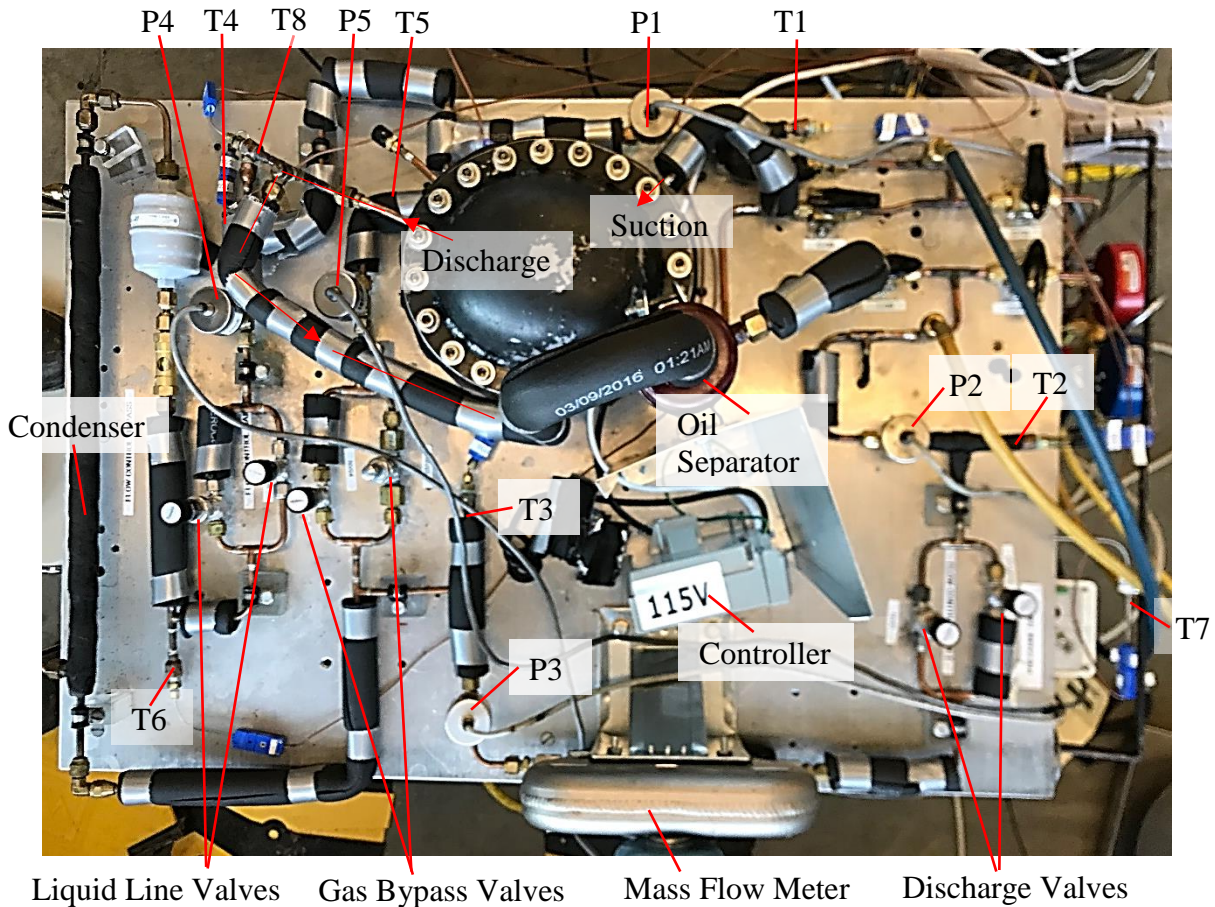


Figure 2.10: Updated Small Hot-Gas Bypass Test Stand. Note that some discharge piping (traced in red arrows) is routed above other piping.

### 2.1.5 Operation

Before the compressor can be switched on in the Small Hot-Gas Bypass Test Stand, power to the pressure transducers, power monitor, and mass flow meter must be turned on, and the cooling fluid on the heat absorption side of the condenser must begin to circulate. Additionally, discharge valves and hot-gas bypass valves must be turned fully open, the liquid line valves must be turned fully closed, and the data acquisition must be started before the compressor is switched on.

Once the compressor begins to operate at constant compression frequency, test stand operation is based on actuating the three sets of valves in the refrigeration circuit. Initially, the valves should be actuated such that a pressure ratio of about 2 is achieved. It is imperative that the fine discharge valve and fine gas bypass valve is actuated such that they are both at 50%

open, so that fine tuning of pressure is possible when targeting certain operating conditions. Pressures and temperatures can be viewed graphically and in real time on the front panel of the data acquisition VI on the computer monitors. Usually, increasing the discharge temperature at startup involves turning the discharge valves to a lower opening percentage. Once this pressure ratio of 2 is achieved, the fine valve on the liquid line can be turned to about 5% open, so that a small mass flow is permitted through the condenser. At this point, the system should be allowed to operate uninterrupted until there is liquid buildup in the liquid line after the condenser (indicated by view in the sight glass after the condenser), and the discharge temperature reaches a steady-state level. If there is no liquid buildup in the liquid line, charge must be added to the system. It is recommended that no more than 15 g of refrigerant is added at a time.

After initial conditions have been established (most importantly there is liquid buildup in the liquid line), the target operating conditions can be approached. Usually the pressure ratio needs to increase, where both the suction pressure is required to decrease, and the discharge pressure needs to increase. First, the desired discharge pressure must be approached by actuating the coarse discharge valve to a smaller opening percentage, it is recommended that the actual discharge pressure is set to be 70 kPa over the target pressure at this point. Second, the desired suction pressure must be approached by actuating the coarse hot-gas bypass valve to a smaller opening percentage, with actuation of the fine gas bypass valve left to reach the target more exactly. Once the desired suction pressure is achieved, the discharge pressure will have been changed, leading to necessary iterations of actuating the discharge and hot-gas bypass valves until the target pressures are achieved.

After the target pressure ratio is achieved at the appropriate suction and discharge pressures, the desired refrigerant superheat temperature can be set through iterative actuation between the fine liquid line valve and the fine hot-gas bypass valve. Opening the fine liquid line valve further will decrease the suction temperature, while simultaneously increasing the suction pressure. The fine hot-gas bypass valve can be further shut to decrease the suction pressure back to the target pressure. Note that reducing hot-gas mass flow will also further reduce the suction temperature. Due to the coupled nature of the hot-gas bypass line and the liquid line, small adjustments and many iterations are necessary to achieve the target suction temperature. The coarse liquid line valve should remain fully closed during normal operation of the Small Hot-Gas Bypass Test Stand.

After the operating conditions are established in the manner detailed above, the test stand must be permitted to reach steady-state at the operating condition, so that the steady-state data can be taken. Once steady-state data is collected, a new target operating condition can be approached. Between operating conditions, the same order of valve manipulation should be followed as is done in initial startup.

## **2.2 Data Acquisition and Software**

All signals collected from sensing devices were recorded as voltages on an Agilent 34980A Multifunction Switch/Measure Unit. Software used for data acquisition is National Instruments' LabVIEW. LabVIEW is used to sample data at 1 Hz from specific channels on the Agilent 34980A, convert the sampled data from a voltage signal to its respective unit, and display the updated value graphically on the front panel. Each data point is also logged on a tabulated text document which can be opened by Microsoft Excel and referred to for further processing. Figure 2.11 displays the front panel of the LabVIEW VI used in plotting the data. Temperature, pressure, mass flow rate, and power is displayed graphically, with each property on a different graph.

The tabulated data logged into a text document displays values of each property at the respective state points. Figure 2.12 shows an example document of data collected by LabVIEW.

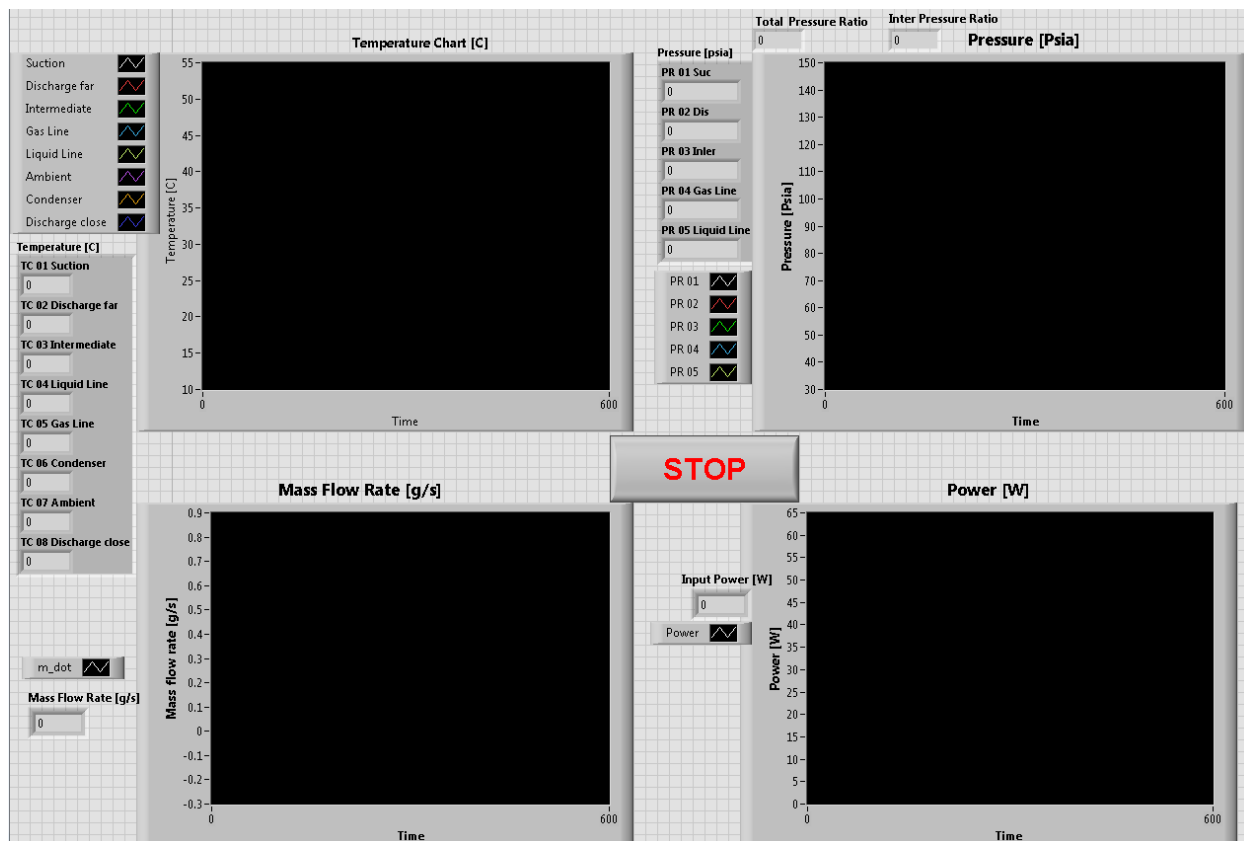


Figure 2.11: Front panel to the VI used for testing on the Small Hot-Gas Bypass Test Stand.

Project information			Label and Units					Data collected							
A	B	C	D	E	F	G	H	I	J	K	L	M	N	O	P
Solvay Compressor Performance Testing															
Testing conducted by Xinye & Cai at Ray W. Herrick Labs @ Purdue															
Date	TC_01 [C]	TC_02 [C]	TC_03 [C]	TC_04 [C]	TC_05 [C]	TC_06 [C]	TC_07 [C]	TC_08 [C]	PR_01 [psia]	PR_02 [psia]	PR_03 [psia]	PR_04 [psia]	PR_05 [psia]	Mass_rate [g/s]	Power [W]
2/13/2019 12:46	-0.536	44.994	27.343	-17.365	13.787	21.203	20.007	68.469	22.193161	158.557829	100.046902	22.934526	22.67508	0.90994	100.953158
2/13/2019 12:46	-0.415	45.021	27.357	-17.413	13.814	21.218	20.014	68.463	22.195517	158.495645	100.040006	22.97416	22.747287	0.909952	101.407107
2/13/2019 12:46	-0.397	45.082	27.354	-17.384	13.821	21.22	19.997	68.498	22.266534	158.468993	100.035074	23.029654	22.790572	0.909915	101.87232
2/13/2019 12:46	-0.417	44.933	27.354	-17.362	13.794	21.203	20.024	68.518	22.273594	158.464054	100.03902	23.033617	22.793162	0.907738	102.033185
2/13/2019 12:46	-0.384	44.917	27.371	-17.354	13.784	21.22	20.005	68.516	22.196695	158.475898	100.032114	22.948795	22.702707	0.905512	101.878197
2/13/2019 12:46	-0.24	44.994	27.359	-17.479	13.779	21.235	20.017	68.514	22.095073	158.444317	100.023246	22.840584	22.607268	0.905271	100.61551

Figure 2.12: Data collection into formatted text document for the Small Hot-Gas Bypass Test Stand.

## 2.3 Tests Performed and Results

### 2.3.1 Air Squared Scroll Prototype

As part of the SBIR Phase I sub-contract with Air Squared Inc., a prototype scroll compressor was tested in the original Small Hot-Gas Bypass Test Stand. Figure 2.8 shows the compressor mounted on the second shelf of the test stand. Designed for close to 200 W cooling

capacity with the working fluid of R134a, the compressor had a compression chamber displacement of  $8.3 \text{ cm}^3$ . The compressor was oil free and made use of a magnetic coupling between the compressor shaft and the motor shaft to seal the refrigerant from the motor. This sealing allowed for rapid prototype testing, and minimum use of lubricated parts where only a set of greased bearings was necessary. Figure 2.13 shows the magnetic coupling connection between the motor shaft and the compressor shaft.

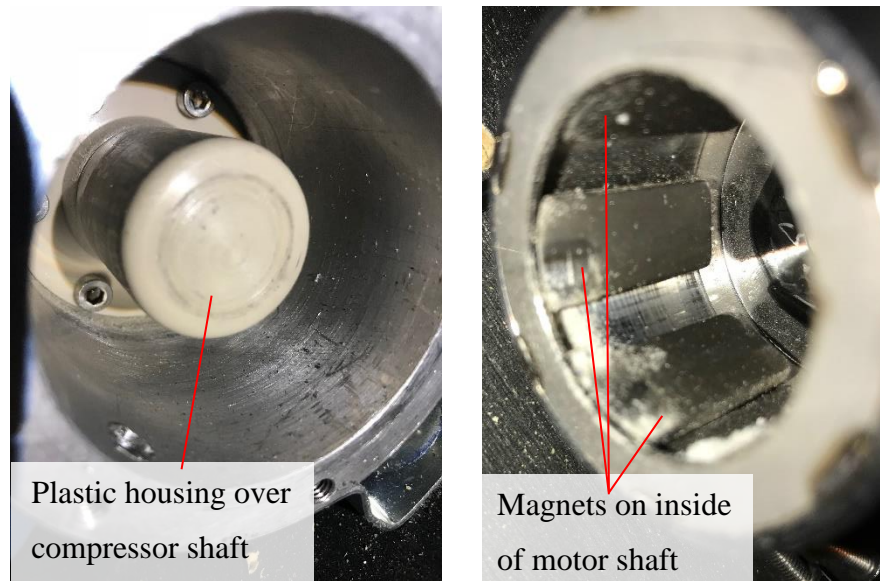


Figure 2.13: Magnetic coupling between compressor shaft and motor shaft on the scroll compressor.

The end of the motor shaft increases in diameter and the cylinder becomes hollow. Permanent magnets are fixed to the inside wall of the hollow portion. This assembly fits over a plastic housing around the compressor shaft. The intended action of the design is such that as the motor shaft rotates, the magnetic force causes the compressor shaft inside the plastic housing to rotate in turn.

Control over the compressor was achieved using a signal/power converter/controller, a Moog Components Group model BDO-Q2-50-40 brushless motor controller. The controller was able to limit the power draw of the motor and control the rotational speed of the motor shaft. The compressor was intended for use in the cold storage of food, with a target evaporator temperature of the freezer being  $-32 \text{ }^\circ\text{C}$ , and the condensing temperature of  $30 \text{ }^\circ\text{C}$ . The tests performed on this compressor were chosen to increase in pressure ratio while also decreasing in evaporating temperature, with the goal of targeting the design operating condition as the highest

pressure ratio and the lowest evaporating temperature. Figure 2.14 displays the tests completed on the prototype scroll compressor.

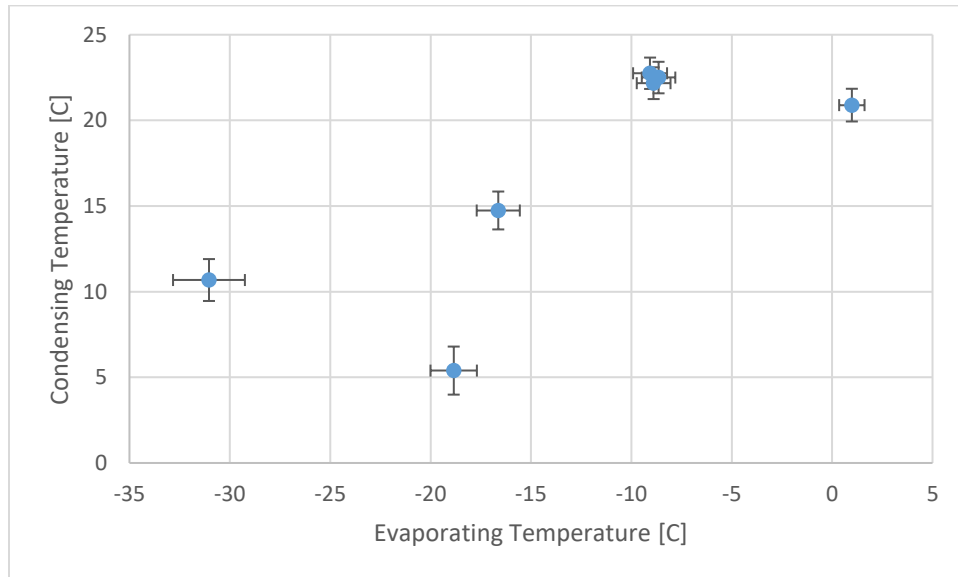


Figure 2.14: Operating conditions performed on the prototype scroll compressor.

Few tests were successful due to various issues experienced with both the prototype compressor, as well as the original Small Hot-Gas Bypass Test Stand. The most prominent issue was due to the decoupling of the magnetic connection between the motor shaft and the compressor shaft. The resistive torque from the compression process was larger than the maximum torque supported by the magnetic connection, causing the two shafts to decouple, which meant that the motor shaft would continue to rotate, and the compressor shaft would cease to rotate. Another issue was high superheat due to insufficient opening control over the valves in the test stand.

Performance of successful tests are described in Figure 2.15, Figure 2.16, Figure 2.17, and Figure 2.18.

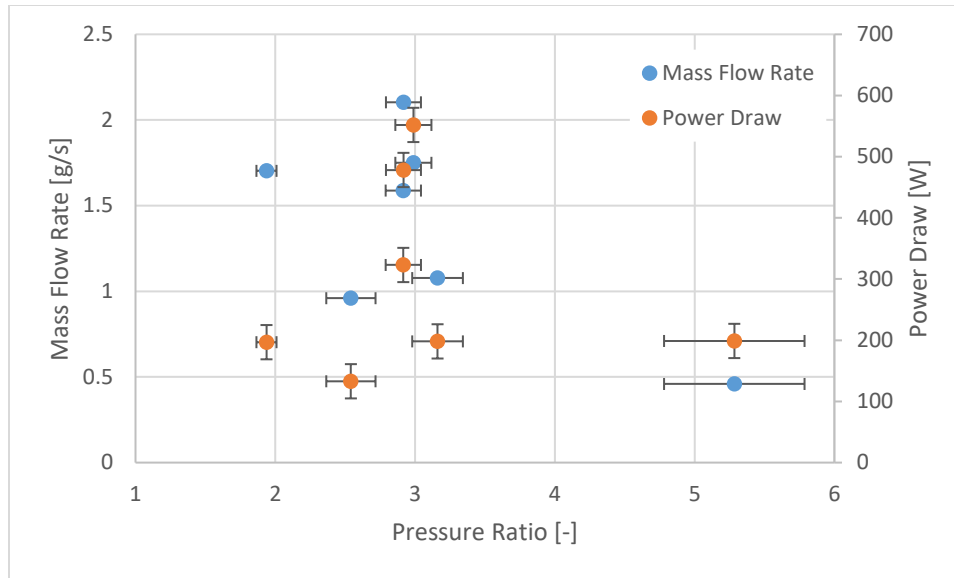


Figure 2.15: Mass flow rate (left axis) and power draw (right axis) across pressure ratio of the prototype scroll compressor.

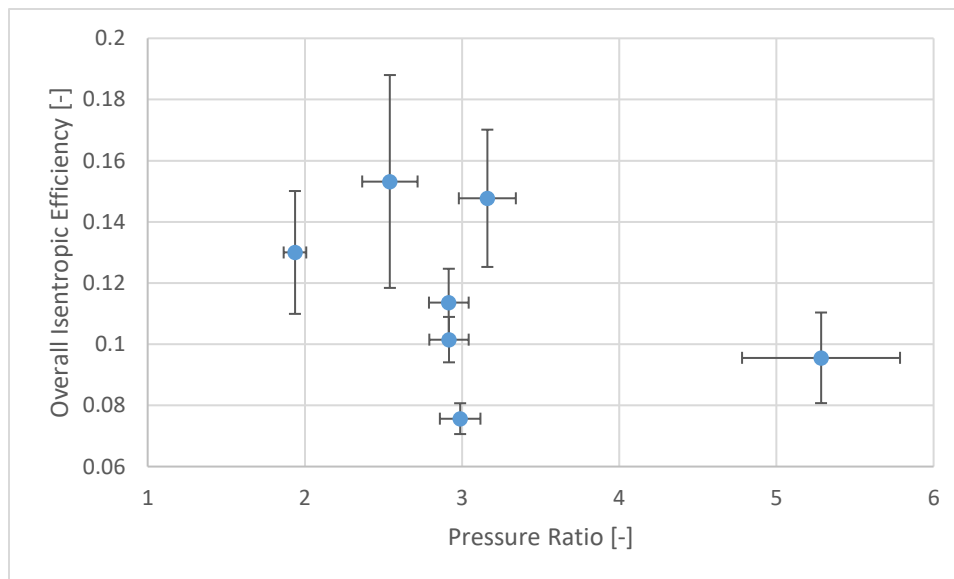


Figure 2.16: Overall compressor efficiency of the prototype scroll compressor.

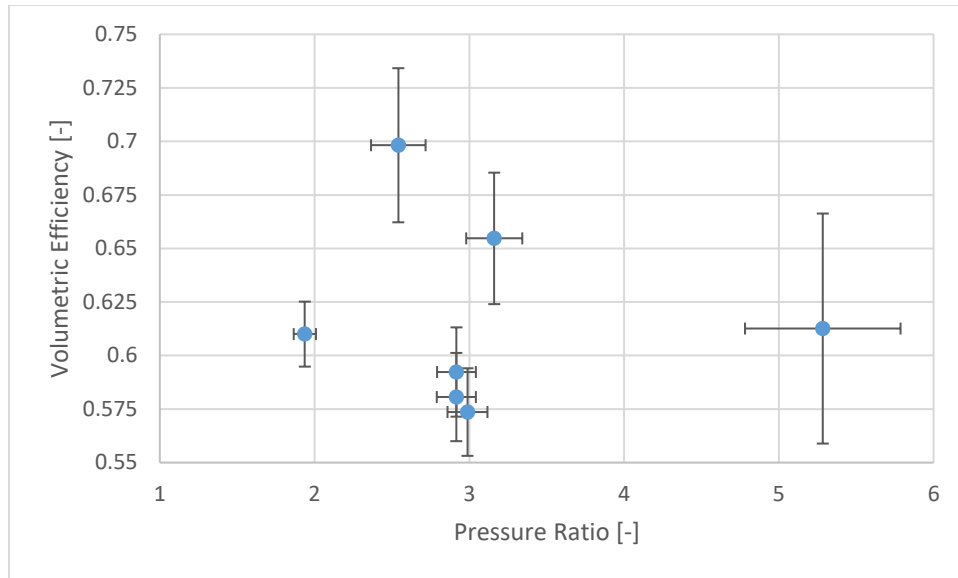


Figure 2.17: Volumetric efficiency of the prototype scroll compressor.

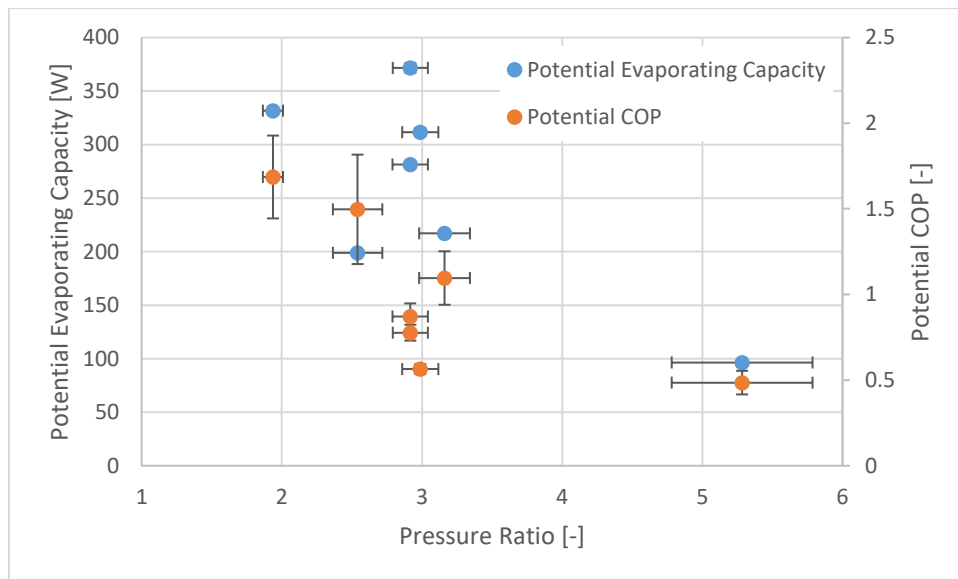


Figure 2.18: Potential evaporating capacity (left axis) and COP (right axis) of the prototype scroll compressor.

Overall, the prototype compressor did not work well. The overall isentropic efficiency of the compressor is between 8 and 16%, which is far below commercially sold scroll compressors. The volumetric efficiency fares better with a range between 55 and 70%, which matches the range seen in refrigerator/freezer scroll compressors on the low end. For most cases, the potential evaporating capacity is above that of the target capacity of just below 200 W and the theoretical

COP is greater than 1, but none of the operating conditions are at the target evaporating and condensing temperature. The closest match has an evaporating temperature of  $-31\text{ }^{\circ}\text{C}$  and condensing temperature of  $10\text{ }^{\circ}\text{C}$ , and even in this lower than target pressure ratio, the compressor maintained an evaporating capacity of just 100 W and a COP below 1, neither meeting the target capacity or performing efficiently.

### **2.3.2 Embraco Reciprocating Compressor**

A commercially available reciprocating compressor was also tested on the updated Small Hot-Gas Bypass Test Stand with the new test stand modifications in place. The compressor is a single-piston Embraco VEM-Y4H reciprocating compressor, which uses a POE oil for lubrication and R134a as the working fluid. The compressor is designed for an operating range between  $-35$  and  $-10\text{ }^{\circ}\text{C}$  with a speed dependent cooling capacity range from 50 to 150 W. The compressor has a displacement of  $3.97\text{ cm}^3$  and was operated at 60 Hz shaft rotation speed. The compressor underwent modifications to be converted into a semi-hermetic compressor. The shell was divided into two portions and a flange was welded to the edges of the shell. The flange has 20 threaded bolt holes to allow for sealing of the compressor with bolts. A 1/32 inch Buna N gasket was cut to provide a pressure seal between the two flange faces. These modifications were done so that the piston cylinder head could be replaced multiple times during testing. Figure 2.19 shows the reciprocating compressor both sealed and opened.

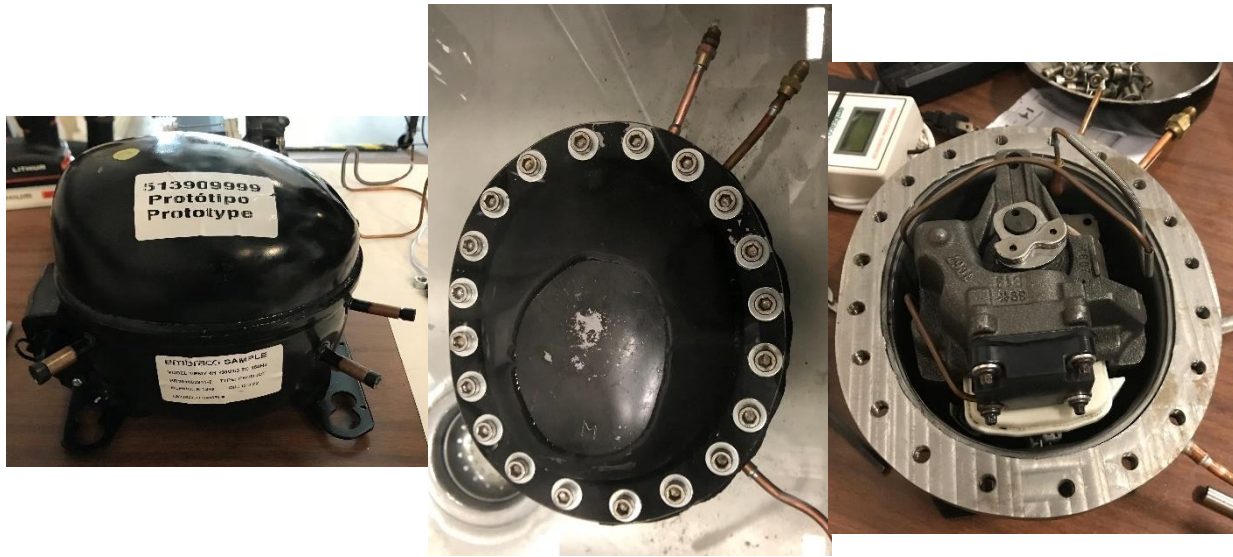


Figure 2.19: Embraco Reciprocating Compressor. (left) original compressor shell, (center) semi-hermetic compressor undergoing a leak test by being placed underwater while pressurized internally, (right) semi-hermetic shell opened to allow for access to compressor internals.

The purpose of testing this compressor was for the material replacement of the piston cylinder head. The piston cylinder head was targeted due to its unique status as the only component in the compression process to experience both suction conditions on one set of surfaces and discharge conditions on another different set of surfaces. Because of this, the piston cylinder head experiences both large pressure and temperature gradients and can be used as a proving point when exchanging the material composition of compressor components. In the original composition, the piston cylinder head is made of aluminum, and has a paper gasket sealing with the discharge valve plate, as displayed in Figure 2.20.

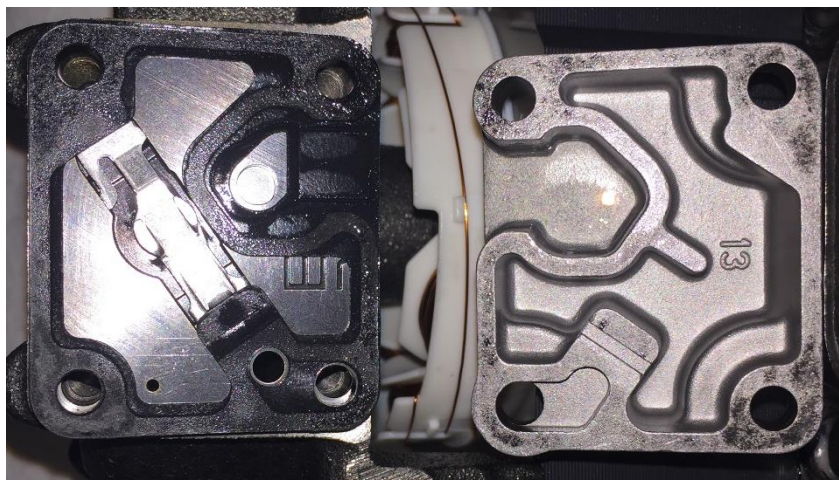


Figure 2.20: Original composition of the piston cylinder head and the paper gasket sealing between the cylinder head (right) and the discharge valve plate (left).

The piston cylinder head was replaced with a polymer cylinder head and the paper gasket was replaced with a 1/64 inch Buna N gasket. Both replacement components were produced by Solvay S. A. Figure 2.21 displays the replacement components.



Figure 2.21: Polymer replacement components for the piston cylinder head of the Embraco reciprocating compressor. (left) Buna N gasket overlaid onto discharge valve plate, (right) polymer piston cylinder head.

The compressor was tested at various operating conditions similar to that of the Air Squared Prototype Scroll compressor. Completed tests with both compositions are displayed in Figure 2.22.

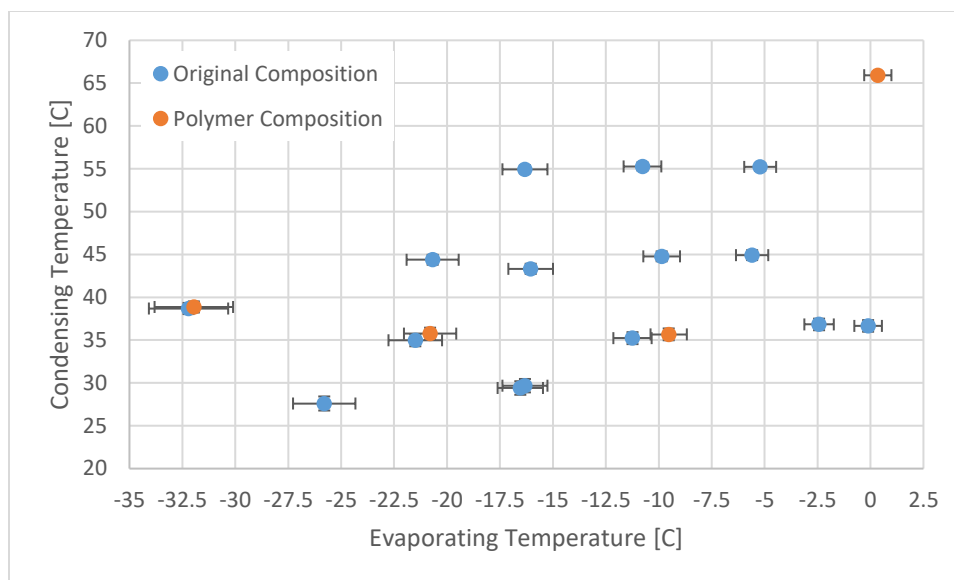


Figure 2.22: Operating conditions for the reciprocating compressor. All tests were performed after the compressor was modified to be semi-hermetic.

In the original composition, many conditions were achievable inside the designated design range of the compressor. Certain tests using the polymer composition were also successful but reaching a steady-state proved to be more difficult than the original composition in most cases, resulting in fewer passable operating conditions.

Performance of the compressor at both operating conditions is detailed in Figure 2.23, Figure 2.24, Figure 2.25, Figure 2.26, Figure 2.27 and Figure 2.28.

In general, the reciprocating compressor performance is poor. An overall isentropic efficiency of 47% at low-pressure ratios and just 27% at higher pressure ratios is a much lower trend than that of typical reciprocating compressors for this application. Volumetric efficiency of the compressor fares marginally better, trending from 75 to 35% as pressure ratio increases, leaving it comparable to the typical reciprocating compressor. This compressor would not be suited for refrigerator/-freezer application because the refrigerator/-freezer operating conditions force a high-pressure ratio. The low efficiencies at high-pressure ratio yield low potential evaporating capacity and COP. While operation of the compressor at pressure ratios up to 8 would technically be more energy wise than other cooling methods due to a COP of higher than 1, the refrigerator/freezer application yields an evaporative capacity of just 50 W at a COP of 0.5, meaning that other cooling methods would perform better in this condition.

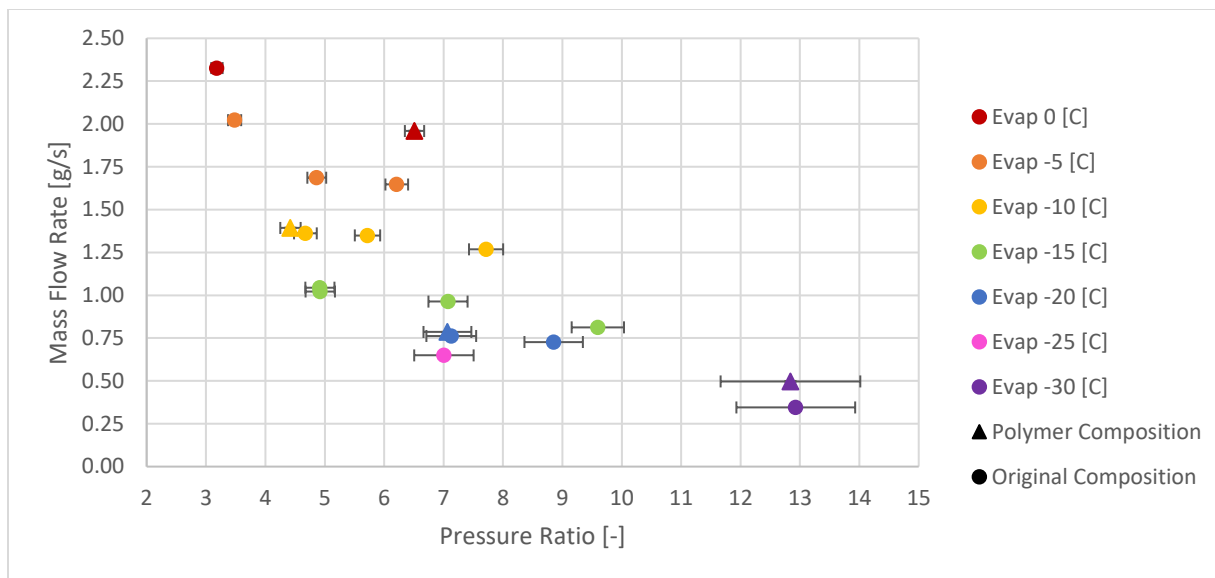


Figure 2.23: Mass flow rate over pressure ratio of both compositions of the reciprocating compressor

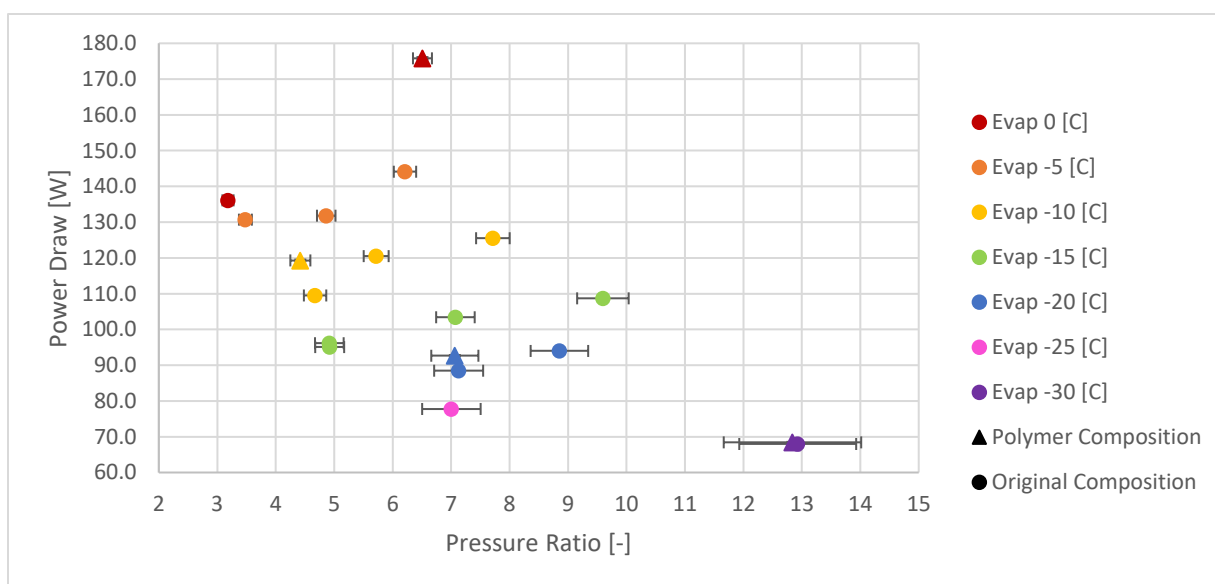


Figure 2.24: Power draw over pressure ratio of both compositions of the reciprocating compressor.

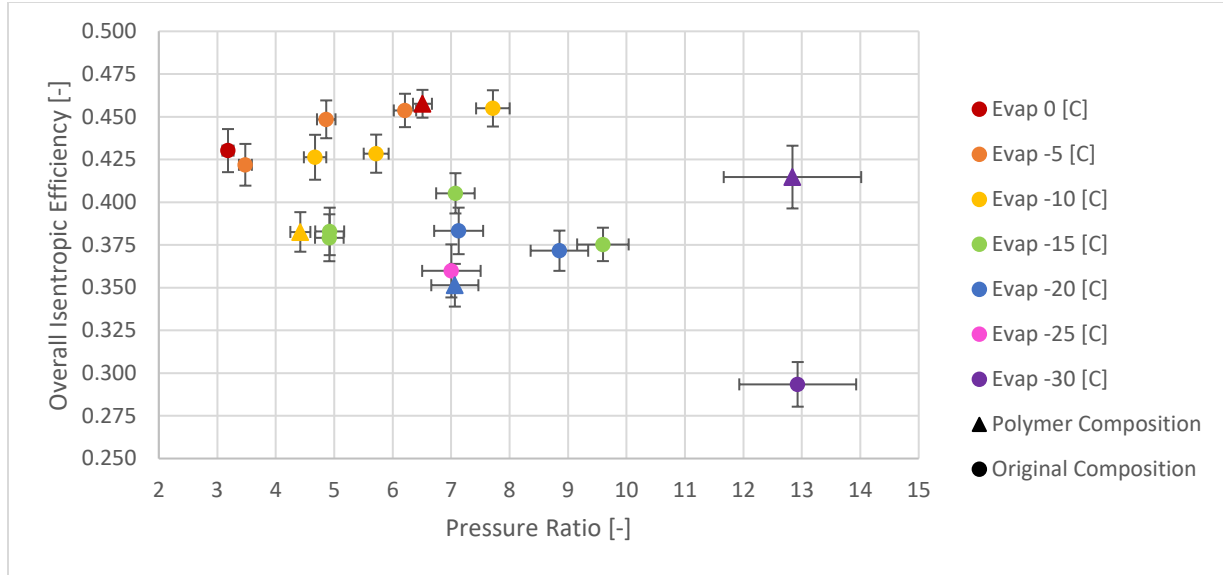


Figure 2.25: Overall compressor efficiency for both compositions of the reciprocating compressor.

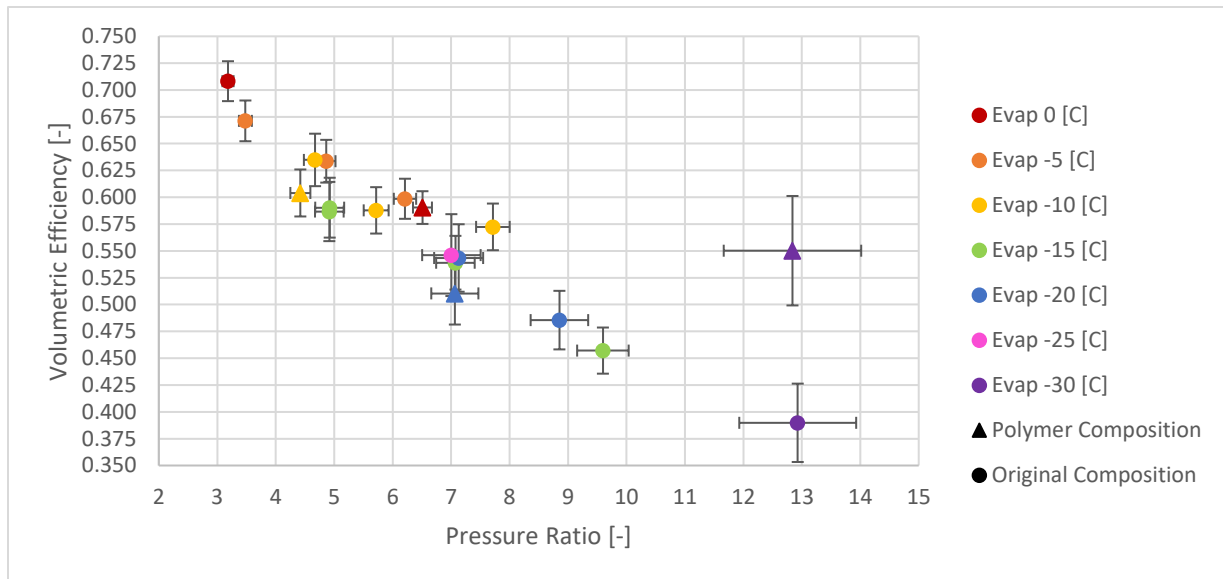


Figure 2.26: Volumetric efficiency of both compositions of the reciprocating compressor.

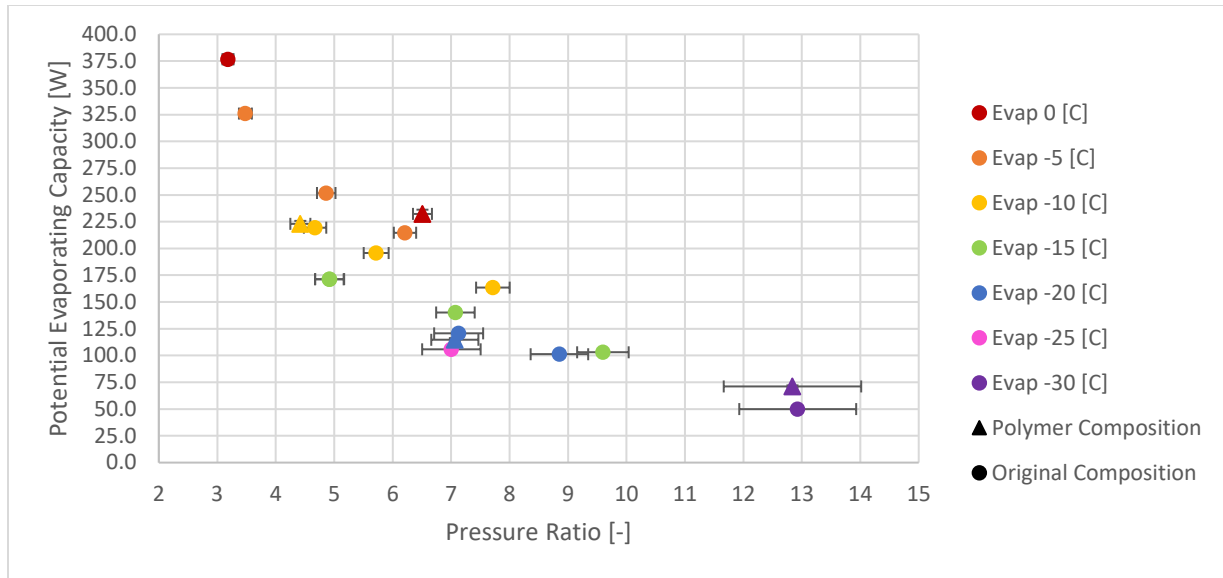


Figure 2.27: Potential evaporating capacity of both compositions of the reciprocating compressor.

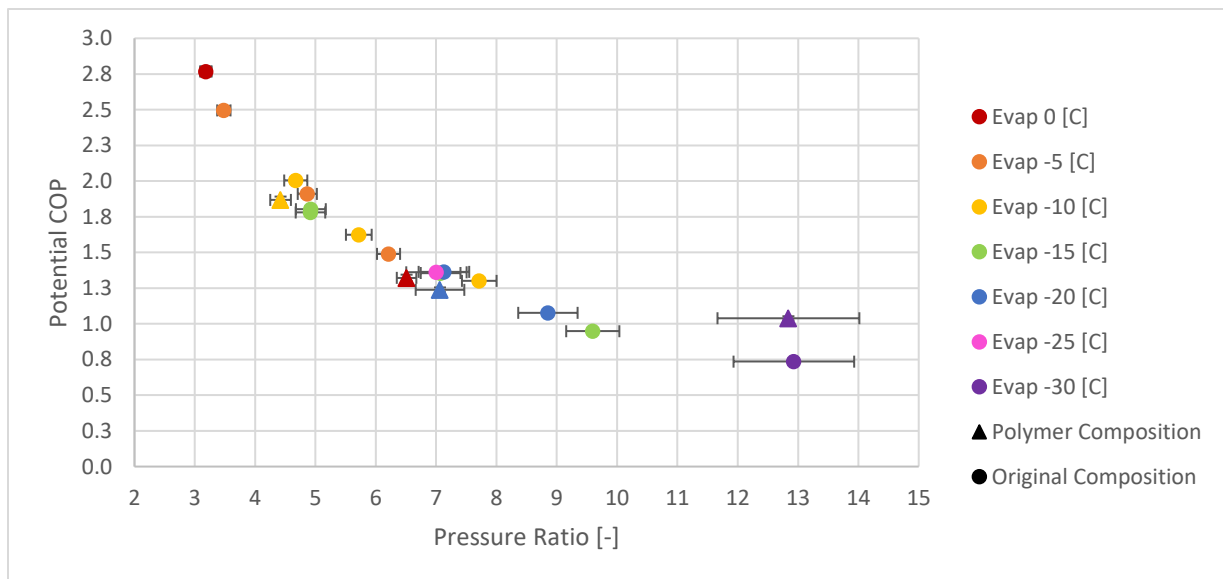


Figure 2.28: Potential COP of both compositions of the reciprocating compressor.

### 2.3.3 Comparison

Between the two compressors, the commercially available reciprocating compressor performed better. Overall isentropic efficiency is higher in all operating conditions in either piston cylinder head composition, mostly due to the lower power draw of the compressor.

Volumetric efficiencies between the two compressors are similar at low-pressure ratios, where the scroll compressor maintains higher volumetric efficiencies at the highest pressure ratios, while the volumetric efficiency decreases for the reciprocating compressor. The potential cooling capacity and COP between the two compressors is also similar, varying from 350 W and a COP of 2 at low-pressure ratio to 50 W and a COP of around 1 at higher pressure ratios.

The prototype nature of the scroll compressor, and the high superheat due to poor test stand control are likely the reasons for the much lower performance of the scroll compressor to the reciprocating compressor. The scroll compressor operated oil free, and with a magnetic coupling between the motor shaft and the compressor shaft. Operating without oil can increase the friction in the compressor, resulting in higher power consumption and more generated heat. The magnetic coupling reduced performance because the compressor could not operate at high frequency due to decoupling of the two shafts. Successful scroll compressor tests had operating frequencies between 25 and 43 Hz, where the compressor would decouple at the traditional 60 Hz.

Differences in attainable superheat on the original test stand and the updated test stand also may have skewed results. Control over the original test stand superheat was minimal, resulting in high superheat, which will increase compressor power draw. Figure 2.29 shows the different superheats achieved between the two test stands (and compressors).

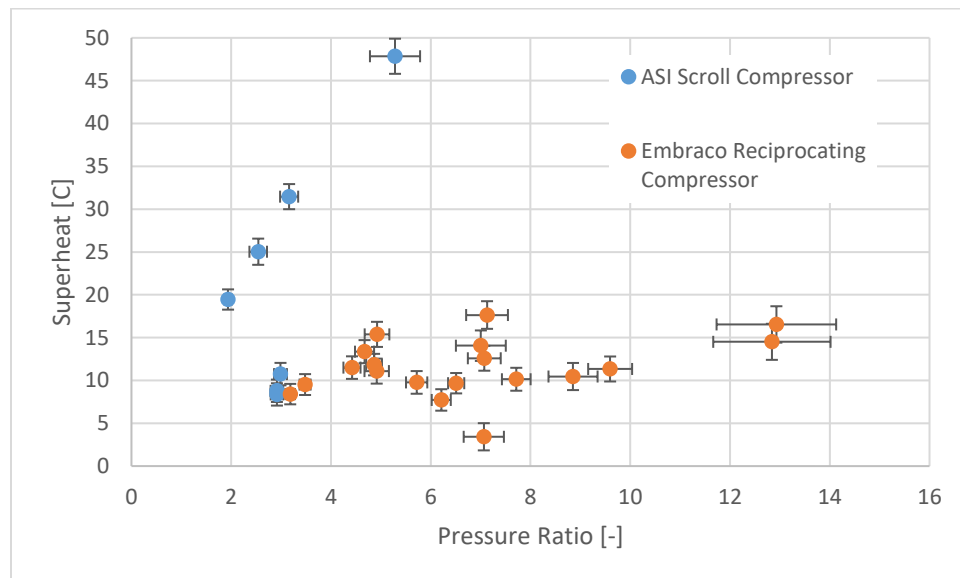


Figure 2.29: Suction superheat comparison between the scroll compressor and the reciprocating compressor. Note that superheat control is a function of the test stand and not the compressor.

Figure 2.29 shows that the scroll compressor experienced a much higher suction superheat than the reciprocating compressor in many of the tests performed on the scroll compressor. This high superheat negatively impacts compressor performance. If the scroll compressor was tested at more comparable suction superheat, it is expected that overall isentropic efficiency would improve and power draw of the compressor would decrease. There are some discrepancies between performance of the original composition and the polymer composition of the reciprocating compressor. These discrepancies can be accounted for when creating a 10-coefficient linear regression (compressor map) from the AHRI 540 standard. Using the original composition data as the source of the map, the polymer data can be compared to this map. Table 2.5 shows the original composition 10-coefficient compressor map, used to solve for the mass flow rate and the work input.

Table 2.5: List of coefficients for the reciprocating compressor with the original composition.

<b>Coefficient</b>	<b>Power Draw [kW]</b>	<b>Mass Flow Rate [kg/s]</b>
$C_1$	9.02018759E-02	5.55318435E-03
$C_2$	9.09113424E-04	-1.55127703E-04
$C_3$	1.34063190E-05	2.15662735E-06
$C_4$	-1.05641439E-07	-9.07477010E-09
$C_5$	-6.56912509E-05	3.39019324E-04
$C_6$	-2.45668776E-05	5.70416273E-06
$C_7$	2.09164123E-07	1.36945979E-08
$C_8$	6.30897000E-05	-9.14268948E-06
$C_9$	1.13446299E-06	-1.01459211E-07
$C_{10}$	1.63368497E-07	7.81883145E-08

These two mapped properties can be used to calculate other performance characteristics like overall isentropic efficiency or potential COP. The closest comparison can be made when the polymer composition data is corrected to the superheat of the original composition map, and the original composition map is run at the conditions of the polymer composition data. Figure 2.30, Figure 2.31, Figure 2.32, Figure 2.33, Figure 2.34, and Figure 2.35 shows the performance between the two sets of data optimized for comparison.

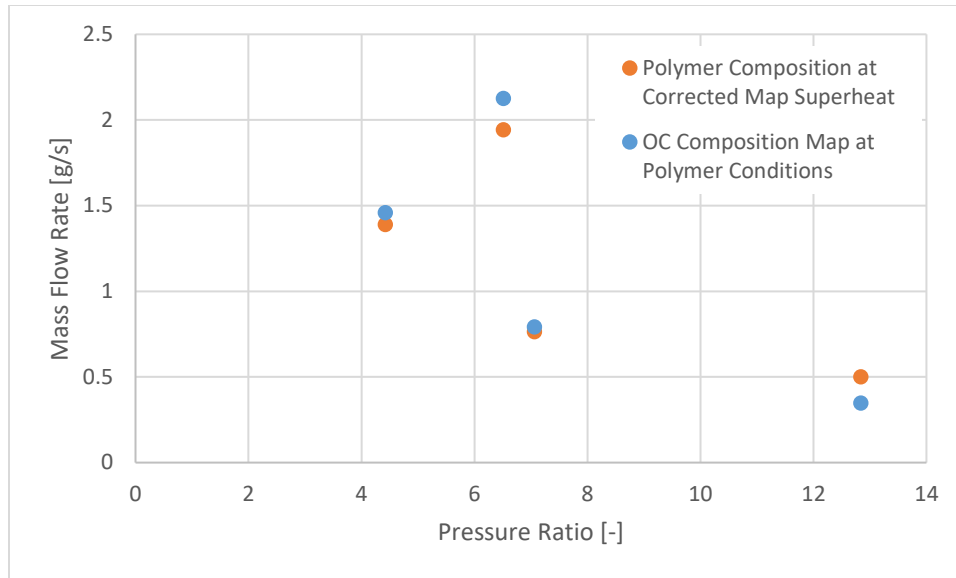


Figure 2.30: Mass flow rate comparison between the superheat corrected polymer data and the original composition map.

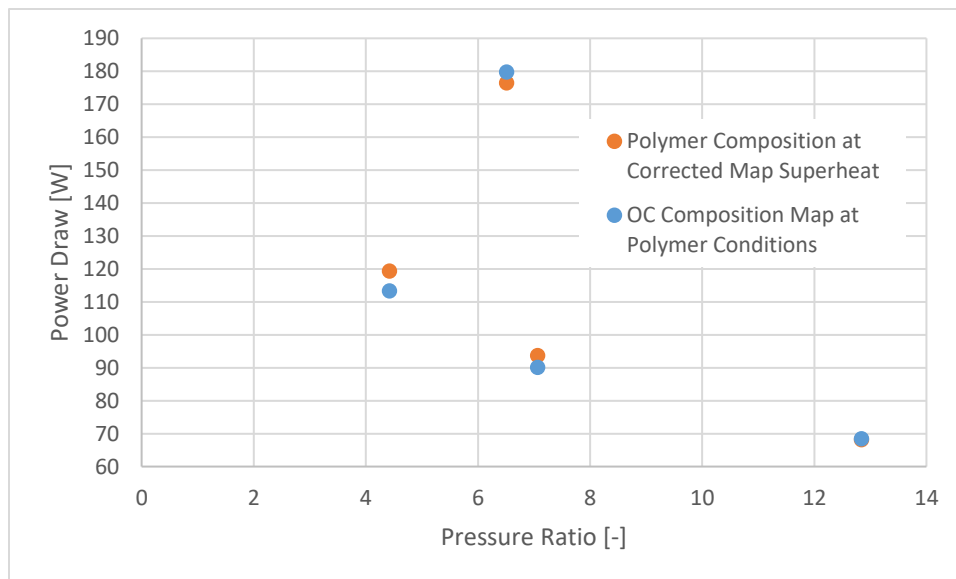


Figure 2.31: Power draw comparison between the superheat corrected polymer data and the original composition map.

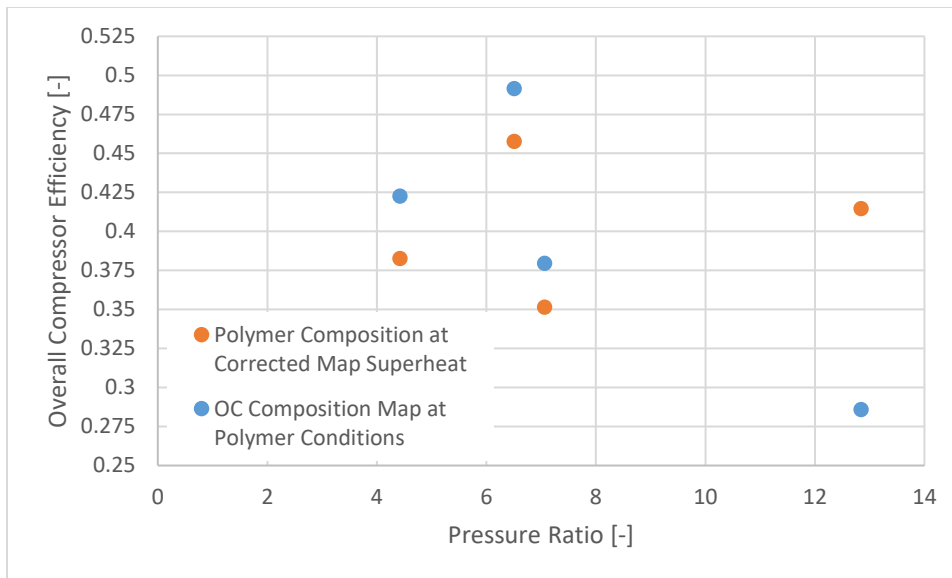


Figure 2.32: Overall compressor efficiency comparison between the superheat corrected polymer data and the original composition map.

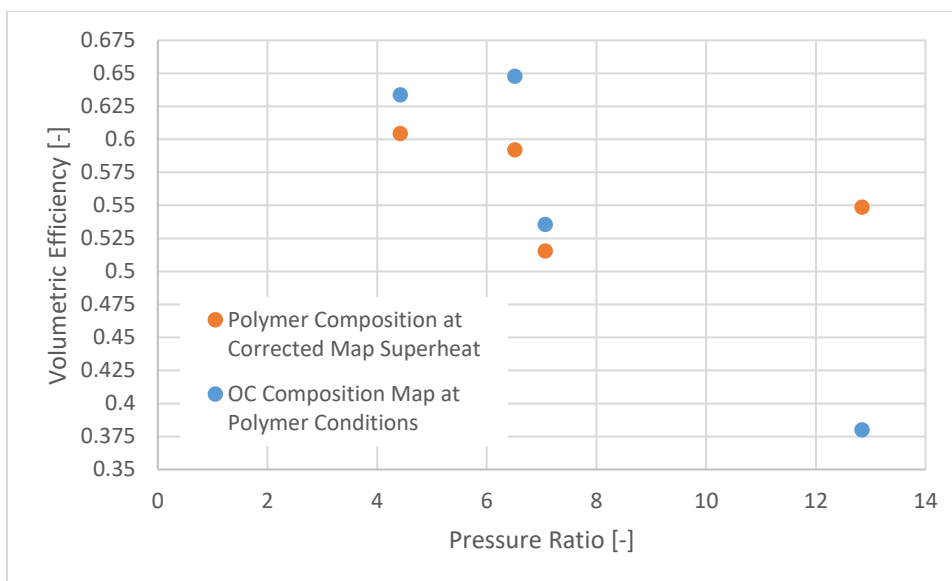


Figure 2.33: Volumetric efficiency comparison between the superheat corrected polymer data and the original composition map.

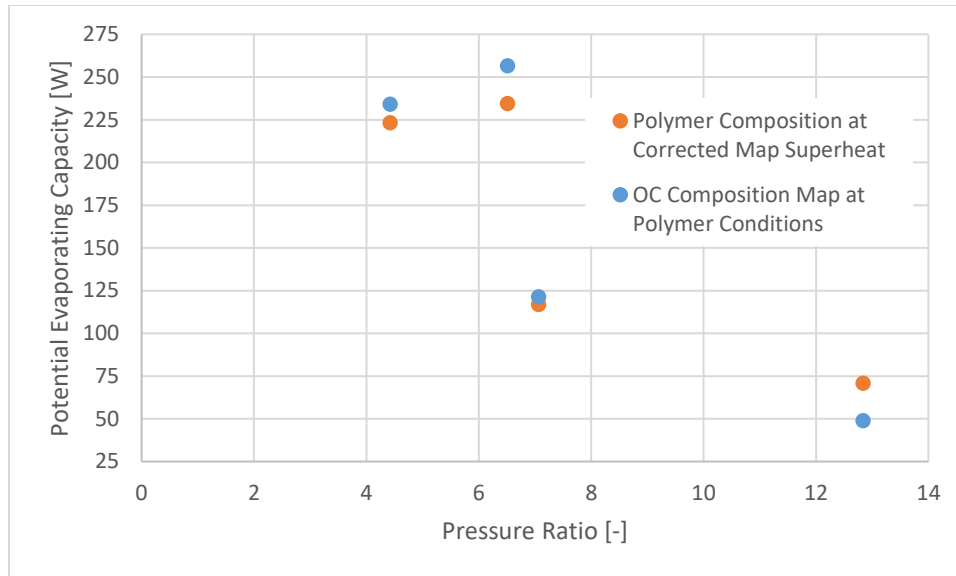


Figure 2.34: Potential evaporating capacity comparison between the superheat corrected polymer data and the original composition map.

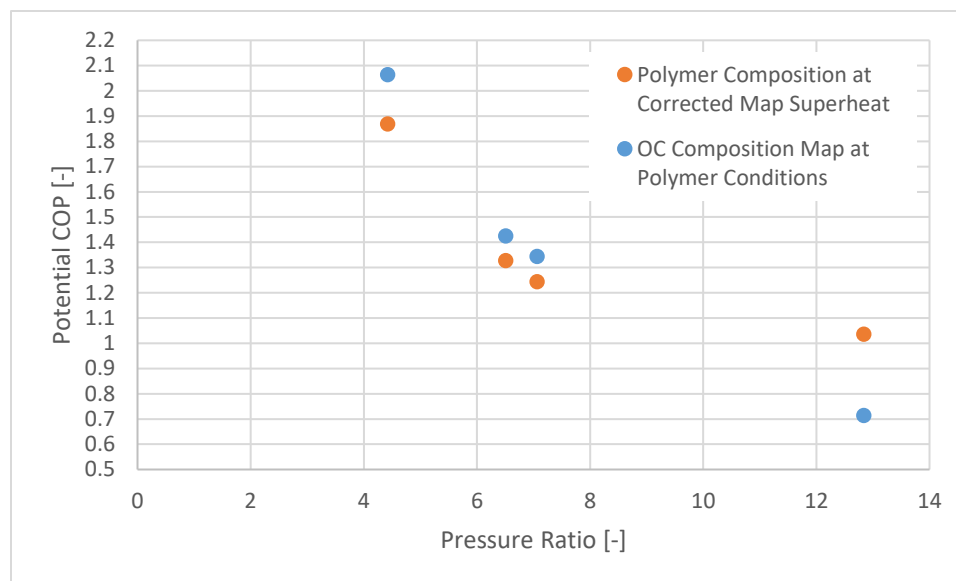


Figure 2.35: Potential COP comparison between the superheat corrected polymer data and the original composition map.

When the polymer data is corrected to match the superheat of the map, and the original composition map is run at the polymer data conditions, performance between the two different compositions of the reciprocating compressor becomes more comparable. In the lower pressure ratios, all performance characteristics match closely between the two compositions, with a slight

decrease in each parameter in the polymer composition. The mass flow rate is lower in the polymer ranging from 0.03 to 0.2 g/s, where there is a decrease of about 5 to 20 W in power draw. These two decreases in mass flow rate and power draw lead to larger decreases in overall isentropic efficiency and volumetric efficiency at around 5%. The lower mass flow rate indicates increased leakage between the discharge chamber and compressor shell when using the polymer cylinder head and rubber gasket. While the polymer cylinder head was modeled to be the same as the original aluminum cylinder head, it is not an exact match, which may create new leakage passes when installed. The rubber gasket also may have expanded or contracted due to temperature gradients between the discharge and suction temperatures. Deformation of the gasket can create new leakage passes. Additionally, efficiency calculations are directly dependent on the suction conditions of the refrigerant and may be more severely affected by the superheat correction.

The highest pressure ratio condition shows that the polymer composition efficiency is significantly better than that of the original composition, even though mass flow rate and power draw are quite similar between the two compositions. It is possible that the consequence of material choice for the piston cylinder head is higher at this higher pressure ratio, due to the higher temperature gradient across the piston cylinder head under these conditions. The polymer cylinder head may have a lower conductive heat transfer rate, where heat transfer from the hot discharge gas to the colder suction gas is limited, resulting in a lower suction superheat and thus a lower input power and higher overall compressor efficiency. It is more likely however, that this point is an outlier and needs to be retested.

### 3. RESIDENTIAL AIR CONDITIONING

#### 3.1 Experimental Setup

##### 3.1.1 Tescor Calorimeter

The inner workings of the calorimeter were well documented by Mösch (2015). Much of the following explanation is based off this reference.

A Tescor Inc. Compressor Calorimeter is used to control the inlet and outlet refrigerant conditions of a compressor. The compressor is installed into a traditional vapor-compression cycle and control of the condenser, evaporator, and expansion valve are maintained. Each component external to the compressor has its own control methods so that refrigerant properties can be controlled at the inlet and outlet of the compressor. In these methods, the calorimeter necessitates connection to a process water loop, which supplies cooling water at approximately 13 °C and pressure differentials from 69 to 241 kPa, an air supply with pressure range from 101 kPa to 690 kPa, and a 480 V 3-phase power supply. Figure 3.1 displays the general layout of the calorimeter.

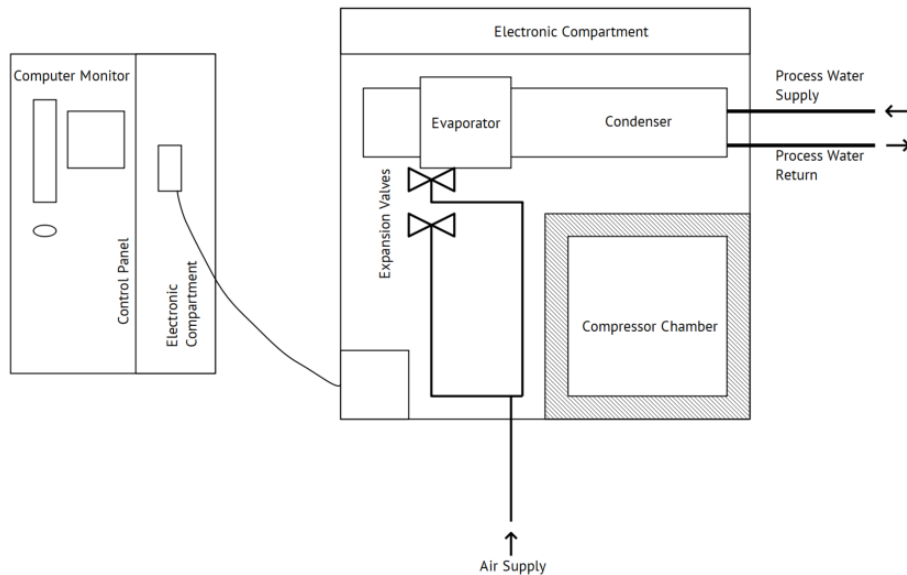


Figure 3.1: General layout of the Tescor Compressor Calorimeter.

High-pressure refrigerant at the outlet of the compressor enters a shell and tube heat exchanger, which utilizes the process water supply for cooling. The refrigerant pressure is

regulated by the cooling temperature of the condenser. Lower condensing temperature enforces a lower compressor discharge pressure, and a higher condensing temperature enforces a higher compressor discharge pressure. Condensing temperature is manipulated by the flow rate of water through a process water loop, which is regulated by a PID controller connected to a control valve, a small bypass metering valve, and a manual bypass ball valve. These three valves regulate the amount of flow that exits the loop, where the water rejected from the loop is replaced with new (colder) process water. Figure 3.2 displays the process water loop on the cooling side of the condenser.

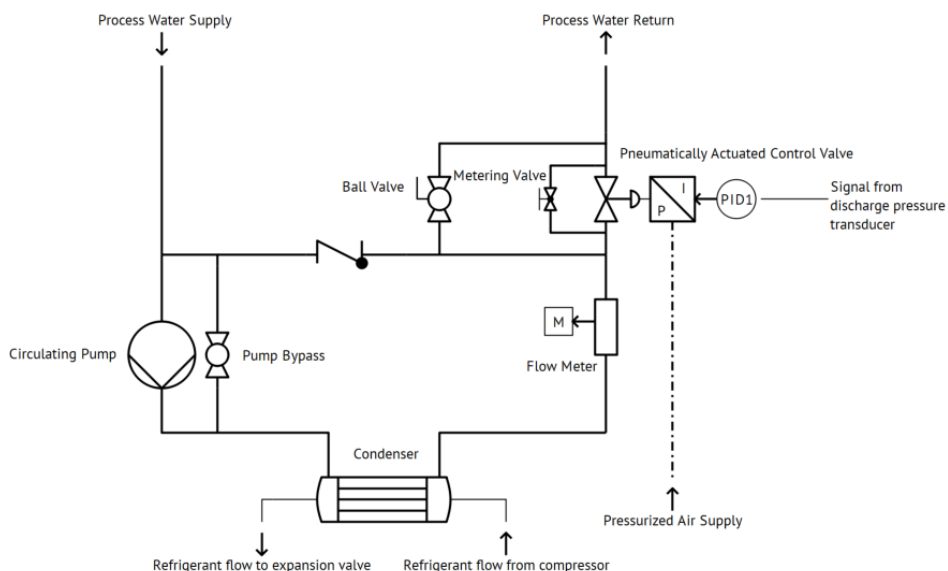


Figure 3.2: Process water circulation loop on the cooling side of the condenser.

The metering and ball bypass valves were introduced to increase the possible volumetric flowrate of water exiting the circulation loop so that more new water can enter the loop and lower the condensing pressure. The maximum opening of the control valve is 26 mm, where maximum opening of all the valves combined is 45 mm. The control valve is controlled via a PID controller, a Yokogawa Model UT37, and is actuated via a linear pneumatic diaphragm. A pressure transducer located at the compressor discharge sends a 4 to 20 mA signal to PID 1 which adjusts a valve that regulates air pressure for actuating the diaphragm. The air pressure range applied to the diaphragm is 121 to 203 kPa. The user sets a target discharge pressure and PID1 actuates the diaphragm based on the difference between the actual discharge pressure and the target discharge pressure.

After the condenser, refrigerant is expanded to the compressor suction pressure via a pneumatically actuated expansion valve (PXV). The user determines the suction pressure of the compressor and adjusts a dial on an air pressure regulator from Ecco Process & Controls. The regulator range is from 14 to 827 kPa. The dial sets the air pressure that flows to a 4-way solenoid valve from Dynamco. If the solenoid valve receives power (the user turns it on), then the air pressure will be sent to the pneumatic expansion valve. Similar to a traditional thermostatic expansion valve, the pneumatic expansion valve allows the same pressure at the valve outlet as the pressure it receives for actuation. If the user desires a suction pressure of 500 kPa, then the dial on the air regulator will allow a downstream pressure of 500 kPa to actuate the pneumatic expansion valve to permit a refrigerant downstream pressure of 500 kPa. Figure 3.3 displays the circuitry to control the pneumatic expansion valve.

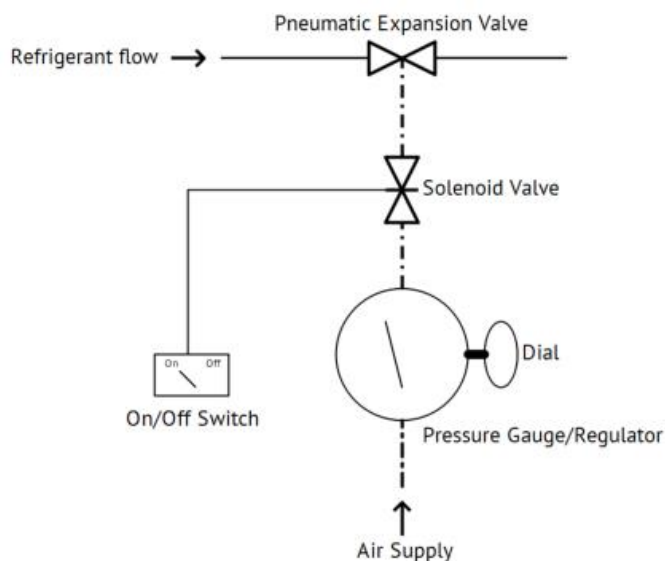


Figure 3.3: Suction pressure control via pneumatic expansion valve (PXV).

In the original assembly of the calorimeter, there were two identical pneumatic expansion valves in parallel. Depending on the capacity of the compressor, both could be used to set the same suction pressure. Engaging the second expansion valve would just permit an increase in mass flow rate through the system.

After the refrigerant is expanded to suction pressure, it enters the evaporator. The evaporator controls the suction temperature of the refrigerant by adjusting the heat input into the refrigerant line. The evaporator consists of a tank filled with secondary refrigerant (R134a) in a

two-phase state with five electric heating elements submersed in the refrigerant. The primary refrigerant line, which later enters the compressor, is also submersed in this secondary refrigerant tank. While the temperature of the evaporator remains constant in steady-state, the heating capacity of the tank is adjusted via the electric heating elements. Depending on the operating condition of the compressor, three fixed 3 kW heating elements and one fixed 6 kW heating element can be switched on or off independently or in combination by the user. During operation of the compressor the final heating element, which is variable with a capacity of 3 kW, is controlled by a second PID controller (PID 2). The user must set the variable heating element to remain powered, but the element may or may not be engaged (generate heat) depending on the actual suction temperature of the refrigerant and the setpoint for that suction temperature. The user sets the suction temperature on the second UT 37 PID controller, and this PID controller determines whether the final heater will activate or remain dormant. The suction temperature is thusly achieved by alternating the heating capacity input to the evaporator and has a resolution of 3 kW. In most operating conditions, it is expected that during steady-state operation, PID 2 will alternate activating and deactivating the final heating element periodically. Figure 3.4 displays the circuitry of the evaporator and the heating elements.

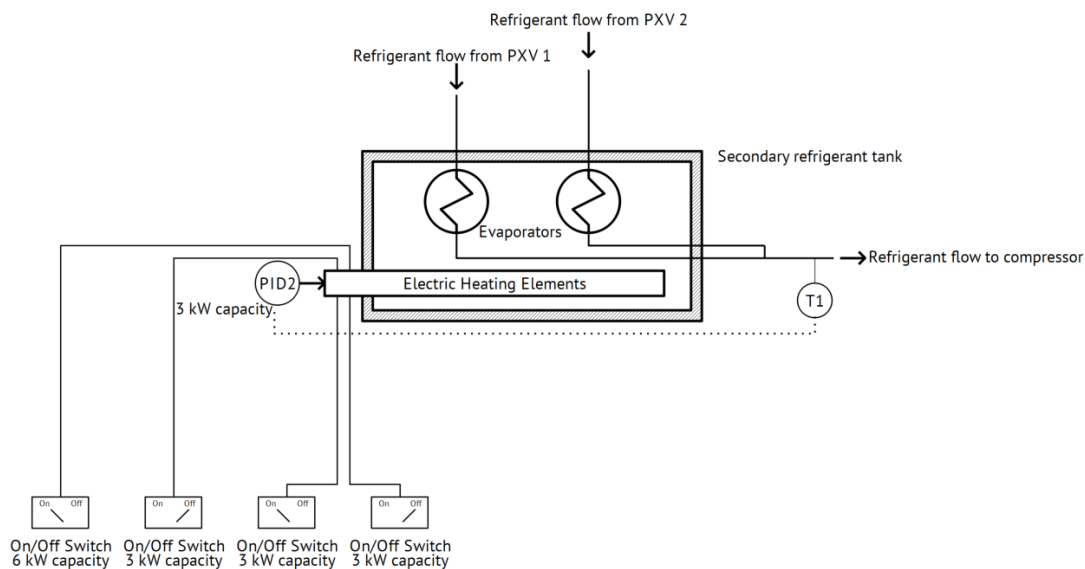


Figure 3.4: Suction temperature control via evaporator in secondary refrigerant tank with heating elements with varying capacity.

At constant evaporating pressure, increasing the heating capacity by switching the fixed heating elements on will increase the suction temperature, where switching the fixed heating elements off will reduce the suction temperature.

After exiting the evaporator, the refrigerant enters the compressor chamber and then the compressor. The compressor chamber has temperature control capabilities via the third UT 37 PID controller (PID 3). PID 3 controls a 1550 W electric heating element that is finned tubular, and manual control over a fan blows air across the heating element and into the compressor chamber. PID 3 references the air temperature inside the chamber and activates or deactivates the heating element based on the target temperature of the air set by the user. Figure 3.5 illustrates the compressor chamber.

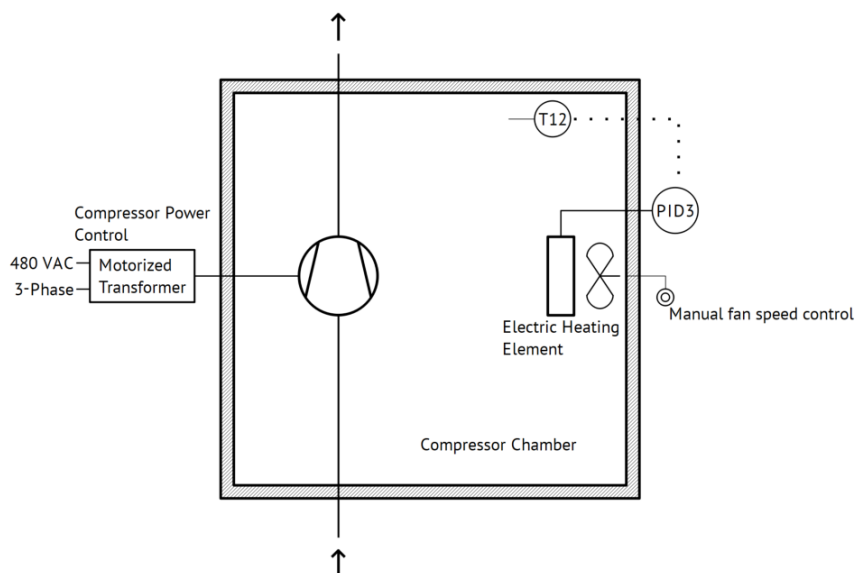


Figure 3.5: Compressor chamber for ambient air temperature control around the compressor.

Also seen in Figure 3.5 is the motorized transformer that converts the 480 VAC supply to either 208, 230, or 260 V in either single phase or three phases to be sent to the compressor.

### 3.1.2 Tescor Calorimeter Instrumentation

The calorimeter is heavily instrumented to allow for detailed black-box analysis of compressor performance. The refrigerant circuit has pressure sampled before and after each main calorimeter component, and the mass flow rate is measured after the condenser. The secondary refrigerant tank has pressure and temperature measurements, and the condensing water loop has

temperature measurements before and after the condenser as well as volumetric flow rate measured after the condenser. All measurements are displayed on the data acquisition VI, and most measurements are displayed on the control panel of the calorimeter.

Temperature sensors are Omega T-Type thermocouples with an accuracy of  $\pm 1$  K. The thermocouples are fully immersed in the flow stream of the refrigerant and the water. The thermocouples output a voltage difference which is converted to temperature via LabVIEW's internal thermocouple measuring VI.

Pressure transducers are Setra model 204 high accuracy absolute capacitance pressure transducers with 4 to 20 mA output. Output is converted to a 1 to 5 V signal using a 250 ohm resistor short circuited across the output terminals. On the low-pressure side the pressure transducers can record from 0 to 689 kPa and have an accuracy of  $\pm 0.76$  kPa. On the high-pressure side the pressure transducers can record from 0 to 6894 kPa with an accuracy of  $\pm 7.58$  kPa. The pressure transducer which measures the secondary refrigerant tank pressure is able to measure from 0 to 3447 kPa with an accuracy of  $\pm 3.79$  kPa. Pressure transducers were calibrated to record in psia, with Table 3.1 displaying the calibration curves for the pressure transducers.

Table 3.1: Pressure transducer calibration curves with formant  $p = a_1 * U + a_0$ .  $U$  is in volts and  $P$  is in psia. The LabVIEW VI for data acquisition later converts this unit to kPa.

Location	Transducer	Slope $a_1$	Offset $a_0$
Compressor Suction	P1	25.104	-25.216
Compressor Discharge	P2	248.81	-255.94
Compressor Chamber Outlet	P3	249.68	-253.82
Condenser Outlet	P4	250.64	-250.03
Mass Flow Meter Outlet	P5	250.83	-248.20
Evaporator Outlet	P6	24.877	-26.112
Secondary Refrigerant Tank	P7	124.96	-126.34

The calorimeter has two methods to calculate the refrigerant mass flow rate, with the primary method to measure it directly via a Coriolis-effect Model DS040 mass flow meter from MicroMotion with a range of 0 to 544 kg/hr and an accuracy of  $\pm 0.2\%$  of the reading. The mass flow meter is located after the condenser, measuring the refrigerant flow in the more stable liquid state. The mass flow meter is connected to the transmitter model RFT9712, which sends a frequency signal to a display/transmitter model 3300, which outputs a 4 to 20 mA signal. This

signal is converted to a 0.88 to 4.4 VDC signal by placing a 220 ohm resistor in parallel. The display on the front panel is in lb/min, with the DAQ recording in kg/hr. The mass flow meter has a calibration curve shown in Equation (3.1).

$$\dot{m}(U) = 5.4243 * U - 4.9588 \quad (3.1)$$

Where  $m$  is in lb/min (later converted to kg/hr and then kg/s) and  $U$  is in volts.

For water flow rate a turbine flow meter model FT12 from EG&G with a measurement range of 0 to 4.542  $m^3/hr$  and an accuracy of  $\pm 0.25\%$  of the reading. The flow meter outputs a frequency which is converted to a 4 to 20 mA signal by a model FC70A flow computer and is shorted to a 0.88 to 4.4 VDC signal with a 220 ohm resistor. The turbine flow meter has a calibration curve shown in Equation (3.2).

$$\dot{V}(U) = 5.0926 * U - 4.9484 \quad (3.2)$$

Where  $\dot{V}$  is in gal/min and  $U$  is in volts.

The compressor power consumption is measured using a Model DL31K5 watt/watthour transducer from Scientific Columbus. The transducer has a range of 0 to 20,000 W and an accuracy of  $\pm 0.09\%$  of the reading. The transducer measures three-phase power draw by utilizing two power meters set in an Aron circuit shown in Figure 3.6.

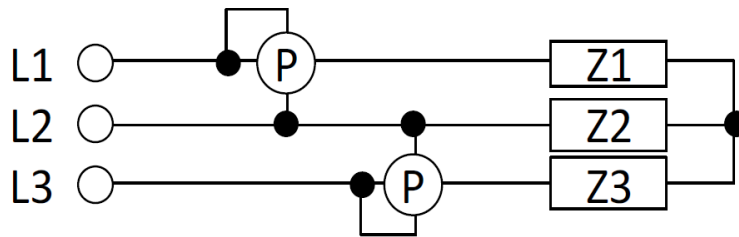


Figure 3.6: Compressor three-phase power measurement for the power supply. Originally illustrated by Mösch (2015).

The compressor voltage and current draw are only measured in the first phase of the three-phase power supplies. A model 3588-2 voltage transducer and model 4044-8 current transducer are used. The voltage transducer has a range of 0 to 600 V with an accuracy of  $\pm 0.25\%$  of reading. The current transducer has a range of 0 to 20 A and an accuracy of  $\pm 0.15\%$  of reading. Each transducer measuring compressor power draw, voltage, or current has an output of 0 to 1 mA, which is converted to a 1 to 5 VDC signal using a 5,000 ohm resistor.

Electric input into the secondary refrigerant tank electrical heaters is monitored with a Scientific Columbus model DL5C5A2 watt/watthour transducer. The transducer has a range of 0 to 18,000 W and an accuracy of  $\pm 0.09\%$ . The transducer outputs a 0 to 1 mA signal which is converted to a 1 to 5 VDC signal using a 5,000 ohm resistor.

Air velocity inside the compressor chamber is measured using a hot wire anemometer from Dwyer model 640-1. The meter has a range of 0 to 5.08 m/s and an accuracy of  $\pm 2\%$ . The meter outputs a signal of 4 to 20 mA which is converted to a 1 to 5 VDC signal using a 250 ohm resistor.

Figure 3.7 displays the circuitry of the calorimeter with the measuring devices.

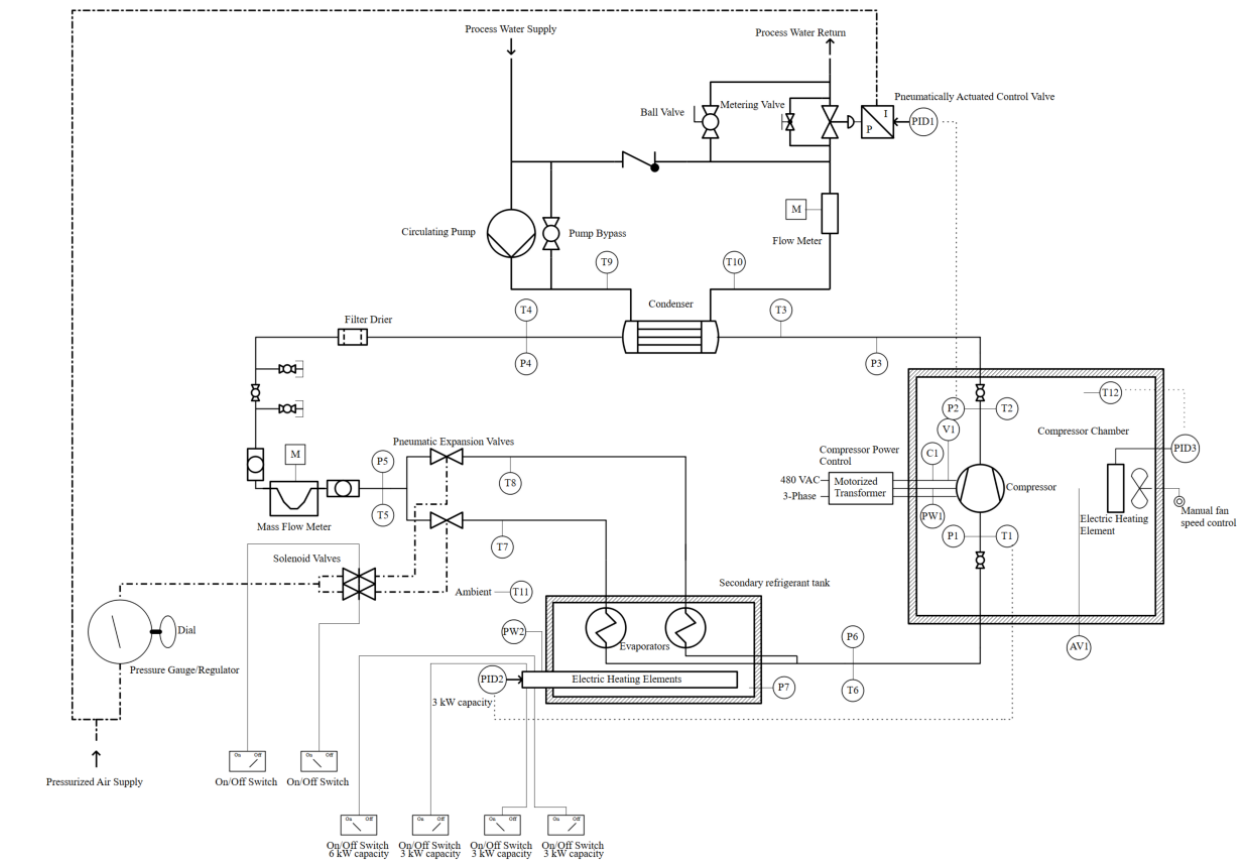


Figure 3.7: Tesco Calorimeter with instrumentation.

### 3.1.3 Modifications

Testing capabilities of the Tesco Compressor Calorimeter Test Stand were expanded to permit additional compressor evaluation. To determine pressure fluctuation at the discharge of a compressor, a high sampling rate capable pressure transducer was placed at the discharge port of

the compressor in the condensing line. To increase the capable testing range of operating conditions, the second PXV was replaced with an electronic expansion valve (EXV).

To determine the effectiveness of discharge pressure fluctuation dampening of currently available compressors in the market, a pressure transducer capable of being sampled at high frequencies was installed in the condensing line immediately after the compressor discharge port. A Kulite model XTEL-190 (M) series pressure transducer was selected due to its infinitesimal resolution and high accuracy. The pressure transducer is able to measure absolute pressure from 0 to 3447.38 kPa with an accuracy of  $\pm 0.1\%$  of full scale ( $\pm 3.447$  kPa). The pressure transducer was installed immediately after the compressor discharge port with 38 cm of straight pipe placed to reduce reflective feedback from downstream of the pressure transducer. Figure 3.8 displays the pressure transducer location in the calorimeter.

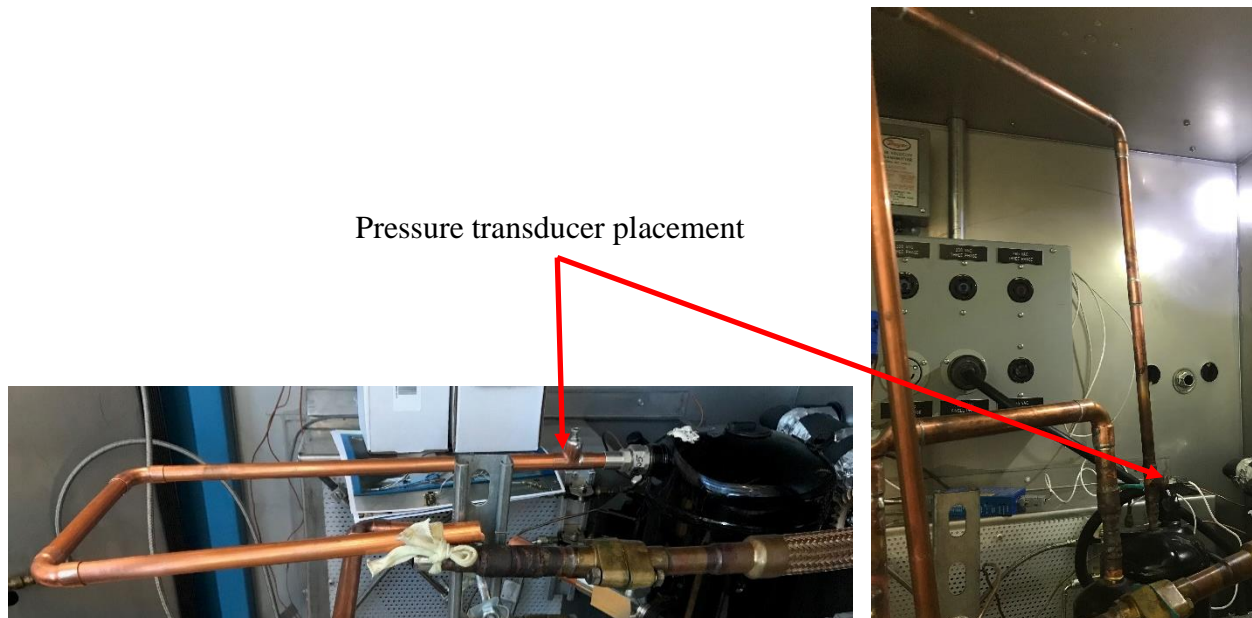


Figure 3.8: Location of pressure transducer in both the scroll (left) and dual rotary (right) compressors in the calorimeter.

The signal from the high sampling frequency pressure transducer must be conditioned via a signal conditioner due to its low maximum output voltage of 100 mV. The signal conditioner is a Kulite model KSC-1. The KSC-1 filters and amplifies the signal from the pressure transducer to a  $\pm 10$  VDC signal which can be read by the DAQ. The signal conditioner also supplies power to the pressure transducer, which it receives from a 12 VDC power source. Conditioning settings are featured as switches on the signal conditioner. The switches were adjusted so that there was a

pre-filter gain of 10, a low pass filter with a 5 kHz cutoff (lowest cutoff available without removing potential data), and post filter gain of 10. The gains were set so that the voltage signal would be within the reading range of the DAQ. Connections to the signal conditioner are in DB9 format, Figure 3.9 is a wiring diagram of the connections made between the high frequency pressure transducer and the DAQ.

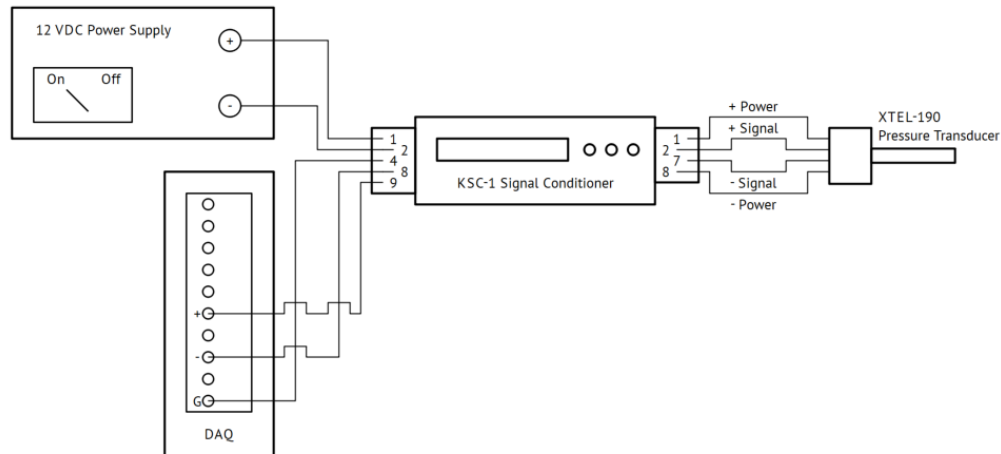


Figure 3.9: High frequency pressure transducer wiring configuration.

Unused pins at the signal conditioner DB9 connections remained unconnected. The high frequency pressure transducer was calibrated using the already in place (P2) calorimeter discharge pressure transducer. The calibration curve for the high frequency pressure transducer is listed in Equation (3.3).

$$p(U) = -335.91 * U + 56.496 \quad (3.3)$$

Where  $p$  is in kPa, and  $U$  is in volts.

The air supply to the two PXVs had a maximum pressure level of 680 kPa, which limited the evaporating pressure to 680 kPa. To increase the operating range of the calorimeter to accommodate higher pressure refrigerants in air conditioning conditions (like R410A), the second PXV was replaced with an EXV that uses a stepper motor to adjust the opening percentage of the expansion valve. The valve is produced by Danfoss, and Danfoss' CoolSelector2 software was used to size the valve to fit the evaporating capacity range of the calorimeter at the intended saturation temperatures. The valve is the model ETS 12.5, which is controlled and powered via a superheat controller model EKD 316. This valve and controller cannot be directly communicated with through LabVIEW, so an Arduino Uno is used to bridge

the gap. The Uno can communicate through a USB connection with LabVIEW and output a 1 to 5 voltage range. The EKD 316 controller can read this voltage, and when set to manual operation the controller adjusts the opening of the EXV. The controller is also supplied with 24 VDC from the calorimeter to power the EXV. Figure 3.10 shows the wiring of the EXV control.

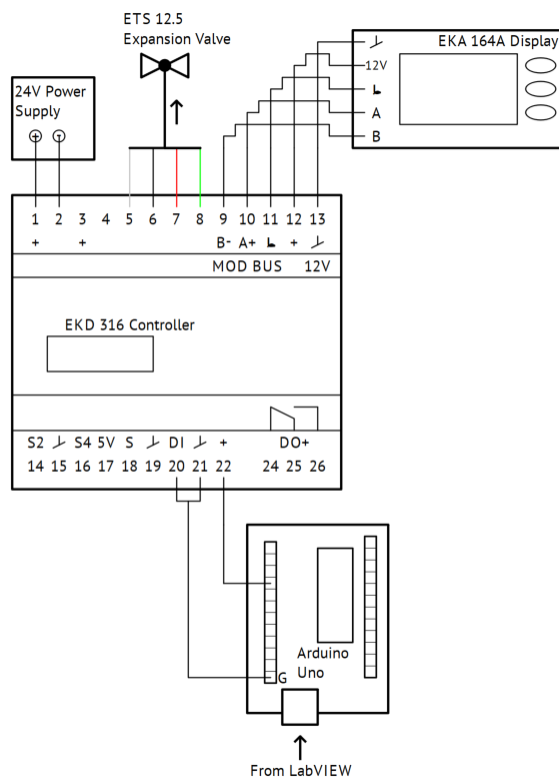


Figure 3.10: Control wiring diagram for the EXV in the calorimeter.

The EKA 164A display by Danfoss is used to send initial commands to the EKD 316 controller, such as initiating manual analog signal control. The display is also used to confirm the opening of the EXV, where the opening percentage signal to the EKA 164A display is from the EKD 316 controller and not the Uno. Figure 3.11 shows the EKA 164A display on the control panel of the calorimeter. The EKD controller operates such that the datum for opening percentage must be set each time the controller/valve is powered on. When using the EXV, a 0% opening signal must be sent to the controller from the Uno to set this datum. The controller will receive the 0% signal and close the valve until a certain resistance torque is experienced by the servo motor due to the inability of the valve to close further. When using the EXV, it is possible to operate on the entire range of evaporating pressures desired, limited only by other components of the calorimeter. Figure 3.12 displays the calorimeter wiring after modification.



Figure 3.11: Left side of the calorimeter control panel where the EKA 164A display for the EXV is boxed in red.

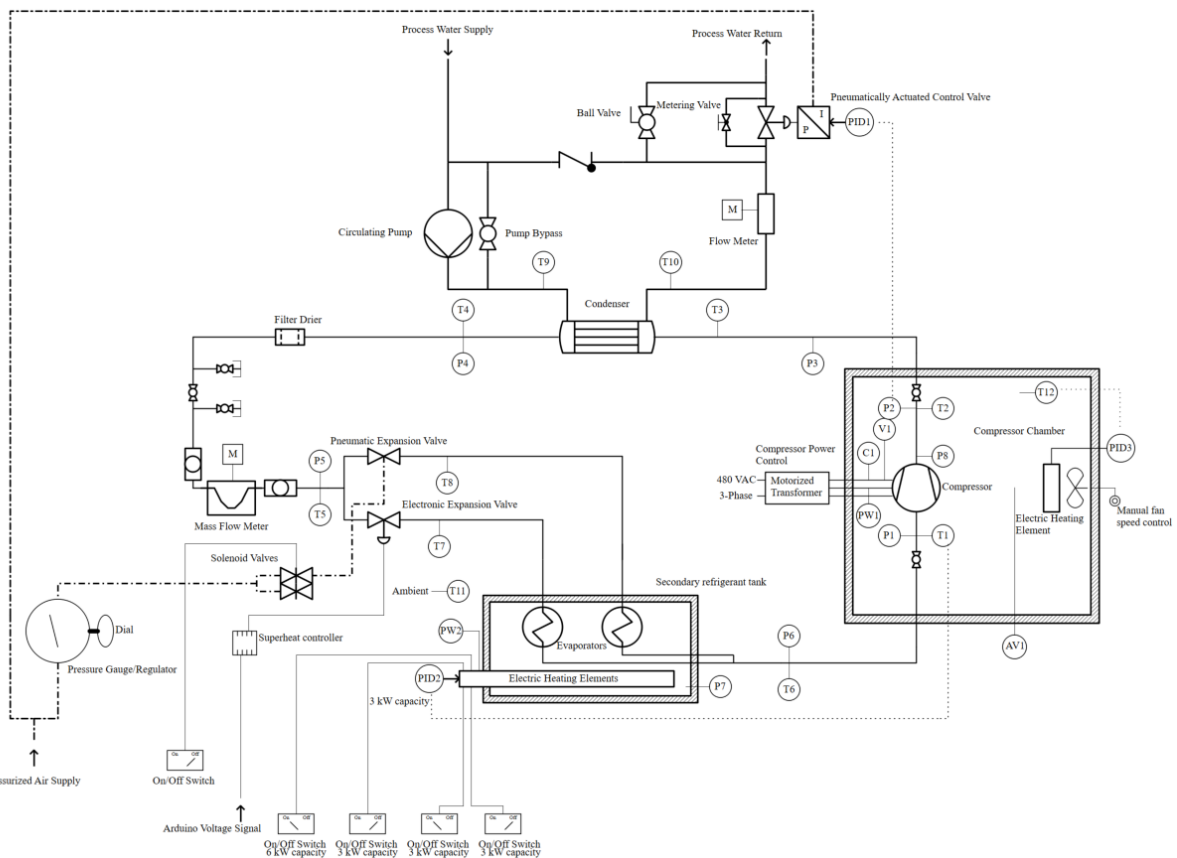


Figure 3.12: Tescor Calorimeter with modifications. Note the replacement of a PXV with an EXV, and the addition of P8 (High Frequency Pressure Transducer from Kulite).

### 3.1.4 Operation

The Tescor Calorimeter Test Stand is controlled mainly via inputs at the control panel, as seen in Figure 3.13.



Figure 3.13: Control Panel for the Tescor Compressor Calorimeter.

Power, process water supply, and pressurized air must first be sent to the calorimeter, and a target operating condition based on evaporating and condensing temperature, suction temperature, and compressor chamber temperature must be selected. Using the three PID controller inputs on the control panel; the setpoint condensing pressure, compressor chamber air temperature, and compressor suction temperature must be input. Using the pressure regulator dial on the side of the control panel or the electronic expansion valve (EXV) control VI, the compressor suction pressure must be set, this correspondingly establishes the evaporator temperature. Using the on/off buttons on the control panel; the condenser circulating water pump, compressor chamber fan, heater, and exhaust, TXV-1 (expansion valve), the sec. cal. heater, and the predetermined number of fixed evaporator heaters must be pushed to on (the button will light up). After all other components in the vapor-compression cycle have been

engaged, the compressor can be switched on using the UUT (Unit Under Test) Start button. It is at this time that the compressor will begin to operate, and a pressure/temperature difference can be observed on the Main VI used for data acquisition. The PID controllers cannot reach the predetermined operating conditions on their own however, and the user must manipulate heat input to the evaporators and the amount of replacement water in the condensing circulating water loop to reach the target conditions.

The pneumatically actuated control valve that limits new water intake into the condenser water loop can only adjust the pressure of the refrigerant in the condenser  $\pm 75$  psia, where the water loop would otherwise be able to realize a pressure range of 250 to 500 psia. The bypass ball and bypass metering valves around the control valve are used to bring the condensing pressure into the controllable range of the control valve. The valves are seen in Figure 3.14.

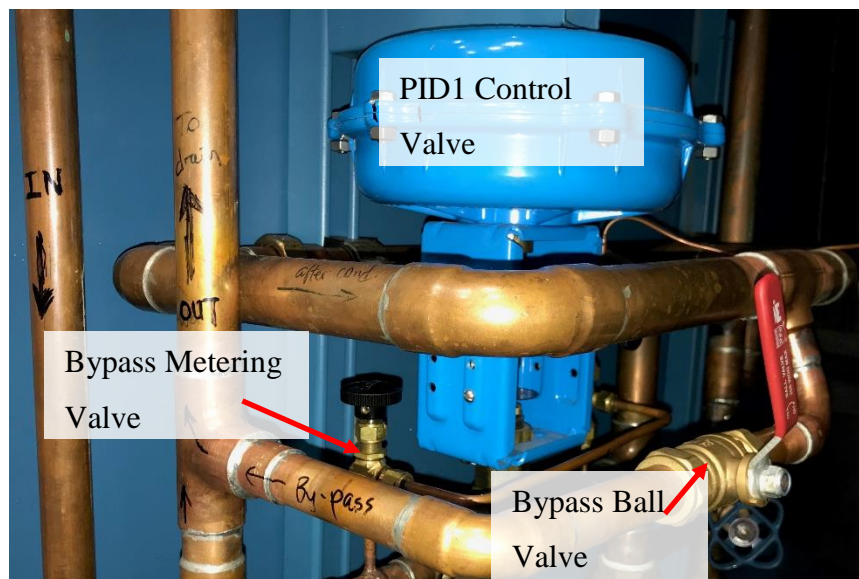


Figure 3.14: Process water control and bypass valves for the calorimeter.

The ball valve is oversized, and movement should be limited to between fully closed and 60% open, where closing the valve raises the condensing pressure and opening the bypass ball valve reduces the pressure. Opening beyond 60% does not reduce the condensing pressure further in normal operating conditions. The ball valve should be adjusted until the target pressure is within 140 kPa, where PID 1 is able to manipulate the control valve to reach the target pressure more exactly. In some cases, the PID controller is not able to reach the target pressure

as exactly as desired, and the metering bypass valve can be actuated to make up the difference. The metering valve has a manipulation range of about  $\pm 70$  kPa.

The electrical heat input also requires user interaction to achieve the desired suction temperature. PID 2 is only able to change the heat input to the evaporator by  $\pm 3$  kW, by engaging or disengaging the 3 kW electric heater. The other fixed heaters must be manually switched on or off via the on/off buttons on the control panel. The number of electric heaters that must be switched on depend on the target suction pressure and temperature. The lower the desired suction temperature, the fewer the amount of fixed heating is necessary. The amount of heat input by the fixed heaters is between 3 and 15 kW, where PID 2 is able to add 3 kW to have a maximum heat input of 18 kW. To achieve the desired suction temperature, the fixed heaters should be turned on or off until the fixed heat input is within 3 kW of necessary heat input, where PID 2 makes up the difference. When reaching steady-state conditions for target suction temperature, it is preferable to have the heat input to the evaporator remain constant, where PID 2 decides to leave the controlled 3 kW heater on or off to reach and maintain the target suction temperature. In most cases, the necessary heat input to the evaporator is not divisible by 3 kW however, and the limitations of PID 2 must be accounted for. The fixed heaters should be switched on or off such that PID 2 engages and disengages heat input to the evaporator in a constant oscillating fashion. In the Main VI, this oscillating pattern should be observable as a square wave in the evaporator capacity graph. For example, if the necessary heat input is 7.5 kW, two 3 kW fixed heaters or the one 6 kW fixed heater should be switched on by the user, and the 1.5 kW difference will be made up by the PID controller by alternatingly engaging and disengaging the 3 kW heater.

After the user adjusts the condensing water bypass valves and the number of engaged fixed heaters, the system should be allowed to reach steady-state (determined by the user). After the appropriate amount of steady-state data is recorded, the operating conditions can be changed to the next state point desired. The same procedure as listed above should be followed, starting with adjusting the setpoint on the PID controllers and adjusting the suction pressure via the air pressure regulator or EXV opening.

When using the EXV VI to reach the desired suction pressure, an iterative process must be used that is not necessary when using the air pressure regulator and the pneumatic expansion valve (TXV-1). The VI merely adjusts the opening percentage of the EXV. While approaching

steady-state from a different operating condition, the suction pressure may change even though the expansion valve opening does not change. This is due to potentially changing condensing pressure or heat input to the evaporator. While the air pressure regulator can account for these changes automatically by adjusting the opening of the pneumatic expansion valve, the user must account for these changes by adjusting the opening of the EXV via the VI. It is recommended that when using the EXV, the following procedure is followed and iterated upon:

1. Adjust condensing pressure to within 10 psia of target condensing pressure.
2. Adjust opening of EXV to establish suction pressure to within 5 psia of target suction pressure.
3. Adjust number of fixed heaters to reach target suction temperature.
4. Repeat Steps 1 to 3 while reducing the magnitude of changes in each iteration until target operating conditions are achieved.

### **3.1.5 Tescor Calorimeter and Compressor Limits**

The Tescor Compressor Calorimeter has operating limits that bound the maximum and minimum discharge (high side) and suction (low side) pressure. The high frequency pressure transducer on the high side has a maximum regular reading level of 3447 kPa, and the low side pressure transducers have maximum regular reading of 689 kPa (with over pressure readings capable to 1034 kPa). The maximum suction pressure is doubly constrained, as the evaporating temperature is capped by the temperature of the secondary two-phase refrigerant tank. The evaporating temperature is dependent on the heat transfer rates from the electrical heating elements to the secondary refrigerant and the secondary refrigerant to the evaporator (primary refrigerant) during transient change of operating conditions. The temperature of the secondary refrigerant will change until steady-state operation with equal heat transfer rates from electrical heating elements to the primary refrigerant is achieved. A maximum saturation temperature of 5 °C (933 kPa for R410A, 546 kPa for R407C) limits the evaporating pressure of the Tescor calorimeter. The minimum pressure level of the high side is constrained by the minimum condensing temperature, which is controlled by the circulating water loop. This minimum condensing temperature has been found to be close to 23° C (1585 kPa with R410A, 1000 kPa with R407C). Minimum pressure on the low side is dependent on the compressor being tested.

## 3.2 Data Acquisition and Software

Similar to the Small Hot-Gas Bypass Test Stand, most signals collected from sensing devices on the Tescor Compressor Calorimeter were recorded as voltages on an Agilent 34980A Multifunction Switch/Measure Unit. The software used for data acquisition is National Instruments' LabVIEW. LabVIEW is used to sample data at 1 Hz from specific channels on the Agilent 34980A, and convert the sampled data from a voltage signal to its respective unit for later data logging and display. There are 3 separate VI's used currently for data acquisition or control on calorimeter, the Main VI, the High Frequency Pressure Transducer VI, and the EXV VI.

### 3.2.1 Calorimeter Data Acquisition Software "Main VI"

The Main VI front panel has 3 tabs with different methods of displaying data for real time observation. The first is a piping and instrumentation diagram that shows the most recent value for each measurement taken, as well as the location (in diagram form) where the measurement was taken in the refrigeration or peripheral circuits. Figure 3.15 shows the piping and instrumentation section of the Main VI.

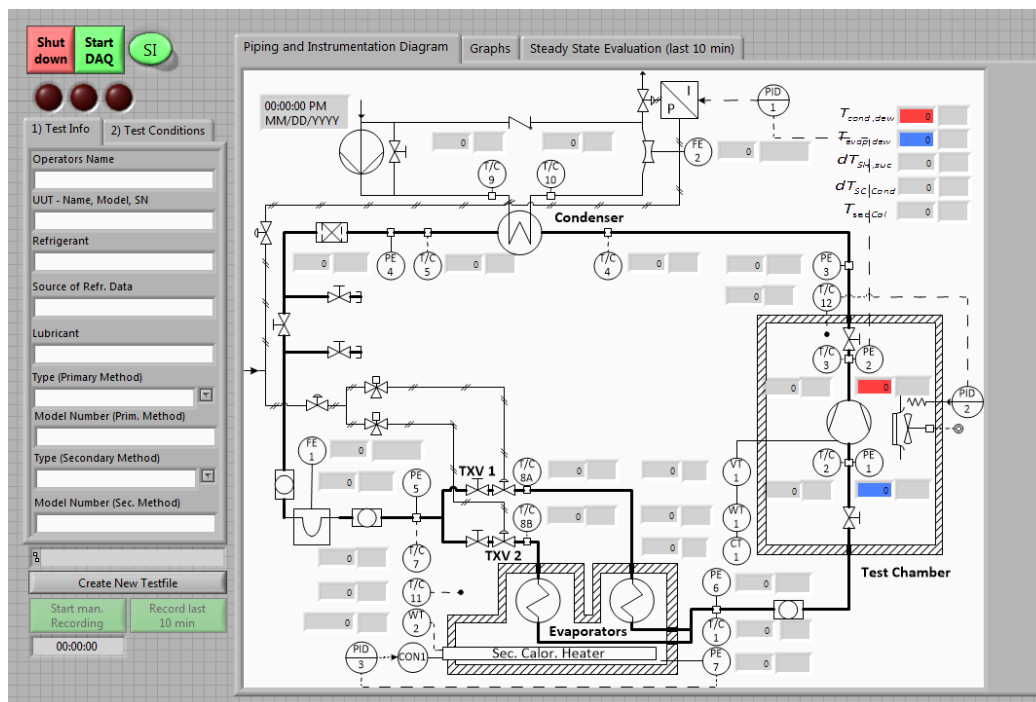


Figure 3.15: Piping and Instrumentation tab on the Main calorimeter VI.

Along with the most recent values of each data point displayed, the VI uses data from Refprop 9.1 (Lemmon, Huber, & McLinden, 2013) to display the condensing and evaporating temperatures, as well as the superheat at suction of the compressor and the subcooling at the outlet of the condenser when R407C is used as the working fluid through the compressor. Additionally, the VI uses Refprop data to determine the temperature of the two-phase R134a in the secondary refrigerant tank used for evaporation. This temperature can be used as a maximum evaporating temperature limit when determining future test plans. At each startup of the Main VI, the properties of R134a and R407C must be imported as text files.

The Graphs tab graphically plots the data being recorded within a 1-hour window. This tab is shown in Figure 3.16.

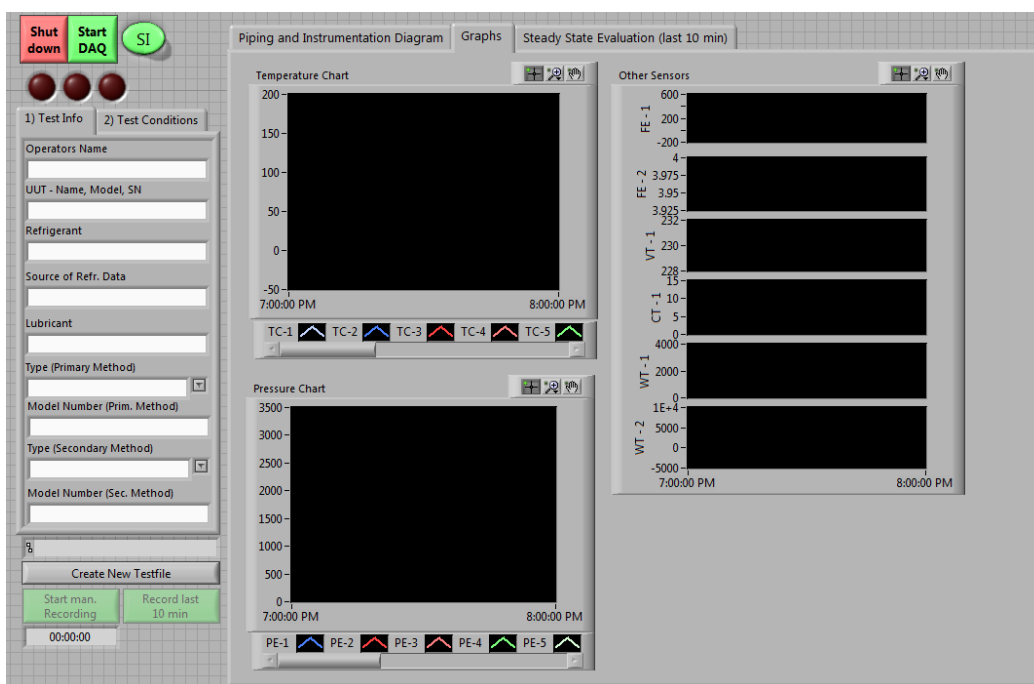


Figure 3.16: Graphs tab of the Main calorimeter VI.

The tab is split into 2 sections. On the left are two larger plots, one displaying all the temperatures and the other displaying all the pressures recorded in the refrigerant circuit. These two plots are used to identify the temperature and pressure lift across the compressor, as well as identify the magnitude of pressure and temperature differences of other sections of the refrigeration, like the difference between compressor discharge and the condenser. On the right side are smaller plots displaying from top to bottom; mass flow rate of the refrigerant, volumetric

flowrate of the condensing water loop, compressor voltage, compressor current, compressor power draw, and electric heating element power draw (total). These are used to describe compressor operation for the temperature and pressure differences seen across the compressor. All plots are set to display the last hour of operation while the DAQ was run.

The last tab on the main VI is used to determine when the unit has operated at steady-state for at least 10 minutes. The Steady-State Evaluation tab is shown in Figure 3.17.

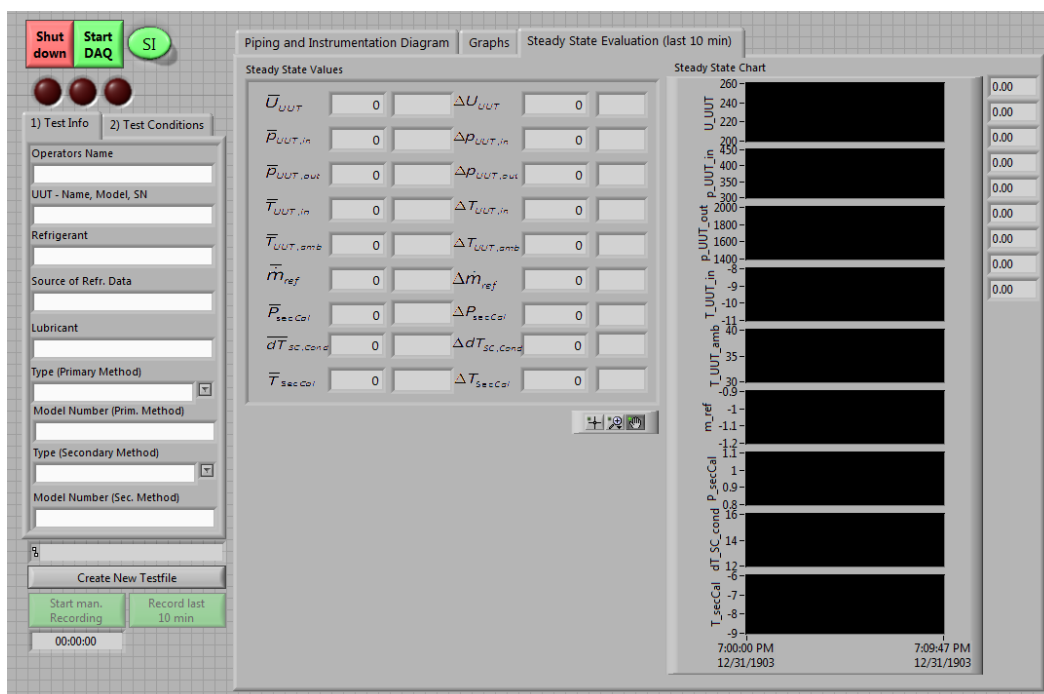


Figure 3.17: Steady State Evaluation tab of the Main calorimeter VI.

This Steady-State Evaluation tab is also split in to a left portion and a right portion. On the left side the average value of certain property is calculated, such as mass flow rate, and the largest deviation from the average is calculated and shown as a percentage for all non-temperature values and as a temperature difference for temperature measurements. As part of steady-state evaluation, the VI has a buffer of 600 previous data points, where those data points are displayed on the graphs on the right. Every time a new data point is collected, the oldest data point in this buffer is deleted. These graphs have a 10-minute window and are used to visually identify steady-state operation or to determine the pattern or behavior that is preventing steady-state operation. There are different labels for each data point displayed on the steady-state plots. Table 3.2 shows the different labels for each parameter collected.

Table 3.2: Descriptions for each data label on the steady-state evaluation page of the Main calorimeter VI.

<b>Data Label</b>	<b>Parameter</b>
$T_{UUT,amb}$	Compressor chamber temperature
$T_{UUT,in}$	Compressor suction temperature
$U_{UUT}$	Compressor voltage
$p_{UUT,in}$	Compressor suction pressure
$p_{UUT,out}$	Compressor discharge pressure
$\dot{m}_{ref}$	Refrigerant mass flow rate
$P_{secCal}$	Electrical heater power draw
$T_{secCal}$	Saturation temperature of the R134a tank

Note that the Main VI itself is split into two portions as well. On the left side of the VI are inputs to be entered by the user, and on the right side is the display tabs of data being recorded. The left side of the VI also maintains control over the VI. The VI can be run without sampling data, where the start DAQ button at the top must be pressed to begin sampling data from the Agilent DAQ. Also at the top left are the shut-down button (to be pressed after DAQ is stopped and testing is complete), and the units button to exchange between SI and English units. At the bottom left, there are controls used for data logging into text files. The “Create New Testfile” button will create a .txt document in the computer folder of the user’s choice. After a new file is created the “Start man. Recording” or “Record Last 10 min.” buttons can be used to log data. Manual recording will record indefinitely and in real time. This button should be used for non-steady-state testing. Recording the last 10 minutes is used for steady-state testing. When the “Record Last 10 min” button is pressed, the VI will log the previous 10 minutes of data. Note that these two data logging buttons should not be used in tandem on the same txt file. If the manual recording button is pressed, and then the record last 10 minutes button is pressed, the last ten minutes of data will write over the oldest 10 minutes of data from the manual record button. Additionally, if the manual record button is still pressed when the last 10 minutes buttons is pressed, manually recorded data will begin to overwrite data at the top of the file, leaving this data incoherent.

The Main VI outputs a .txt file of the data collected whenever data recording buttons are pushed. Figure 3.18 shows the format of the output text file.



Figure 3.18: Data output from the Main VI on the calorimeter.

The data from the text file is then copied into an excel file to be divided into columns and average the data. The averaged data is then processed to determine compressor performance.

### 3.2.2 High Frequency Pressure Transducer VI

As discussed in the modifications section, a high sampling speed pressure transducer was placed at the discharge port of the compressor. The sampling rate intended for this pressure transducer is 1000 Hz, which is significantly faster than the 1 Hz sampling rate of the Main VI. The Agilent DAQ is unable to sample at 1000 Hz, so a separate DAQ method was required for the added pressure transducer. A cDAQ-9171 was used for communication with the PC, and a NI 9201 analog input module was used to read the voltage signal output from the pressure transducer. Both items were manufactured by National Instruments. The NI 9201 reads voltages from -10 to 10 Volts and is able to sample at 500 kHz, which is well beyond the desired sampling rate as well as the data logging capability of the computer. A separate VI was also used to sample data from the high frequency pressure transducer. Figure 3.19 displays the front panel of the high frequency pressure transducer VI.

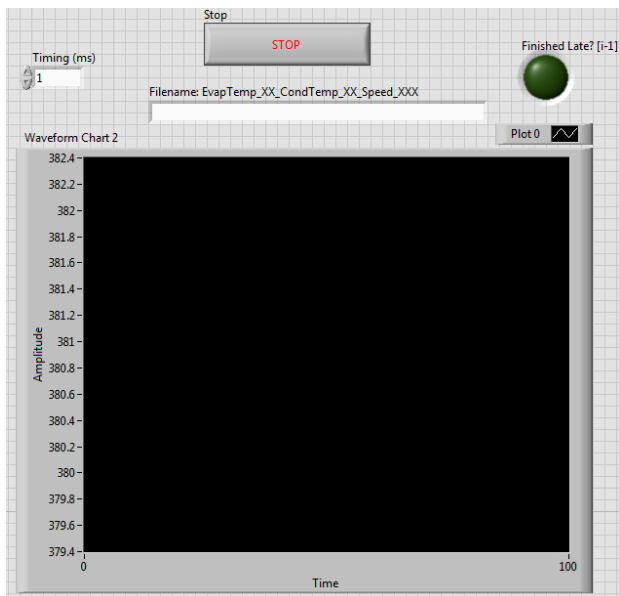


Figure 3.19: High Frequency Pressure Transducer VI. Note the Y-axis “Amplitude” is pressure in psia.

For pressure fluctuation sampling, the pressure transducer samples once every millisecond (1000 Hz), but the timing input can be manipulated for other testing purposes via the timing input at the top left. When the VI is run, data begins to be logged to a txt file named by the user much like the main VI. The data will continue to be logged onto the txt file until the user stops the VI with the STOP button. The graph displays pressure recorded by the pressure transducer in a 100-sample window. This allows the user to observe real time pressure fluctuation. In the top right an indicator is used to determine whether a sampling loop was completed late, which would vary the data sampling rate of the pressure transducer. While the VI was kept as simple as possible to reduce computation power, the computer would occasionally be unable to sample inside the 1 ms allotted sampling rate, triggering the indicator. In the event of a loop delay, the data is unusable due to the varied resolution and a new data set must be collected.

Data collection is similar to that of the Main VI, where a text file is formatted to be an excel file, and then processed in that format. Figure 3.20 shows the data file for the High Frequency Pressure Transducer VI.

Data recorded from the High Frequency Pressure Transducer VI is processed in MATLAB to determine pressure fluctuation.

Date	1/23/2019	Testing information	
Time	10:33 AM		
Operator Name	Cai Rohleder		
Label	Discharge Pressure	Relative Time	Data label/Units
Units	[psi]	[ms]	
10:33:09 AM	379.19683	1	
10:33:09 AM	379.44726	2	
10:33:09 AM	379.19683	3	
10:33:09 AM	380.448978	4	
10:33:09 AM	380.699407	5	
10:33:09 AM	381.200266	6	
10:33:09 AM	380.699407	7	
10:33:09 AM	380.448978	8	
10:33:09 AM	379.44726	9	
10:33:09 AM	379.697689	10	
10:33:09 AM	379.697689	11	

Figure 3.20: High Frequency Pressure Transducer VI data output.

### 3.2.3 EXV Control VI

After replacement of one of the second PXVs with an EXV, a control VI was used to manipulate the opening of the EXV for evaporating pressure control. EXV control was established via a superheat controller by Danfoss, type EKD 316, and an Arduino Uno by Arduino. The Uno was used to communicate with LabVIEW on the PC via a USB connection and the EKD 316, and the EKD 316 maintained control over the EXV. Figure 3.10 in section 3.1.3 shows a connection diagram of the EXV control. To control the opening of the EXV, the user inputs the desired EXV opening into the EXV Control VI, and the control VI sends a serial command to the Uno via the USB connection. The Uno processes the serial command and calculates a constant voltage output between 1 and 5 Volts DC, where 0% open is 1 VDC and 100% open is 5 VDC. The voltage output is sent to the EKD 316, which interprets this voltage and manipulates the EXV motor to adjust the opening of the EXV to the desired percentage. The opening of the EXV can be confirmed via the EKD controller display on the Tesco Compressor Calorimeter Control Panel seen in Figure 3.11 in section 3.1.3. Figure 3.21 shows the front panel of the EXV Control VI used to communicate with the Uno.

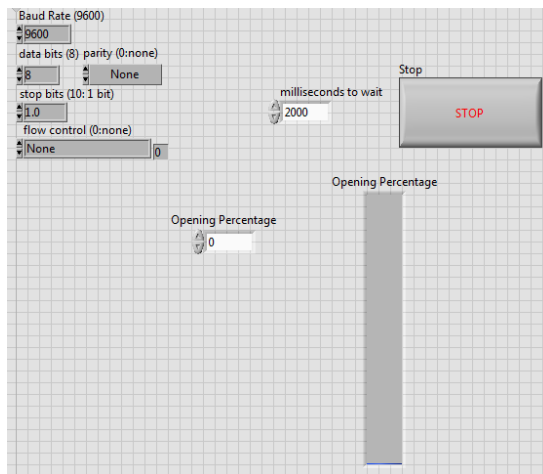


Figure 3.21: EXV Control VI for the calorimeter EXV.

In the top are serial communication inputs used to adjust the serial output to the Uno, which should remain unchanged. “milliseconds to wait” is an input to determine the cycle speed of the loop that sends a serial output to the Uno. As the Uno has relatively low processing power and can only adjust its own output so quickly, the timing should be set to 2000 milliseconds or slower. The VI constantly sends a serial command to the Uno when the VI is run. Due to the zeroing process of the EXV, the EXV opening should always start at 0 when the VI is run. The “Opening Percentage” input can then be adjusted from 0 to the desired opening percentage of the EXV after the VI is run. When testing using the EXV is complete, the user must set the EXV opening back to 0 before the VI is stopped with the STOP button.

### 3.3 Tests Performed and Results

#### 3.3.1 Copeland Scroll Compressor

A commercially available 5 ton (17.58 kW) scroll compressor from Copeland model ZF13KVE-TF5-261 was first tested in the calorimeter. While the compressor has vapor injection capability, the vapor injection port was kept closed to ensure a more standard compression process. A vapor injection compressor was selected for testing due to the possible pressure dampening modifications planned in later stages of a company sponsored project. The scroll compressor has a displacement rate of  $0.003913889 \text{ m}^3/\text{s}$  at 60 Hz shaft rotation, utilizes R407C as a working fluid, and POE oil for lubrication. Tests performed on this compressor targeted

varying pressure ratios at varying evaporating temperatures. Figure 3.22 displays the tests successfully completed with the scroll compressor.

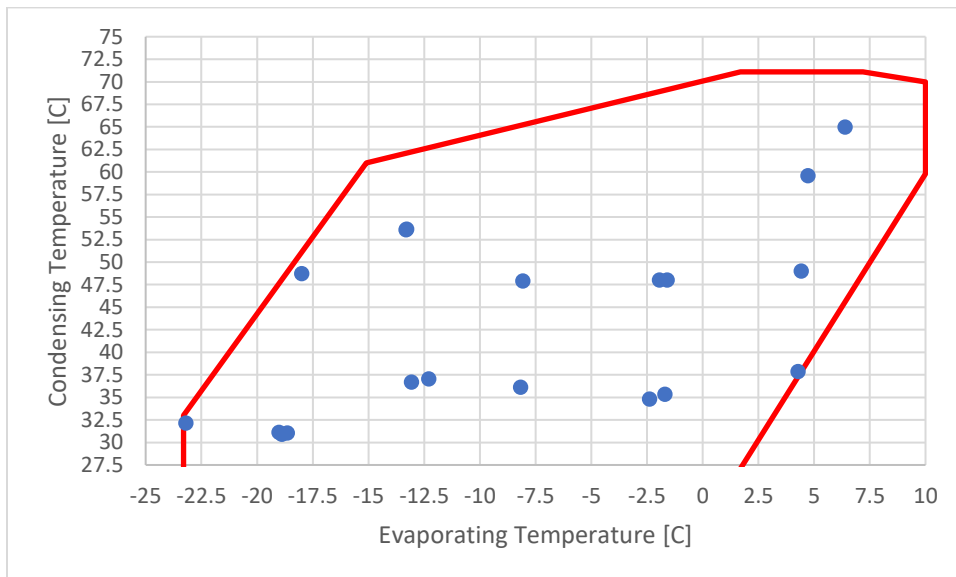


Figure 3.22: Operating points tested on the Copeland scroll compressor. Red lines indicate the operating boundaries of the compressor when installed in the calorimeter (Mösch, 2015).

A total of 19 tests successfully achieved steady-state. Performance of the scroll compressor is outlined in Figure 3.23, Figure 3.24, Figure 3.25, Figure 3.26, Figure 3.27, Figure 3.28, and Figure 3.29.

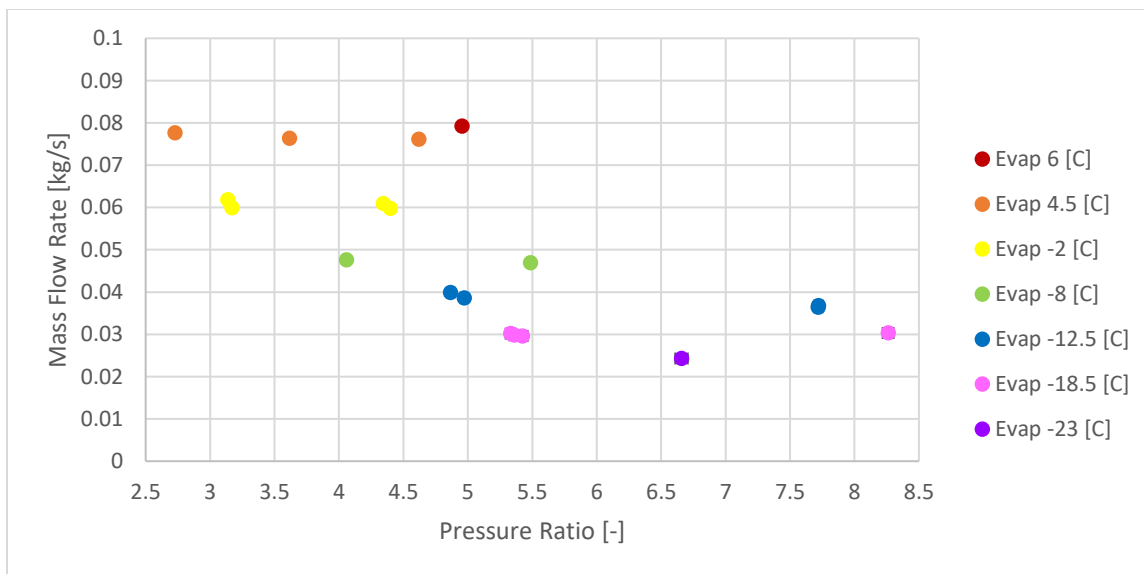


Figure 3.23: Mass flow rate with varying pressure ratio of the Copeland scroll compressor.

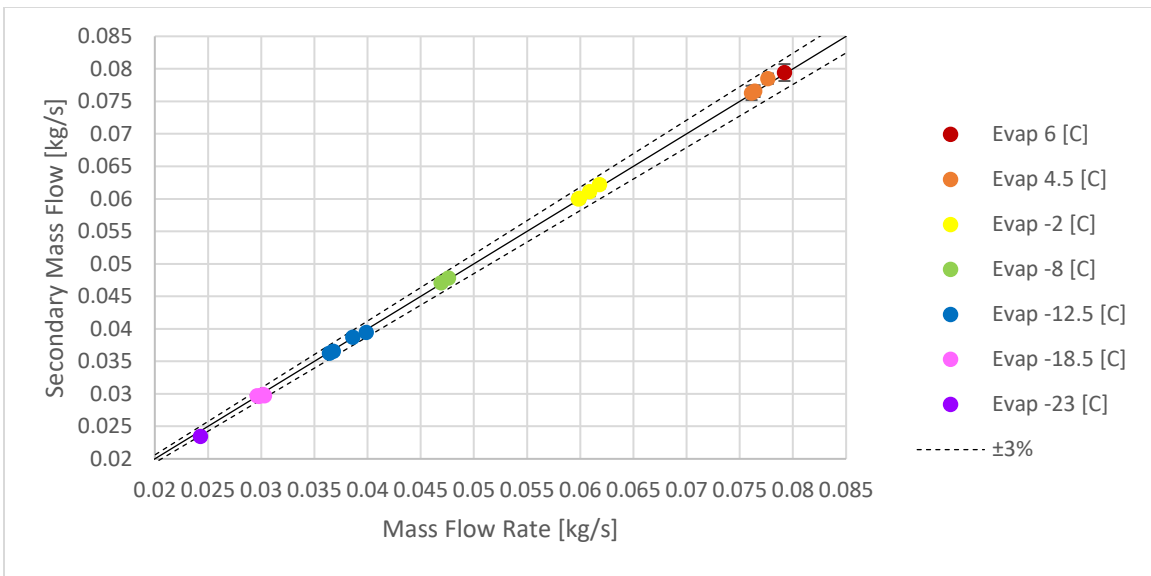


Figure 3.24: Mass flow corroboration between primary and secondary calculation methods for the Copeland scroll compressor.

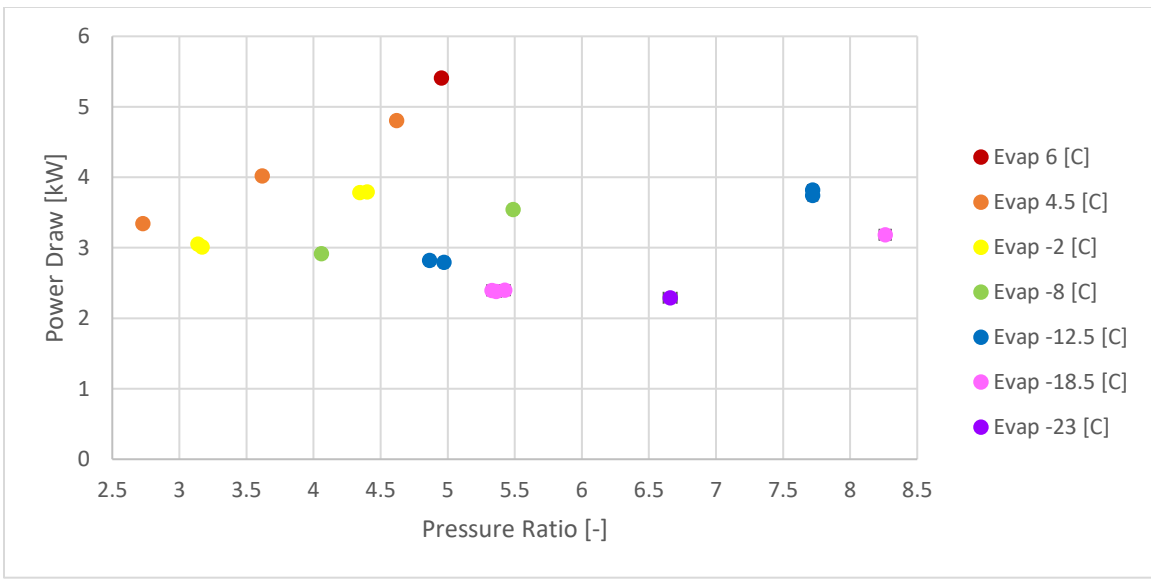


Figure 3.25: Power draw with varying pressure ratio of the Copeland scroll compressor.

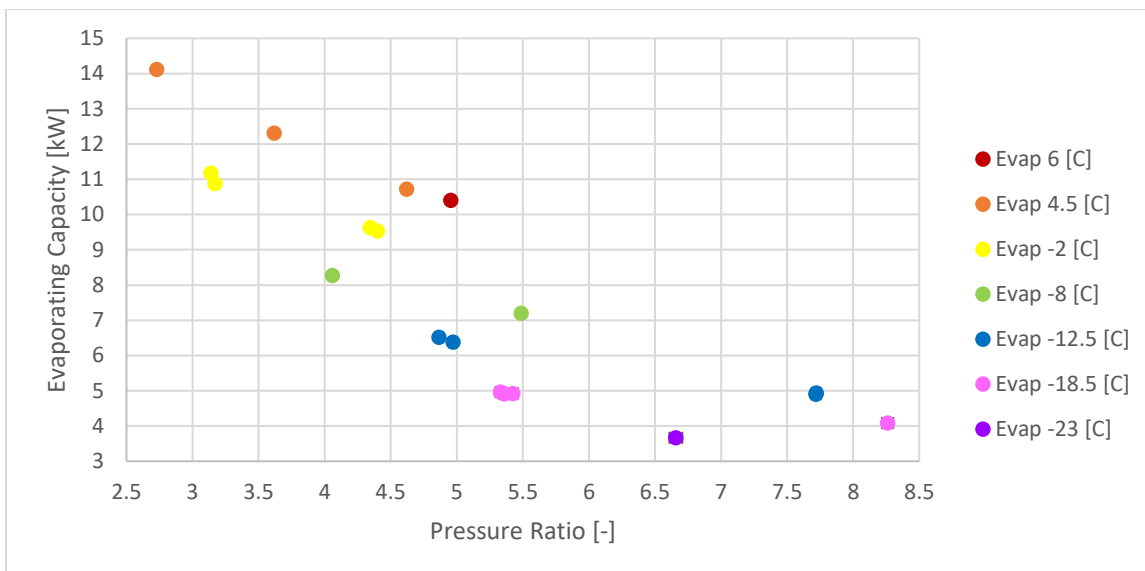


Figure 3.26: Evaporating capacity with varying pressure ratio of the Copeland scroll compressor.

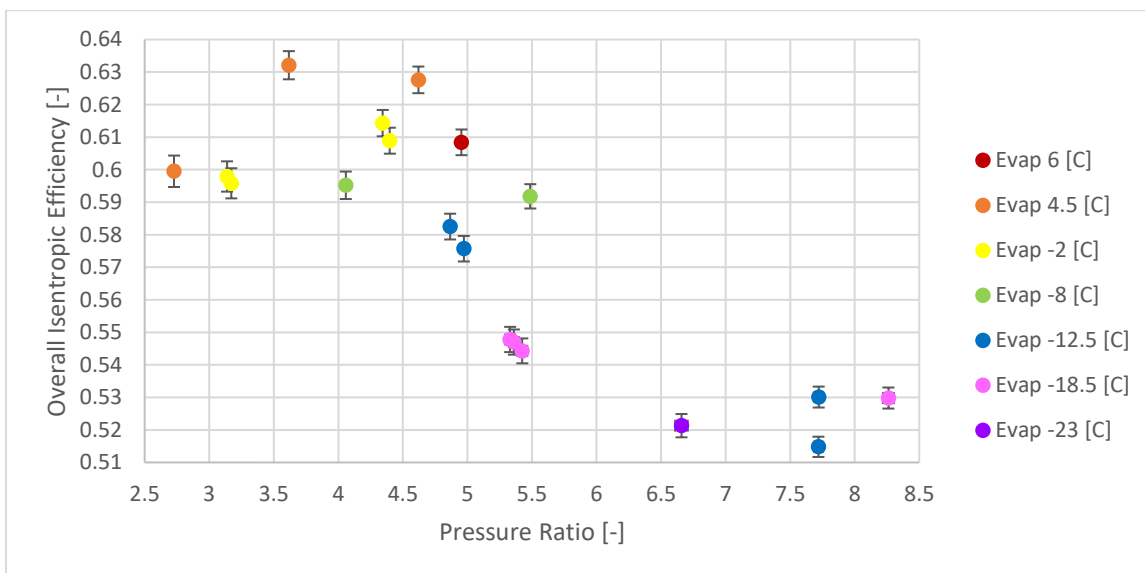


Figure 3.27: Overall isentropic compressor efficiency with varying pressure ratio of the Copeland scroll compressor.

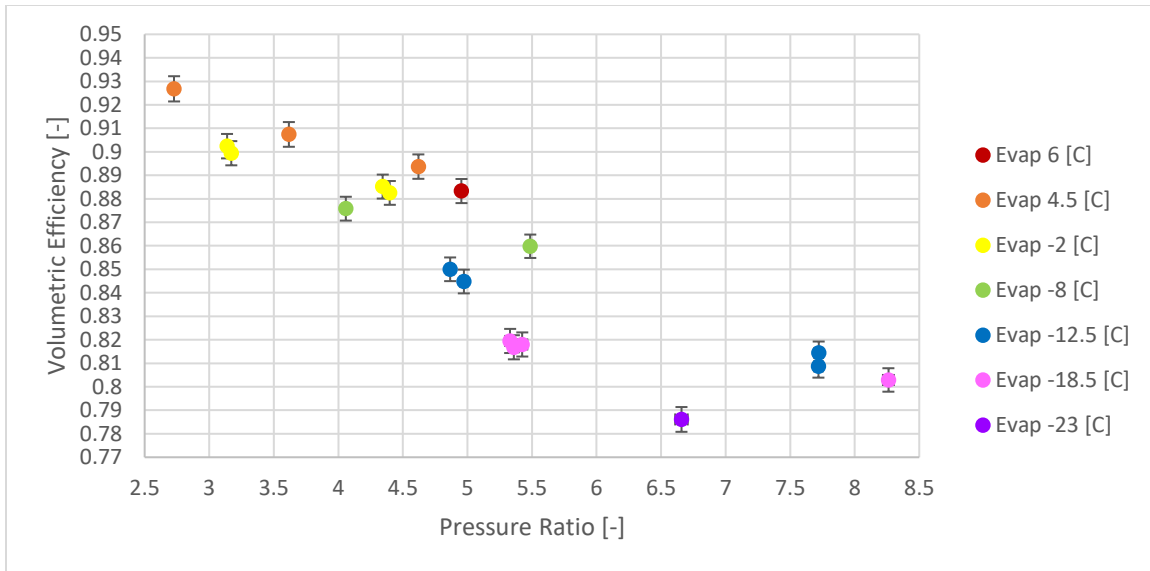


Figure 3.28: Volumetric efficiency with varying pressure ratio of the Copeland scroll compressor.

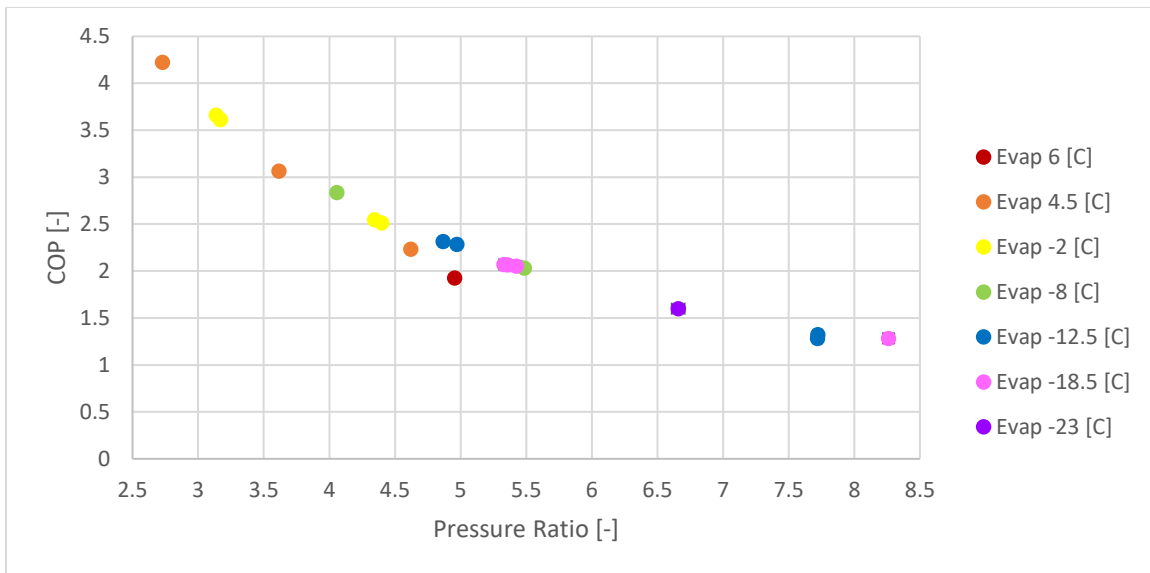


Figure 3.29: Coefficient of performance with varying pressure ratio of the Copeland scroll compressor.

The scroll compressor maintains equitable performance to other scroll compressors used in domestic heat pumps. As the pressure ratio increases, the overall isentropic efficiency decreases from a range of 60 to 65% to close to 50%, whereas the volumetric efficiency linearly

decreases from 93 to 72%. These higher pressure ratios are not commonly seen in the residential air conditioning application but could be seen in residential heat pumping applications.

Pressure fluctuation was measured/calculated for each operating point shown in Figure 3.22. The range of tests lead to pressure fluctuation measurements in cases of over-compression, under-compression, and compression at the ideal pressure ratio. The ideal pressure ratio for the Copeland scroll was determined via the pressure ratio with the highest overall isentropic efficiency, which is determined to be close to 4. Figure 3.30, Figure 3.31 and Figure 3.32 display pressure fluctuation at each case.

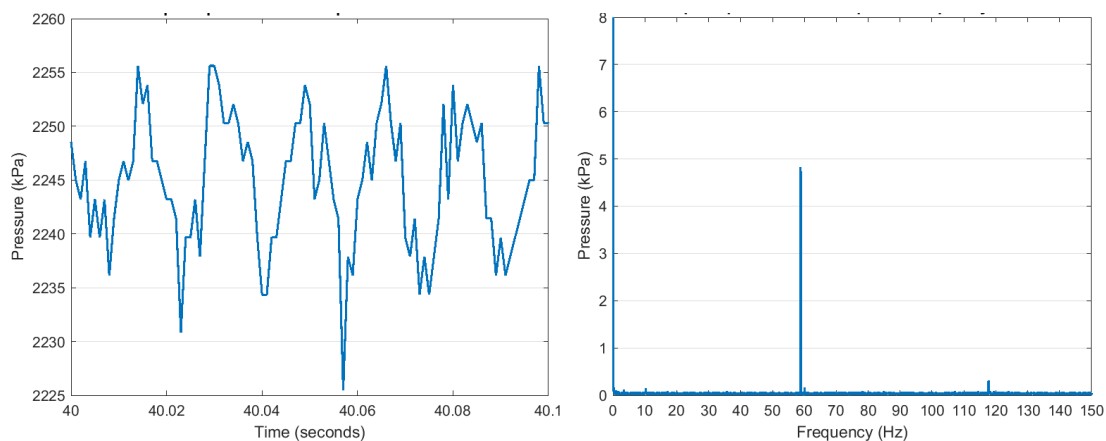


Figure 3.30: Time (left) and frequency (right) domain of the scroll compressor discharge at an evaporating temperature of  $-13.3\text{ C}$  and condensing temperature of  $54.7\text{ C}$  (pressure ratio of 7.7). This is a case of under-compression.

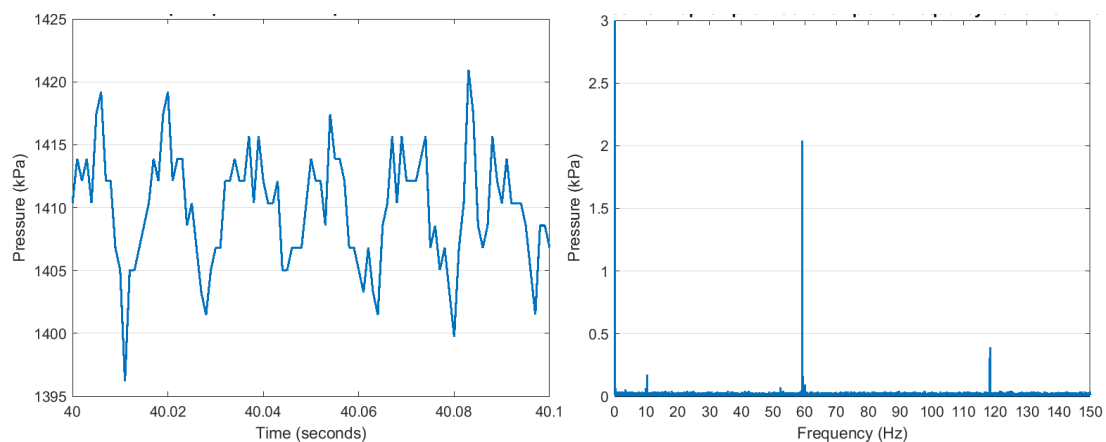


Figure 3.31: Time (left) and frequency (right) domain of the scroll compressor discharge at an evaporating temperature of  $-8.1\text{ C}$  and condensing temperature of  $36.1\text{ C}$  (pressure ratio of 4.1). This case operates near the ideal pressure ratio of the compressor.

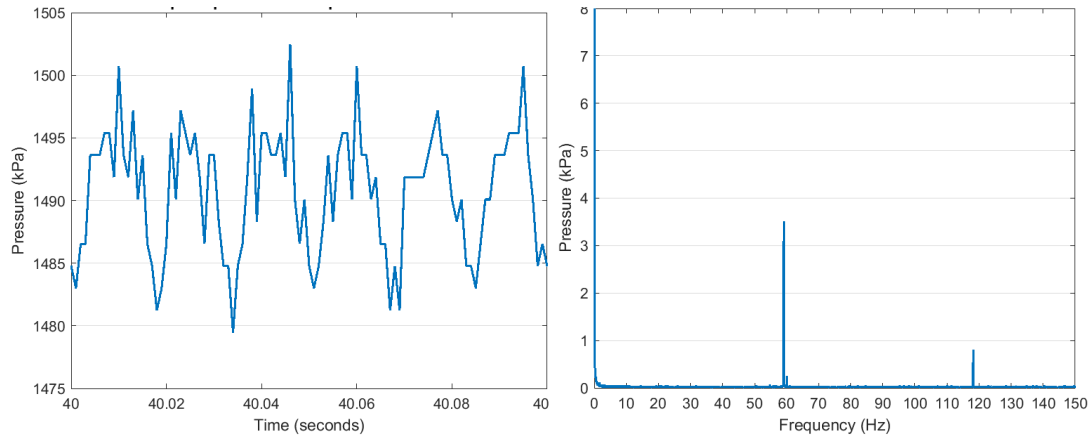


Figure 3.32: Time (left) and frequency (right) domain of the scroll compressor discharge at an evaporating temperature of 4.3 C and condensing temperature of 37.9 C (pressure ratio of 2.7). This is a case of over-compression.

Due to the 60 Hz discharge rate of the Copeland scroll compressor, the DAQ was able to sample just over 16 points per discharge. Fluctuation can be clearly seen in the time domain of each figure, and the isolation of fluctuation magnitude to the collective sine waves at each frequency is seen in the frequency domain of each figure. The figures show the expected trend of the highest pressure fluctuation corresponding with the discharge frequency of the compressor at 60 Hz. In all operating conditions, the highest pressure fluctuation was seen at the 60 Hz discharge rate. While the three cases selected for Figure 3.30, Figure 3.31, and Figure 3.32 reflect the anticipated pattern of pressure fluctuation maximized in under-compression, minimized in ideal pressure ratios, and in between for over-compression cases, when the results are aggregated for all tests, pressure fluctuation has no clear correlation with pressure ratio.

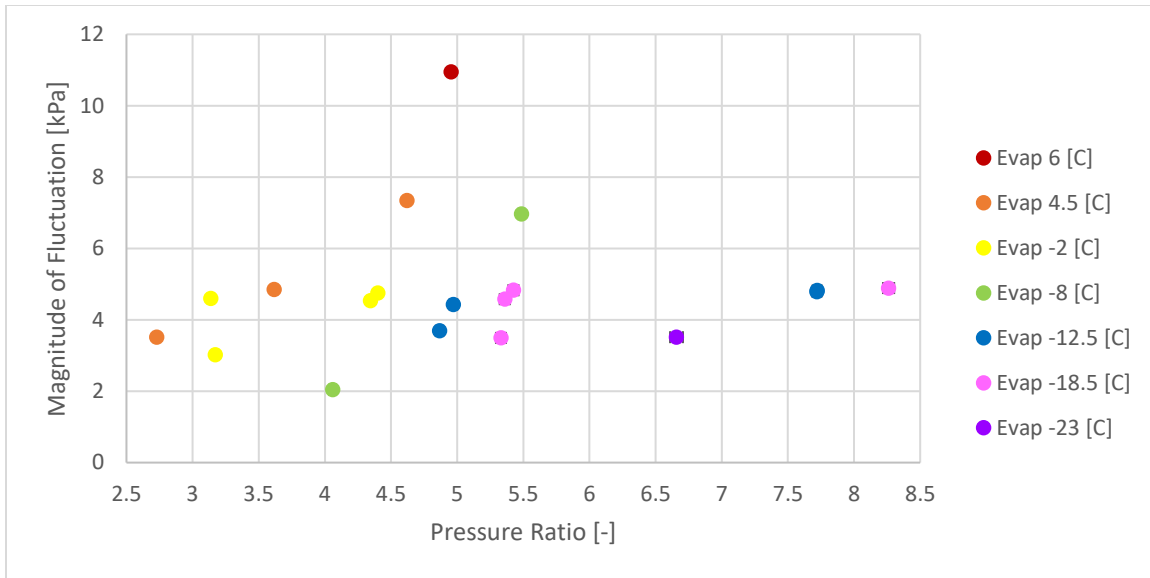


Figure 3.33: Pressure fluctuation with varying pressure ratio of the Copeland scroll compressor.

Pressure fluctuation remains fairly constant at approximately 4 kPa across all pressure ratios aside from the highest evaporating pressure ratio reaching close to 12 kPa. The compressor has a discharge valve and a check valve to reduce the possibility of back flow, and before the refrigerant is sent out of the discharge port, it passes through a discharge plenum. It is possible that these internal dampening efforts by the manufacturer limits the pressure fluctuation at discharge to 4 kPa or lower regardless of pressure ratio.

### 3.3.2 Highly Dual Rotary Compressor

A commercially available 4 ton (14.07 kW) dual rotary compressor from Highly model AUH410R-C9EU was also tested to investigate performance and pressure fluctuation at discharge. This compressor has two discharge chambers of equal size that rotate 180° out of phase of one other. The dual rotary compressor has a displacement of  $0.0000408 \text{ m}^3/\text{s}$  at 60 Hz shaft rotation speed and utilizes R410A as a working fluid and POE oil for lubrication. Similar to the Copeland scroll compressor, tests on the dual rotary compressor targeted a variety of pressure ratios at varying evaporating temperatures. Due to this compressor's inclusion in other projects it was tested more extensively than the Copeland scroll compressor.

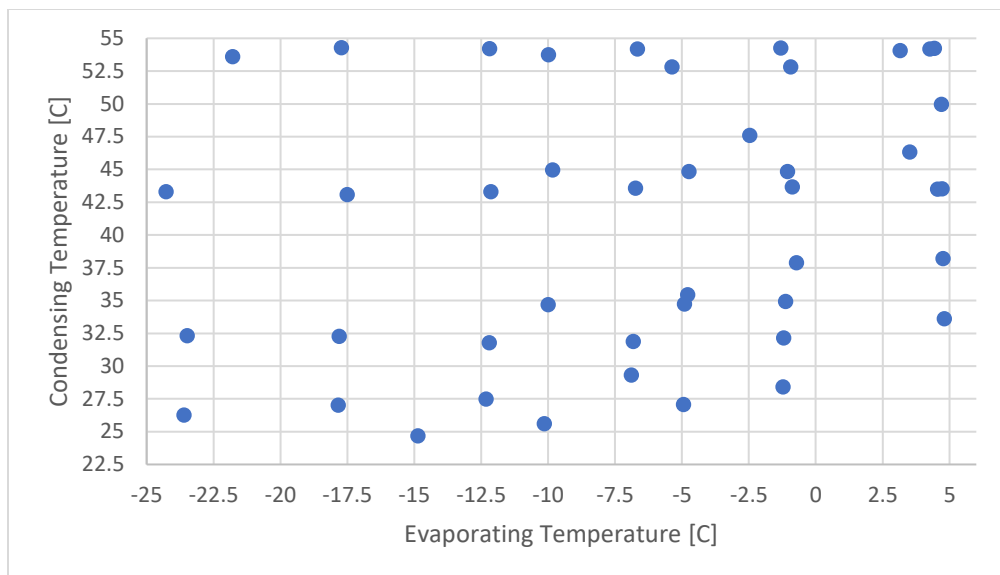


Figure 3.34: Operating points tested on the dual rotary compressor.

A total of 44 tests were successfully achieved on the dual rotary compressor, where operating conditions were bounded by the compressor calorimeter. Note that the bounds of the operating range were adjusted due to the change in refrigerant from R407C in the scroll compressor to R410A in the dual rotary. This refrigerant change reduced the maximum condensing temperature from 65 °C to 55 °C. Figure 3.35, Figure 3.36, Figure 3.37, Figure 3.38, Figure 3.39, Figure 3.40, and Figure 3.41 detail the dual rotary compressor performance.

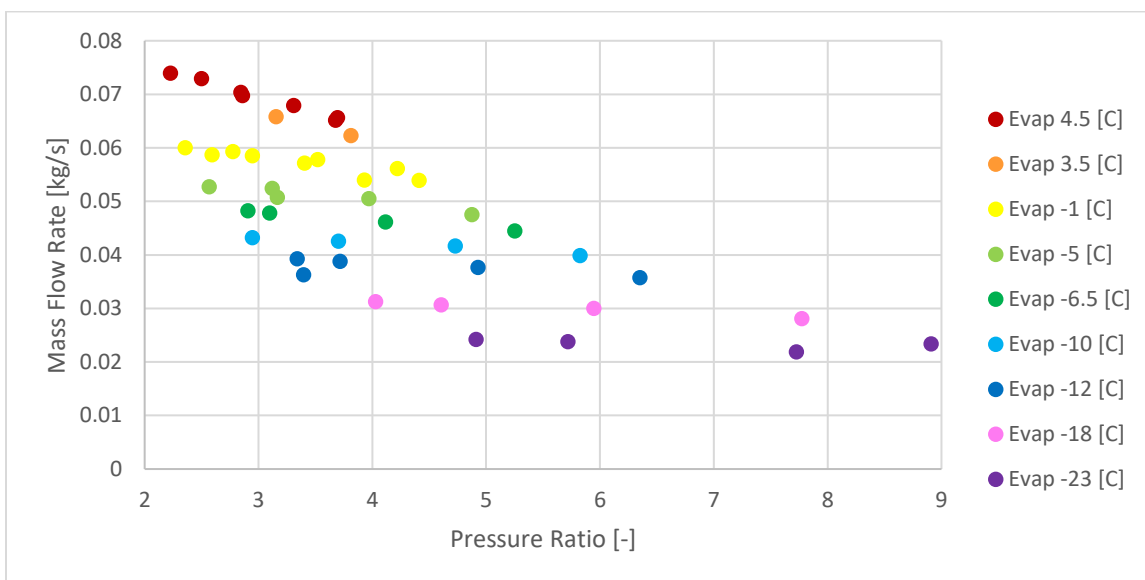


Figure 3.35: Mass flow rate with varying pressure ratio of the dual rotary compressor.

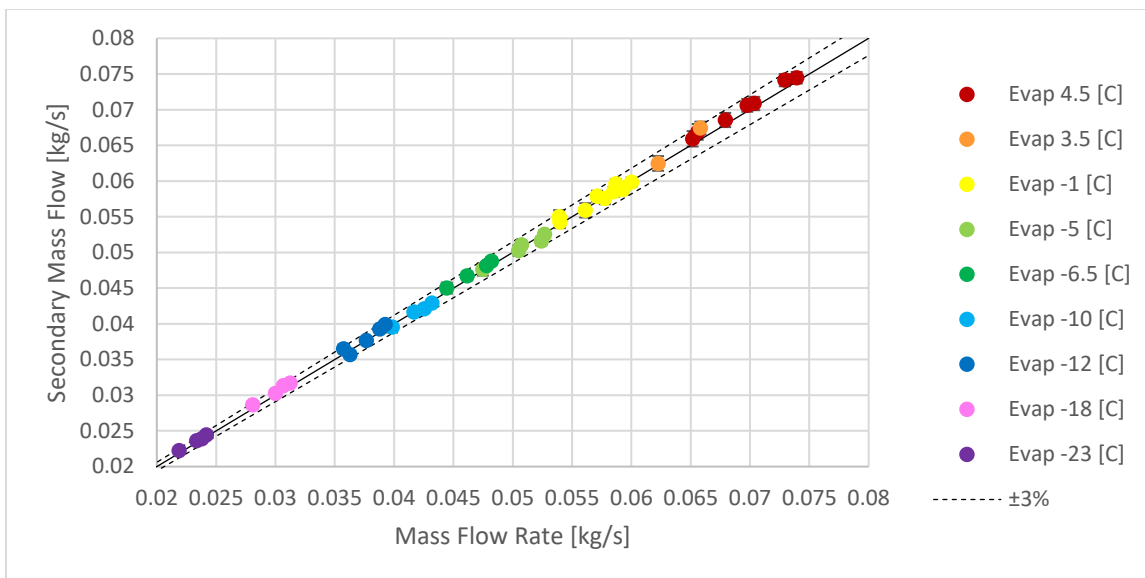


Figure 3.36: Mass flow rate deviation between the primary mass flow measurement and the secondary mass flow calculation.

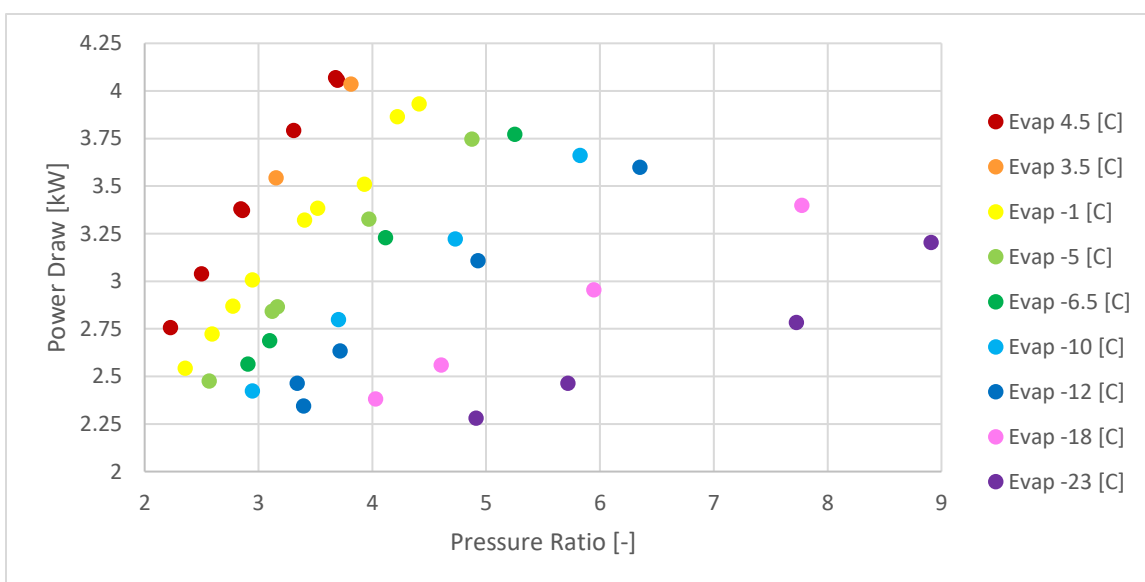


Figure 3.37: Power draw with varying pressure ratio of the dual rotary compressor.

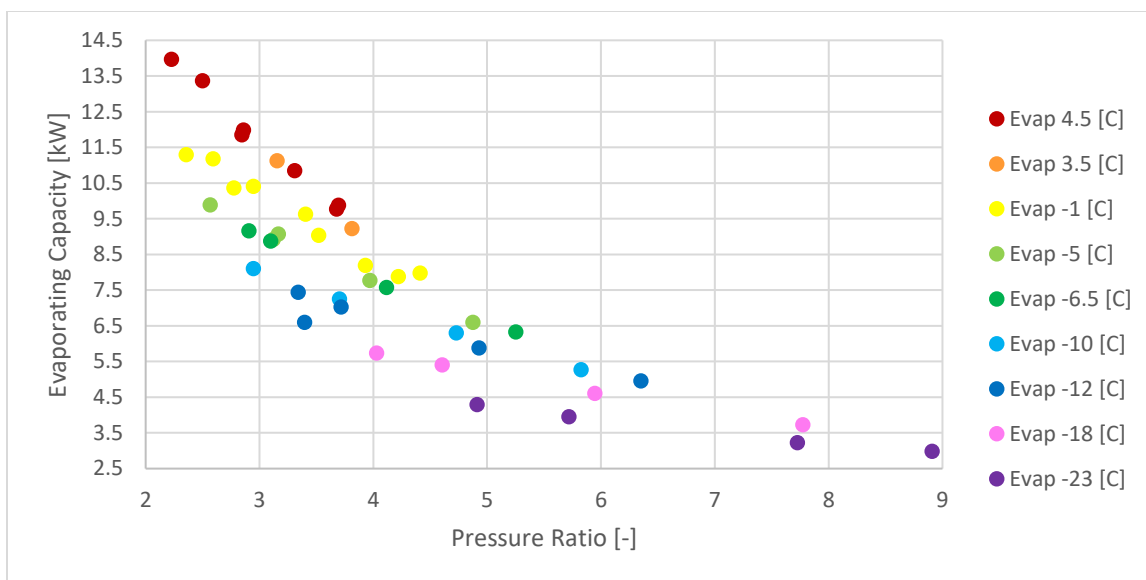


Figure 3.38: Evaporating capacity with varying pressure ratio of the dual rotary compressor.

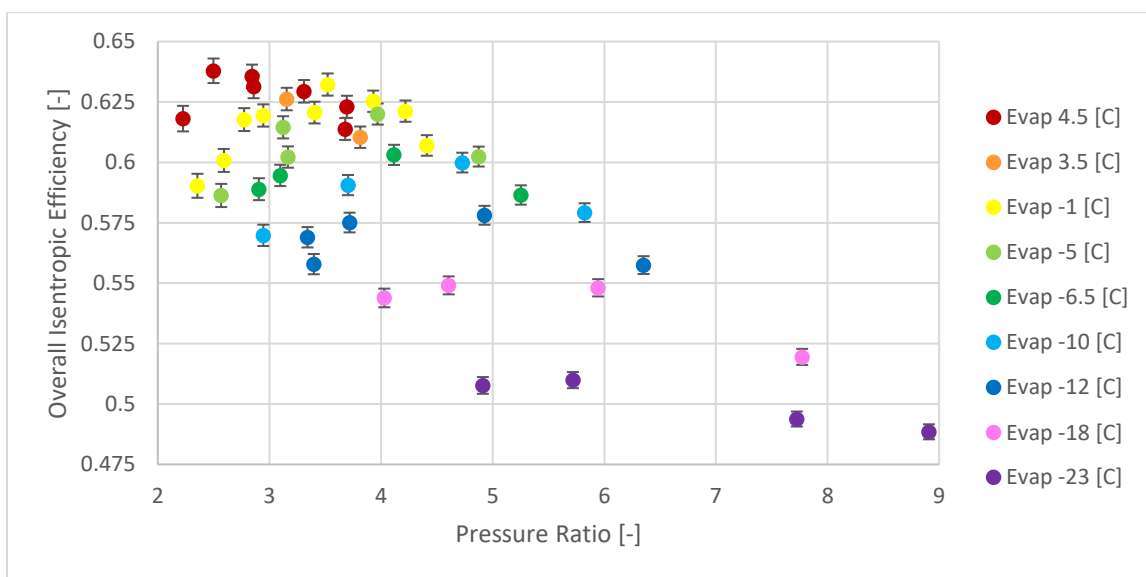


Figure 3.39: Overall isentropic efficiency with varying pressure ratio of the dual rotary compressor.

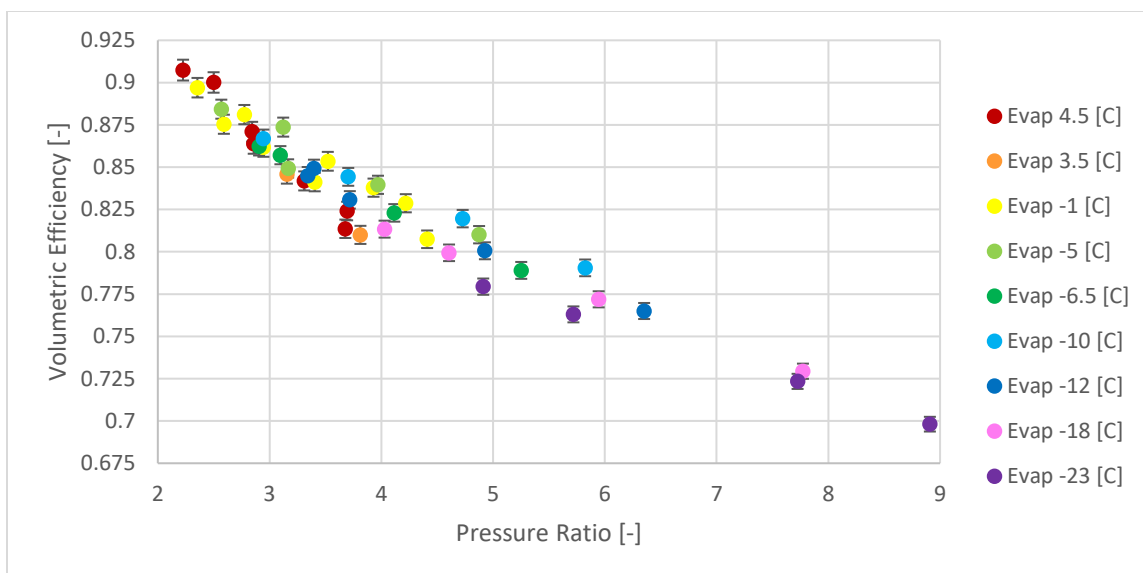


Figure 3.40: Volumetric efficiency with varying pressure ratio of the dual rotary compressor.

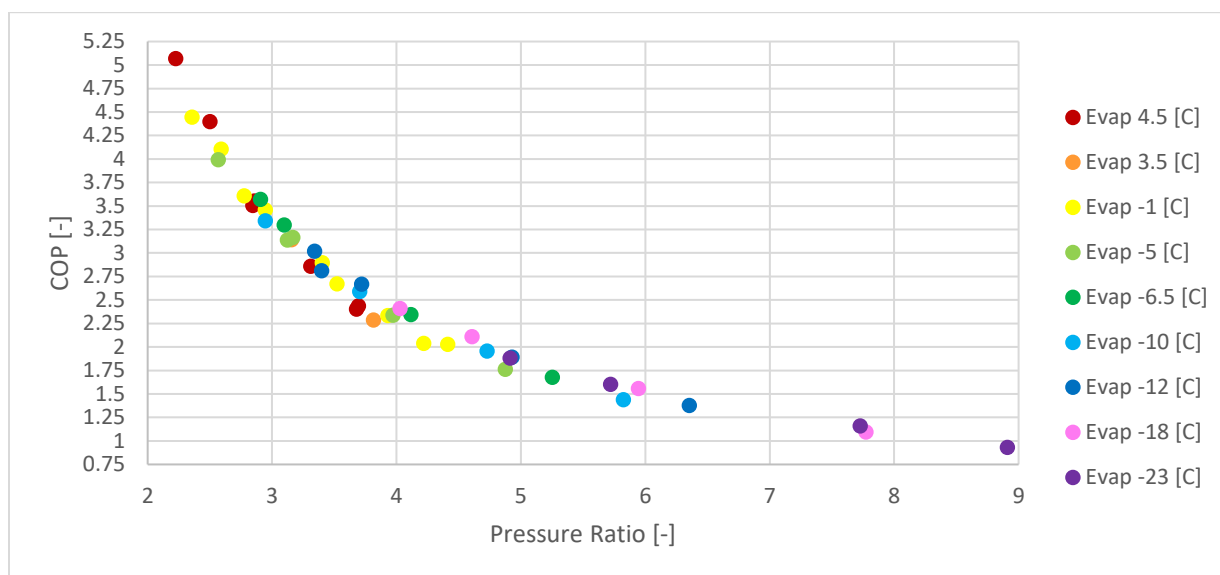


Figure 3.41: Coefficient of performance with varying pressure ratio of the dual rotary compressor.

The dual rotary compressor performance is slightly lower than the performance of the Copeland scroll compressor, with overall isentropic efficiencies from 57 to 63% at lower pressure ratios to 50% at higher pressure ratios. The volumetric efficiency sees a similar slightly lower efficiency, trending linearly from 90% to 70% with increasing pressure ratio.

Like the Copeland scroll compressor, pressure fluctuation in the dual rotary compressor was measured for each operating point shown in Figure 3.34. Based on the highest overall isentropic efficiencies of the dual rotary compressor at a pressure ratio of 3.5, the ideal pressure ratio was determined to be approximately 3.5. Figure 3.42, Figure 3.43, and Figure 3.44 show each compression case for the dual rotary compressor in both the time and frequency domains.

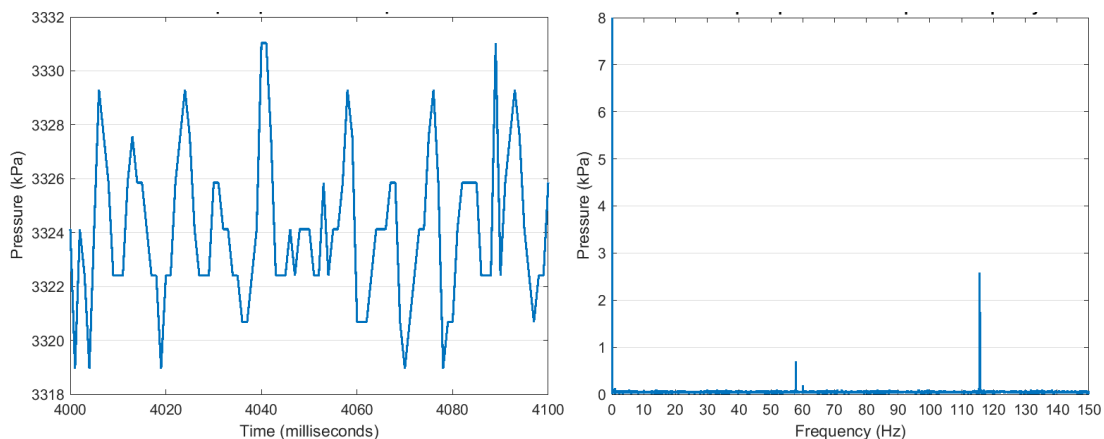


Figure 3.42: Time (left) and frequency (right) domain of the dual rotary compressor discharge at an evaporating temperature of  $-21.8\text{ C}$  and condensing temperature of  $53.6\text{ C}$  (pressure ratio of 8.9). This is a condition of under compression.

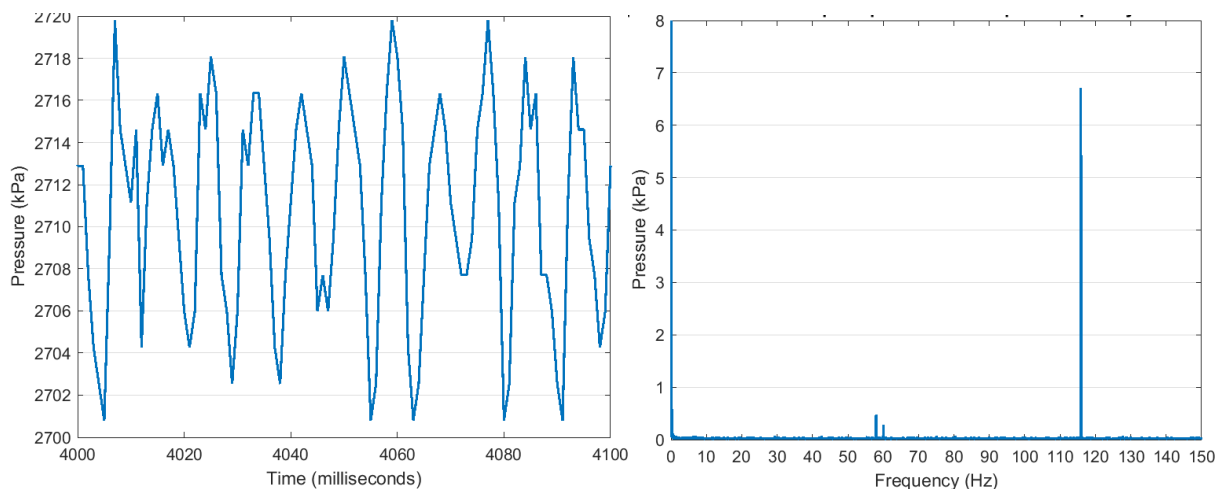


Figure 3.43: Time (left) and frequency (right) domain of the dual rotary compressor discharge at an evaporating temperature of  $-1.1\text{ C}$  and condensing temperature of  $44.8\text{ C}$  (pressure ratio of 3.5). This condition operates near the ideal pressure ratio of the compressor.

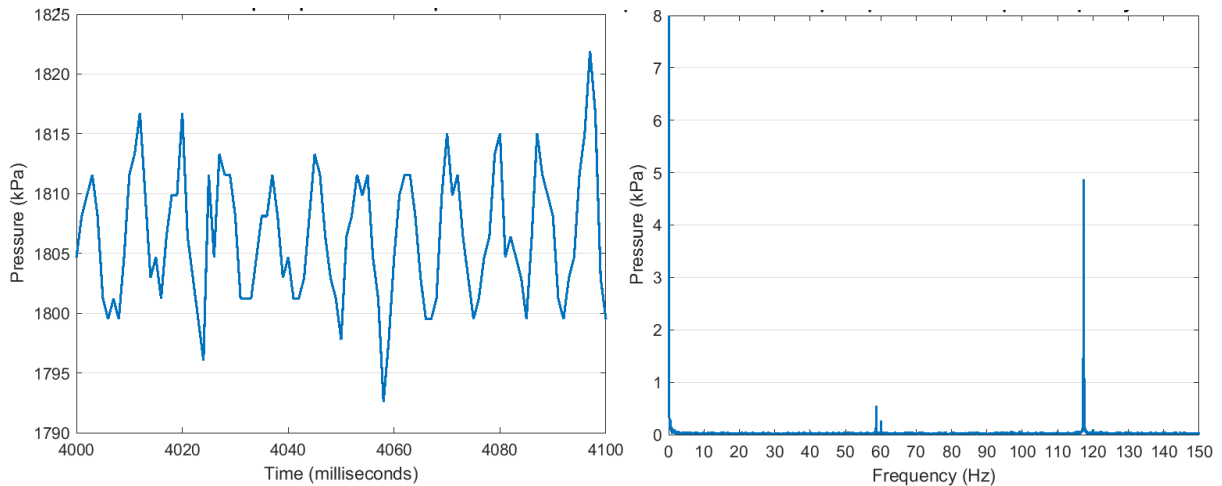


Figure 3.44: Time (left) and frequency (right) domain of the dual rotary compressor discharge at an evaporating temperature of  $-1.2\text{ C}$  and condensing temperature of  $28.4\text{ C}$  (pressure ratio of 2.6). This is a condition of over compression.

Due to the two compression chambers discharging  $180^\circ$  out of phase with one another at a motor shaft speed of  $60\text{ Hz}$ , the discharge rate of the dual rotary compressor is  $120\text{ Hz}$ . With the doubling in discharge rate compared to the Copeland scroll compressor, the DAQ is only able to sample just over 8 points per discharge. In the time domain the doubled discharge rate is reflected in a “sine” wave with a period half that of the Copeland scroll compressor. In the frequency domain, the  $120\text{ Hz}$  discharge rate matches in all cases with the frequency of the highest level of pressure fluctuation.

Similar to the Copeland scroll compressor, the pressure fluctuation does not follow the expected pattern of pressure fluctuations dependent on pressure ratio. The magnitude of pressure fluctuation for each of the operating points tested is shown in Figure 3.45.

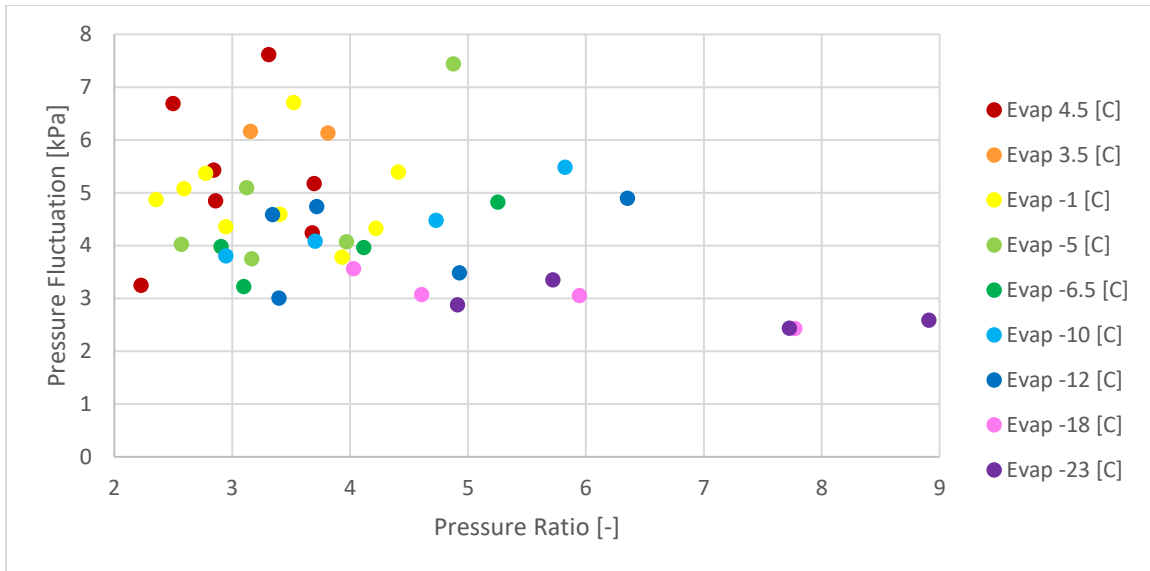


Figure 3.45: Pressure fluctuation with varying pressure ratio of the dual rotary compressor.

The pressure fluctuation is actually largest at the ideal pressure ratio and seems to taper off with increasing under-compression conditions. When the data is plotted in a different manner however a clearer trend can be observed.

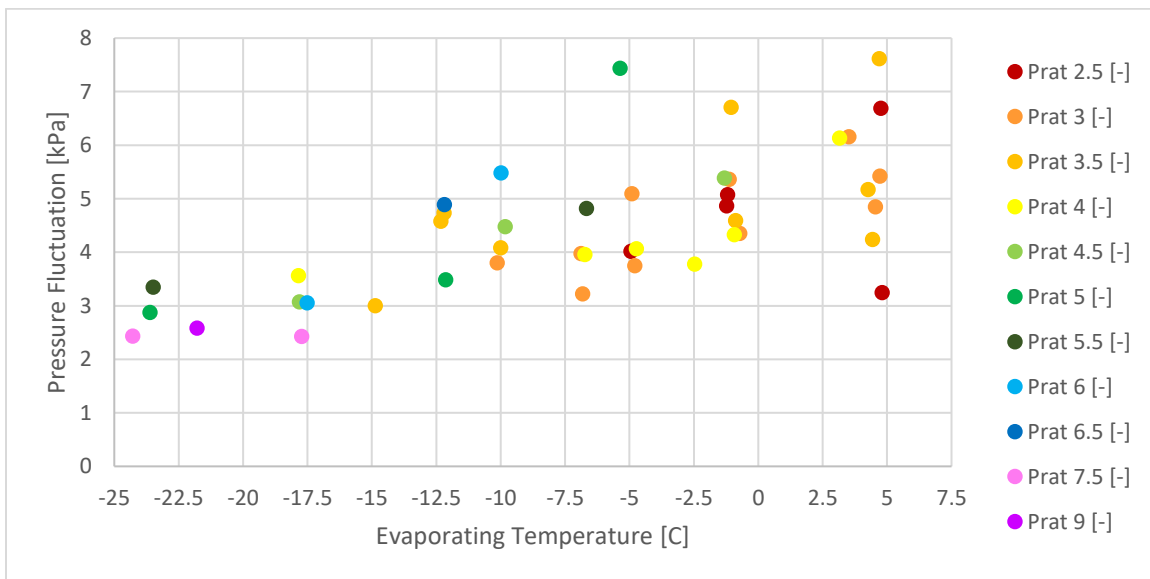


Figure 3.46: Pressure fluctuation with varying evaporating temperature of the dual rotary compressor.

In Figure 3.46 a positive correlation between evaporating temperature and pressure fluctuation is evident. Like the Copeland scroll compressor, the pressure fluctuation

measurements were taken after the discharge port of the dual rotary compressor, with all manufacturer dampening methods left in place. The dual rotary compressor has a high-side pressure shell, where the discharge of both compression chambers is sent into the shell of the compressor. This shell acts as a partial dead volume, which potentially absorbs significant pressure waves before the refrigerant is rejected into the condensing line. Additionally, the rotary compressor utilizes discharge valves, removing the possibility of under-compression situations, further limiting pressure fluctuation.

### 3.3.3 Map Comparison

The data collected for both the Copeland scroll and dual rotary compressors was divided into two pairs of training and testing data sets each. The first pair is used in comparing the AHRI 10 Coefficient map, Li's map, and Mendoza's (et al.) map in predicting performance given the full operating range of the compressor.

The data for the Copeland scroll is displayed in Figure 3.47. When comparing general performance predictions on the Copeland scroll, 8 operating points that span the entire operating range are used. The remaining 11 data points are used to compare the maps between one another.

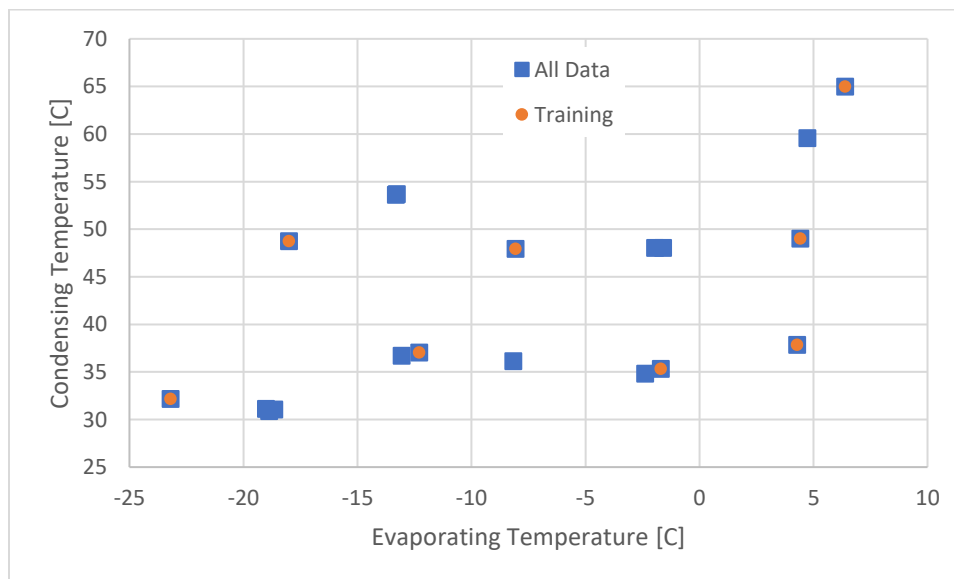


Figure 3.47: Copeland scroll data used in comparing the three different maps. Note that operating points that are not used in training the maps are used for comparing map predictions.

The data for the dual rotary is displayed in Figure 3.48.

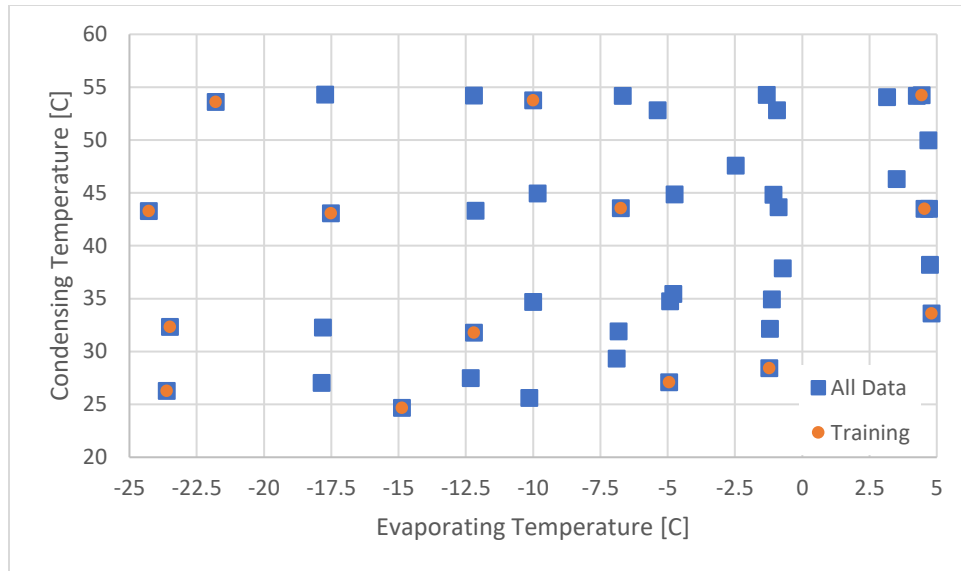


Figure 3.48: Dual rotary data used in comparing the three different maps. Note that operating points that are not used in training the maps are used for comparing map predictions.

When comparing general performance predictions on the dual rotary, 14 operating points that span the entire operating range is used. The remaining 30 data points are used to compare the maps between one another. The resulting map coefficients generated using data that spanned the entire operating range and by using MATLAB to compute the least squares problem is tabulated in Table 3.3, Table 3.4, and Table 3.5.

Table 3.3: AHRI 10 Coefficient performance predictions with a training set that covers the entire operating range.

Coefficient	Power Draw [kW]		Mass Flow Rate [kg/s]	
	Copeland Scroll	Dual Rotary	Copeland Scroll	Dual Rotary
$C_1$	0.009026512	1.364038879	0.000281179	0.085190404
$C_2$	0.012590466	-0.03248299	0.000396794	0.003176128
$C_3$	0.14348089	0.031911589	0.004469202	-0.001304756
$C_4$	-2.48748E-05	-0.001180412	3.11819E-05	5.59839E-05
$C_5$	0.000296406	0.000682837	0.00010388	-3.13112E-05
$C_6$	-0.00231356	0.000336269	-9.84065E-05	2.3966E-05
$C_7$	-1.25775E-05	-1.23769E-05	2.35852E-07	4.22224E-07
$C_8$	-1.17756E-05	8.48417E-06	1.04193E-07	-5.08219E-07
$C_9$	1.98834E-06	6.85405E-06	-1.25118E-06	1.55713E-07
$C_{10}$	2.04834E-05	-6.3654E-07	6.94292E-07	-1.79098E-07

Table 3.4: Li Correlation performance predictions with a training set that covers the entire operating range.

<b>Coefficient</b>	<b>Copeland Scroll</b>	<b>Dual Rotary</b>
<b>Power Draw [kW]</b>		
$a_1$	1.579220779	1.356667563
$a_2$	-113.9777131	9.498229025
$a_3$	-1426.959363	-1537.394521
$\dot{W}_{Loss}$	2.532420482	1.750365285
<b>Volumetric Efficiency [-]</b>		
$b_1$	0.993715738	0.95846773
$b_2$	-0.028153911	-0.035452175
$dp$	4.48933E-05	2.01176E-05

Table 3.5: Mendoza (et al.) Correlation performance predictions with a training set that covers the entire operating range.

<b>Coefficient</b>	<b>Copeland Scroll</b>	<b>Dual Rotary</b>
<b>Overall Isentropic Efficiency [-]</b>		
$a_1$	-0.35105205	-0.389506259
$a_2$	0	0
$a_3$	-0.004548617	0.003772558
$a_4$	0	0
<b>Volumetric Efficiency [-]</b>		
$b_1$	-0.098402901	-0.148897397
$b_2$	0	0
$b_3$	0	0

Using these coefficients in the respective equations described in Section 1.2.1, the correlations were applied to the data for each compressor that was not used for training. Figure 3.49, Figure 3.50, Figure 3.51, and Figure 3.52 compare the map accuracy for mass flow rate, power draw, overall isentropic efficiency, and volumetric efficiency. Note that each correlation predicts two of the four parameters being compared, each one predicting parameters different from another. To get a better comparison of the maps, the remaining two parameters of each map were determined indirectly using the parameters directly predicted by the map and the equations discussed in Section 1.4.3. For example, in the Li Correlation, power draw and volumetric efficiency are calculated from the correlations, and then mass flowrate is calculated using Equation (1.4) and overall isentropic efficiency is calculated using data from the tests, the

“backed-out” mass flowrate, and the correlation used to calculate power draw using Equation (1.3). In the x-axis of each plot are the parameters using measured data, and in the y-axis of each plot are parameters using correlation predicted data.

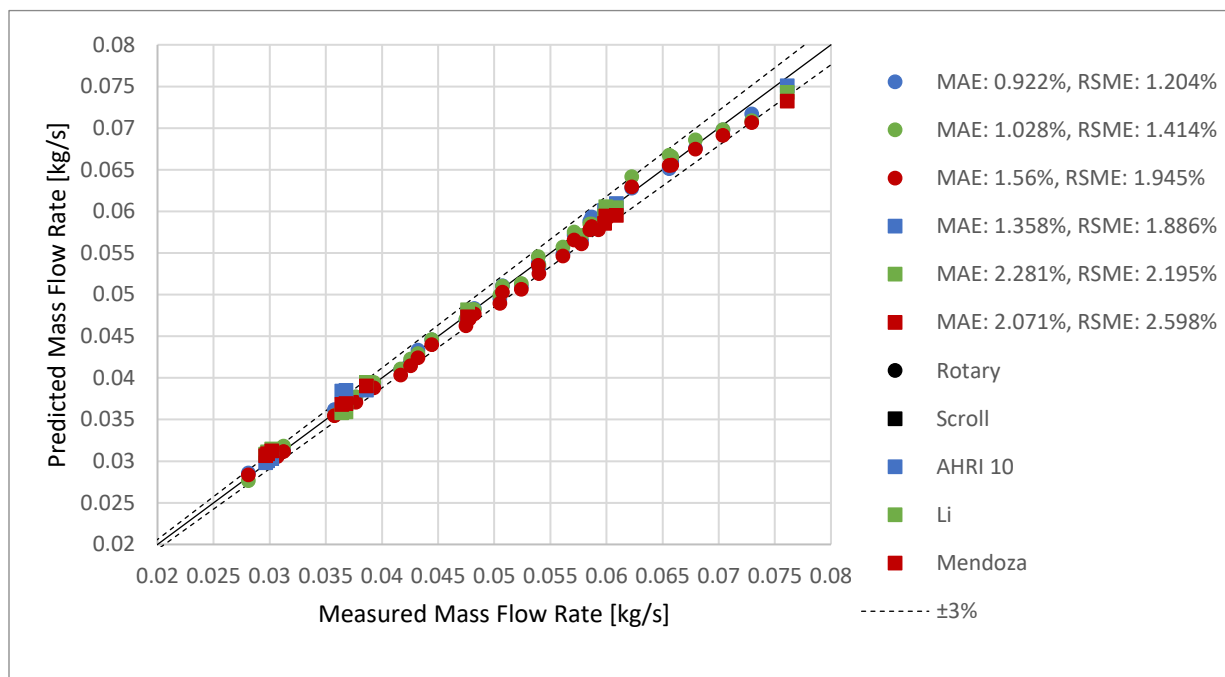


Figure 3.49: Mass flow rate comparison between the 3 maps using training data that spans the entire operating range of the respective compressors.

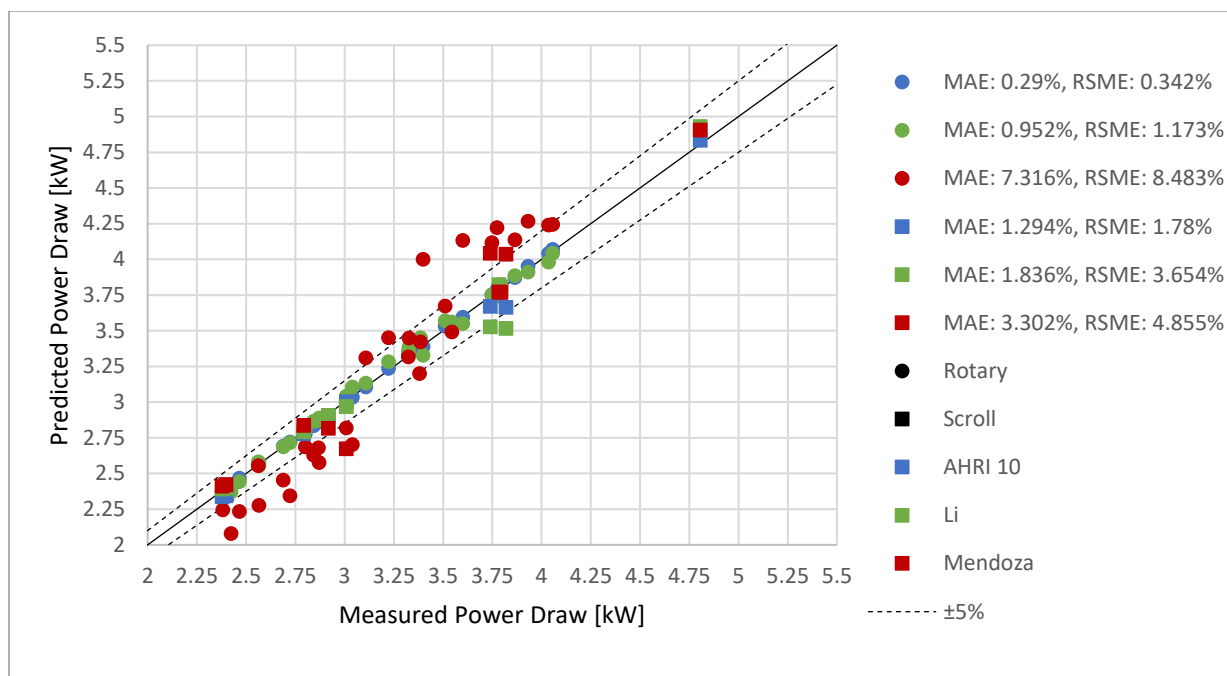


Figure 3.50: Power draw comparison between the 3 maps using training data that spans the entire operating range of the respective compressors.

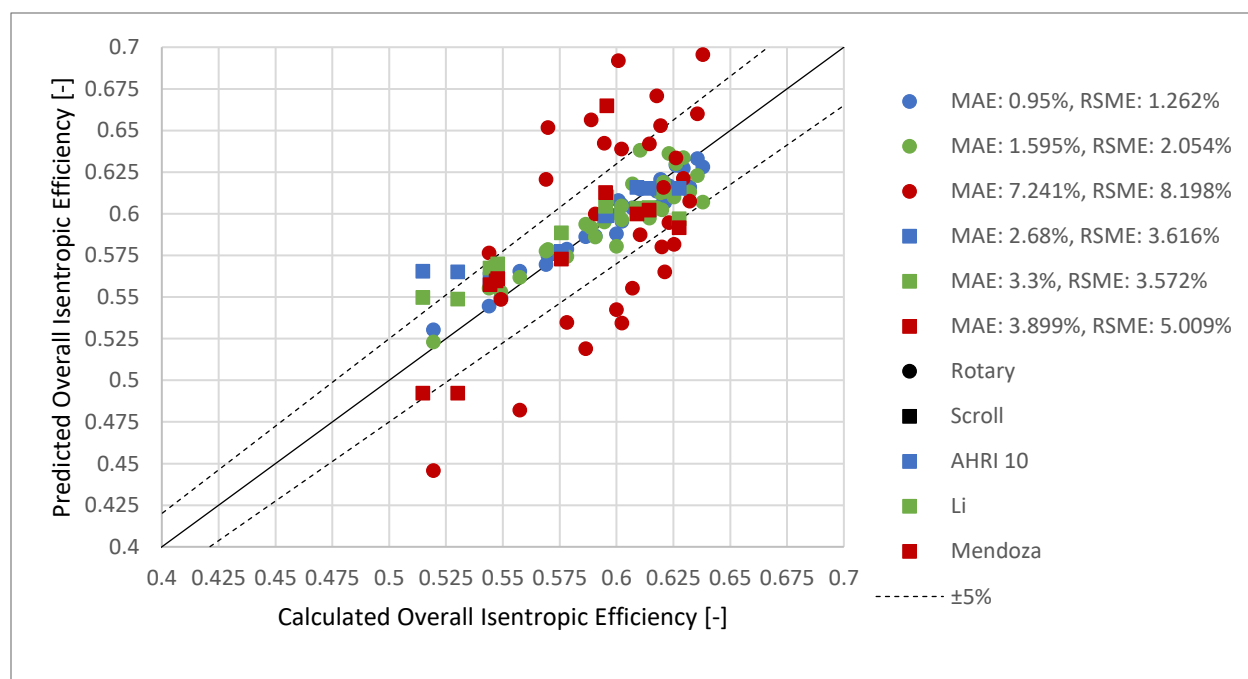


Figure 3.51: Overall isentropic efficiency comparison between the 3 maps using training data that spans the entire operating range of the respective compressors.

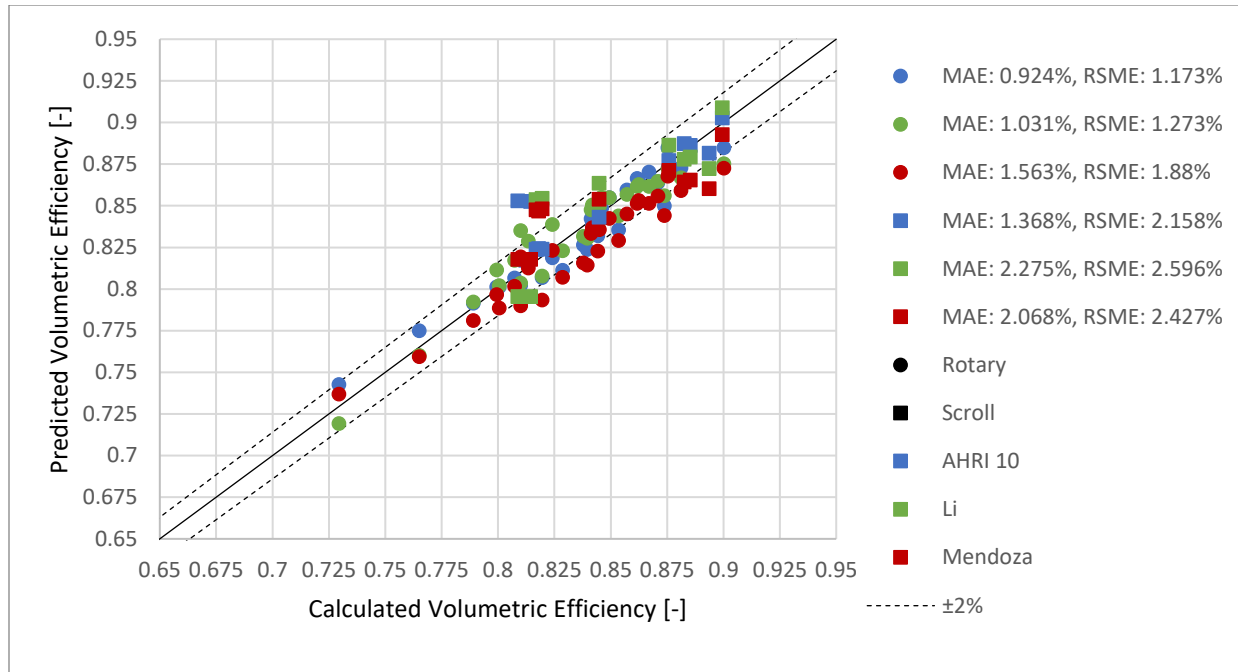


Figure 3.52: Volumetric efficiency comparison between the 3 maps using training data that spans the entire operating range of the respective compressors.

When using training data that spans the entire operating range of each compressor, all 3 maps predict the mass flow rate and the volumetric efficiency well, to within 3% and 2% respectively. The Li Correlation and the AHRI 10 Coefficient maps predict all parameters to within 4% and 3% respectively, indicating that both maps are adept at making performance predictions when the training data set spans the entire operating range.

The Mendoza Correlation does not perform well when predicting overall isentropic efficiency, yielding an average accuracy close to 9%, making the map inapplicable in this case. This is due to the nullification of non-dimensional terms in the map itself. Because the map is able to account for variable speed application as well as varying refrigerant, the map was not used to its full extent. In both compressors, the speed and refrigerant was held constant, forcing the non-dimensional terms accounting for each parameter to become unity, essentially removing them from the equation. For overall isentropic efficiency, the correlation became dependent on just the pressure ratio and an inverted temperature difference. While the volumetric efficiency is still predicted accurately, the correlation solely becomes dependent on the pressure ratio.

Between the Copeland scroll and the dual rotary compressor, the AHRI 10 Coefficient Correlation and the Li Correlation are more accurate when predicting performance for the rotary

compressor. The Mendoza Correlation is split between the two compressors with more accuracy when predicting volumetric efficiency and mass flow rate for the dual rotary compressor, and more accuracy with overall efficiency and power draw with the Copeland scroll compressor.

The data for both compressors were also split into a training and testing data set that discerns the accuracy of each map when trying to extrapolate compressor performance to operating conditions that are outside of the training data set. Figure 3.53 plots the training data set for extrapolation on the Copeland scroll compressor.

When comparing extrapolation performance predictions on the Copeland scroll, 7 operating points that span the entire operating range is used. The remaining 12 data points are used to compare the maps between one another.

The extrapolation training data is plotted in Figure 3.54. When comparing extrapolation performance predictions on the dual rotary, 20 operating points that span the entire operating range is used. The remaining 24 data points are used to compare the maps between one another.

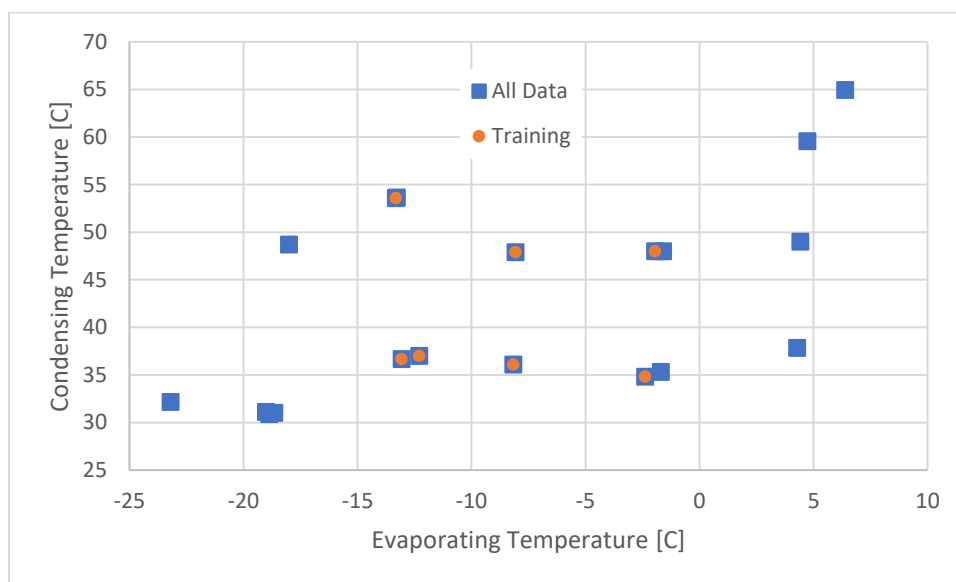


Figure 3.53: Copeland scroll data used in comparing the three different maps for extrapolation predictions. Note that operating points that are not used in training the maps are used for comparing map predictions.

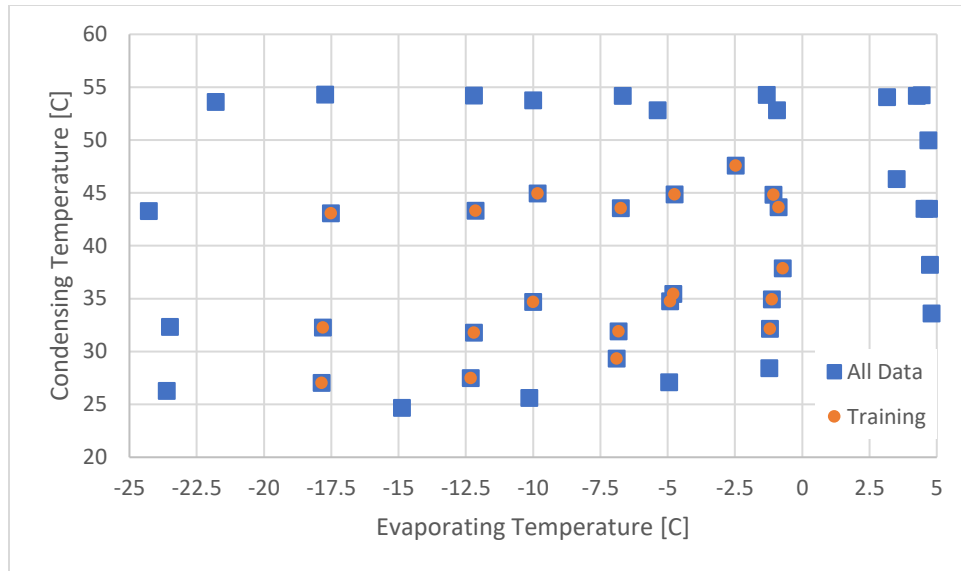


Figure 3.54: Dual rotary data used in comparing the three different maps for extrapolation predictions. Note that operating points that are not used in training the maps are used for comparing map predictions.

Like in the general performance case, the resulting extrapolation map coefficients is generated using extrapolation data and by using MATLAB to compute the least squares problem. The coefficients for each map are tabulated in Table 3.6, Table 3.7, and Table 3.8.

Table 3.6: AHRI 10 Coefficient performance predictions with an extrapolation focused training set.

Coefficient	Power Draw [kW]		Mass Flow Rate [kg/s]	
	Copeland Scroll	Dual Rotary	Copeland Scroll	Dual Rotary
$C_1$	0.001506738	0.034796858	2.86387E-05	0.004909166
$C_2$	-0.007172524	-0.058907042	-0.000130987	0.000674581
$C_3$	0.02187844	0.129538591	0.000416523	0.004627623
$C_4$	-0.05985078	-0.000749776	-0.001161427	1.50245E-05
$C_5$	-0.014802706	0.002225004	-0.000180828	7.72037E-05
$C_6$	0.002881536	-0.001986076	8.6084E-05	-0.00012263
$C_7$	-0.00123461	7.12854E-06	-2.67549E-05	-6.28063E-08
$C_8$	0.0008291	9.32003E-06	1.531E-05	6.85906E-08
$C_9$	0.00028732	-1.36451E-05	3.87911E-06	-1.07212E-06
$C_{10}$	-3.56307E-05	1.7162E-05	-1.41829E-06	1.03439E-06

Table 3.7: Li Correlation performance predictions with an extrapolation focused training set.

<b>Coefficient</b>	<b>Copeland Scroll</b>	<b>Dual Rotary</b>
<b>Power Draw [kW]</b>		
$a_1$	1.880255297	1.273704621
$a_2$	-633.4534145	-15.53753949
$a_3$	-4935.658258	-1508.687805
$\dot{W}_{Loss}$	8.834052658	1.919205345
<b>Volumetric Efficiency [-]</b>		
$b_1$	0.960553431	0.966661709
$b_2$	-0.021861791	-0.037586771
$dp$	5.5121E-05	7.70511E-05

Table 3.8: Mendoza (et al.) performance predictions with an extrapolation focused training set.

<b>Coefficient</b>	<b>Copeland Scroll</b>	<b>Dual Rotary</b>
<b>Overall Isentropic Efficiency [-]</b>		
$a_1$	-0.404229437	-0.404229437
$a_2$	0	0
$a_3$	-0.003483957	-0.003483957
$a_4$	0	0
<b>Volumetric Efficiency [-]</b>		
$b_1$	-0.136622837	-0.136622837
$b_2$	0	0
$b_3$	0	0

Similar to the general analysis, these coefficients were applied to their respective correlations and used to predict performance on the operating conditions that were not used in the training data set. Parameters not directly correlated in each map were calculated in the same manner as the previous map comparison as well. Figure 3.55, Figure 3.56, Figure 3.57, and Figure 3.58 shows the accuracy of each map by parameter when trying to extrapolate data.

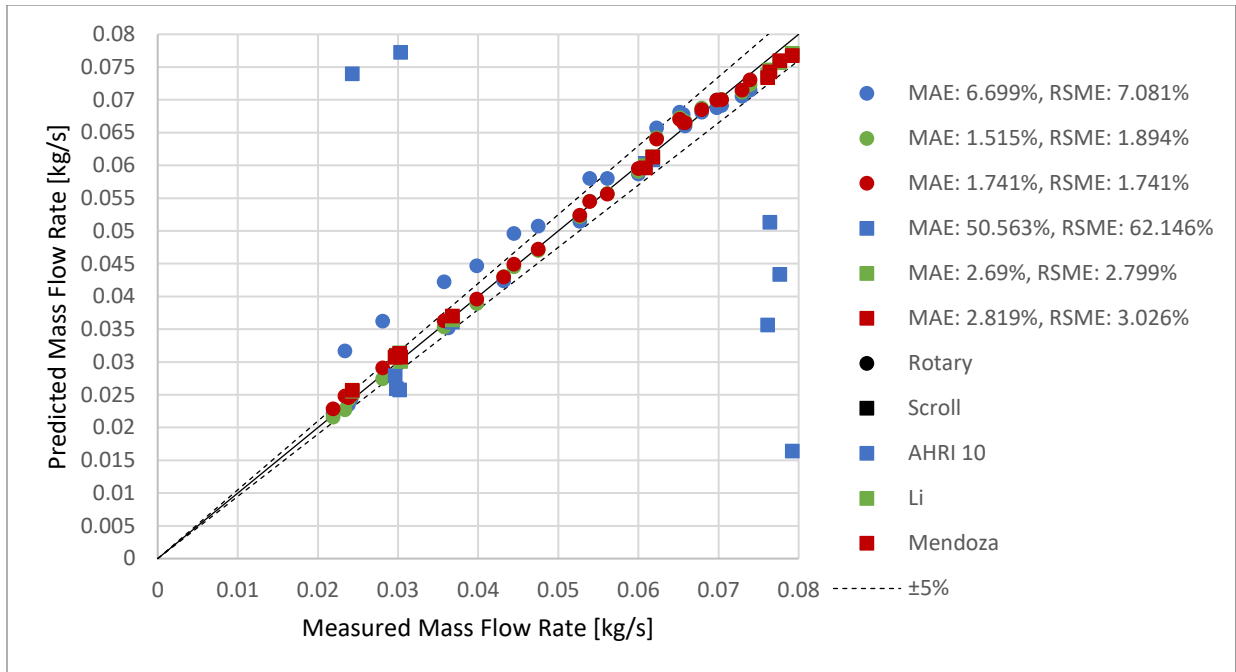


Figure 3.55: Mass flow rate comparison between the 3 maps using extrapolation training data.

The benefits of using a correlation other than the AHRI 10 Coefficient Correlation is clear when attempting to extrapolate compressor performance outside of the operating range of the training data. There is no accuracy when predicting performance for the scroll compressor when using the 10-coefficient map, while with the rotary compressor the 10 coefficient map fares well when predicting power draw. The Li and Mendoza correlation are accurate in predicting the mass flow rate, with average errors for both compressors of 3% or less. This is due to the accuracy of the volumetric efficiency prediction of both compressors yielding accuracies of 3% or less. At average errors of less than 3% for power draw and overall isentropic efficiency in the dual rotary compressor and 5% in the scroll compressor, the Li Correlation is the most accurate. The Mendoza Correlation loses accuracy in power draw and overall isentropic efficiency, yielding average errors of around 10 % in the dual rotary compressor. The Mendoza Correlation fares slightly better with the Copeland Scroll compressor when predicting power draw and overall isentropic efficiency with average errors around 6%.

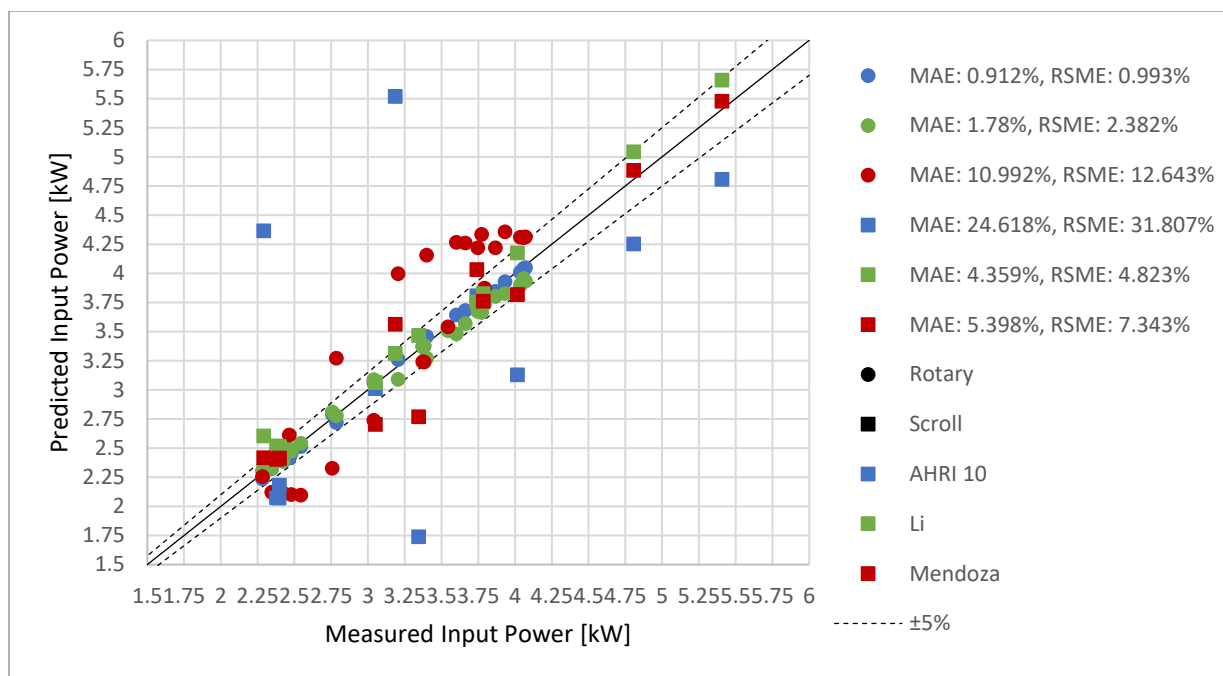


Figure 3.56: Power draw comparison between the 3 maps using extrapolation training data.

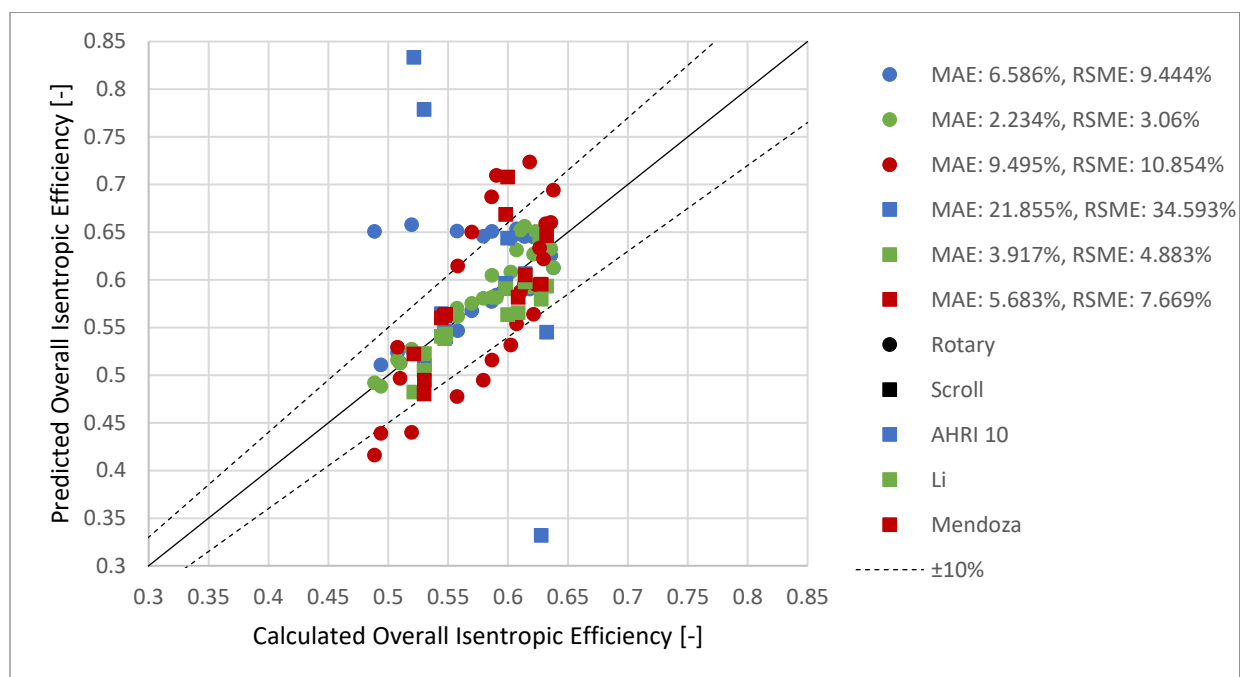


Figure 3.57: Overall isentropic efficiency comparison between the 3 maps using extrapolation training data.

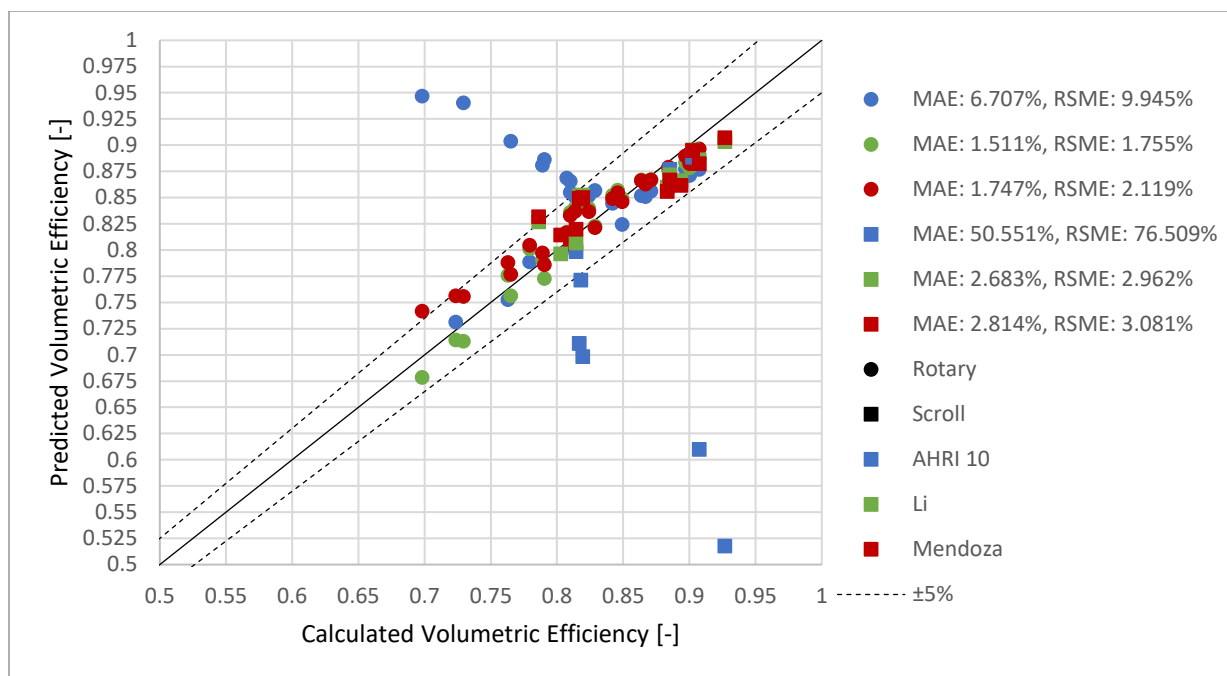


Figure 3.58: Volumetric efficiency comparison between the 3 maps using extrapolation training data.

Even though the Mendoza Correlation has the same unity concerns as in the general analysis, the correlation is able to extrapolate performance comparatively better than the AHRI 10 Coefficient Correlation. This means that the non-dimensional factors of the Mendoza Correlation remain more applicable in extrapolation than the (dimensioned) polynomial in the AHRI 10 Coefficient Correlation.

Similar to the general application, the Li Correlation is most accurate when predicting performance of the rotary compressor, and the Mendoza Correlation is split. For the Mendoza Correlation, volumetric efficiency and mass flow rate is more accurately predicted for the rotary compressor, and overall isentropic efficiency and power draw is more accurately predicted for the Copeland scroll compressor.

The amount of data points selected for training to create the compressor maps is likely the reasoning for the difference in accuracy of the AHRI 10 Coefficient correlation between the scroll and the rotary compressor in the extrapolation case. There are proportionally more points selected in the rotary compressor than the scroll compressor, and the AHRI 10 Coefficient correlation is more accurate in extrapolation predictions for the rotary compressor than the scroll compressor. This indicates that the AHRI 10 coefficient correlation becomes less accurate with

less data used for training. The Li and Mendoza correlation are more tolerant to the lower proportion of data points between the scroll and rotary compressor in the extrapolation case, where differences in accuracy between the two compressors are minimal in comparison to the AHRI 10 Coefficient correlation.

## 4. CONCLUSION AND RECOMMENDATIONS

Utilizing and modifying two compressor test stands, four compressors were tested, and their performance evaluated and compared. In the Hot-Gas Bypass Test Stand, the performances of a reciprocating compressor and a scroll compressor were investigated for applications in domestic refrigerator/freezers. The reciprocating compressor was able to successfully complete more tests in a broader operating range and operated at much higher overall isentropic efficiencies than the scroll compressor. Volumetric efficiencies between the reciprocating and scroll compressor were similar. The reciprocating compressor was also able to provide a larger cooling capacity than the scroll, leading to higher COPs than the scroll compressor. The clear superiority of the reciprocating compressor over the scroll compressor in a refrigerator freezer application is marred somewhat due to the prototype nature of the scroll compressor tested, as well as the reduced control over the test stand when evaluating the scroll compressor. High power input to the motor while yielding lower shaft rotation frequency is likely due to high friction experienced by operating without oil, as well as decoupling of the motor shaft and the compressor shaft due to an unstable connection via magnets. Suction superheat of the scroll compressor was also higher in most tests, also contributing to higher necessary input power at the same conditions.

In the Tescor Compressor Calorimeter, the performances of a scroll compressor and a rotary compressor were investigated for applications in residential air conditioning/heat pumping. Both compressors had almost equivalent overall isentropic compressor efficiencies, while the scroll compressor efficiency was slightly higher. The volumetric efficiencies between the two compressors were not equivalent, where the scroll compressor had higher efficiencies than the rotary compressor. Due to the increased volumetric efficiency, the scroll compressor is the better performer in the tested conditions. The pressure fluctuation at the discharge of the scroll and rotary compressors were also measured. While both compressors experienced low fluctuation, the rotary compressor exhibited slightly higher pressure fluctuation levels than the scroll compressor. In both cases, the pressure fluctuation is low enough that investigation into the use of a novel parallel muffling design is not warranted.

Three correlations created to predict compressor performance were also investigated using data from the calorimeter testing. This was done to determine the applicability of the AHRI 540 Standard 10-Coefficient correlation in performance predictions both inside and outside the

testing range and evaluate possible alternatives. It was found that the 10-Coefficient Correlation is the most accurate when predicting compressor performance inside the testing range, although the Li Correlation is almost as accurate. The 10-Coefficient Correlation becomes inapplicable when attempting to predict compressor performance outside of the testing range. In this extrapolation case the Li and Mendoza correlations remain accurate, with the Li Correlation the most accurate. It is suggested that the 10-Coefficient Correlation be used to predict performance inside the testing range and the Li Correlation be used to predict performance outside of the testing range.

While control over the Hot-Gas Bypass Test Stand and the Tesco Calorimeter Test Stand is acceptable, there are improvements that could be made to increase capability and control in each test stand. In the Hot-Gas Bypass Test Stand it is important to maintain a condensing line full of subcooled liquid so that expansion across the liquid line valves remains in constant quality, which leads to better control over the suction temperature of the compressor. Users have experienced difficulty in maintaining subcooled liquid just before the liquid line expansion valve due to the in-plane layout of the refrigerant circuitry. Reorganizing the refrigerant circuitry to utilize gravity in the condensing line would force liquid buildup just before the expansion valves and increase user control over the suction superheat.

The calorimeter has been modified with two valves to increase the range of capable operating conditions; the water bypass valve and the EXV. Currently, the operator must actuate the opening percentage of each valve using knowledge they gained from previous use of the calorimeter. Replacing the bypass valve with a motor actuated valve, and then implementing PID control over both valves would reduce testing time. The setpoint of the bypass valve would be the desired discharge pressure, and the setpoint of the EXV would be the desired suction pressure. Testing time is also increased by the low resolution of the electrical heating elements. In most cases, the user must wait for the PID controller on the 'variable' 3 kW heater to oscillate turning the heater on and off before steady-state operation is achieved. Replacing this heater with a variable heater that has a finer resolution will allow the evaporator to reach capacities that are not a multiple of 3 kW much easier. Lastly, the suction pressure transducers of the calorimeter should be replaced with pressure transducers with a higher maximum pressure reading to permit testing of refrigerants that operate at higher pressures.

## REFERENCES

- AHRI. (2015). *Performance Rating Of Positive Displacement Refrigerant Compressors and Compressor Units*. Arlington: AHRI.
- ANSI/ASHRAE. (2011). *Standard Methods for Volatile-Refrigerant Mass Flow Measurements Using Calorimeters*. Atlanta: ASHRAE.
- ASHRAE Standards Committee. (2010). *Methods of Testing for Rating the Performance of Positive Displacement Refrigerant Compressors and Condensing Units that Operate at Subcritical Temperatures of the Refrigerant*. Atlanta: ASHRAE.
- Bansal, P., Vineyard, E., & Abdelaziz, O. (2011). Advances in Household Appliances - A Review. *Applied Thermal Engineering*, 3748 - 3760.
- Bell, I. (2011). *Theoretical and Experimental Analysis of Liquid Flooded Compression in Scroll Compressors*. West Lafayette: Purdue University.
- Bertsch, S. S., & Groll, E. A. (2008). Two-stage Air-source Heat Pump for Residential Heating and Cooling Applications in Northern U.S. Climates. *International Journal of Refrigeration* 31, 1282-1292.
- Bradshaw, C. R. (2012). *A Miniature-Scale Linear Compressor for Electronics Cooling*. West Lafayette: Purdue University.
- Choi, S., Han, U., Cho, H., & Lee, H. (2018). Review: Recent Advances in Household Refrigerator Cycle Technologies. *Applied Thermal Engineering*, 560 - 574.
- Dabiri, A. E., & Rice, C. K. (1981). A Compressor Simulation Model With Corrections for the Level of Suction Gas Superheat. *ASHRAE Transactions V. 87 Pt 22*. Atlanta: ASHRAE.
- F-Chart Software. (2018, September). Engineering Equation Solver. Madison, Wisconsin, United States of America: F-Chart Software.
- Frigo, M., & Johnson, S. G. (2018, May). *FFTW*. Retrieved from FFTW: <http://www.fftw.org/>
- Geppert, J., & Stamminger, R. (2013). Analysis of Effecting Factors on Domestic Refrigerators' Energy Consumption in Use. *Energy Conservation and Management*, 974 - 800.
- Ghadiri, F., & Rasti, M. (2014). The Effect of Selecting Proper Refrigeration Cycle Components on Optimizing Energy Consumption of the Household Refrigerators. *Applied Thermal Engineering*, 335 - 340.

- Groll, E. A. (2017). Analysis of Energy Utilization Systems Lecture 1: Introduction. West Lafayette, Indiana, United States of America: Purdue University.
- Huang, P. X. (2012). Gas Pulsations: A Shock Tube Mechanism. *International Compressor Engineering Conference* (pp. 1304 1-10). West Lafayette: Purdue University.
- Huang, P. X. (2012). Under-Compression (Over-Expansion) - An Isochoric Or Adiabatic Process. *International Compressor Engineering Conference* (pp. 1305 1 - 10). West Lafayette: Purdue University.
- Huang, P. X., Yonkers, S., & Hokey, D. (2014). Gas Pulsation Control Using a Shunt Pulsation Trap. *International Compressor Engineering Conference* (pp. 1136 1-10). West Lafayette: Purdue University.
- Jähnig, D. I., Reindl, D. T., & Klein, S. A. (2000). A Semi-Empirical Method for Representing Domestic Refrigerator/Freezer Compressor Calorimeter Test Data. *ASHRAE Transactions Volume 106 Pt. 2* (p. 122 to 130). Minneapolis: ASHRAE.
- Kim, M.-H., & Bullard, C. W. (2002). Thermal Performance Analysis of Small Hermetic Refrigeration and Air-Conditioning Compressors. *JSME International Journal*, 857-864.
- Lemmon, E. W., Huber, M. L., & McLinden, M. O. (2013). Reference Fluid Thermodynamic and Transport Properties [REFPROP]. *NIST Standard Reference Database 23. Version 9.1*. Gaithersburg: National Institute of Standards and Technology.
- Li, W. (2012). Simplified Steady-State Modeling for Hermetic Compressors with Focus on Extrapolation. *International Journal of Refrigeration* 35, 1722-1733.
- Lin, P., & Avelar, V. (2017). White Paper 254. *The Different Types of Cooling Compressors*. Schneider Electric.
- Mathworks. (2018). *fft*. Retrieved from <https://www.mathworks.com/help/matlab/ref/fft.html#buuutyt-6>
- Mathworks. (2018). MATLAB R2018a. *MATLAB*. Mathworks.
- Mendoza-Miranda, J. M., Mota-Babiloni, A., Ramírez-Minguela, J. J., Muñoz-Carpio, V. D., Carrera-Rodríguez, M., Navarro-Esbrí, J., & Salazar-Hernandez, C. (2016). Comparative evaluation of R1234yf, R1234ze(E) and R450A as alternatives to R134a in variable speed reciprocating compressor. *Energy* 114, 753-766.
- Mösch, T. (2015). *Performance Tests of a Scroll Compressor With Vapor Injection Using a Compressor Calorimeter*. Dresden: Technische Universität Dresden.

- Mtsuzaka, T., & Nagatomo, S. (1982). Rolling Piston Type Rotary Compressor Performance Analysis. *International Compressor Engineering Conference*. West Lafayette: Purdue University.
- Payne, W. V., & Domanski, P. A. (2002). A Comparison Of An R22 And An R410A Air Conditioner Operating at High Ambient Temperatures. *International Refrigeration and Air Conditioning Conference*. West Lafayette: Purdue University.
- Rigola, J., Pe´rez-Segarra, C. D., & Oliva, A. (2005). Parametric Studies on Hermetic Reciprocating Compressors. *International Journal of Refrigeration*, 253 - 266.
- Sakaino, K., Muramatsu, S., Shida, S., & Ohinata, O. (1984). Some Approaches Towards a High Efficient Rotary Compressor. *International Compressor Engineering Conference*. West Lafayette: Purdue University.
- Soedel, W. (2007). *Sound and Vibrations of Positive Displacement Compressors*. Boca Raton: Taylor & Francis Group, LLC.
- Swagelok. (2007, December). *Valve Sizing Technical Bulletin*. Retrieved from [www.swagelok.com](http://www.swagelok.com)
- Taylor, B. N., & Kuyatt, C. E. (1994). *Guidelines for Evaluating and Expressing the Uncertainty of NIST Measurement Results*. Gaithersburg: National Institute of Standards and Technology.
- Wang, L., Zhao, Y., Li, L., Bu, G., & Shu, P. (2007). Research on Oil-Free Hermetic Refrigeration Scroll Compressor. *Journal of Power and Energy*, 1049 - 1056.
- Weisstein, W. W. (2019). *Euler Formula*. Retrieved from Mathworld - A Wolfram Web Resource: <http://mathworld.wolfram.com/EulerFormula.html>
- Winandy, E., Saavedra, C. O., & Lebrun, J. (2002). Experimental Analysis and Simplified Modelling of a Hermetic Scroll Refrigeration Compressor. *Applied Thermal Engineering*, 107 - 120.

## APPENDIX A: OIL-FREE SCROLL COMPRESSOR DATA

Table 4.1: Measurement Data for the Scroll Compressor on the Hot-Gas Bypass Test Stand.

<b>Test</b>	<b>Shaft Speed</b>	<b>T1</b>	<b>T2</b>	<b>T3</b>	<b>T4</b>	<b>T5</b>	<b>T6</b>	<b>T7</b>
<b>[-]</b>	<b>[Hz]</b>	<b>[C]</b>						
1	24.70	20.44	54.28	37.44	1.78	33.12	1.47	23.23
2	26.02	6.18	44.97	31.50	- 10.66	25.23	4.60	23.08
3	26.07	16.80	41.25	25.57	11.54	22.89	5.27	22.89
4	29.25	14.83	62.99	38.89	7.66	28.75	2.35	23.86
5	42.15	-0.28	78.81	52.57	-8.53	35.04	7.78	22.53
6	37.18	1.67	81.67	52.26	-8.57	34.36	5.86	22.50
7	32.82	-0.10	79.47	51.42	-7.83	31.03	5.86	22.53

Table 4.1 Continued.

<b>Test</b>	<b>P1</b>	<b>P2</b>	<b>P3</b>	<b>P4</b>	<b>P5</b>	<b>Mass Flow Rate</b>	<b>Current Draw</b>
<b>[-]</b>	<b>[kPa]</b>	<b>[kPa]</b>	<b>[kPa]</b>	<b>[kPa]</b>	<b>[kPa]</b>	<b>[g/s]</b>	<b>[A]</b>
1	303.58	588.05	317.89	301.70	302.61	1.70	4.28
2	139.57	354.70	350.56	139.64	139.59	0.96	2.89
3	80.32	424.40	301.34	78.88	78.91	0.46	4.32
4	153.30	484.59	274.82	151.20	150.64	1.08	4.30
5	211.70	617.63	390.82	214.69	210.27	2.10	10.40
6	208.24	622.28	376.77	211.01	206.70	1.75	12.00
7	209.68	611.51	377.14	211.79	209.63	1.59	7.02

Table 4.2: Calculated Performance Data for the Scroll Compressor on the Hot-Gas Bypass Test Stand.

<b>Test</b>	<b>Condensing Temperature</b>	<b>Evaporating Temperature</b>	<b>Suction Superheat</b>	<b>Power Draw</b>	<b>Overall Isentropic Efficiency</b>
<b>[-]</b>	<b>[C]</b>	<b>[C]</b>	<b>[C]</b>	<b>[kW]</b>	<b>[-]</b>
1	20.89	0.9821	19.45	0.1968	0.13
2	5.393	-18.85	25.03	0.1329	0.1532
3	10.68	-31.04	47.85	0.1988	0.09555
4	14.74	-16.63	31.46	0.1981	0.1477
5	22.5	-8.646	8.368	0.4783	0.1015
6	22.75	-9.068	10.74	0.5519	0.07567
7	22.17	-8.891	8.792	0.323	0.1136

Table 4.2 Continued.

<b>Test</b>	<b>Volumetric Efficiency</b>	<b>Potential Evaporating Capacity</b>	<b>Pressure Ratio</b>	<b>Potential COP</b>
<b>[-]</b>	<b>[-]</b>	<b>[kW]</b>	<b>[-]</b>	<b>[-]</b>
1	0.61	0.3317	1.937	1.686
2	0.6982	0.1989	2.541	1.497
3	0.6126	0.0965	5.284	0.4854
4	0.6547	0.2171	3.161	1.096
5	0.5923	0.3716	2.917	0.777
6	0.5736	0.3116	2.988	0.5646
7	0.5806	0.2815	2.916	0.8715

## APPENDIX B: RECIPROCATING COMPRESSOR DATA

Table 4.3: Measurement Data for the Reciprocating Compressor on the Hot-Gas Bypass Test Stand.

<b>Test</b>	<b>Composition</b>	<b>Shaft Speed</b>	<b>T1</b>	<b>T2</b>	<b>T3</b>	<b>T4</b>	<b>T5</b>
<b>[-]</b>	<b>[-]</b>	<b>[Hz]</b>	<b>[C]</b>	<b>[C]</b>	<b>[C]</b>	<b>[C]</b>	<b>[C]</b>
1	Original	60	8.29	52.33	39.68	-1.00	29.41
2	Original	60	2.12	46.69	33.50	-11.86	21.22
3	Original	60	-3.86	38.07	26.20	-21.98	12.29
4	Original	60	-15.67	38.98	21.95	-32.54	6.74
5	Original	60	7.09	52.10	39.76	-3.32	28.28
6	Original	60	-1.15	40.63	31.35	-17.20	16.81
7	Original	60	-5.23	40.97	31.33	-16.83	16.63
8	Original	60	-11.75	33.73	26.88	-26.03	7.62
9	Original	60	6.26	53.14	35.68	-6.42	23.44
10	Original	60	2.51	56.57	30.01	-5.96	18.78
11	Original	60	-0.09	50.13	32.23	-10.63	19.69
12	Original	60	-0.62	56.23	26.39	-11.48	10.50
13	Original	60	-3.47	45.69	27.66	-16.78	13.87
14	Original	60	-4.98	55.26	25.10	-16.91	-0.58
15	Original	60	-10.22	45.03	26.74	-21.08	1.61
16	Polymer	60	1.97	49.20	35.59	-10.38	21.77
17	Polymer	60	-17.38	38.24	27.37	-21.07	7.99
18	Polymer	60	-17.45	38.93	36.02	-31.79	11.32
19	Polymer	60	10.03	66.32	61.70	-0.13	9.59

Table 4.3 Continued.

<b>Test</b>	<b>T6</b>	<b>T7</b>	<b>T8</b>	<b>P1</b>	<b>P2</b>	<b>P3</b>
<b>[-]</b>	<b>[C]</b>	<b>[C]</b>	<b>[C]</b>	<b>[kPa]</b>	<b>[kPa]</b>	<b>[kPa]</b>
1	24.13	20.72	66.18	291.82	929.00	684.29
2	20.99	20.90	65.38	191.13	893.16	660.06
3	20.57	20.77	61.31	124.41	886.93	645.14
4	21.02	20.69	54.94	75.93	982.00	620.01
5	21.62	21.09	67.37	268.09	933.34	719.57
6	20.23	20.95	60.02	153.88	757.64	715.97
7	20.02	20.95	60.54	155.31	763.69	718.54
8	19.25	20.79	56.74	102.64	718.97	716.21
9	20.34	21.10	72.08	238.11	1158.09	714.77
10	20.26	21.21	74.96	241.58	1500.52	699.62
11	20.39	21.09	71.36	201.83	1154.06	696.21

Table 4.3 Continued.

12	19.95	21.15	75.52	194.75	1502.52	706.44
13	20.08	21.19	69.39	157.05	1110.88	694.41
14	19.54	21.16	71.41	155.29	1490.29	681.60
15	19.60	20.97	65.65	128.98	1141.84	714.54
16	20.60	20.54	70.13	204.49	904.07	725.60
17	19.53	20.54	61.40	128.29	906.32	719.92
18	18.32	20.38	54.72	76.84	986.57	942.95
19	19.68	21.31	84.37	296.70	1931.57	1775.69

Table 4.3 Continued.

<b>Test</b>	<b>P4</b>	<b>P5</b>	<b>Mass Flow Rate</b>	<b>Power Draw</b>
<b>[-]</b>	<b>[kPa]</b>	<b>[kPa]</b>	<b>[g/s]</b>	<b>[kW]</b>
1	289.263	293.591	2.326	0.1361
2	190.530	192.068	1.362	0.1095
3	126.234	128.352	0.762	0.0885
4	80.128	82.146	0.345	0.0680
5	268.121	265.736	2.022	0.1307
6	156.605	153.981	1.022	0.0951
7	158.805	156.491	1.044	0.0962
8	108.145	106.957	0.649	0.0778
9	239.911	240.731	1.686	0.1318
10	243.793	245.192	1.647	0.1441
11	204.377	205.006	1.350	0.1205
12	197.294	197.655	1.268	0.1255
13	160.994	162.418	0.963	0.1034
14	158.739	161.559	0.813	0.1087
15	133.988	135.537	0.727	0.0940
16	204.427	205.851	1.393	0.1193
17	132.936	136.153	0.786	0.0927
18	85.356	81.186	0.497	0.0684
19	295.581	301.028	1.959	0.1758

Table 4.4: Calculated Performance Data for the Reciprocating Compressor on the Hot-Gas Bypass Test Stand.

<b>Test</b>	<b>Condensing Temperature</b>	<b>Evaporating Temperature</b>	<b>Suction Superheat</b>	<b>Power Draw</b>	<b>Overall Isentropic Efficiency</b>
<b>[-]</b>	<b>[C]</b>	<b>[C]</b>	<b>[C]</b>	<b>[kW]</b>	<b>[-]</b>
1	36.66	-0.1116	8.405	0.1361	0.4302
2	35.23	-11.24	13.36	0.1095	0.4263
3	34.98	-21.5	17.64	0.0885	0.3832
4	38.69	-32.21	16.54	0.0680	0.2934
5	36.83	-2.428	9.521	0.1307	0.4219
6	29.41	-16.54	15.38	0.0951	0.3829
7	29.68	-16.32	11.09	0.0962	0.3792
8	27.6	-25.8	14.06	0.0778	0.3598
9	44.92	-5.591	11.85	0.1318	0.4485
10	55.22	-5.21	7.724	0.1441	0.4537
11	44.78	-9.863	9.771	0.1205	0.4284
12	55.28	-10.77	10.14	0.1255	0.4549
13	43.32	-16.05	12.59	0.1034	0.4052
14	54.94	-16.32	11.34	0.1087	0.3753
15	44.38	-20.68	10.46	0.0940	0.3716
16	35.67	-9.531	11.5	0.1193	0.3826
17	35.76	-20.8	3.423	0.0927	0.3514
18	38.87	-31.96	14.51	0.0684	0.4147
19	65.93	0.346	9.679	0.1758	0.4576

Table 4.4 Continued.

<b>Test</b>	<b>Volumetric Efficiency</b>	<b>Potential Evaporating Capacity</b>	<b>Pressure Ratio</b>	<b>Potential COP</b>
<b>[-]</b>	<b>[-]</b>	<b>[kW]</b>	<b>[-]</b>	<b>[-]</b>
1	0.7082	0.3767	3.183	2.768
2	6.35E-01	0.2194	4.673	2.004
3	5.434E-01	0.1207	7.129	1.364
4	0.3898	0.04997	12.93	0.7352
5	0.6712	0.326	3.481	2.495
6	0.5903	0.1714	4.923	1.803
7	0.5867	0.1712	4.917	1.78
8	0.5461	0.1058	7.005	1.361
9	0.6336	0.2518	4.864	1.91
10	0.5986	0.2147	6.211	1.49
11	0.5878	0.1957	5.718	1.624
12	0.5724	0.1634	7.715	1.301

Table 4.4 Continued.

13	0.539	0.1402	7.074	1.356
14	0.4571	0.103	9.597	0.9481
15	0.4855	0.1012	8.853	1.077
16	0.6040	0.223	4.421	1.868
17	0.5104	0.1147	7.064	1.238
18	0.5502	0.07113	12.84	1.039
19	0.5904	0.2323	6.51	1.322

## APPENDIX C: COPELAND SCROLL COMPRESSOR DATA

Table 4.5: Measurement Data for the Scroll Compressor on the Tesco Calorimeter.

<b>Test</b>	<b>T1</b>	<b>T2</b>	<b>T3</b>	<b>T4</b>	<b>T5</b>	<b>T6</b>	<b>T7</b>	<b>T8</b>
<b>[-]</b>	<b>[°C]</b>							
1	9.52	75.04	70.90	24.42	24.61	7.82	2.49	24.58
2	9.59	92.43	87.03	38.68	38.55	7.88	6.60	25.28
3	-7.59	88.14	78.46	22.01	22.51	-15.58	-12.08	16.86
4	3.68	81.55	75.84	26.27	26.39	0.56	-1.77	21.68
5	17.66	109.88	104.88	58.33	58.06	16.93	20.13	24.27
6	-1.66	121.45	109.63	46.21	45.71	-7.08	-2.63	28.48
7	-7.30	89.35	79.49	22.28	22.68	-15.33	-12.55	23.03
8	9.41	73.68	69.74	25.23	25.36	7.91	3.45	-7.22
9	9.37	91.12	86.00	39.28	39.16	7.71	6.16	-6.80
10	3.75	98.78	91.50	39.37	39.12	0.62	0.99	23.14
11	-2.46	87.66	80.27	27.58	27.70	-7.29	-6.42	-16.65
12	-1.88	118.86	107.70	46.35	45.84	-7.15	-2.31	-15.79
13	-7.52	87.87	78.50	22.20	22.52	-15.37	-12.05	-20.92
14	15.38	70.74	67.56	28.00	28.08	14.73	9.32	-1.14
15	15.42	86.67	82.74	40.04	39.96	14.58	12.99	0.24
16	15.44	101.05	96.43	52.08	51.83	14.56	16.78	0.92
17	-1.11	87.92	80.64	27.80	27.97	-5.83	-5.87	-17.81
18	-6.82	115.51	102.29	41.35	40.76	-14.64	-6.87	-20.95
19	-13.29	96.00	83.00	24.22	24.46	-22.96	-15.90	-27.91

Table 4.5 Continued.

<b>Test</b>	<b>T9</b>	<b>T10</b>	<b>T11</b>	<b>T12</b>	<b>P1</b>	<b>P2</b>	<b>P3</b>	<b>P4</b>
<b>[-]</b>	<b>[°C]</b>	<b>[°C]</b>	<b>[°C]</b>	<b>[°C]</b>	<b>[kPa]</b>	<b>[kPa]</b>	<b>[kPa]</b>	<b>[kPa]</b>
1	18.46	21.44	25.65	34.10	423.18	1341.77	1347.78	1363.05
2	34.35	37.12	26.77	34.12	429.89	1891.11	1898.10	1914.97
3	19.74	21.32	23.86	34.12	224.72	1204.57	1214.53	1233.32
4	22.21	24.61	25.41	34.19	342.47	1389.58	1395.04	1414.21
5	51.99	55.19	32.84	34.12	572.57	2836.63	2842.23	2854.26
6	44.04	45.78	30.69	34.14	281.08	2169.76	2178.75	2196.81
7	20.05	21.63	24.64	34.15	223.50	1212.44	1217.37	1240.01
8	18.75	21.80	25.59	34.07	433.58	1360.45	1365.44	1380.89
9	34.23	37.04	26.93	34.09	435.23	1890.84	1896.49	1912.70
10	36.29	38.46	26.37	34.13	343.74	1886.27	1893.58	1911.24
11	24.60	26.53	25.17	34.08	283.83	1411.18	1418.71	1436.49
12	44.12	45.87	28.73	34.10	281.51	2173.43	2182.21	2201.20
13	19.92	21.53	24.07	34.06	226.89	1209.46	1218.63	1236.98
14	19.34	23.01	25.83	34.10	533.50	1455.41	1459.03	1470.61

Table 4.5 Continued.

15	33.10	36.54	27.93	33.96	536.00	1938.62	1943.55	1956.87
16	45.98	49.19	30.67	33.99	541.56	2501.91	2507.52	2520.51
17	24.74	26.74	26.66	34.02	292.62	1423.86	1433.03	1449.88
18	39.59	41.03	25.72	34.09	233.03	1925.09	1934.70	1953.21
19	22.45	23.75	23.21	34.12	187.43	1247.88	1258.65	1276.88

Table 4.5 Continued.

<b>Test</b>	<b>P5</b>	<b>P6</b>	<b>P7</b>	<b>Refrigerant Mass Flow Rate</b>	<b>Water Volumetric Flow Rate</b>
<b>[-]</b>	<b>[kPa]</b>	<b>[kPa]</b>	<b>[kPa]</b>	<b>[kg/s]</b>	<b>[m<sup>3</sup>/h]</b>
1	1350.82	412.00	458.63	0.05993	4.034
2	1901.39	418.20	453.83	0.05982	4.019
3	1223.02	209.15	257.95	0.02979	4.015
4	1404.80	329.64	373.11	0.04762	4.019
5	2836.53	564.18	582.41	0.07920	4.026
6	2189.77	266.23	305.54	0.03643	4.015
7	1229.55	208.17	255.86	0.02962	4.015
8	1367.89	422.78	459.39	0.06180	4.038
9	1898.87	424.07	446.13	0.06089	4.025
10	1900.10	330.23	373.23	0.04692	4.024
11	1428.20	269.37	311.85	0.03861	4.015
12	2193.63	266.76	303.37	0.03679	4.023
13	1230.22	211.38	257.69	0.03018	4.020
14	1453.11	525.38	565.11	0.07764	4.044
15	1939.21	527.31	557.10	0.07639	4.033
16	2503.12	532.72	551.10	0.07611	4.037
17	1442.27	278.56	319.27	0.03988	4.031
18	1945.66	217.48	260.21	0.03032	4.021
19	1269.86	171.18	223.57	0.02429	4.017

Table 4.5 Continued.

<b>Test</b>	<b>C1</b>	<b>V1</b>	<b>PW1</b>	<b>PW2</b>
<b>[-]</b>	<b>[A]</b>	<b>[V]</b>	<b>[kW]</b>	<b>[kW]</b>
1	10.65	230.10	3.00818	10.86511
2	12.64	230.28	3.79299	9.52833
3	9.25	229.71	2.37778	4.90850
4	10.35	229.65	2.91700	8.26856
5	16.41	230.03	5.40711	10.40230
6	12.66	230.29	3.81884	4.89981
7	9.47	230.12	2.39849	4.92188
8	10.83	230.14	3.05037	11.17195

Table 4.5 Continued.

9	12.50	229.76	3.78264	9.63054
10	11.77	229.75	3.54074	7.19590
11	10.25	230.31	2.79277	6.37558
12	12.45	230.23	3.73980	4.93868
13	9.49	229.92	2.39630	4.96069
14	11.38	229.55	3.34413	14.12077
15	13.00	229.65	4.01697	12.30923
16	14.88	230.02	4.80559	10.72020
17	10.27	229.91	2.81994	6.52149
18	11.09	229.86	3.18521	4.08721
19	9.16	230.05	2.29062	3.66606

Table 4.6: Calculated Performance Data for the Scroll Compressor on the Tesco Calorimeter.

<b>Test</b>	<b>Condensing Temperature</b>	<b>Evaporating Temperature</b>	<b>Suction Superheat</b>	<b>Power Draw</b>	<b>Overall Isentropic Efficiency</b>
<b>[-]</b>	<b>[C]</b>	<b>[C]</b>	<b>[C]</b>	<b>[kW]</b>	<b>[-]</b>
1	34.82	-2.383	12.65	3.008	0.5958
2	48.02	-1.942	12.3	3.793	0.6089
3	30.89	-18.88	13.02	2.378	0.547
4	36.12	-8.167	12.86	2.917	0.5952
5	64.97	6.393	11.71	5.407	0.6084
6	53.6	-13.32	13.03	3.819	0.5148
7	31.12	-19.01	13.42	2.398	0.5443
8	35.33	-1.702	11.82	3.05	0.5979
9	48.01	-1.594	11.7	3.783	0.6143
10	47.91	-8.068	12.88	3.541	0.5918
11	36.69	-13.07	11.94	2.793	0.5757
12	53.67	-13.28	12.76	3.74	0.5301
13	31.03	-18.65	12.83	2.396	0.5478
14	37.85	4.285	11.55	3.344	0.5995
15	49.01	4.423	11.48	4.017	0.6321
16	59.57	4.729	11.2	4.806	0.6276
17	37.03	-12.29	12.43	2.82	0.5825
18	48.73	-18	12.85	3.185	0.5298
19	32.16	-23.19	11.99	2.291	0.5213

Table 4.6 Continued.

<b>Test</b>	<b>Volumetric Efficiency</b>	<b>Evaporating Capacity</b>	<b>Pressure Ratio</b>	<b>COP</b>
<b>[-]</b>	<b>[-]</b>	<b>[kW]</b>	<b>[-]</b>	<b>[-]</b>
1	0.8994	10.87	3.171	3.612
2	0.8825	9.528	4.399	2.512
3	0.8168	4.908	5.36	2.064
4	0.8758	8.269	4.058	2.835
5	0.8833	10.4	4.954	1.924
6	0.8087	4.9	7.719	1.283
7	0.818	4.922	5.425	2.052
8	0.9024	11.17	3.138	3.662
9	0.8852	9.631	4.344	2.546
10	0.8598	7.196	5.487	2.032
11	0.8448	6.376	4.972	2.283
12	0.8144	4.939	7.721	1.321
13	0.8195	4.961	5.331	2.07
14	0.9268	14.12	2.728	4.223

Table 4.6 Continued.

15	0.9074	12.31	3.617	3.064
16	0.8937	10.72	4.62	2.231
17	0.85	6.521	4.866	2.313
18	0.8029	4.087	8.261	1.283
19	0.7861	3.666	6.658	1.6

## APPENDIX D: ROTARY COMPRESSOR DATA

Table 4.7: Measurement Data for the Rotary Compressor on the Tescor Calorimeter.

<b>Test</b>	<b>T1</b>	<b>T2</b>	<b>T3</b>	<b>T4</b>	<b>T5</b>	<b>T6</b>	<b>T7</b>	<b>T8</b>
<b>[-]</b>	<b>[°C]</b>							
1	-2.25	0.45	116.14	106.12	52.75	52.37	-6.06	-10.53
2	-0.78	1.43	75.23	69.88	23.34	23.55	-7.86	-10.74
3	-1.93	0.38	86.89	80.32	32.53	32.40	-7.31	-10.56
4	-2.36	-0.03	100.64	92.68	43.66	43.47	-4.58	-10.29
5	-8.43	-4.85	78.61	71.88	22.50	22.60	-11.71	-15.50
6	8.85	9.85	67.79	64.49	26.57	26.64	1.87	-1.80
7	8.45	9.56	76.21	72.30	33.51	33.64	2.59	-1.67
8	7.90	8.97	89.63	84.72	43.61	43.60	2.84	-1.51
9	8.44	9.68	103.23	97.13	51.83	51.76	3.02	-1.31
10	3.96	5.46	68.88	65.01	25.22	25.31	-2.46	-5.51
11	2.88	4.56	79.23	74.71	33.27	33.40	-1.92	-5.41
12	3.70	5.23	94.11	88.20	43.55	43.54	-1.45	-5.06
13	6.91	8.30	96.38	90.66	46.45	46.46	3.15	20.74
14	3.54	5.44	108.62	100.98	51.83	51.66	0.35	9.71
15	14.75	15.45	82.21	78.41	40.57	40.31	23.26	9.94
16	14.23	15.14	100.40	95.15	50.46	50.05	29.14	9.98
17	4.41	6.00	81.26	76.12	31.78	31.74	-0.31	21.56
18	14.67	15.50	92.96	88.34	45.46	45.16	28.35	10.11
19	13.95	14.57	66.65	63.95	28.21	28.30	24.83	8.92
20	14.53	15.16	73.63	70.50	32.89	32.82	22.86	9.60
21	13.03	14.09	102.02	96.55	50.43	50.08	28.67	8.69
22	13.48	14.25	88.20	83.74	41.57	41.28	25.83	8.39
23	-11.53	-7.53	86.44	77.76	23.52	23.66	-13.34	19.79
24	-11.20	-7.03	94.57	84.68	28.85	28.70	-11.77	20.54
25	-4.21	-1.58	78.44	72.20	23.38	23.53	-8.21	20.23
26	-18.69	-12.65	97.05	84.18	23.36	23.50	-17.35	19.41
27	-4.43	-1.63	84.72	77.79	27.79	27.72	-7.61	20.60
28	-18.87	-12.66	105.12	90.53	29.49	29.19	-15.27	20.24
29	1.71	3.50	73.92	69.23	24.75	24.82	-3.10	21.04
30	2.46	4.33	78.56	73.41	27.36	27.33	-2.90	20.72
31	8.52	9.67	72.74	68.94	27.32	27.36	2.73	20.61
32	9.46	10.54	79.23	74.80	33.16	33.19	3.77	22.03
33	-11.92	-7.23	109.91	97.75	40.04	39.47	-7.41	24.02
34	-12.26	-7.18	130.85	115.01	51.74	50.61	-12.47	25.64
35	-5.86	-2.48	102.55	93.82	39.84	39.49	-6.47	24.40
36	-20.49	-13.21	123.15	102.57	40.75	39.65	-13.58	20.30
37	-4.88	-1.62	120.61	109.23	51.27	50.50	-6.74	26.19
38	-18.95	-12.44	137.73	117.75	51.25	49.85	-17.00	23.74

Table 4.7 Continued.

39	1.94	3.94	95.13	88.46	39.60	39.31	-1.53	24.62
40	1.55	3.67	111.60	103.04	50.89	50.30	-0.87	25.98
41	8.33	9.58	88.62	83.73	39.15	39.03	4.20	24.05
42	8.37	9.63	105.28	98.64	50.58	50.17	4.54	26.56
43	13.75	14.50	82.17	78.42	38.57	38.44	23.43	9.25
44	14.26	15.10	100.18	95.21	50.51	50.23	27.99	10.07

Table 4.7 Continued.

<b>Test</b>	<b>T9</b>	<b>T10</b>	<b>T11</b>	<b>T12</b>	<b>P1</b>	<b>P2</b>	<b>P3</b>	<b>P4</b>
<b>[-]</b>	<b>[°C]</b>	<b>[°C]</b>	<b>[°C]</b>	<b>[°C]</b>	<b>[kPa]</b>	<b>[kPa]</b>	<b>[kPa]</b>	<b>[kPa]</b>
1	48.97	50.63	26.60	34.12	572.85	3336.01	3344.89	3357.29
2	17.94	20.19	22.20	34.25	570.01	1678.56	1685.33	1703.08
3	27.89	29.95	22.81	34.13	572.76	2121.55	2131.70	2147.08
4	39.17	41.03	25.10	34.11	576.04	2723.73	2732.08	2746.59
5	18.15	20.08	22.38	34.10	482.21	1637.84	1646.09	1663.46
6	18.45	21.41	23.49	34.10	767.38	1807.23	1811.66	1827.80
7	25.83	28.60	24.58	33.96	769.82	2135.36	2142.91	2156.76
8	36.84	39.37	27.07	34.00	771.42	2715.80	2722.86	2735.90
9	45.85	48.22	28.05	34.10	774.52	3267.90	3275.60	3286.75
10	18.15	20.79	22.57	34.28	679.61	1745.43	1749.89	1767.50
11	26.61	29.10	24.48	34.11	680.50	2124.55	2131.84	2146.00
12	37.81	40.06	26.37	34.13	684.28	2716.68	2724.21	2737.41
13	40.28	42.65	28.22	34.15	737.08	2896.95	2904.20	2915.92
14	46.93	48.96	27.74	34.32	670.05	3266.44	3274.59	3287.04
15	33.51	36.63	23.72	34.23	925.15	2631.59	2633.88	2647.61
16	45.63	48.37	25.33	34.24	917.12	3373.53	3377.01	3389.65
17	26.98	29.46	22.42	34.34	682.98	2162.27	2165.56	2182.29
18	40.29	43.24	23.66	34.23	924.41	3060.20	3062.94	3075.87
19	21.11	24.65	23.29	34.15	927.57	2065.17	2066.67	2080.22
20	26.37	29.75	22.74	34.24	926.09	2314.70	2316.56	2330.56
21	45.79	48.45	26.15	34.22	881.35	3360.72	3364.61	3377.27
22	36.50	39.42	23.21	34.23	891.32	2811.90	2814.37	2828.62
23	21.14	22.85	20.95	34.28	432.61	1742.97	1750.64	1769.75
24	26.77	28.37	22.19	34.24	433.30	1995.86	2003.41	2022.47
25	20.19	22.27	21.22	34.28	528.12	1764.46	1771.79	1789.96
26	21.62	22.98	20.73	34.25	347.86	1708.51	1716.57	1736.40
27	24.85	26.84	22.00	34.24	530.35	1971.77	1979.00	1996.92
28	28.07	29.33	22.17	34.25	349.45	1998.52	2006.97	2026.75
29	20.57	23.07	22.02	34.25	636.85	1850.40	1856.59	1873.81
30	23.42	25.82	21.91	34.18	638.24	1976.82	1982.71	2000.08
31	21.88	24.80	21.74	34.25	768.09	1990.34	1994.55	2010.47
32	28.24	31.03	23.55	34.25	779.80	2296.67	2302.15	2318.19

Table 4.7 Continued.

33	38.38	39.83	25.17	34.22	438.16	2604.74	2611.14	2629.13
34	50.65	51.89	26.43	34.20	434.53	3377.43	3383.98	3399.67
35	37.41	39.21	25.31	34.25	531.57	2618.91	2624.85	2642.13
36	39.88	40.94	22.92	34.29	338.88	2617.83	2624.84	2643.30
37	49.49	51.06	26.75	34.27	530.58	3370.48	3376.85	3391.57
38	50.54	51.58	24.83	34.26	373.11	3323.94	3330.84	3346.66
39	36.33	38.49	25.18	34.22	640.04	2634.65	2639.85	2656.54
40	48.31	50.24	25.84	34.26	641.54	3369.64	3375.31	3389.07
41	34.72	37.39	24.49	34.18	775.91	2641.21	2645.37	2661.12
42	47.07	49.39	26.80	34.27	765.19	3374.66	3379.51	3392.91
43	32.80	35.97	22.82	34.35	920.43	2630.33	2632.69	2647.06
44	45.51	48.31	27.18	34.25	912.16	3369.85	3373.60	3385.54

Table 4.7 Continued.

<b>Test</b>	<b>P5</b>	<b>P6</b>	<b>P7</b>	<b>Refrigerant Mass Flow Rate</b>	<b>Water Volumetric Flow Rate</b>
<b>[-]</b>	<b>[kPa]</b>	<b>[kPa]</b>	<b>[kPa]</b>	<b>[kg/s]</b>	<b>[m<sup>3</sup>/h]</b>
1	3350.59	557.31	346.18	0.0398	4.0411
2	1692.86	554.63	359.35	0.0432	4.0510
3	2137.36	557.24	351.35	0.0426	4.0338
4	2737.88	560.53	343.74	0.0417	4.0358
5	1655.32	465.79	317.91	0.0363	4.0475
6	1813.57	754.91	479.09	0.0600	4.0533
7	2143.10	757.17	474.16	0.0593	4.0345
8	2724.10	758.62	461.01	0.0578	4.0324
9	3276.84	761.77	457.67	0.0561	4.0348
10	1755.92	665.62	417.60	0.0527	4.0518
11	2135.29	666.74	408.97	0.0524	4.0339
12	2727.13	670.30	402.25	0.0505	4.0349
13	2906.34	723.46	452.23	0.0540	4.0198
14	3277.69	655.38	411.69	0.0475	4.0239
15	2630.99	920.24	574.89	0.0704	3.9978
16	3376.36	903.82	559.06	0.0652	3.9963
17	2169.61	667.62	430.95	0.0507	3.9904
18	3061.30	918.97	570.81	0.0679	4.0009
19	2063.41	927.07	591.26	0.0739	4.0100
20	2313.07	931.06	589.01	0.0729	3.9962
21	3365.49	867.55	536.62	0.0622	3.9858
22	2813.93	885.19	552.44	0.0658	3.9929
23	1761.07	421.45	289.85	0.0312	3.9869
24	2014.29	421.88	290.02	0.0307	3.9766
25	1780.22	518.89	345.79	0.0393	3.9971

Table 4.7 Continued.

26	1728.93	335.80	242.42	0.0242	3.9821
27	1987.48	519.75	343.18	0.0388	3.9833
28	2019.29	337.37	241.45	0.0238	3.9750
29	1861.57	628.49	405.97	0.0482	3.9988
30	1988.74	628.72	408.06	0.0478	3.9888
31	1997.63	761.23	488.13	0.0587	3.9964
32	2303.50	772.69	490.44	0.0585	3.9849
33	2621.76	426.57	285.76	0.0300	3.9751
34	3394.38	422.76	279.27	0.0281	3.9843
35	2633.64	520.84	335.05	0.0377	3.9778
36	2634.45	326.52	231.43	0.0219	3.9744
37	3385.84	520.47	332.20	0.0357	3.9841
38	3340.82	360.50	244.21	0.0234	3.9810
39	2646.38	630.20	398.79	0.0462	3.9792
40	3381.74	632.36	389.65	0.0444	3.9852
41	2647.86	767.83	477.01	0.0571	3.9894
42	3383.22	757.36	465.75	0.0539	3.9867
43	2629.67	917.79	566.94	0.0698	3.9927
44	3372.97	906.00	555.02	0.0656	3.9884

Table 4.7 Continued.

<b>Test</b>	<b>C1</b>	<b>V1</b>	<b>PW1</b>	<b>PW2</b>
<b>[-]</b>	<b>[A]</b>	<b>[V]</b>	<b>[kW]</b>	<b>[kW]</b>
1	15.72	229.74	3.6606	5.2722
2	11.46	230.05	2.4236	8.1010
3	12.61	229.55	2.8004	7.2521
4	14.04	229.25	3.2227	6.3013
5	11.19	229.27	2.3456	6.5957
6	11.79	229.97	2.5431	11.3028
7	12.81	229.21	2.8701	10.3584
8	14.64	229.52	3.3854	9.0389
9	16.44	229.78	3.8646	7.8800
10	11.56	229.11	2.4765	9.8868
11	12.79	229.88	2.8426	8.9177
12	14.40	229.27	3.3267	7.7765
13	15.03	229.41	3.5110	8.1964
14	15.91	229.67	3.7467	6.5995
15	14.64	229.64	3.3811	11.8480
16	17.29	229.46	4.0715	9.7756
17	12.82	229.56	2.8673	9.0746
18	16.21	229.28	3.7935	10.8462
19	12.45	229.66	2.7567	13.9727

Table 4.7 Continued.

20	13.42	229.79	3.0402	13.3723
21	17.16	229.22	4.0358	9.2258
22	15.23	229.72	3.5444	11.1280
23	11.20	229.03	2.3821	5.7349
24	11.78	229.32	2.5613	5.4054
25	11.49	229.66	2.4652	7.4397
26	10.94	229.47	2.2807	4.2901
27	12.00	229.56	2.6336	7.0259
28	11.53	229.88	2.4644	3.9515
29	11.78	229.27	2.5649	9.1588
30	12.20	229.82	2.6890	8.8711
31	12.30	229.48	2.7230	11.1751
32	13.28	229.47	3.0080	10.4052
33	13.10	229.19	2.9551	4.6043
34	14.73	230.00	3.3990	3.7245
35	13.67	229.91	3.1084	5.8831
36	12.42	229.94	2.7840	3.2269
37	15.46	230.02	3.5995	4.9574
38	14.02	228.99	3.2045	2.9812
39	14.10	229.92	3.2304	7.5726
40	16.12	229.79	3.7730	6.3237
41	14.43	229.67	3.3232	9.6258
42	16.74	230.10	3.9320	7.9774
43	14.61	229.59	3.3730	11.9879
44	17.23	230.06	4.0568	9.8826

Table 4.8: Calculated Performance Data for the Rotary Compressor on the Tesco Calorimeter.

<b>Test</b>	<b>Condensing Temperature</b>	<b>Evaporating Temperature</b>	<b>Suction Superheat</b>	<b>Power Draw</b>	<b>Overall Isentropic Efficiency</b>
<b>[-]</b>	<b>[C]</b>	<b>[C]</b>	<b>[C]</b>	<b>[kW]</b>	<b>[-]</b>
1	53.75	-9.991	11.24	3.661	0.5792
2	25.6	-10.14	12.35	2.424	0.5698
3	34.69	-9.996	11.17	2.8	0.5906
4	44.96	-9.83	10.58	3.223	0.5999
5	24.67	-14.87	10.99	2.346	0.5579
6	28.41	-1.225	11.58	2.543	0.5903
7	34.94	-1.126	11.2	2.87	0.6177
8	44.84	-1.061	10.55	3.385	0.6322
9	52.83	-0.9363	11.13	3.865	0.6212
10	27.08	-4.942	11.02	2.477	0.5863
11	34.74	-4.903	10.08	2.843	0.6145
12	44.85	-4.736	10.59	3.327	0.62
13	47.59	-2.47	11.34	3.511	0.6253
14	52.81	-5.369	11.47	3.747	0.6024
15	43.51	4.719	10.9	3.381	0.6356
16	54.24	4.436	11.18	4.071	0.6138
17	35.45	-4.793	11.48	2.867	0.6022
18	49.96	4.693	11	3.793	0.6294
19	33.61	4.804	9.787	2.757	0.6181
20	38.2	4.752	10.23	3.04	0.6379
21	54.07	3.151	11.44	4.036	0.6104
22	46.32	3.513	10.96	3.544	0.6262
23	27.02	-17.85	11.03	2.382	0.5439
24	32.27	-17.81	11.5	2.561	0.5491
25	27.49	-12.32	11.24	2.465	0.569
26	26.27	-23.61	11.86	2.281	0.5077
27	31.79	-12.2	11.14	2.634	0.5751
28	32.32	-23.49	11.73	2.464	0.5099
29	29.32	-6.887	10.78	2.565	0.5889
30	31.89	-6.822	11.6	2.689	0.5946
31	32.16	-1.196	11.15	2.723	0.6008
32	37.88	-0.7249	11.55	3.008	0.6194
33	43.08	-17.51	11.01	2.955	0.5481
34	54.29	-17.73	11.3	3.399	0.5195
35	43.31	-12.14	10.23	3.108	0.5781
36	43.29	-24.28	12.01	2.784	0.4938
37	54.2	-12.19	11.11	3.6	0.5575
38	53.59	-21.79	10.25	3.204	0.4885
39	43.56	-6.738	11.14	3.23	0.6031

Table 4.8 Continued.

40	54.19	-6.669	10.77	3.773	0.5865
41	43.66	-0.8807	10.79	3.323	0.6206
42	54.26	-1.313	11.27	3.932	0.607
43	43.49	4.552	10.04	3.373	0.6314
44	54.19	4.26	11.06	4.057	0.623

Table 4.8 Continued.

<b>Test</b>	<b>Volumetric Efficiency</b>	<b>Evaporating Capacity</b>	<b>Pressure Ratio</b>	<b>COP</b>
<b>[-]</b>	<b>[-]</b>	<b>[kW]</b>	<b>[-]</b>	<b>[-]</b>
1	0.7905	5.272	5.824	1.44
2	0.8669	8.101	2.945	3.343
3	0.8443	7.252	3.704	2.59
4	0.8196	6.301	4.728	1.955
5	0.8492	6.596	3.397	2.812
6	0.897	11.3	2.355	4.444
7	0.8811	10.36	2.774	3.609
8	0.8535	9.039	3.521	2.67
9	0.8287	7.88	4.219	2.039
10	0.8843	9.887	2.568	3.992
11	0.8737	8.918	3.122	3.137
12	0.8396	7.776	3.97	2.338
13	0.8379	8.196	3.93	2.335
14	0.8101	6.599	4.875	1.761
15	0.871	11.85	2.844	3.504
16	0.8136	9.776	3.678	2.401
17	0.8493	9.075	3.166	3.165
18	0.8419	10.85	3.31	2.859
19	0.9074	13.97	2.226	5.069
20	0.9001	13.37	2.499	4.398
21	0.81	9.226	3.813	2.286
22	0.8459	11.13	3.155	3.14
23	0.8134	5.735	4.029	2.408
24	0.7994	5.405	4.606	2.11
25	0.8449	7.44	3.341	3.018
26	0.7794	4.29	4.912	1.881
27	0.8307	7.026	3.718	2.668
28	0.763	3.952	5.719	1.603
29	0.8624	9.159	2.906	3.571
30	0.8571	8.871	3.097	3.299
31	0.8754	11.18	2.591	4.104
32	0.8617	10.41	2.945	3.459

Table 4.8 Continued.

33	0.7719	4.604	5.945	1.558
34	0.7294	3.724	7.773	1.096
35	0.8006	5.883	4.927	1.893
36	0.7234	3.227	7.725	1.159
37	0.765	4.957	6.352	1.377
38	0.6981	2.981	8.909	0.9303
39	0.823	7.573	4.116	2.344
40	0.789	6.324	5.252	1.676
41	0.8412	9.626	3.404	2.897
42	0.8074	7.977	4.41	2.029
43	0.8638	11.99	2.858	3.554
44	0.8241	9.883	3.694	2.436

## APPENDIX E: OIL-FREE SCROLL COMPRESSOR EES ANALYSIS SCRIPT

"ASI Scroll Compressor Data Analysis"

!"Input steady state data to be analyzed"

R\$='R134a'

Row = "7" TableRun#

P[1]=**lookup**('Raw Data', Row, 'Suction Pressure') "Suction Pressure"  
 P[2]=**lookup**('Raw Data', Row, 'Discharge Pressure') "Discharge Pressure"  
 P[3]=**lookup**('Raw Data', Row, 'Intermediate Pressure') "Intermediate (Condensing Temperature)"  
 P[4]=**lookup**('Raw Data', Row, 'Gas Line Pressure') "Gas Line Suction Pressure"  
 P[5]=**lookup**('Raw Data', Row, 'Liquid Line Pressure') "Liquid Line Suction Pressure"  
 P[6]=P[3]

"Condenser Outlet Pressure (Liquid Line)"

T[1]=**lookup**('Raw Data', Row, 'Suction Temperature') "Suction Temperature"  
 T[2]=**lookup**('Raw Data', Row, 'Discharge Temperature') "Discharge Temperature"  
 T[3]=**lookup**('Raw Data', Row, 'Intermediate Temperature')  
 "Intermediate Temperature"  
 T[4]=**lookup**('Raw Data', Row, 'Gas Line Temperature') "Gas Line Suction Temperature"  
 T[5]=**lookup**('Raw Data', Row, 'Liquid Line Temperature')  
 "Liquid Line Suction Temperature"  
 T\_Ambient=**lookup**('Raw Data', Row, 'Ambient Temperature')  
 "Ambient Temperature"  
 T[6]=**lookup**('Raw Data', Row, 'Condenser Temperature')  
 "Condenser Outlet Temperature (Liquid Line)"

m\_dot\_r=**lookup**('Raw Data', Row, 'Mass Flow Rate') "Mass flowrate through the test stand"  
 W\_dot\_Motor=**lookup**('Raw Data', Row, 'Power Draw') "Power input to the compressor controller/motor"  
 Freq\_Motor=(**lookup**('Raw Data', Row, 'Shaft Speed')) "RPM of the motor shaft~="RPM of the  
 compressor shaft (Input: RPM/60)"  
 V\_D=0.0000083 [m^3]

!"Analysis of Data Collected"

T\_Condenser\_Hot\_Gas=**temperature**(R\$,P=P[3],x=1) "Hot Gas By-Pass Test Stand Condensing  
 Temperature"  
 T\_Condenser\_Cycle=**temperature**(R\$,P=P[2],x=1) "Cycle Condensing Temperature"  
 T\_Evaporator=**temperature**(R\$,P=P[1],x=1) "Evaporating Temperature"  
 T\_Liq\_Line\_Evap=**temperature**(R\$,P=P[5],x=1) "Evaporating Temperature of the Liquid Line of  
 the Test Stand"  
 T\_Superheat=T[1]-T\_Evaporator "Superheat into the compressor on the test  
 stand"  
 T\_Subcooling\_Liq\_Line=T\_Condenser\_Hot\_Gas-T[6] "Subcooling of liquid line at the outlet of the  
 condenser"  
 T\_Superheat\_Liq\_Line=T[5]-T\_Liq\_Line\_Evap "Superheat of the liquid line after throttling"

"Suction"

h[1]=**enthalpy**(R\$,P=P[1],T=T[1])  
 s[1]=**entropy**(R\$,P=P[1],T=T[1])  
 v[1]=**volume**(R\$,P=P[1],T=T[1])

$x[1]=\text{quality}(R\$, P=P[1], T=T[1])$

#### "Discharge"

$h[2]=\text{enthalpy}(R\$, P=P[2], T=T[2])$   
 $s[2]=\text{entropy}(R\$, P=P[2], T=T[2])$   
 $v[2]=\text{volume}(R\$, P=P[2], T=T[2])$   
 $x[2]=\text{quality}(R\$, P=P[2], T=T[2])$   
 $s\_2s=s[1]$   
 $h\_2s=\text{enthalpy}(R\$, P=P[2], s=s\_2s)$

$h\_is[1]=h[1]$   
 $h\_is[2]=h\_2s$

#### "Intermediate"

$h[3]=\text{enthalpy}(R\$, P=P[3], T=T[3])$   
 $s[3]=\text{entropy}(R\$, P=P[3], T=T[3])$   
 $v[3]=\text{volume}(R\$, P=P[3], T=T[3])$   
 $x[3]=\text{quality}(R\$, P=P[3], T=T[3])$

#### "Gas Suction"

$h[4]=\text{enthalpy}(R\$, P=P[4], T=T[4])$   
 $s[4]=\text{entropy}(R\$, P=P[4], T=T[4])$   
 $v[4]=\text{volume}(R\$, P=P[4], T=T[4])$   
 $x[4]=\text{quality}(R\$, P=P[4], T=T[4])$

#### "Liquid Suction"

$T\_5\_Line=\text{temperature}(R\$, P=P[5], x=1)$   
 $h[5]=h[6]\text{"enthalpy}(R\$, P=P[5], T=T[5])"}$   
 $s[5]=\text{entropy}(R\$, P=P[5], h=h[5])$   
 $v[5]=\text{volume}(R\$, P=P[5], h=h[5])$   
 $x[5]=\text{quality}(R\$, P=P[5], h=h[5])$

#### "Test Stand Condenser"

$h[6]=\text{enthalpy}(R\$, P=P[6], T=T[6])$   
 $s[6]=\text{entropy}(R\$, P=P[6], T=T[6])$   
 $v[6]=\text{volume}(R\$, P=P[6], T=T[6])$   
 $x[6]=\text{quality}(R\$, P=P[6], T=T[6])$

#### "Plotting Purposes"

$h\_Hot\_Gas[3]=h[3]$   
 $h\_Hot\_Gas[4]=h[4]$   
 $h\_Hot\_Gas[5]=h[1]$   
 $P\_Hot\_Gas[3]=P[3]$   
 $P\_Hot\_Gas[4]=P[4]$   
 $P\_Hot\_Gas[5]=P[1]$

$h\_Liq\_Line[4]=h[3]$   
 $h\_Liq\_Line[5]=h[6]$   
 $h\_Liq\_Line[6]=h[5]$   
 $h\_Liq\_Line[7]=h[1]$   
 $P\_Liq\_Line[4]=P[3]$   
 $P\_Liq\_Line[5]=P[6]$   
 $P\_Liq\_Line[6]=P[5]$   
 $P\_Liq\_Line[7]=P[1]$

**"Flow Mixing Analysis"**

$$m_{\dot{r}} = m_{\dot{liq}} + m_{\dot{hot}}$$

$$m_{\dot{r}} h[1] = (m_{\dot{liq}} h[5]) + (m_{\dot{hot}} h[4])$$

**"Condenser Analysis"**

$$Q_{\dot{Cond}} = m_{\dot{liq}} (h[3] - h[6])$$

$$\Delta \text{Enthalpy}_{\text{Condenser}} = h[3] - h[6]$$

**"Simulated Cooling Capacity"****"Compressor Suction"**

$$P_{\text{sim}}[1] = P[1]$$

$$T_{\text{sim}}[1] = T[1]$$

$$h_{\text{sim}}[1] = h[1]$$

**"Compressor Discharge"**

$$P_{\text{sim}}[2] = P[2]$$

$$T_{\text{sim}}[2] = T[2]$$

$$h_{\text{sim}}[2] = h[2]$$

**"Condenser Outlet"**

$$P_{\text{sim}}[3] = P_{\text{sim}}[2]$$

$$T_{\text{sim\_SC}} = 5 \text{ [C]}$$

$$T_{\text{sim\_Cond}} = \text{temperature}(R\$, P = P_{\text{sim}}[2], x = 1)$$

$$T_{\text{sim}}[3] = T_{\text{sim\_Cond}} - T_{\text{sim\_SC}}$$

$$h_{\text{sim}}[3] = \text{enthalpy}(R\$, T = T_{\text{sim}}[3], P = P_{\text{sim}}[3])$$

**"Evaporator Inlet"**

$$h_{\text{sim}}[4] = h_{\text{sim}}[3]$$

$$P_{\text{sim}}[4] = P_{\text{sim}}[1]$$

$$T_{\text{sim}}[4] = \text{temperature}(R\$, h = h_{\text{sim}}[4], P = P_{\text{sim}}[4])$$

**"Cooling Capacity"**

$$Q_{\dot{\text{sim\_Evap}}} = m_{\dot{r}} (h_{\text{sim}}[1] - h_{\text{sim}}[4])$$

$$\text{COP} = Q_{\dot{\text{sim\_Evap}}} / W_{\dot{\text{Motor}}}$$

**"Compressor Analysis"**

$$P_{\text{Rat}} = P[2] / P[1]$$

$$W_{\dot{\text{Compressor}}} = m_{\dot{r}} (h[2] - h[1])$$

**compressor"**

$$\eta_{\text{Motor}} = (W_{\dot{\text{Compressor}}}) / (W_{\dot{\text{Motor}}})$$

**refrigerant"**

$$\eta_{\text{Isentropic\_Enthalpy}} = (h_{2s} - h[1]) / (h[2] - h[1])$$

$$\eta_{\text{Overall}} = (m_{\dot{r}} (h_{2s} - h[1])) / W_{\dot{\text{Motor}}}$$

$$\eta_{\text{Volume}} = (m_{\dot{r}} v[1]) / (\text{Freq\_Motor} * V_D)$$

**"Pressure Ratio"****"Work input into the refrigerant by the****"Efficiency of motor to input work into the****"Isentropic Efficiency"****"Overall Isentropic Compressor Efficiency"****"Volumetric Efficiency"**

## APPENDIX F: RECIPROCATING COMPRESSOR EES ANALYSIS SCRIPT

"Reciprocating Compressor Data Analysis"

"!Input steady state data to be analyzed"

R\$='R134a'

Row = "7" TableRun#

P[1]=**lookup**('Raw Data', Row, 'Suction Pressure') "Suction Pressure"  
 P[2]=**lookup**('Raw Data', Row, 'Discharge Pressure') "Discharge Pressure"  
 P[3]=**lookup**('Raw Data', Row, 'Intermediate Pressure') "Intermediate (Condensing Temperature)"  
 P[4]=**lookup**('Raw Data', Row, 'Gas Line Pressure') "Gas Line Suction Pressure"  
 P[5]=**lookup**('Raw Data', Row, 'Liquid Line Pressure') "Liquid Line Suction Pressure"  
 P[6]=P[3]

"Condenser Outlet Pressure (Liquid Line)"

T[1]=**lookup**('Raw Data', Row, 'Suction Temperature') "Suction Temperature"

T[2]=**lookup**('Raw Data', Row, 'Discharge Temperature Close')

"Discharge Temperature"

T[3]=**lookup**('Raw Data', Row, 'Intermediate Temperature')

"Intermediate Temperature"

T[4]=**lookup**('Raw Data', Row, 'Gas Line Temperature') "Gas Line Suction Temperature"

T[5]=**lookup**('Raw Data', Row, 'Liquid Line Temperature')

"Liquid Line Suction Temperature"

T\_Ambient=**lookup**('Raw Data', Row, 'Ambient Temperature')

"Ambient Temperature"

T[6]=**lookup**('Raw Data', Row, 'Condenser Temperature')

"Condenser Outlet Temperature (Liquid Line)"

m\_dot\_r=**lookup**('Raw Data', Row, 'Mass Flow Rate') "Mass flowrate through the test stand"

W\_dot\_Motor=**lookup**('Raw Data', Row, 'Power Draw') "Power input to the compressor controller/motor"

Freq\_Motor=(**lookup**('Raw Data', Row, 'Shaft Speed')) "RPM of the motor shaft~RPM of the compressor shaft (Input: RPM/60)"

V\_D=0.00000397 [m^3]

"!Analysis of Data Collected"

T\_Condenser\_Hot\_Gas=**temperature**(R\$,P=P[3],x=1) "Hot Gas By-Pass Test Stand Condensing Temperature"

T\_Condenser\_Cycle=**temperature**(R\$,P=P[2],x=1) "Cycle Condensing Temperature"

T\_Evaporator=**temperature**(R\$,P=P[1],x=1) "Evaporating Temperature"

T\_Liq\_Line\_Evap=**temperature**(R\$,P=P[5],x=1) "Evaporating Temperature of the Liquid Line of the Test Stand"

T\_Superheat=T[1]-T\_Evaporator "Superheat into the compressor on the test stand"

T\_Subcooling\_Liq\_Line=T\_Condenser\_Hot\_Gas-T[6] "Subcooling of liquid line at the outlet of the condenser"

T\_Superheat\_Liq\_Line=T[5]-T\_Liq\_Line\_Evap "Superheat of the liquid line after throttling"

"Suction"

h[1]=**enthalpy**(R\$,P=P[1],T=T[1])

s[1]=**entropy**(R\$,P=P[1],T=T[1])

$v[1]=\text{volume}(R\$,P=P[1],T=T[1])$   
 $x[1]=\text{quality}(R\$,P=P[1],T=T[1])$   
 $\rho[1]=\text{density}(R\$,P=P[1],T=T[1])$

#### "Discharge"

$h[2]=\text{enthalpy}(R\$,P=P[2],T=T[2])$   
 $s[2]=\text{entropy}(R\$,P=P[2],T=T[2])$   
 $v[2]=\text{volume}(R\$,P=P[2],T=T[2])$   
 $x[2]=\text{quality}(R\$,P=P[2],T=T[2])$   
 $s\_2s=s[1]$   
 $h\_2s=\text{enthalpy}(R\$,P=P[2],s=s\_2s)$

$h\_is[1]=h[1]$   
 $h\_is[2]=h\_2s$

#### "Intermediate"

$h[3]=\text{enthalpy}(R\$,P=P[3],T=T[3])$   
 $s[3]=\text{entropy}(R\$,P=P[3],T=T[3])$   
 $v[3]=\text{volume}(R\$,P=P[3],T=T[3])$   
 $x[3]=\text{quality}(R\$,P=P[3],T=T[3])$

#### "Gas Suction"

$h[4]=\text{enthalpy}(R\$,P=P[4],T=T[4])$   
 $s[4]=\text{entropy}(R\$,P=P[4],T=T[4])$   
 $v[4]=\text{volume}(R\$,P=P[4],T=T[4])$   
 $x[4]=\text{quality}(R\$,P=P[4],T=T[4])$

#### "Liquid Suction"

$T\_5\_Line=\text{temperature}(R\$,P=P[5],x=1)$   
 $h[5]=h[6]\text{"enthalpy}(R\$,P=P[5],T=T[5])"}$   
 $s[5]=\text{entropy}(R\$,P=P[5],h=h[5])$   
 $v[5]=\text{volume}(R\$,P=P[5],h=h[5])$   
 $x[5]=\text{quality}(R\$,P=P[5],h=h[5])$

#### "Test Stand Condenser"

$h[6]=\text{enthalpy}(R\$,P=P[6],T=T[6])$   
 $s[6]=\text{entropy}(R\$,P=P[6],T=T[6])$   
 $v[6]=\text{volume}(R\$,P=P[6],T=T[6])$   
 $x[6]=\text{quality}(R\$,P=P[6],T=T[6])$

#### "Plotting Purposes"

$h\_Hot\_Gas[3]=h[3]$   
 $h\_Hot\_Gas[4]=h[4]$   
 $h\_Hot\_Gas[5]=h[1]$   
 $P\_Hot\_Gas[3]=P[3]$   
 $P\_Hot\_Gas[4]=P[4]$   
 $P\_Hot\_Gas[5]=P[1]$

$h\_Liq\_Line[4]=h[3]$   
 $h\_Liq\_Line[5]=h[6]$   
 $h\_Liq\_Line[6]=h[5]$   
 $h\_Liq\_Line[7]=h[1]$   
 $P\_Liq\_Line[4]=P[3]$   
 $P\_Liq\_Line[5]=P[6]$

P\_Liq\_Line[6]=P[5]  
P\_Liq\_Line[7]=P[1]

#### "Flow Mixing Analysis"

m\_dot\_r=m\_dot\_liq+m\_dot\_hot  
m\_dot\_r\*h[1]=(m\_dot\_liq\*h[5])+(m\_dot\_hot\*h[4])

#### "Condenser Analysis"

Q\_dot\_Cond=m\_dot\_liq\*(h[3]-h[6])  
DELTAEnthalpy\_Condenser=h[3]-h[6]

#### "Simulated Cooling Capacity"

##### "Compressor Suction"

P\_sim[1] = P[1]  
T\_sim[1] = T[1]  
h\_sim[1] = h[1]

##### "Compressor Discharge"

P\_sim[2] = P[2]  
T\_sim[2] = T[2]  
h\_sim[2] = h[2]

##### "Condenser Outlet"

P\_sim[3] = P\_sim[2]  
T\_sim\_SC = 5 [C]  
T\_sim\_Cond = **temperature**(R\$, P = P\_sim[2], x = 1)  
T\_sim[3] = T\_sim\_Cond - T\_sim\_SC  
h\_sim[3] = **enthalpy**(R\$, T = T\_sim[3], P = P\_sim[3])

##### "Evaporator Inlet"

h\_sim[4] = h\_sim[3]  
P\_sim[4] = P\_sim[1]  
T\_sim[4] = **temperature**(R\$, h = h\_sim[4], P = P\_sim[4])

##### "Cooling Capacity"

Q\_dot\_sim\_Evap = m\_dot\_r\*(h\_sim[1] - h\_sim[4])  
COP = Q\_dot\_sim\_Evap/W\_dot\_Motor

#### "Compressor Analysis"

P\_Rat = P[2]/P[1]  
W\_dot\_Compressor=m\_dot\_r\*(h[2]-h[1])  
**compressor"**  
eta\_Motor=(W\_dot\_Compressor)/(W\_dot\_Motor)  
**refrigerant"**  
eta\_Isentropic\_Enthalpy=(h\_2s-h[1])/(h[2]-h[1])  
eta\_Overall=(m\_dot\_r\*(h\_2s-h[1]))/W\_dot\_Motor  
eta\_Volume=(m\_dot\_r\*v[1])/(Freq\_Motor\*V\_D)

#### "Pressure Ratio"

"Work input into the refrigerant by the

"Efficiency of motor to input work into the

"Isentropic Efficiency"

"Overall Isentropic Compressor Efficiency"

"Volumetric Efficiency"

#### "IAHRI 10 Coefficient Map Original Composition: Used to compare NEW to MAP"

T\_SH\_Map = 12 [C]

$m\_dot\_r\_map = 5.55318435E-03 - 1.55127703E-04 * T\_Condenser\_Cycle + 2.15662735E-06 * T\_Condenser\_Cycle^2 - 9.07477010E-09 * T\_Condenser\_Cycle^3 + 3.39019324E-04 * T\_Evaporator + 5.70416273E-06 * T\_Evaporator^2 + 1.36945979E-08 * T\_Evaporator^3 - 9.14268948E-06 * T\_Condenser\_Cycle * T\_Evaporator - 1.01459211E-07 * T\_Condenser\_Cycle * T\_Evaporator^2 + 7.81883145E-08 * T\_Condenser\_Cycle^2 * T\_Evaporator$

$W\_dot\_Motor\_map = 9.02018759E-02 + 9.09113424E-04 * T\_Condenser\_Cycle + 1.34063190E-05 * T\_Condenser\_Cycle^2 - 1.05641439E-07 * T\_Condenser\_Cycle^3 - 6.56912509E-05 * T\_Evaporator - 2.45668776E-05 * T\_Evaporator^2 + 2.09164123E-07 * T\_Evaporator^3 + 6.30897000E-05 * T\_Condenser\_Cycle * T\_Evaporator + 1.13446299E-06 * T\_Condenser\_Cycle * T\_Evaporator^2 + 1.63368497E-07 * T\_Condenser\_Cycle^2 * T\_Evaporator$

### "Property Changes"

#### "State 1"

$T\_map[1] = \text{temperature}(R\$, P = P[1], x = 1) + T\_SH\_Map$   
 $h\_map[1] = \text{enthalpy}(R\$, P = P[1], T = T\_map[1])$   
 $s\_map[1] = \text{entropy}(R\$, P = P[1], T = T\_map[1])$   
 $v\_map[1] = \text{volume}(R\$, P = P[1], T = T\_map[1])$   
 $\rho\_map[1] = \text{density}(R\$, P = P[1], T = T\_map[1])$   
 $x\_map[1] = \text{quality}(R\$, P = P[1], T = T\_map[1])$

#### "State 2"

$s\_map\_2s = s\_map[1]$   
 $h\_map\_2s = \text{enthalpy}(R\$, P = P[2], s = s\_map\_2s)$

### "Cooling Capacity"

$Q\_dot\_sim\_Evap\_map = m\_dot\_r\_map * (h\_map[1] - h\_sim[4])$

"Simulated evaporating capacity using the OC compressor map at polymer conditions"

$COP\_map = Q\_dot\_sim\_Evap\_map / W\_dot\_Motor\_map$

"Simulated COP using the OC compressor map at polymer conditions"

### "Compressor Analysis"

$\eta_{a\_Overall\_map} = (m\_dot\_r\_map * (h\_map\_2s - h\_map[1])) / W\_dot\_Motor\_map$

"Overall Isentropic Compressor Efficiency using the OC compressor map at polymer conditions"

$\eta_{a\_Volume\_map} = (m\_dot\_r\_map * v\_map[1]) / (Freq\_Motor * V\_D)$

"Volumetric Efficiency using the OC compressor

map at polymer conditions"

"!Superheat correction: Note that the map mass flow rate or power draw is not actually used, just the superheat of the map"
"Correcting the polymer data to match the superheat of the map. The SH corrected polymer data will be compared to the OC compressor map at polymer conditions"

"Mass Flow Correction at map superheat"

$T\_SH\_new = T\_SH\_Map$   
 $T\_new[1] = \text{temperature}(R\$, P = P[1], x = 1) + T\_SH\_new$   
 $\rho\_new[1] = \text{density}(R\$, P = P[1], T = T\_new[1])$   
 $h\_new[1] = \text{enthalpy}(R\$, P = P[1], T = T\_new[1])$   
 $v\_new[1] = \text{volume}(R\$, P = P[1], T = T\_new[1])$   
 $s\_new[1] = \text{entropy}(R\$, P = P[1], T = T\_new[1])$

$h\_new\_2s = \text{enthalpy}(R\$, P = P[2], s = s\_new[1])$

$$(m\_dot\_new/m\_dot\_r) = 1 + 0.75*((rho\_new[1]/rho[1]) - 1)$$

"In this equation, m\_dot\_new is the SH adjusted mass flowrate of the polymer data, and m\_dot\_r is the original polymer data. This equation merely adjusts the polymer data to a new superheat."

"Work Flow Correction at map superheat"

$$(W\_dot\_new/W\_dot\_Motor) = (m\_dot\_new/m\_dot\_r)*((h\_new\_2s - h\_new[1])/(h\_2s - h[1]))$$

"In this equation, W\_dot\_new is the SH adjusted mass flowrate of the polymer data, and W\_dot\_Motor is the original polymer data. This equation merely adjusts the polymer data to a new superheat."

"New Efficiencies"

$$eta\_Overall\_is\_new=(m\_dot\_new*(h\_new\_2s-h\_new[1]))/W\_dot\_New$$

"Overall isentropic efficiency of the SH corrected polymer data"

$$eta\_Volume\_new=(m\_dot\_new*v\_new[1])/(Freq\_Motor*V\_D)$$

"Volumetric efficiency of the SH corrected polymer data"

"Simulated Cooling Capacity of SH corrected (map) superheat "

"Compressor Suction"

$$T\_sim\_new[1] = T\_new[1]$$

$$h\_sim\_new[1] = h\_new[1]$$

$$Q\_dot\_sim\_Evap\_new = m\_dot\_new*(h\_sim\_new[1] - h\_sim[4])$$

"Simulated evaporating capacity using the new map SH with the polymer data. Note that the map mass flow rate or power draw is not actually used, just the superheat of the map"

$$COP\_new = Q\_dot\_sim\_Evap\_new/W\_dot\_new$$

## APPENDIX G: COPELAND SCROLL COMPRESSOR EES ANALYSIS SCRIPT

R\$='R407C'

"Data Analysis"

Row = TableRun# "15 [-]"

Test\_Number = **lookup**('Raw Data', Row, 'Test')  
 T\_Evap\_Suction=**lookup**('Raw Data', Row, 'TC1: T\_evap\_suc')  
 T\_Comp\_Suction=**lookup**('Raw Data', Row, 'TC2: T\_comp\_suc')  
 T\_Comp\_Discharge=**lookup**('Raw Data', Row, 'TC3: T\_comp\_dis')  
 T\_Cond\_In=**lookup**('Raw Data', Row, 'TC4: T\_cond\_ref\_in')  
 T\_Cond\_Out=**lookup**('Raw Data', Row, 'TC5: T\_cond\_ref\_out')  
 T\_Liq=**lookup**('Raw Data', Row, 'TC7: T\_liq')  
 T\_TXV\_1\_Out=**lookup**('Raw Data', Row, 'TC8A: T\_txv1\_out')  
 T\_TXV\_2\_Out=**lookup**('Raw Data', Row, 'TC8B: T\_txv2\_out')

T[1]=T\_Evap\_Suction  
 T[2]=T\_Comp\_Suction  
 T[3]=T\_Comp\_Discharge  
 T[4]=T\_Cond\_In  
 T[5]=T\_Cond\_Out  
 T[6]=T\_Liq  
 T[7]=T\_TXV\_1\_Out  
 T[8]=T\_TXV\_2\_Out

P\_Comp\_Suction=**lookup**('Raw Data', Row, 'PE1: p\_comp\_suc')  
 P\_Comp\_Discharge=**lookup**('Raw Data', Row, 'PE2: p\_comp\_dis')  
 P\_Cond\_In=**lookup**('Raw Data', Row, 'PE3: p\_cond\_ref\_in')  
 P\_Cond\_Out=**lookup**('Raw Data', Row, 'PE4: p\_cond\_ref\_out')  
 P\_Liq=**lookup**('Raw Data', Row, 'PE5: p\_liq')  
 P\_Evap\_Suction=**lookup**('Raw Data', Row, 'PE6: p\_evap\_suc')

P[1]=P\_Evap\_Suction  
 P[2]=P\_Comp\_Suction  
 P[3]=P\_Comp\_Discharge  
 P[4]=P\_Cond\_In  
 P[5]=P\_Cond\_Out  
 P[6]=P\_Liq  
 P[7]=**pressure**(R\$, T=T[7], h=h[7])  
 "P[8]=**pressure**(R\$, T=T[8], h=h[8])"

h[1]=**enthalpy**(R\$, T=T[1], P=P[1])  
 h[2]=**enthalpy**(R\$, T=T[2], P=P[2])  
 h[3]=**enthalpy**(R\$, T=T[3], P=P[3])  
 h\_3s=**enthalpy**(R\$, P=P[3], s=s\_3s)

$h[4]=\text{enthalpy}(R\$, T=T[4], P=P[4])$   
 $h[5]=\text{enthalpy}(R\$, T=T[5], P=P[5])$   
 $h[6]=\text{enthalpy}(R\$, T=T[6], P=P[6])$   
 $h[7]=h[6]$   
 $h[8]=h[6]$

$s[2]=\text{entropy}(R\$, T=T[2], P=P[2])$   
 $s_{3s}=s[2]$

$\rho[2]=\text{density}(R\$, T=T[2], P=P[2])$

$T_{\text{Superheat}}=T[2]-\text{temperature}(R\$, P=P[1], x=1)$   
 $T_{\text{Evap}} = \text{temperature}(R\$, P = P[2], x = 1)$   
 $T_{\text{Cond}} = \text{temperature}(R\$, P = P[3], x = 1)$   
 $P_{\text{Evap}} = P[2]$   
 $P_{\text{Cond}} = P[3]$   
 $P_{\text{Rat}} = P[3]/P[2]$

#### "Analysis"

$V_{\text{dot\_TH}} = 0.003917 \text{ [m}^3/\text{s]} \text{ "14.1*convert(m}^3/\text{h,m}^3/\text{s)}"$   
 $m_{\text{dot}}=\text{lookup}(\text{'Raw Data'}, \text{Row}, \text{'FE1: dmdt\_ref'})$   
 $\eta_{\text{V}}=m_{\text{dot}}/(V_{\text{dot\_TH}}*\rho[2])$   
 $P_{\text{Compressor}}=\text{lookup}(\text{'Raw Data'}, \text{Row}, \text{'WT1: P\_UUT'})$   
 $\eta_{\text{C\_O}}=(m_{\text{dot}}*(h_{3s}-h[2]))/P_{\text{Compressor}}$   
 $\eta_{\text{C\_is}}=(h_{3s}-h[2])/(h[3]-h[2])$   
 $\text{COP} = Q_{\text{dot\_Evap}}/P_{\text{Compressor}}$

#### "Secondary Calorimeter Mass Flow Analysis"

$AU_{\text{loss}} = 0.004508 \text{ [kW/K]}$   
 $T_{\text{amb}} = \text{lookup}(\text{'Raw Data'}, \text{Row}, \text{'TC11: T\_secCal\_amb'})$   
 $P_{\text{sec\_cal}} = \text{lookup}(\text{'Raw Data'}, \text{Row}, \text{'PE7: p\_secCal'})$   
 $T_{\text{sec\_cal}} = \text{temperature}(R134a, P = P_{\text{sec\_cal}}, x = 0.5)$   
 $Q_{\text{dot\_Evap}} = (m_{\text{dot\_sec}}*(h[1] - h[7])) - (AU_{\text{loss}}*(T_{\text{amb}} - T_{\text{sec\_cal}}))$   
 $Q_{\text{dot\_Evap}} = \text{lookup}(\text{'Raw Data'}, \text{Row}, \text{'WT2: P\_secCal'})$   
 $\eta_{\text{V\_sec}}=m_{\text{dot\_sec}}/(V_{\text{dot\_TH}}*\rho[2])$   
 $\eta_{\text{C\_O\_sec}}=(m_{\text{dot\_sec}}*(h_{3s}-h[2]))/P_{\text{Compressor}}$   
 $m_{\text{dot\_diff}} = m_{\text{dot}} - m_{\text{dot\_sec}}$   
 $m_{\text{dot\_PD}} = (m_{\text{dot\_diff}}/m_{\text{dot}})*100 \text{ [%]}$

#### "10 Coefficient Map"

$m_{\text{dot\_map}}=1.08623618\text{E-}01+4.22436507\text{E-}03*T_{\text{Evap}}+6.13336512\text{E-}05*T_{\text{Evap}}^2+4.70222310\text{E-}07*T_{\text{Evap}}^3-2.71739986\text{E-}03*T_{\text{Cond}}+5.75507833\text{E-}05*T_{\text{Cond}}^2-4.16878880\text{E-}07*T_{\text{Cond}}^3-7.03033154\text{E-}05*T_{\text{Evap}}*T_{\text{Cond}}+7.14610666\text{E-}07*T_{\text{Evap}}*T_{\text{Cond}}^2-4.10755755\text{E-}07*T_{\text{Evap}}^2*T_{\text{Cond}}$   
 $\text{DELTA}m_{\text{dot\_map}} = m_{\text{dot\_map}} - m_{\text{dot}}$   
 $m_{\text{dot\_map\_PD}} = (\text{DELTA}m_{\text{dot\_map}}/m_{\text{dot}})*100 \text{ [%]}$

$$P\_Compressor\_map = -3.87172918E+00 - 1.60668851E-01 * T\_Evap - 8.59211799E-04 * T\_Evap^2 - 9.70297738E-06 * T\_Evap^3 + 4.04463018E-01 * T\_Cond - 8.07493266E-03 * T\_Cond^2 + 6.23768640E-05 * T\_Cond^3 + 8.26602171E-03 * T\_Evap * T\_Cond - 8.90977076E-05 * T\_Evap * T\_Cond^2 + 4.60294862E-06 * T\_Evap^2 * T\_Cond$$
$$DELTA\_P\_Compressor\_map = P\_Compressor\_map - P\_Compressor$$
$$P\_Compressor\_map\_PD = (DELTA\_P\_Compressor\_map / P\_Compressor) * 100 \text{ [%]}$$

## APPENDIX H: ROTARY COMPRESSOR EES ANALYSIS SCRIPT

R\$='R410A'

"Data Analysis"

Row = TableRun#" 40 [-]"

Test\_Number = **lookup**('Raw Data', Row, 'Test')  
 T\_Evap\_Suction=**lookup**('Raw Data', Row, 'TC1: T\_evap\_suc')  
 T\_Comp\_Suction=**lookup**('Raw Data', Row, 'TC2: T\_comp\_suc')  
 T\_Comp\_Discharge=**lookup**('Raw Data', Row, 'TC3: T\_comp\_dis')  
 T\_Cond\_In=**lookup**('Raw Data', Row, 'TC4: T\_cond\_ref\_in')  
 T\_Cond\_Out=**lookup**('Raw Data', Row, 'TC5: T\_cond\_ref\_out')  
 T\_Liq=**lookup**('Raw Data', Row, 'TC7: T\_liq')  
 T\_TXV\_1\_Out=**lookup**('Raw Data', Row, 'TC8A: T\_txv1\_out')  
 T\_TXV\_2\_Out=**lookup**('Raw Data', Row, 'TC8B: T\_txv2\_out')  
 T\_chamb\_amb = **lookup**('Raw Data', Row, 'TC12: T\_chamb\_amb')

T[1]=T\_Evap\_Suction  
 T[2]=T\_Comp\_Suction  
 T[3]=T\_Comp\_Discharge  
 T[4]=T\_Cond\_In  
 T[5]=T\_Cond\_Out  
 T[6]=T\_Liq  
 T[7]=T\_TXV\_1\_Out  
 T[8]=T\_TXV\_2\_Out

P\_Comp\_Suction=**lookup**('Raw Data', Row, 'PE1: p\_comp\_suc')  
 P\_Comp\_Discharge=**lookup**('Raw Data', Row, 'PE2: p\_comp\_dis')  
 P\_Cond\_In=**lookup**('Raw Data', Row, 'PE3: p\_cond\_ref\_in')  
 P\_Cond\_Out=**lookup**('Raw Data', Row, 'PE4: p\_cond\_ref\_out')  
 P\_Liq=**lookup**('Raw Data', Row, 'PE5: p\_liq')  
 P\_Evap\_Suction=**lookup**('Raw Data', Row, 'PE6: p\_evap\_suc')

P[1]=P\_Evap\_Suction  
 P[2]=P\_Comp\_Suction  
 P[3]=P\_Comp\_Discharge  
 P[4]=P\_Cond\_In  
 P[5]=P\_Cond\_Out  
 P[6]=P\_Liq  
 P[7]=**pressure**(R\$, T=T[7], h=h[7])  
 P[8]=**pressure**(R\$, T=T[8], h=h[8])

h[1]=**enthalpy**(R\$, T=T[1], P=P[1])  
 h[2]=**enthalpy**(R\$, T=T[2], P=P[2])  
 h[3]=**enthalpy**(R\$, T=T[3], P=P[3])  
 h\_3s=**enthalpy**(R\$, P=P[3], s=s\_3s)

$h[4]=\text{enthalpy}(R\$, T=T[4], P=P[4])$   
 $h[5]=\text{enthalpy}(R\$, T=T[5], P=P[5])$   
 $h[6]=\text{enthalpy}(R\$, T=T[6], P=P[6])$   
 $h[7]=h[6]$   
 $h[8]=h[6]$

#### "Statepoint Properties"

##### "State 2"

$s[2] = \text{entropy}(R\$, T = T[2], P = P[2])$

##### "State 3"

$s_{3s}=s[2]$

$T_{3s} = \text{temperature}(R\$, P = P[3], s = s_{3s})$

$\text{DELTA}h_{is} = h_{3s} - h[2]$

$\rho[2]=\text{density}(R\$, T=T[2], P=P[2])$

$T_{\text{Superheat}}=T[2]-\text{temperature}(R\$, P=P[1], x=1)$   
 $T_{\text{Evap}} = \text{temperature}(R\$, P = P[2], x = 1)$   
 $T_{\text{Cond}} = \text{temperature}(R\$, P = P[3], x = 1)$   
 $P_{\text{Evap}} = P[2]$   
 $P_{\text{Cond}} = P[3]$   
 $P_{\text{Rat}} = P[3]/P[2]$

#### "Analysis"

$V_{\text{dot\_TH}_i}=0.0000408 \text{ [m}^3\text{]}$   
 $V_{\text{dot\_TH}} = V_{\text{dot\_TH}_i} \cdot 60 \text{ [1/s]}$   
 $m_{\text{dot}}=\text{lookup}(\text{'Raw Data'}, \text{Row}, \text{'FE1: dmdt\_ref'})$   
 $\eta_V=m_{\text{dot}}/(V_{\text{dot\_TH}} \cdot \rho[2])$   
 $P_{\text{Compressor}}=\text{lookup}(\text{'Raw Data'}, \text{Row}, \text{'WT1: P\_UUT'})$   
 $\eta_{C\_O}=(m_{\text{dot}} \cdot (h_{3s}-h[2]))/P_{\text{Compressor}}$   
 $\eta_{C\_is}=(h_{3s}-h[2])/(h[3]-h[2])$   
 $\text{COP} = Q_{\text{dot\_Evap}}/P_{\text{Compressor}}$

#### "Secondary Calorimeter Mass Flow Analysis"

$AU_{\text{loss}} = 0.004508 \text{ [kW/K]}$   
 $T_{\text{amb}} = \text{lookup}(\text{'Raw Data'}, \text{Row}, \text{'TC11: T\_secCal\_amb'})$   
 $P_{\text{sec\_cal}} = \text{lookup}(\text{'Raw Data'}, \text{Row}, \text{'PE7: p\_secCal'})$   
 $T_{\text{sec\_cal}} = \text{temperature}(R134a, P = P_{\text{sec\_cal}}, x = 0.5)$   
 $Q_{\text{dot\_Evap}} = (m_{\text{dot\_sec}} \cdot (h[1] - h[7])) - (AU_{\text{loss}} \cdot (T_{\text{amb}} - T_{\text{sec\_cal}}))$   
 $Q_{\text{dot\_Evap}} = \text{lookup}(\text{'Raw Data'}, \text{Row}, \text{'WT2: P\_secCal'})$   
 $\eta_{V\_sec}=m_{\text{dot\_sec}}/(V_{\text{dot\_TH}} \cdot \rho[2])$

$\eta_{C\_O\_sec} = (m_{dot\_sec} * (h_{3s} - h_{[2]})) / P\_Compressor$   
 $m_{dot\_diff} = m_{dot} - m_{dot\_sec}$   
 $m_{dot\_PD} = (m_{dot\_diff} / m_{dot}) * 100 \text{ [%]}$

#### "10 Coefficient Map"

$m_{dot\_map} = 1.84371096E-01 + 3.60187445E-03 * T\_Evap + 1.86085991E-04 * T\_Evap^2 + 6.26599976E-06 * T\_Evap^3 - 9.77087205E-03 * T\_Cond + 2.50755526E-04 * T\_Cond^2 - 2.10996889E-06 * T\_Cond^3 - 2.49749915E-05 * T\_Evap * T\_Cond + 4.82658691E-07 * T\_Evap * T\_Cond^2 + 9.38832684E-07 * T\_Evap^2 * T\_Cond$   
 $DELTA m_{dot\_map} = m_{dot\_map} - m_{dot}$   
 $m_{dot\_map\_PD} = (DELTA m_{dot\_map} / m_{dot}) * 100 \text{ [%]}$

$P\_Compressor\_map = 1.29515427E+00 - 4.10387907E-02 * T\_Evap - 1.39995135E-03 * T\_Evap^2 - 9.77060730E-06 * T\_Evap^3 + 3.55634800E-02 * T\_Cond + 2.70702050E-04 * T\_Cond^2 - 2.81123550E-07 * T\_Cond^3 + 9.71628144E-04 * T\_Evap * T\_Cond + 5.03988538E-06 * T\_Evap * T\_Cond^2 + 1.58023318E-05 * T\_Evap^2 * T\_Cond$   
 $DELTA P\_Compressor\_map = P\_Compressor\_map - P\_Compressor$   
 $P\_Compressor\_map\_PD = (DELTA P\_Compressor\_map / P\_Compressor) * 100 \text{ [%]}$

## APPENDIX I: MATLAB FFT SCRIPT

```

close all
clear
clc

EXCEL_File = 'Jan-23-19 Time 10 33_EvapTemp_10F_CondTemp_110F.xlsx'; %Name of
data file
sheet = 1; %sheet number where data is located
%EXCELRange = 'B2:C135401'; %Manually input data range (RFI)
evaptemp = '10F';
condtemp = '110F';
date = 'Jan-23-19 Time 10 33';
samplenum = '01';
Unit = 'kPa';

t_Domain = xlsread(EXCEL_File,sheet, '', 'basic'); %'basic' %data conversion
into MATLAB
for deletedex = 1:1:6
    t_Domain(1,:) = [];
end

t = t_Domain(:,3); %selection of time data
L_t = length(t); %count of data points
s_Freq = 1000/(t(2)-t(1)); %Sampling frequency
Max_Freq = s_Freq/2; %Maximum frequency identifiable at sampling rate
p = 6.89476*t_Domain(:,2); %selection of amplitude data

p_ave = mean(p);
y_min = p_ave - 3;
y_max = p_ave + 3;

% figure %1
fig_1 = plot(t,p, '-o', 'LineWidth', 1.5)% '-
o')%, 'MarkerIndices', 1:1:length(p));
xlim([1600 1700]) %Manual selection of time stretch to observe
ylim([y_min y_max]) %Automatic selection of amplitude range to observe
xlabel('Time (milliseconds)')
ylabel('Pressure (kPa)')
title([date, ' EvapTemp ', evaptemp, ' CondTemp ', condtemp, ' Time Domain
', samplenum, ' ', Unit])
ax = gca;
ax.YGrid = 'on';
%savestring =
[date, '_EvapTemp_', evaptemp, '_CondTemp_', condtemp, '_Dynamic_', samplenum, Un
it, '.png'];
%saveas(fig_1, savestring)

%Frequency Domain Analysis
P = fft(p); %Fast Fourier Transform of amplitude data

P_mag = abs(P); %Identify absolute value of frequency domain data

```

```

P_mag_scale = P_mag/(L_t/2);    %Conversion of amplitude data into measured
units ([-] to [psi])

% figure %2
% plot(P_mag_scale)

step_Freq = Max_Freq/(L_t/2);  %Resolution of frequency steps

%P_mag_h = P_mag
P_mag_h = P_mag(1:(L_t/2));    %Consider only first half of the spectrum
P_mag_h = P_mag_h/(L_t/2);    %Conversion of amplitude data into measured
units ([-] to [psi])

Freq = 0:step_Freq:(Max_Freq - step_Freq); %Creation of frequency matrix

figure
fig_2 = plot(Freq,1*P_mag_h, '-o', 'LineWidth', 1.5);
%fig_2 = plot(1*P_mag_h, 'LineWidth', 1.5);
xlim([0 150])
xticks([0:10:150])
ylim([0 8])
yticks([0:3:15])
xlabel('Frequency (Hz)')
ylabel('Pressure (kPa)')
title([date, ' EvapTemp ', evaptemp, ' CondTemp ', condtemp, ' Frequency Domain
', samplenum, ' ', Unit])
ax = gca;
ax.YGrid = 'on';
%savestringf =
[date, ' EvapTemp_', evaptemp, '_CondTemp_', condtemp, '_Dynamic_', samplenum, 'f
', Unit, '.png'];
%saveas(fig_2, savestringf)

%P_mag_h(1:100) = [];
%Freq(1:100) = [];
L_t = length(P_mag_h);
max_P = max(P_mag_h)
k = find(P_mag_h == max_P);
Freq_max_P = Freq(k)
P_sum = 0;
for iter = 1:1:(L_t - 1)
    if P_mag_h(iter) > 0.05
        P_sum = P_sum+P_mag_h(iter);
    end
end
P_sum = P_sum

```

## APPENDIX J: AHRI 10-COEFFICIENT CORRELATION MATLAB SCRIPT

```

%%%%%%%%%%%%%%%%%%%%%%%%%%%%%%%%%%%%%%%%%%%%%%%%%%%%%%%%%%%%%%%%%%%%%%%%
% This script is used to identify the semi-empirical curve fits based on
% 10Coeff (2015)
%Data must be input in txt format
%%%%%%%%%%%%%%%%%%%%%%%%%%%%%%%%%%%%%%%%%%%%%%%%%%%%%%%%%%%%%%%%%%%%%%%%

clc
close all;
clear all;
format long;

%% reading data for curve fitting
data_small = load('Copeland_Scroll_extrapolationtraining.txt');
P_Suc_fit = data_small(:,1); % Suction pressure [kPa]
P_Dis_fit = data_small(:,2); % Discharge pressure [kPa]
eta_V_fit=data_small(:,3); % Volumetric efficieny [-]
m_dot_fit = data_small(:,4); % Mass flow rate [kg/s]
P_input_fit = data_small(:,5); % Power draw [kW]
eta_is_O_fit = data_small(:,6); % Overall isentropic efficiency [-]
eta_is_fit = data_small(:,7); % Isentropic efficiency [-]
T_Suc_fit = data_small(:,8); % Suction temperature [C]
T_Dis_fit = data_small(:,9); % Discharge temperature [C]
T_Dis_is_fit = data_small(:,10); % Isentropic discharge temperature [C]
T_amb_fit = data_small(:,11); % Ambient compressor temperature [C]
DELTAh_is_fit = data_small(:,12); % Isentropic enthalpy difference across
compressor [kJ/kg]
rho_Suc_fit = data_small(:,13); % Suction density [kg/m^3]
T_Evap_fit = data_small(:,14); % Evaporating temperature [C]
T_Cond_fit = data_small(:,15); % Condensing temperature [C]
Q_dot_Evap_fit = data_small(:,16); % Evaporating Capacity [kW]

%% reading all data
data = load('Copeland_Scroll_extrapolationtesting.txt');
P_Suc = data(:,1); % Suction pressure [kPa]
P_Dis = data(:,2); % Discharge pressure [kPa]
eta_V=data(:,3); % Volumetric efficieny [-]
m_dot = data(:,4); % Mass flow rate [kg/s]
P_input = data(:,5); % Power draw [kW]
eta_is_O = data(:,6); % Overall isentropic efficiency [-]
eta_is = data(:,7); % Isentropic efficiency [-]
T_Suc = data(:,8); % Suction temperature [C]
T_Dis = data(:,9); % Discharge temperature [C]
T_Dis_is = data(:,10); % Isentropic discharge temperature [C]
T_amb = data(:,11); % Ambient compressor temperature [C]
DELTAh_is = data(:,12); % Isentropic enthalpy difference across compressor
[kJ/kg]
rho_Suc = data(:,13); % Suction density [kg/m^3]
T_Evap = data(:,14); % Evaporating temperature [C]
T_Cond = data(:,15); % Condensing temperature [C]
Q_dot_Evap = data(:,16); % Evaporating Capacity [kW]

```

```

%%k = 1.073859;           % (R410A) Polytropic coefficient used as isentropic
refrigerant coefficient
k = 1.047152;           % (R407C) Polytropic coefficient used as isentropic
refrigerant coefficient
N_Comp = 60;             % Compressor speed      [Hz]
V_Comp = 0.00006528333; % Compressor displacement [m^3]

%% Calling Empirical Curves
% Initial Guess for eta_V coefficients
c0 = [0 0 0 0 0 0 0 0 0 0];
b0 = [0 0 0 0 0 0 0 0 0 0];
a0 = [0 0 0 0 0 0 0 0 0 0];

% Establishing LMA choice for least squares analysis
options=optimoptions(@lsqnonlin, 'Algorithm', 'levenberg-marquardt');
% Finding the coefficients for the eta_V curve via least squares analysis
[a, resnorm_P_input]=lsqnonlin(@(a)
Coeff10_SemiEmpirical_P_input(T_Evap_fit', T_Cond_fit', P_input_fit', a), a0,
[], [], options)
[b, resnorm_m_dot]=lsqnonlin(@(b) Coeff10_SemiEmpirical_m_dot(T_Evap_fit',
T_Cond_fit', m_dot_fit', b), b0, [], [], options)
[c, resnorm_Q_dot_Evap]=lsqnonlin(@(c)
Coeff10_SemiEmpirical_Q_dot_Evap(T_Evap_fit', T_Cond_fit', Q_dot_Evap_fit',
c), c0, [], [], options)

%% Calculating Performance based on empirical curves
T_1 = zeros(1, size(data,1));
T_2 = zeros(1, size(data,1));
T_3 = zeros(1, size(data,1));
T_4 = zeros(1, size(data,1));
T_5 = zeros(1, size(data,1));
T_6 = zeros(1, size(data,1));
T_7 = zeros(1, size(data,1));
T_8 = zeros(1, size(data,1));
T_9 = zeros(1, size(data,1));
T_10 = zeros(1, size(data,1));
Q_dot_Evap_curve = zeros(1, size(data,1));
eta_V_curve = zeros(1, size(data,1));
eta_is_0_curve = zeros(1, size(data,1));
m_dot_curve = zeros(1, size(data,1));
P_input_curve = zeros(1, size(data,1));
count = zeros(1, size(data,1));
for i=1:1:size(data,1)
    % Performance from 10Coeff (2015)
    T_1(i) = 1;
    T_2(i) = T_Evap(i);
    T_3(i) = T_Cond(i);
    T_4(i) = (T_Evap(i)^2);
    T_5(i) = (T_Evap(i)*T_Cond(i));
    T_6(i) = (T_Cond(i)^2);
    T_7(i) = (T_Evap(i)^3);
    T_8(i) = ((T_Evap(i)^2)*(T_Cond(i)));
    T_9(i) = ((T_Evap(i))*(T_Cond(i)^2));
    T_10(i) = (T_Cond(i)^3);

```

```

    P_input_curve(i) = a(1)*T_1(i) + a(2)*T_2(i) + a(3)*T_3(i) + a(4)*T_4(i)
+ a(5)*T_5(i) + a(6)*T_6(i) + a(7)*T_7(i) + a(8)*T_8(i) + a(9)*T_9(i) +
a(10)*T_10(i);
    m_dot_curve(i) = b(1)*T_1(i) + b(2)*T_2(i) + b(3)*T_3(i) + b(4)*T_4(i) +
b(5)*T_5(i) + b(6)*T_6(i) + b(7)*T_7(i) + b(8)*T_8(i) + b(9)*T_9(i) +
b(10)*T_10(i);
    Q_dot_Evap_curve(i) = c(1)*T_1(i) + c(2)*T_2(i) + c(3)*T_3(i) +
c(4)*T_4(i) + c(5)*T_5(i) + c(6)*T_6(i) + c(7)*T_7(i) + c(8)*T_8(i) +
c(9)*T_9(i) + c(10)*T_10(i);

    count(i) = i;

    % Calculation of volumetric and overall isentropic efficiency
    eta_V_curve(i) = (m_dot_curve(i))/(rho_Suc(i)*V_Comp*N_Comp);
    eta_is_O_curve(i) = (m_dot_curve(i)*DELTAh_is(i))/(P_input_curve(i));
end

%% Plotting performance from empirical curves

figure
plot(count, eta_V, 'o')
hold on
plot(count, eta_V_curve, 'o')
grid on
xlim([0 size(data,1)+1])
xticks([0:1:size(data,1)+1])

figure
plot(count, eta_is_O, 'o')
hold on
plot(count, eta_is_O_curve, 'o')
grid on
xlim([0 size(data,1)+1])
xticks([0:1:size(data,1)+1])

figure
plot(count, m_dot, 'o')
hold on
plot(count, m_dot_curve, 'o')
grid on
xlim([0 size(data,1)+1])
xticks([0:1:size(data,1)+1])

figure
plot(count, P_input, 'o')
hold on
plot(count, P_input_curve, 'o')
grid on
xlim([0 size(data,1)+1])
xticks([0:1:size(data,1)+1])

figure
plot(count, Q_dot_Evap, 'o')
hold on

```

```

plot(count, Q_dot_Evap_curve, 'o')
grid on
xlim([0 size(data,1)+1])
xticks([0:1:size(data,1)+1])

% figure
% plot(eta_V, eta_V_curve, 'o')
% grid on
% xlim([0.75 1])
% xticks([0.75:0.05:1])
% ylim([0.75 1])
% yticks([0.75:0.05:1])
%
% figure
% plot(eta_is_0, eta_is_0_curve, 'o')
% grid on
% xlim([0.5 0.7])
% xticks([0.5:0.05:0.7])
% ylim([0.5 0.7])
% yticks([0.5:0.05:0.7])

%% Writing data to a text file

file_name = 'Scroll_10Coeff_Correlation_extrapolation_0313_2.xlsx';

P_input_curve = P_input_curve';
m_dot_curve = m_dot_curve';
Q_dot_Evap_curve = Q_dot_Evap_curve';
eta_V_curve = eta_V_curve';
eta_is_0_curve = eta_is_0_curve';

OUTPUT = table(P_input, P_input_curve, eta_V, eta_V_curve, m_dot,
m_dot_curve, eta_is_0, eta_is_0_curve, Q_dot_Evap, Q_dot_Evap_curve);
writetable(OUTPUT,file_name,'Sheet',1,'Range','B2')

COEFFICIENTS = table(a, b, c, resnorm_P_input, resnorm_m_dot,
resnorm_Q_dot_Evap);
writetable(COEFFICIENTS,file_name,'Sheet',1,'Range','B50')

TRAINING = table(P_Suc_fit, P_Dis_fit, eta_V_fit, m_dot_fit, P_input_fit,
eta_is_0_fit, eta_is_fit, T_Suc_fit, T_Dis_fit, T_Dis_is_fit, T_amb_fit,
DELTAh_is_fit, rho_Suc_fit, T_Evap_fit, T_Cond_fit, Q_dot_Evap_fit);
writetable(TRAINING,file_name,'Sheet',2,'Range','B2')

TESTING = table(P_Suc, P_Dis, eta_V, m_dot, P_input, eta_is_0, eta_is, T_Suc,
T_Dis, T_Dis_is, T_amb, DELTAh_is, rho_Suc, T_Evap, T_Cond, Q_dot_Evap);
writetable(TESTING,file_name,'Sheet',3,'Range','B2')

```



```

%Calculation of semi-empirical overall isentropic efficiency using 4
constants

T_1 = 1;
T_2 = T_Evap;
T_3 = T_Cond;
T_4 = (T_Evap.^2);
T_5 = (T_Evap.*T_Cond);
T_6 = (T_Cond.^2);
T_7 = (T_Evap.^3);
T_8 = ((T_Evap.^2).*(T_Cond));
T_9 = ((T_Evap).*(T_Cond.^2));
T_10 = (T_Cond.^3);

P_input_curve = a(1).*T_1 + a(2).*T_2 + a(3).*T_3 + a(4).*T_4 + a(5).*T_5 +
a(6).*T_6 + a(7).*T_7 + a(8).*T_8 + a(9).*T_9 + a(10).*T_10;
%Calculation of the difference between the semi-empirical efficiency to the
%actual efficiency
P_input_diff = P_input_curve - P_input;

%Relative difference between the two efficiencies in decimal units
P_input_reldiff = abs(P_input_diff./P_input);

end

```

## EVAPORATING CAPACITY

```

function Q_dot_Evap_reldiff = Coeff10_SemiEmpirical_Q_dot_Evap(T_Evap,
T_Cond, Q_dot_Evap, c)
%%%%%%%%%%%%%%%%%%%%%%%%%%%%%%%%%%%%%%%%%%%%%%%%%%%%%%%%%%%%%%%%%%%%%%%%
%%%%%%%%%%%%%%%%%%%%%%%%%%%%%%%%%%%%%%%%%%%%%%%%%%%%%%%%%%%%%%%%%%%%%%%%
% This function returns the relative difference between the semi empirical
% overall isentropic efficiency from AHRI 10-Coefficient to the actual
% overall isentropic efficiency
% found in the data set provided by the parent script)
%%%%%%%%%%%%%%%%%%%%%%%%%%%%%%%%%%%%%%%%%%%%%%%%%%%%%%%%%%%%%%%%%%%%%%%%
%%%%%%%%%%%%%%%%%%%%%%%%%%%%%%%%%%%%%%%%%%%%%%%%%%%%%%%%%%%%%%%%%%%%%%%%

%Calculation of semi-empirical overall isentropic efficiency using 4
constants

T_1 = 1;
T_2 = T_Evap;
T_3 = T_Cond;
T_4 = (T_Evap.^2);
T_5 = (T_Evap.*T_Cond);
T_6 = (T_Cond.^2);
T_7 = (T_Evap.^3);
T_8 = ((T_Evap.^2).*(T_Cond));
T_9 = ((T_Evap).*(T_Cond.^2));
T_10 = (T_Cond.^3);

```

```
Q_dot_Evap_curve = c(1).*T_1 + c(2).*T_2 + c(3).*T_3 + c(4).*T_4 + c(5).*T_5  
+ c(6).*T_6 + c(7).*T_7 + c(8).*T_8 + c(9).*T_9 + c(10).*T_10;  
%Calculation of the difference between the semi-empirical efficiency to the  
%actual efficiency  
Q_dot_Evap_diff = Q_dot_Evap_curve - Q_dot_Evap;  
  
%Relative difference between the two efficiencies in decimal units  
Q_dot_Evap_reldiff = abs(Q_dot_Evap_diff./Q_dot_Evap);  
  
end
```

## APPENDIX L: LI CORRELATION MATLAB SCRIPT

```

%%%%%%%%%%%%%%%%%%%%%%%%%%%%%%%%%%%%%%%%%%%%%%%%%%%%%%%%%%%%%%%%%%%%%%%%
% This script is used to identify the semi-empirical curve fits based on Li
% (2012)
%Data must be input in txt format
%%%%%%%%%%%%%%%%%%%%%%%%%%%%%%%%%%%%%%%%%%%%%%%%%%%%%%%%%%%%%%%%%%%%%%%%
clc
close all;
clear all;
format long;

%% reading data for curve fitting
data_small = load('Copeland_Scroll_extrapolationtraining.txt');
P_Suc_fit = data_small(:,1); % Suction pressure [kPa]
P_Dis_fit = data_small(:,2); % Discharge pressure [kPa]
eta_V_fit=data_small(:,3); % Volumetric efficieny [-]
m_dot_fit = data_small(:,4); % Mass flow rate [kg/s]
P_input_fit = data_small(:,5); % Power draw [kW]
eta_is_O_fit = data_small(:,6); % Overall isentropic efficiency [-]
eta_is_fit = data_small(:,7); % Isentropic efficiency [-]
T_Suc_fit = data_small(:,8); % Suction temperature [C]
T_Dis_fit = data_small(:,9); % Discharge temperature [C]
T_Dis_iso_fit = data_small(:,10); % Isentropic discharge temperature [C]
T_amb_fit = data_small(:,11); % Ambient compressor temperature [C]
DELTAh_is_fit = data_small(:,12); % Isentropic enthalphy difference across
compressor [kJ/kg]
rho_Suc_fit = data_small(:,13); % Suction density [kg/m^3]

%% reading all data
data = load('Copeland_Scroll_extrapolationtesting.txt');
P_Suc = data(:,1); % Suction pressure [kPa]
P_Dis = data(:,2); % Discharge pressure [kPa]
eta_V=data(:,3); % Volumetric efficieny [-]
m_dot = data(:,4); % Mass flow rate [kg/s]
P_input = data(:,5); % Power draw [kW]
eta_is_O = data(:,6); % Overall isentropic efficiency [-]
eta_is = data(:,7); % Isentropic efficiency [-]
T_Suc = data(:,8); % Suction temperature [C]
T_Dis = data(:,9); % Discharge temperature [C]
T_Dis_iso = data(:,10); % Isentropic discharge temperature [C]
T_amb = data(:,11); % Ambient compressor temperature [C]
DELTAh_is = data(:,12); % Isentropic enthalphy difference across compressor
[kJ/kg]
rho_Suc = data(:,13); % Suction density [kg/m^3]

%k = 1.073859; % (R410A) Polytropic coefficient used as isentropic
refrigerant coefficient
k = 1.047152; % (R407C) Polytropic coefficient used as isentropic
refrigerant coefficient
N_Comp = 60; % Compressor speed [Hz]
V_Comp = 0.00006528333; % Compressor displacement [m^3]

```

```

%% Calculation of volumetric flowrate based off eta_V from data set
%V_dot_Suc_fit = eta_V_fit*N_Comp*V_Comp;
%V_dot_Suc = eta_V*N_Comp*V_Comp;
V_dot_Suc_fit = m_dot_fit./rho_Suc_fit;
V_dot_Suc = m_dot./rho_Suc;

%% Calling Empirical Curves
% Initial Guess for eta_V coefficients
b0 = [0 0 0];
a0 = [0 0 0 0];

% Establishing LMA choice for least squares analysis
options=optimoptions(@lsqnonlin, 'Algorithm', 'levenberg-marquardt');
% Finding the coefficients for the eta_V curve via least squares analysis
[b, resnorm_eta_V]=lsqnonlin(@(b) Li_SemiEmpirical_eta_V(P_Suc_fit',
P_Dis_fit', eta_V_fit', k, b), b0, [], [],options)
[a, resnorm_P_input] = lsqnonlin(@(a) Li_SemiEmpirical_P_input(P_Suc_fit',
P_Dis_fit', V_dot_Suc_fit', P_input_fit', k, a), a0, [], [],options)

%% Calculating performance based on empirical curves

eta_V_curve = zeros(1, size(data,1));
inv_eta_is_O_curve = zeros(1, size(data,1));
eta_is_O_curve = zeros(1, size(data,1));
Term_1 = zeros(1, size(data,1));
Term_2 = zeros(1, size(data,1));
Term_3 = zeros(1, size(data,1));
Term_4 = zeros(1, size(data,1));
Term_5 = zeros(1, size(data,1));
Term_6 = zeros(1, size(data,1));
m_dot_curve = zeros(1, size(data,1));
P_input_curve = zeros(1, size(data,1));
Numer_eta_is_O_curve = zeros(1, size(data,1));
Denomen_eta_is_O_curve = zeros(1, size(data,1));
count = zeros(1, size(data,1));
for i=1:1:size(data,1)
    % Volumetric Efficiency from Li (2012)
    eta_V_curve(i)=b(1)+b(2)*(P_Dis(i)/(P_Suc(i)*(1-b(3))))^(1.0/k);

    % Inverse of overall isentropic efficiency
    inv_eta_is_O_curve(i) = (a(1) + (a(2)/P_Suc(i)) + (a(3)/P_Dis(i)));
    % Overall isentropic efficiency DOES NOT SEEM TO WORK FOR SOME REASON
    % DO NOT USE
    % eta_is_O_curve(i) = 1/(inv_eta_is_O_curve(i));

    % Power input
    Term_1(i) = P_Suc(i);
    Term_2(i) = V_dot_Suc(i);
    Term_3(i) = (k/(k-1));
    Term_4(i) = (((P_Dis(i)/P_Suc(i))^(k-1)/k) - 1);
    Term_5(i) = inv_eta_is_O_curve(i);
    Term_6(i) = a(4);
    P_input_curve(i) = (Term_1(i)*Term_2(i)*Term_3(i)*Term_4(i)*Term_5(i) +
Term_6(i));

```

```

% Calculation of mass flow rate
m_dot_curve(i) = rho_Suc(i)*V_Comp*N_Comp*eta_V_curve(i);

% Calculation of overall isentropic efficiency
Numer_eta_is_O_curve(i) = m_dot_curve(i)*DELTAh_is(i);
Denomen_eta_is_O_curve(i) = P_input_curve(i);
eta_is_O_curve(i) = Numer_eta_is_O_curve(i)/Denomen_eta_is_O_curve(i);

count(i) = i;
end

%% Plotting newly calculated performance
% figure
% plot(count, eta_V, 'o')
% hold on
% plot(count, eta_V_curve, 'o')
% grid on
% xlim([0 size(data,1)+1])
% xticks([0:1:size(data,1)+1])
%
% figure
% plot(count, eta_is_O, 'o')
% hold on
% plot(count, eta_is_O_curve, 'o')
% grid on
% xlim([0 size(data,1)+1])
% xticks([0:1:size(data,1)+1])
%
% figure
% plot(count, m_dot, 'o')
% hold on
% plot(count, m_dot_curve, 'o')
% grid on
% xlim([0 size(data,1)+1])
% xticks([0:1:size(data,1)+1])

figure
plot(count, P_input, 'o')
hold on
plot(count, P_input_curve, 'o')
grid on
xlim([0 size(data,1)+1])
xticks([0:1:size(data,1)+1])
% ylim([0 5])
% yticks([0:0.25:5])

% figure
% plot(eta_V, eta_V_curve, 'o')
% grid on
% xlim([0.75 1])
% xticks([0.75:0.05:1])
% ylim([0.75 1])
% yticks([0.75:0.05:1])

```

```

%
% figure
% plot(eta_is_O, eta_is_O_curve, 'o')
% grid on
% xlim([0.5 0.7])
% xticks([0.5:0.05:0.7])
% ylim([0.5 0.7])
% yticks([0.5:0.05:0.7])

%% Writing data to a text file

file_name = 'Scroll_Li_Correlation_extrapolation_0313.xlsx';

P_input_curve = P_input_curve';
m_dot_curve = m_dot_curve';
eta_V_curve = eta_V_curve';
eta_is_O_curve = eta_is_O_curve';

OUTPUT = table(P_input, P_input_curve, eta_V, eta_V_curve, m_dot,
m_dot_curve, eta_is_O, eta_is_O_curve);
writetable(OUTPUT,file_name,'Sheet',1,'Range','B2')

COEFFICIENTS = table(a, b, resnorm_eta_V, resnorm_P_input);
writetable(COEFFICIENTS,file_name,'Sheet',1,'Range','B50')

TRAINING = table(P_Suc_fit, P_Dis_fit, eta_V_fit, m_dot_fit, P_input_fit,
eta_is_O_fit, eta_is_fit, T_Suc_fit, T_Dis_fit, T_Dis_iso_fit, T_amb_fit,
DELTAh_is_fit, rho_Suc_fit);
writetable(TRAINING,file_name,'Sheet',2,'Range','B2')

TESTING = table(P_Suc, P_Dis, eta_V, m_dot, P_input, eta_is_O, eta_is, T_Suc,
T_Dis, T_Dis_iso, T_amb, DELTAh_is, rho_Suc);
writetable(TESTING,file_name,'Sheet',3,'Range','B2')

```

## APPENDIX M: LI CORRELATION LEAST SQUARE SOLVER

### POWER DRAW

```
function P_input_reldiff = Li_SemiEmpirical_P_input(P_Suc, P_Dis, V_dot_Suc,
P_input, k, a)
%%%%%%%%%%%%%%%%%%%%%%%%%%%%%%%%%%%%%%%%%%%%%%%%%%%%%%%%%%%%%%%%%%%%%%%%
%%%%%%%%
% This function returns the relative difference between the semi empirical
% Power input from Li (2012) to the actual Power input
% found in the data set provided by the parent script)
%%%%%%%%%%%%%%%%%%%%%%%%%%%%%%%%%%%%%%%%%%%%%%%%%%%%%%%%%%%%%%%%%%%%%%%%

% Inverse of overall isentropic efficiency
inv_eta_is_0 = (a(1) + (a(2)./P_Suc) + (a(3)./P_Dis));

% Power input
Term_1 = P_Suc;
Term_2 = V_dot_Suc;
Term_3 = (k/(k-1));
Term_4 = (((P_Dis./P_Suc).^((k-1)/k)) - 1);
Term_5 = inv_eta_is_0;
Term_6 = a(4);
P_input_curve = Term_1.*Term_2.*Term_3.*Term_4.*Term_5 + Term_6;

%Calculation of the difference between the semi-empirical Power input to the
%actual Power input
P_input_diff = P_input_curve - P_input;

%Relative difference between the two Power inputs in decimal units
P_input_reldiff = abs(P_input_diff./P_input);
end
```

### VOLUMETRIC EFFICIENCY

```
function eta_V_reldiff = Li_SemiEmpirical_eta_V(P_Suc, P_Dis, eta_V, k, b)
%%%%%%%%%%%%%%%%%%%%%%%%%%%%%%%%%%%%%%%%%%%%%%%%%%%%%%%%%%%%%%%%%%%%%%%%
%%%%%%%%
% This function returns the relative difference between the semi empirical
% volumetric efficiency from Li (2012) to the actual volumetric efficiency
% found in the data set provided by the parent script)
%%%%%%%%%%%%%%%%%%%%%%%%%%%%%%%%%%%%%%%%%%%%%%%%%%%%%%%%%%%%%%%%%%%%%%%%

%Calculation of semi-empirical volumetric efficiency using 3 constants
eta_V_curve = b(1) + b(2)*((P_Dis./(P_Suc*(1 - b(3))))).^ (1/k));

%Calculation of the difference between the semi-empirical efficiency to the
```

```
%actual efficiency
eta_V_diff = eta_V_curve - eta_V;

%Relative difference between the two efficiencies in decimal units
eta_V_reldiff = abs(eta_V_diff./eta_V);

end
```

## APPENDIX N: MENDOZA-MIRANDA CORRELATION MATLAB SCRIPT

```

%%%%%%%%%%%%%%%%%%%%%%%%%%%%%%%%%%%%%%%%%%%%%%%%%%%%%%%%%%%%%%%%%%%%%%%%
% This script is used to identify the semi-empirical curve fits based on
% Mendoza (2016)
%Data must be input in txt format
%%%%%%%%%%%%%%%%%%%%%%%%%%%%%%%%%%%%%%%%%%%%%%%%%%%%%%%%%%%%%%%%%%%%%%%%

clc
close all;
clear all;
format long;

%% reading data for curve fitting
data_small = load('Copeland_Scroll_extrapolationtraining.txt');
P_Suc_fit = data_small(:,1);      % Suction pressure      [kPa]
P_Dis_fit = data_small(:,2);      % Discharge pressure  [kPa]
eta_V_fit=data_small(:,3);        % Volumetric efficieny [-]
m_dot_fit = data_small(:,4);      % Mass flow rate      [kg/s]
P_input_fit = data_small(:,5);    % Power draw          [kW]
eta_is_O_fit = data_small(:,6);   % Overall isentropic efficiency [-]
eta_is_fit = data_small(:,7);     % Isentropic efficiency [-]
T_Suc_fit = data_small(:,8);      % Suction temperature [C]
T_Dis_fit = data_small(:,9);      % Discharge temperature [C]
T_Dis_is_fit = data_small(:,10);  % Isentropic discharge temperature [C]
T_amb_fit = data_small(:,11);     % Ambient compressor temperature [C]
DELTAh_is_fit = data_small(:,12); % Isentropic enthalphy difference across
compressor [kJ/kg]
rho_Suc_fit = data_small(:,13);   % Suction density     [kg/m^3]

%% reading all data
data = load('Copeland_Scroll_extrapolationtesting.txt');
P_Suc = data(:,1);               % Suction pressure     [kPa]
P_Dis = data(:,2);               % Discharge pressure   [kPa]
eta_V=data(:,3);                 % Volumetric efficieny [-]
m_dot = data(:,4);               % Mass flow rate       [kg/s]
P_input = data(:,5);             % Power draw           [kW]
eta_is_O = data(:,6);            % Overall isentropic efficiency [-]
eta_is = data(:,7);              % Isentropic efficiency [-]
T_Suc = data(:,8);               % Suction temperature  [C]
T_Dis = data(:,9);               % Discharge temperature [C]
T_Dis_is = data(:,10);           % Isentropic discharge temperature [C]
T_amb = data(:,11);              % Ambient compressor temperature [C]
DELTAh_is = data(:,12);          % Isentropic enthalphy difference across compressor
[kJ/kg]
rho_Suc = data(:,13);            % Suction density     [kg/m^3]

%k = 1.073859;                   % (R410A) Polytropic coefficient used as isentropic
refrigerant coefficient
k = 1.047152;                    % (R407C) Polytropic coefficient used as isentropic
refrigerant coefficient
N_Comp = 60;                      % Compressor speed     [Hz]

```

```

V_Comp = 0.00006528333;      % Compressor displacement [m^3]

%% Calling Empirical Curves
% Initial Guess for eta_V coefficients
b0 = [0 0 0];
a0 = [0 0 0 0];

% Establishing LMA choice for least squares analysis
options=optimoptions(@lsqnonlin, 'Algorithm', 'levenberg-marquardt');
% Finding the coefficients for the eta_V curve via least squares analysis
[b, resnorm_eta_V]=lsqnonlin(@(b) Mendoza_SemiEmpirical_eta_V(P_Suc_fit',
P_Dis_fit', eta_V_fit', b), b0, [],[],options)
[a, resnorm_P_input] = lsqnonlin(@(a)
Mendoza_SemiEmpirical_eta_is_O(P_Suc_fit', P_Dis_fit', T_Suc_fit',
T_Dis_is_fit', T_amb_fit', eta_is_O_fit', a), a0, [],[],options)

%% Calculating Performance based on empirical curves
pi_V2 = zeros(1, size(data,1));
pi_V4 = zeros(1, size(data,1));
pi_V5 = zeros(1, size(data,1));
pi_iso2 = zeros(1, size(data,1));
pi_iso3 = zeros(1, size(data,1));
pi_iso6 = zeros(1, size(data,1));
pi_iso7 = zeros(1, size(data,1));
eta_V_curve = zeros(1, size(data,1));
eta_is_O_curve = zeros(1, size(data,1));
m_dot_curve = zeros(1, size(data,1));
P_input_curve = zeros(1, size(data,1));
count = zeros(1, size(data,1));
for i=1:1:size(data,1)
    % Volumetric Efficiency from Mendoza (2016)
    pi_V2(i) = P_Dis(i)/P_Suc(i);
    pi_V4(i) = 1;
    pi_V5(i) = 1;

    eta_V_curve(i) = (pi_V2(i)^(b(1)))*(pi_V4(i)^(b(2)))*(pi_V5(i)^(b(3)));

    % Overall Isentropic Efficiency from Mendoza (2016)
    pi_iso2(i) = P_Dis(i)/P_Suc(i);
    pi_iso3(i) = 1;
    pi_iso6(i) = 1/(((T_Suc(i) + T_Dis_is(i))/2) - T_amb(i));
    pi_iso7(i) = 1;

    eta_is_O_curve(i) =
(pi_iso2(i)^(a(1)))*(pi_iso3(i)^(a(2)))*(pi_iso6(i)^(a(3)))*(pi_iso7(i)^(a(4)
));

    count(i) = i;

    % Calculation of mass flow rate and power
    m_dot_curve(i) = rho_Suc(i)*V_Comp*N_Comp*eta_V_curve(i);
    P_input_curve(i) = (m_dot_curve(i)*DELTAh_is(i))/(eta_is_O_curve(i));
end

```

```

%% Plotting performance from empirical curves

figure
plot(count, eta_V, 'o')
hold on
plot(count, eta_V_curve, 'o')
grid on
xlim([0 size(data,1)+1])
xticks([0:1:size(data,1)+1])

figure
plot(count, eta_is_0, 'o')
hold on
plot(count, eta_is_0_curve, 'o')
grid on
xlim([0 size(data,1)+1])
xticks([0:1:size(data,1)+1])

figure
plot(count, m_dot, 'o')
hold on
plot(count, m_dot_curve, 'o')
grid on
xlim([0 size(data,1)+1])
xticks([0:1:size(data,1)+1])

figure
plot(count, P_input, 'o')
hold on
plot(count, P_input_curve, 'o')
grid on
xlim([0 size(data,1)+1])
xticks([0:1:size(data,1)+1])

% figure
% plot(eta_V, eta_V_curve, 'o')
% grid on
% xlim([0.75 1])
% xticks([0.75:0.05:1])
% ylim([0.75 1])
% yticks([0.75:0.05:1])
%
% figure
% plot(eta_is_0, eta_is_0_curve, 'o')
% grid on
% xlim([0.5 0.7])
% xticks([0.5:0.05:0.7])
% ylim([0.5 0.7])
% yticks([0.5:0.05:0.7])

%% Writing data to a text file

file_name = 'Scroll_Mendoza_Correlation_extrapolation_0313.xlsx';

```

```
P_input_curve = P_input_curve';
m_dot_curve = m_dot_curve';
eta_V_curve = eta_V_curve';
eta_is_0_curve = eta_is_0_curve';

OUTPUT = table(P_input, P_input_curve, eta_V, eta_V_curve, m_dot,
m_dot_curve, eta_is_0, eta_is_0_curve);
writetable(OUTPUT,file_name,'Sheet',1,'Range','B2')

COEFFICIENTS = table(a, b, resnorm_eta_V, resnorm_P_input);
writetable(COEFFICIENTS,file_name,'Sheet',1,'Range','B50')

TRAINING = table(P_Suc_fit, P_Dis_fit, eta_V_fit, m_dot_fit, P_input_fit,
eta_is_0_fit, eta_is_fit, T_Suc_fit, T_Dis_fit, T_Dis_is_fit, T_amb_fit,
DELTAh_is_fit, rho_Suc_fit);
writetable(TRAINING,file_name,'Sheet',2,'Range','B2')

TESTING = table(P_Suc, P_Dis, eta_V, m_dot, P_input, eta_is_0, eta_is, T_Suc,
T_Dis, T_Dis_is, T_amb, DELTAh_is, rho_Suc);
writetable(TESTING,file_name,'Sheet',3,'Range','B2')
```

## APPENDIX O: MENDOZA-MIRANDA CORRELATION LEAST SQUARES SOLVERS

### VOLUMETRIC EFFICIENCY

```
function eta_V_reldiff = Mendoza_SemiEmpirical_eta_V(P_Suc, P_Dis, eta_V, b)
%%%%%%%%%%%%%%%%%%%%%%%%%%%%%%%%%%%%%%%%%%%%%%%%%%%%%%%%%%%%%%%%%%%%%%%%
%%%%%%%%%%%%%%%%%%%%%%%%%%%%%%%%%%%%%%%%%%%%%%%%%%%%%%%%%%%%%%%%%%%%%%%%
% This function returns the relative difference between the semi empirical
% volumetric efficiency from Mensoza (2016) to the actual volumetric
efficiency
% found in the data set provided by the parent script)
%%%%%%%%%%%%%%%%%%%%%%%%%%%%%%%%%%%%%%%%%%%%%%%%%%%%%%%%%%%%%%%%%%%%%%%%

%Calculation of semi-empirical volumetric efficiency using 3 constants
%eta_V_curve = b(1) + b(2)*((P_Dis./(P_Suc*(1 - b(3))))^(1/k));
pi_2 = P_Dis./P_Suc;
pi_4 = 1;
pi_5 = 1;

eta_V_curve = (pi_2^(b(1))).*(pi_4^(b(2))).*(pi_5^(b(3)));
%Calculation of the difference between the semi-empirical efficiency to the
%actual efficiency
eta_V_diff = eta_V_curve - eta_V;

%Relative difference between the two efficiencies in decimal units
eta_V_reldiff = abs(eta_V_diff./eta_V);

end
```

### OVERALL ISENTROPIC EFFICIENCY

```
function eta_is_O_reldiff = Mendoza_SemiEmpirical_eta_is_O(P_Suc, P_Dis,
T_Suc, T_Dis_is, T_amb, eta_is_O, a)
%%%%%%%%%%%%%%%%%%%%%%%%%%%%%%%%%%%%%%%%%%%%%%%%%%%%%%%%%%%%%%%%%%%%%%%%
%%%%%%%%%%%%%%%%%%%%%%%%%%%%%%%%%%%%%%%%%%%%%%%%%%%%%%%%%%%%%%%%%%%%%%%%
% This function returns the relative difference between the semi empirical
% overall isentropic efficiency from Mensoza (2016) to the actual overall
isentropic efficiency
% found in the data set provided by the parent script)
%%%%%%%%%%%%%%%%%%%%%%%%%%%%%%%%%%%%%%%%%%%%%%%%%%%%%%%%%%%%%%%%%%%%%%%%

%Calculation of semi-empirical overall isentropic efficiency using 4
constants
pi_2 = P_Dis./P_Suc;
pi_3 = 1;
pi_6 = 1./(((T_Suc + T_Dis_is)./2) - T_amb);
pi_7 = 1;
```

```
eta_is_0_curve =  
(pi_2.^(a(1))).*(pi_3.^(a(2))).*(pi_6.^(a(3))).*(pi_7.^(a(4)));  
%Calculation of the difference between the semi-empirical efficiency to the  
%actual efficiency  
eta_is_0_diff = eta_is_0_curve - eta_is_0;  
  
%Relative difference between the two efficiencies in decimal units  
eta_is_0_reldiff = abs(eta_is_0_diff./eta_is_0);  
  
end
```